3D Induced-Pluripotent Stem Cell Model of Metabolic Heart Diseases for Drug Discovery and Disease Modelling



Ujang Purnama

Merton College

Department of Physiology, Anatomy and Genetics

University of Oxford

A thesis submitted for the degree of *Doctor of Philosophy*

Trinity Term 2022

Acknowledgements

This four-year work presented in this thesis was completed with the support and contribution of a number of people. I am very grateful for the opportunity to contribute to the advancement of the scientific field. This work would not have been possible without the support from the funding of Indonesia Endowment Fund for Education (LPDP) scholarship – Ministry of Finance Republic of Indonesia, Rosetrees Trust, and Novo Nordisk. I would like to firstly thank my supervisor Professor Carolyn Carr for a countless support, advice, and guidance throughout my challenging yet rewarding learning journey and for the availability for scientific discussion whenever and wherever. I would also like to thank Professor Lisa Heather for the advice, her valuable scientific input, and ideas. Thank you to Professor Kim Dora for the support from the start until the end of my DPhil project. I also owe a thank you to my transfer, confirmation of status, and viva examiners Prof. Nicola Smart, Dr. Sevasti Zervou, Dr. Oliver Rider, Dr. Katja Gehmlich, and Prof. Luc Bertrand for their valuable contribution.

I would also like to give a huge thank you to past and present members of the CMRG for making my DPhil enjoyable and for their friendship and advice: Dr. Cher-Rin Chong, Dr. Matthew Kerr, Dr. Sophia Malandraki-Miller, Dr. Azrul Abdul Kadir, Dr. Colleen Lopez, Dr. Maria da Luz Sousa Fialho, Dr. David Dearlove, Dr. Kerstin Timm, Dr. Jack Miller, Dr. James Grist, Dr. Justin Lau, Dr. Tony Zhou, Vicky Ball, Stephanie Anderson, Ryan Carter, Kaitlyn Dennis, Riona Devereux, Prof. Damian Tyler, Dr. Rhys Evans, and Prof. Kieran Clark for the advice and support. In particular, to Claudia Montes Aparicio for being a great friend, providing help, technical and emotional support in the lab since day one of my DPhil journey. To my cell culture squad, Marcos Castro-Guarda for his kindness, generosity, and helping me with experiments even at an abnormal time like 11pm at night when I was

finishing up. To Dr. Rita Alonaizan, Hazal Gezmis, Dr. Sonia Iftekhar, Fatemeh Kermani, Kirsti Brisk, and Mala Gunadasa-Rohling for the friendship, advice and genuine help on all experiment and cell culture related.

I would also like to thank collaborators and everyone who helped and assisted me throughout this research: Dr. Andreas Koschinski, Dr. Sally Cowley, and Emmanuelle Massourides for the iPS cell lines and advice on cell culture techniques, Dr. Yuling Ma and Dr. Taiyi Wang for help with cell culture, patch clamp and multielectrode array, Dr. Michal Maj and Ni Li for help with flow cytometry, Magda Woulna for SR-FTIR experiments, Dr. Alan Wainman at the Dunn School Bioimaging Facility, and the administration and support team at DPAG including Sarah Noujaim, Talitha Smith, Philip Thornton-Evison, Gary Mort, and Lee Brown. Adding to this list, I would like to thank my students: Abigail Tankard, Sichen Liu, Anna McQueen, and Madeline Oshodi for assisting me in my experiments.

A huge thank you also goes to my colleague/friends who also happened to be my housemates: Dr. Javier Gilbert-Jaramillo, Catriona Rooney, Indra Rudiansyah, et al., and Jeff Touchard-Paxton and the Touchard-Paxton family for the friendship, laughter, and keeping me sane during several periods of lockdowns during a pandemic and motivating me to keep up with my thesis through scientific discussion, data analysis, and most importantly English and grammatical help.

Finally, a very special thank you to my family for the support. To my parents for the unconditional love and encouragement. I would not be here without all you have done for me, and I am very grateful to be part of the family.

Abstract

Cardiovascular disease is the leading cause of mortality in patients with cardiometabolic diseases such as type 2 diabetes. Elucidating and understanding the early stages of the disease is vital for seeking possible treatments. Despite numerous studies using in vitro and animal models, current preclinical models do not accurately recapitulate the adult human heart. Moreover, there are noticeable differences between rodents and humans, providing a challenge when studying the effect of cardiometabolic diseases. Therefore, there is a pressing need for an in vitro model to bridge the gap, to aid identification of disease mechanism and to provide an accurate, predictive tool for drug testing. Human induced-pluripotent stem cell-derived cardiomyocytes (hiPSC-CMs) have potential as a predictive tool but are hindered by their immature phenotype.

The work presented in this thesis aims to answer several questions regarding the potential of using matured hiPSC-CM cultured in 2D and 3D cell culture (as engineered heart tissue) as an advanced in vitro model, to model cardiometabolic diseases such as type 2 diabetes and Duchenne muscular dystrophy (DMD). To improve the maturation of hiPSC-CMs, culturing the cells in 2D and 3D in a media containing oleic acid resulted in maturation of sarcomere actinin structure, electrophysiological properties, gene expression, and a metabolic switch to fatty acid oxidation, recapitulating more mature cardiomyocytes. The effect of oleic acid supplementation on the hiPSC-CM maturation was also characterised using novel synchrotron-based micro-FTIR absorption spectroscopy.

Modelling the effect of type 2 diabetes on hiPSC-CMs was performed by exposing the 2D and 3D cultured cells to a diabetic medium, which was developed by manipulating concentrations of glucose, insulin, and palmitic acid. An increase in fatty acid metabolism and a blunted insulin signalling cascade in hiPSC-CMs cultured in this media was observed,

indicating that the cells had become insulin resistant. Modelling the effect of DMD was performed by using DMD patient-derived hiPSCs. Structural and metabolic maturation of hiPSC-CMs from DMD patients were found to be delayed in comparison to that of a healthy cell line. DMD hiPSC-CMs had altered functional properties such as reduced contraction speed and force. Insulin resistance was also observed in the DMD hiPSC-CMs, suggesting insulin resistance in DMD patients may be partly endogenous.

Finally, healthy, insulin resistant, and DMD hiPSC-CMs in 2D and 3D (engineered heart tissue – EHT) were treated with several drugs such as isoprenaline, isoliquiritigenin, metformin, perhexiline, and molidustat, to assess if the cell models recapitulate the human and animal model findings.

Overall, the results show that metabolically matured hiPSC-CMs cultured in 2D, or 3D generate a clinically relevant in vitro model to study the pathophysiological effects of cardiometabolic diseases. This can be a valuable predictive tool to speed up the drug discovery process and improve candidate drug success in clinical trials.

Research Outcomes

Publications:

1. **Purnama, U**., Castro-Guarda, M., Saswat, O.M., Carr, C. (2022). Modelling diabetic cardiomyopathy: using human stem cell derived cardiomyocytes to complement animal models. *MDPI Metabolites.*
2. **Purnama, U***., da Luz Sousa Fialho, M*., Dennis, K. M., Montes Aparicio, C. N., Castro-Guarda, M., Massourides, E., Tyler, D. J., Carr, C. A., & Heather, L. C. (2021). Activation of HIF1α Rescues the hypoxic response and reverses Metabolic dysfunction in the diabetic heart. *Diabetes*, db210398. https://doi.org/10.2337/db21-0398
3. Lopez, C. A., Al-Siddiqi, H., **Purnama, U**., Iftekhar, S., Bruyneel, A., Kerr, M., Nazir, R., da Luz Sousa Fialho, M., Malandraki-Miller, S., Alonaizan, R., Kermani, F., Heather, L. C., Czernuszka, J., & Carr, C. A. (2021). Physiological and pharmacological stimulation for in vitro maturation of substrate metabolism in human induced pluripotent stem cell-derived cardiomyocytes. *Scientific reports*, *11*(1), 7802. https://doi.org/10.1038/s41598-021-87186-y
4. Wang, T., Streeter, H., Wang, X., **Purnama, U**., Lyu, M., Carr, C., & Ma, Y. L. (2019). A Network Pharmacology Study of the Multi-Targeting Profile of an Antiarrhythmic Chinese Medicine Xin Su Ning. *Frontiers in pharmacology*, *10*, 1138. https://doi.org/10.3389/fphar.2019.01138
5. Malandraki-Miller, S., Lopez, C. A., Alonaizan, R., **Purnama, U.**, Perbellini, F., Pakzad, K., & Carr, C. A. (2019). Metabolic flux analyses to assess the differentiation of adult cardiac progenitors after fatty acid supplementation. *Stem cell research*, *38*, 101458. https://doi.org/10.1016/j.scr.2019.101458

***** *Denotes authors contributed equally*

Manuscripts under review process for publication:

1. Gilbert-Jaramillo, J., **Purnama, U.**, Molnar, Z., James, W. (2022). Zika virus-induces metabolic alterations in foetal neuronal progenitors that could influence in neurodevelopment during early pregnancy. *Submitted to review*. *BioRxiv*. https://doi.org/10.1101/2022.08.24.505080

Scientific presentations:

Oral

1. Ujang Purnama, Maria da Luz Sousa Fialho, Kaitlyn MJH Dennis, Claudia N Montes Aparicio, Marcos Castro-Guarda, Damian J Tyler, Carolyn Carr, Lisa Heather. *Activation of HIF1α rescues the hypoxic response and reverses metabolic dysfunction in the diabetic heart*. Society for Heart and Vascular Metabolism (SHVM) Annual Conference. Jena, Germany, 23 – 24 September 2021. **The best pitch award winner**
2. Ujang Purnama, Lisa C Heather, Carolyn A Carr. *Modelling the human diabetic heart, using engineered heart tissue, for in vitro testing of cardioprotective drugs.* Oxford Metabolic Health (OMH) Annual Symposium. Oxford, UK, 8 July 2021. **OMH oral prize winner**
3. Ujang Purnama. *Modelling human diabetic heart using engineered heart tissue for in vitro testing of cardioprotective drugs.* Sherrington Talks. Oxford, UK. 11 June 2021.

4. Ujang Purnama. *Human iPSC-CM and engineered heart tissue as a platform to model the human diabetic heart for viersonalized medicine*. Personalised Medicine Annual Symposium. Oxford, UK, 11 March 2021.

Posters

1. Ujang Purnama, Lisa C Heather, Carolyn A Carr. *Generating insulin-resistant engineered heart tissue to provide a human in vitro model of the diabetic heart for disease modelling and drug testing*. International Society for Stem Cell Research (ISSCR) Annual Conference, San Francisco, USA. 15 – 18 June 2022
2. Ujang Purnama, Anna McQueen, Madeline Oshodi, Carolyn A Carr. *Investigating the utilisation of human induced pluripotent stem cell-derived cardiomyocytes to study metabolic alterations in the heart of Duchenne muscular dystrophy patients*. International Society for Heart Research (ISHR) Annual Conference, Berlin, Germany. 12 – 15 June 2022
3. Ujang Purnama, Lisa C Heather, Carolyn A Carr. *Modelling the human diabetic heart, using engineered heart tissue, for in vitro testing of cardioprotective drugs.* International Society for Stem Cell Research (ISSCR) Annual Conference, virtual meeting, 21 – 26 June 2021. Winning the first prize winner for the ISSCR 2021 Annual Meeting through active participation in the meeting, featured in member spotlight
4. Ujang Purnama, Lisa C Heather, Carolyn A Carr. *Modelling the human diabetic heart, using engineered heart tissue, for in vitro testing of cardioprotective drugs.* EMBO Workshop: Cardiomyocyte Biology Virtual Meeting. Ascona, Switzerland, 30 May – 2 June 2021
5. Ujang Purnama. *Fatty acid-stimulated maturation of human iPSC-derived cardiomyocytes in engineered heart tissue*. Sherrington poster day for second year graduate students. Oxford, UK, 8 November 2019
6. Ujang Purnama, Colleen A Lopez, Taiyi Wang, Carolyn A Carr. *Fatty acid-stimulated maturation of hiPSC-derived cardiomyocytes in engineered heart tissue*. British Heart Foundation Research of Excellent (BHF CRE) Annual Conference. Oxford, UK, 2 October 2019
7. Ujang Purnama, Colleen A Lopez, Carolyn A Carr. *Fatty acid-stimulated maturation of human iPSC-derived cardiomyocytes in engineered heart tissue*. British Society for Cardiovascular Research (BSCR) Autumn meeting. Cambridge, UK, 9-10 September 2019 (**published abstract**)

Table of Contents

1 INTRODUCTION 2

1.1 CARDIOMETABOLIC DISEASES 2
1.2 METABOLISM IN THE HEALTHY ADULT HEART 2
1.3 METABOLISM IN THE FOETAL HEART 5
1.4 DIABETIC CARDIOMYOPATHY 6
1.4.1 Metabolism in diabetic cardiomyopathy 8
1.4.2 Mechanisms implicated in the pathology of diabetic cardiomyopathy 10
1.5 CARDIAC INSULIN RESISTANCE DUE TO DUCHENNE MUSCULAR DYSTROPHY 16
1.6 METABOLISM IN THE HEART IN DUCHENNE MUSCULAR DYSTROPHY 19
1.7 MODELLING CARDIOMETABOLIC DISEASES 19
1.7.1 Animal models and primary tissue 20
1.7.2 Human induced-pluripotent stem cell derived cardiomyocytes (hiPSC-CM) 22
1.7.3 Organoids and Organ-on-a-chip 24
1.7.4 Engineered heart tissue (EHT) 24
1.8 THESIS AIMS 27

2 MATERIALS AND METHODS 30

2.1 HUMAN INDUCED PLURIPOTENT STEM CELLS LINES 30
2.1.1 Healthy cells 30
2.1.2 Duchene Muscular Dystrophy (DMD) cells 30
2.2 HUMAN IPSC CELL CULTURE 31
2.2.1 Maintenance of human iPSC cell culture 31
2.2.2 Recovery of human iPSCs 31
2.2.3 Passaging protocol 31
2.2.4 Freezing human iPSCs for long term storage 32
2.2.5 Human induced-pluripotent stem cell differentiation into cardiomyocytes 32
2.2.6 Dissociation and replating of Human iPSC-CM 33
2.3 GENERATING ENGINEERED HEART TISSUE 34
2.4 QUANTITATIVE PCR 36
2.4.1 Primer Design 36
2.4.2 Total RNA extraction and purification 36
2.4.3 Complementary DNA (cDNA) synthesis 37
2.4.4 Quantitative PCR reaction 38
2.4.5 Analysis of qPCR data 39
2.5 IMMUNOHISTOCHEMISTRY AND IMMUNOCYTOCHEMISTRY 39
2.5.1 Tissue Cryo-sectioning 39
2.5.2 Sample preparation for immunostaining 39
2.5.3 Immunostaining 40

2.5.4 Oil Red O staining *40*
2.5.5 MitoTracker red CMXRos staining *40*
2.6 FLOW CYTOMETRY 41
2.7 ASSESSING CELL METABOLISM USING RADIOLABELLED COMPOUNDS 42
2.7.1 Glycolytic flux (5-^{3}H-glucose) *42*
2.7.2 ^{3}H palmitate oxidation and ^{3}H oleate oxidation *44*
2.8 ASSESSING CELL METABOLISM USING ENZYMATIC REACTION AND PENTRA ANALYSIS 46
2.8.1 Lactate assay *46*
2.8.2 Glucose assay *46*
2.8.3 Lactate dehydrogenase (LDH) Assay *47*
2.9 ASSESSING CELL VIABILITY 47
2.9.1 Alamar Blue assay *47*
2.9.2 Cell counting kit-8 (CCK-8) *47*
2.9.3 Automated cell counting *48*
2.10 WESTERN BLOT 48
2.11 MUSCLEMOTION 49
2.12 MULTIELECTRODE ARRAY 49
2.13 PATCH CLAMP 51
2.14 PROTEOMICS AND TRANSCRIPTOMICS ANALYSIS 52
2.15 TRANSMISSION ELECTRON MICROSCOPY (TEM) 52
2.16 STATISTIC AND DATA ANALYSIS 53

3 METABOLIC MATURATION OF HUMAN INDUCED PLURIPOTENT STEM CELLS DERIVED CARDIOMYOCYTES IN 2D AND ENGINEERED HEART TISSUE 55

3.1 ABSTRACT 55
3.2 INTRODUCTION 56
3.2.1 Differentiation of human iPSCs into cardiomyocytes *56*
3.2.2 Maturation of human iPSC-CM *57*
3.3 CHAPTER AIMS 60
3.4 MATERIALS AND METHODS 61
3.4.1 Human iPSCs differentiation into cardiomyocyte *61*
3.4.2 Reagent preparation and treatment *61*
3.4.3 Sample preparation for infra-red (IR) spectroscopy *62*
3.4.4 Engineered heart tissue *62*
3.5 RESULTS 63
3.5.1 Differentiating iPSC into cardiomyocytes using modified GiWi protocol *63*
3.5.2 The effect of oleic acid and PPAR agonist on iPSC-CM maturation *68*
3.5.3 Synchrotron-based micro-FTIR absorption spectroscopy for characterising oleate enhancement of maturation of cardiomyocytes *75*

3.5.4 Engineered heart tissue increases cell maturation *79*
3.5.5 Combination of engineered heart tissue and metabolic maturation further increased cell maturation *82*
3.6 DISCUSSION 90
3.6.1 GiWi Protocol by activating and inhibiting Wnt pathway with Wnt-c59 molecules improves differentiation outcomes *90*
3.6.2 Addition of oleic acid and PPAR agonist enhances hiPSC-CM maturation *91*
3.6.3 Combination of engineered heart tissue and metabolic maturation further increase cell maturation *93*
3.7 CONCLUSION 95
4 MODELLING THE EFFECT OF DIABETES ON HUMAN IPSC-CM IN 2D AND EHT 97
4.1 ABSTRACT 97
4.2 INTRODUCTION 98
4.2.1 Insulin resistance in diabetic cardiomyopathy *98*
4.2.2 Modelling diabetic cardiomyopathy using hiPSC-CM *98*
4.3 CHAPTER AIMS 100
4.4 MATERIALS AND METHODS 101
4.4.1 Protocol to induce insulin resistance in hiPSC-CM in 2D and EHT *101*
4.4.2 Insulin resistance in hiPSC-CMs analysis using qPCR, Western blot, radiolabelled experiment, muscle motion, proteomic and transcriptomic analysis *102*
4.4.3 Cell viability assay *102*
4.4.4 Proteomics and transcriptomics *103*
4.5 RESULTS 104
4.5.1 Human iPSC-CM in 2D and EHT treatment with palmitic acid *104*
4.5.2 Further optimisations of the protocol to induce insulin resistance in human iPSC-CMs in 2D and EHT *108*
4.5.3 Characterising the effect of insulin resistance on hiPSC-CM in 2D and EHTs *111*
4.5.4 Metabolic changes in hiPSC-CM in 2D monolayer and EHT using the IR media *113*
4.5.5 Assessing the effect of insulin resistance in 2D and EHT during hypoxia *116*
4.5.6 Assessing the effect of insulin resistance on subcellular structure of hiPSC-CM in 2D and EHTs using Transmission electron microscopy *120*
4.5.7 Assessing the effect of insulin resistance on contractility using Musclemotion *122*
4.5.8 Assessing the effect of insulin resistance on the inflammatory cytokines *125*
4.5.9 Assessing protein and gene expression using proteomic and transcriptomic analysis *125*
4.6 DISCUSSION 130
4.7 CONCLUSION 134

5 DRUG TESTING ON HEALTHY AND INSULIN RESISTANT HUMAN INDUCED PLURIPOTENT STEM CELL DERIVED CARDIOMYOCYTES IN 2D AND EHT 136

5.1 ABSTRACT 136
5.2 INTRODUCTION 137
5.2.1 Isoprenaline and isoliquiritigenin 138
5.2.2 Metformin 138
5.2.3 Perhexiline 139
5.2.4 Molidustat (HIF stabilisator) 140
5.3 CHAPTER AIMS 142
5.4 MATERIALS AND METHODS 142
5.4.1 Preparation of the drugs used for the experiments 142
5.5 RESULTS 144
5.5.1 Assessing the effect of isoliquiritigenin and isoprenaline on healthy human iPSC-CM in 2D monolayer and EHT 144
5.5.2 Assessing the effect of isoprenaline on IR EHT 149
5.5.3 Assessing the effect of metformin on healthy and insulin resistant hiPSC-CM in 2D monolayer and EHT 150
5.5.4 Assessing the effect of perhexiline on healthy and insulin resistant hiPSC-CM in 2D monolayer and EHT 157
5.5.5 Molidustat activates HIF1α signalling and downstream metabolic adaptation in human cardiomyocytes 161
5.5.6 Molidustat overrides the blunted HIF signalling caused by insulin resistance 166
5.6 DISCUSSION 169
5.6.1 The effect of isoliquiritigenin and isoprenaline in hiPSC-CMs cultured in 2D and EHT 169
5.6.2 The effect of metformin on insulin-resistant hiPSC-CM in 2D and EHT 169
5.6.3 The effect of Perhexiline on insulin-resistant hiPSC-CM in 2D and EHT 170
5.6.4 Molidustat can restore HIF signalling in hiPSC-CM in 2D and EHT 171
5.7 CONCLUSION 172

6. MODELLING THE EFFECT OF DUCHENNE MUSCULAR DYSTROPHY ON HUMAN IPSC-CM IN 2D AND EHT 174

6.1 ABSTRACT 174
6.2 INTRODUCTION 175
6.3 CHAPTER AIMS 176
6.4 MATERIALS AND METHODS 176
6.5 RESULTS 177
6.5.1 Investigating the effect of Duchenne muscular dystrophy (DMD) on metabolism in the heart using hiPSC-CMs model in 2D and EHTs 177

6.5.2 Validation of dystrophin mutation in hiPSC-CM *177*
6.5.3 Characterisation of the structure of hiPSC-CM from DMD patients *180*
6.5.4 Metabolism in hiPSC-CM from DMD patients *183*
6.5.5 The contractility of hiPSC-CM from control and DMD *185*
6.5.6 The effect of isoprenaline on DMD EHT *187*
6.5.7 The effect of metformin on DMD hiPSC-CM in 2D and EHT *188*
6.6 DISCUSSION 190
6.7 CONCLUSION 193
7. GENERAL DISCUSSION 195
7.1 THESIS FINDINGS AND DISCUSSION 195
7.2 CONCLUSION 198
7.3 STUDY LIMITATIONS AND CHALLENGES 198
7.4 FUTURE DIRECTIONS 200
APPENDICES 201
BIBLIOGRAPHY 212

Abbreviations

2D	Two dimensional
3D	Three dimensional
ABA	Alamar Blue
ACEI	Angiotensin-converting enzyme inhibitor
AGE	Advanced glycation end product
AMPK	5’ adenosine monophosphate-activated protein kinase
ATP	Adenosine Triphosphate
BCA	Bicinchoninic acid
BMP4	Bone morphogenetic protein 4
BNIP3	bcl2/adenovirus E1B 19kDa-interacting protein 3
BSA	Bovine serum albumin
BTS	N-Benzyl-p-toluenesulfonamide
CCK-8	Cell counting kit 8
cDNA	Complementary DNA
COVID-19	Corona virus disease 2019
CPT1	Carnitine palmitoyltransferase 1
CVPT	Catecholaminergic polymorphic ventricular tachycardia
Cx-43	Connexin-43
DAG	Diacylglycerol
DAPC	Dystrophin-associated protein complex
DAPI	4′,6-diamidino-2-phenylindole
DbCM	Diabetic cardiomyopathy
DGC	Dystrophin-associated glycoprotein complex
DM	Diabetes mellitus
DMD	Duchenne muscular dystrophy
DMEM	Dulbecco’s Modified Eagle Media
DMSO	Dimethyl sulfoxide
DNA	Deoxyribonucleic acid
dNTP	Deoxynucleotide triphosphate
DPBS	Dulbecco’s phosphate-buffered saline
EB	Embryoid body
EBSS	Earle’s balance salt solution
EHT	Engineered heart tissue
ER	Endoplasmic reticulum
FA	Fatty acid
FABP	Fatty acid binding protein
$FADH_2$	Flavin adenine dinucleotide
FAO	Fatty acid oxidation
FATP	Fatty acid transport protein
FIH	Factor inhibiting HIF
FOXO1	Forkhead box protein O1
FPS	Frame per second
FTIR	Fourier transform infrared
GAPDH	Glyceraldehyde-3-phosphate dehydrogenase
GC	Guanine cytosine
GFR Matrigel	Growth factor reduced Matrigel
GLUT1	Glucose transporter type 1

GLUT4	Glucose transporter type 4
GRMD	Golden retriever muscular dystrophy
GSK-3β	Glycogen synthase kinase - 3β
HCl	Hydrochloric acid
HEPES	4-(2-hydroxyethyl)-1-piperazineethanesulfonic acid
hESC	Human embryonic stem cell
HFpEF	Heart failure with preserved ejection fraction
HIF1α	Hypoxia inducible factor 1α
hiPSC	Human induced pluripotent stem cell
hiPSC-CM	Human induced pluripotent stem cell derived cardiomyocytes
HK	Hexokinase
HKG	Housekeeping gene
Hx	Hypoxia
IKK-β	Inhibitor of nuclear factor kappa-B kinase subunit β
IL-6	Interleukin-6
IR	Infrared or insulin resistance
IRS (1/2)	Insulin receptor substrate (1/2)
JNK	c-Jun N-terminal kinase
KCl	Potassium chloride
KOH	Potassium hydroxide
LDHA	Lactate dehydrogenase A
LKB1	Liver kinase B 1
MAPK	Mitogen-activated protein kinase
MCP-1	Monocyte chemoattractant protein – 1
MEA	Multielectrod array
miR-451	MicroRNA-451
MLC2v	Ventricular myosin light chain 2
mRNA	Messenger RNA
mTOR	Mammalian target of rapamycin
MYH6/7	Myosin heavy chain 6/7
NADH	Nicotinamide adenine dinucleotide
NF-κB	Nuclear factor kappa B
NKM	Nicht Kardiomyozyten Medium
Nx	Normoxia
OA	Oleic acid or Oleate
OCT	Optimal cutting temperature
ORO	Oil red o
PA	Palmitic acid or Palmitate
pAkt	Phosphorylated Akt
PDH	Pyruvate dehydrogenase
PDK (1/4)	Pyruvate dehydrogenase kinase (1/4)
PDMS	Polydimethylsiloxane
PFA	Paraformaldehyde
PFK	Phosphofructokinase
PHD2	Prolyl hydroxylase 2
PGC1α	Peroxisome proliferator-activated receptor gamma co-activator-1α
PI3K	Phosphatidylinositol 3-kinase
PKC	Protein kinase C
PPARα	Peroxisome proliferator-activated receptor α
qPCR	Quantitative Polymerase Chain Reaction

RAAS	Renin-angiotensin-aldosterone system
RB-	RPMI with 1% B27 minus insulin
RB+	RPMI with 1% B27 complete
RGD	Arginylglycylaspartic acid
RNA	Ribonucleic acid
ROCK	Rho-associated protein kinase
ROS	Reactive oxygen species
RPM	Revolutions per minute
RPMI	Roswell Park Memorial Institute 1640
RT	Room temperature
RTK	Receptor tyrosine kinase
SARS-CoV-2	Severe acute respiratory syndrome coronavirus 2
SDS-PAGE	Sodium dodecyl sulphate–polyacrylamide gel electrophoresis
SR	Synchrotron radiation
SREBP-1	Sterol regulatory binding protein 1
STZ	Streptozocin
T1DM	Type 1 diabetes mellitus
T2DM	Type 2 diabetes mellitus
TAG	Triacylglycerol
TCA	Tricarboxylic acid
TEM	Transmission electron microscopy
TF	Transcription factor
TGFβ	Transforming growth factor beta
TNF	Tumour necrosis factor
UCP	Uncoupling protein
VHL	Von Hippel-Lindau
VN	Vitronectin
ZDF	Zucker diabetic fatty
ZV	Zombie violet



INTRODUCTION

CHAPTER 1

1 INTRODUCTION

1.1 Cardiometabolic diseases

Cardiovascular diseases are the main cause of death worldwide with cardiometabolic diseases (e.g., type-2 diabetes mellitus) as one of the risk factors[1]. Diabetes is a global problem affecting nearly half a billion people worldwide and projected to surpass 700 million individuals by 2045[1]. The development of diabetes increases the risk of cardiovascular disease such that 30% of diabetic patients are diagnosed with cardiovascular disease, and this is the leading cause of mortality for individuals with diabetes[2]. Cardiometabolic complications are derived from multiple causes including diet, lifestyle, living environment, genetic, and epigenetic factors[3], with the genetic factors present from birth and environmental factors developing throughout life. Acquired cardiometabolic disease or metabolic syndrome is defined as having three out of five of the following phenotypes: obesity, elevated triglycerides, reduced high-density lipoprotein cholesterol, hypertension, and elevated fasting glucose. These factors are the leading cause of diabetes-related and cardiovascular disease[4]. The growing prevalence of type-2 diabetes and insulin resistance has led to an increasing number of deaths caused by cardiometabolic disease[2]. The work in this thesis aims to generate a cardiac in vitro model of two cardiometabolic diseases linked to insulin resistance: diabetic cardiomyopathy and Duchenne muscular dystrophy (DMD).

1.2 Metabolism in the healthy adult heart

The human heart consumes approximately 6 kg of ATP, or about 20 times its own weight, per day. This energy can be generated from multiple sources such as fat, carbohydrate, protein, ketone bodies, and lactate[5]. The bulk of the energy (~95%) is generated through oxidative phosphorylation of fatty acids (FA) and glucose[6]. Fatty acid oxidation (FAO)

accounts for 70% of the total ATP produced by the heart under fasting state. Glucose metabolism yields much less ATP than FAO, with a theoretical yield of 38 moles of ATP for the complete oxidation of glucose versus 129 moles ATP per mole of palmitate. When palmitate is completely oxidised, between 1.25 – 2 more molecules of ATP are produced per carbon atom than when glucose is similarly oxidised. It is a more oxygen efficient mode of energy production, yielding 3.17 moles ATP/moles atomic oxygen utilised versus 2.8 moles ATP/moles atomic oxygen utilised for FAO of palmitate[7].

As the largest contributors for energy generation in the heart, fatty acids have an important role in heart metabolism in health and disease. Free fatty acids enter the cytoplasm of cardiomyocytes via membrane transporters such as FA translocase/CD36 (FAT/CD36), plasma membrane FA binding protein ($FABP_{pm}$), and FA transport proteins (FATP1 and 6)[8]. Insulin and AMP-activated protein kinase (AMPK) play a role in the translocation of FAT/CD36 to the membrane, which increases the uptake of fatty acids[9,10]. Once in the cytosol, FA are esterified into long chain fatty acyl-CoA (LCFA CoA) and are then stored in the myocardial lipid pool or transported into mitochondria via carnitine palmitoyl transferase-1 (CPT-1) for mitochondrial β-oxidation. This process results in acetyl-CoA molecules for the Krebs cycle and the hydrogen carriers NADH and $FADH_2$ for the electron transport chain (**Figure 1.1**).

Glucose metabolism also plays a major role in energy generation in the heart. Glucose uptake into the cytoplasm is mediated by glucose transporters (GLUT) including insulin-independent GLUT1 and insulin-dependent GLUT4. The latter is translocated to the plasma membrane in response to stimuli such as insulin and AMPK activation[11–13]. Once in the cytosol, glucose is phosphorylated by hexokinase (HK) to glucose-6-phosphate which proceeds through a variety of processes, including glycolysis, glycogenesis, pentose phosphate pathway, and hexosamine biosynthetic pathways. Small amounts of energy are

produced independently of oxygen by glycolysis which is regulated by phosphofructokinase (PFK). Depending on the oxygen availability, the end product of glycolysis, pyruvate, enters the mitochondria for oxidation or is reduced into lactate in the cytosol. When there is sufficient ATP available, cytosolic citrate from the Krebs Cycle can inhibit PFK thus reducing glucose metabolism[8].

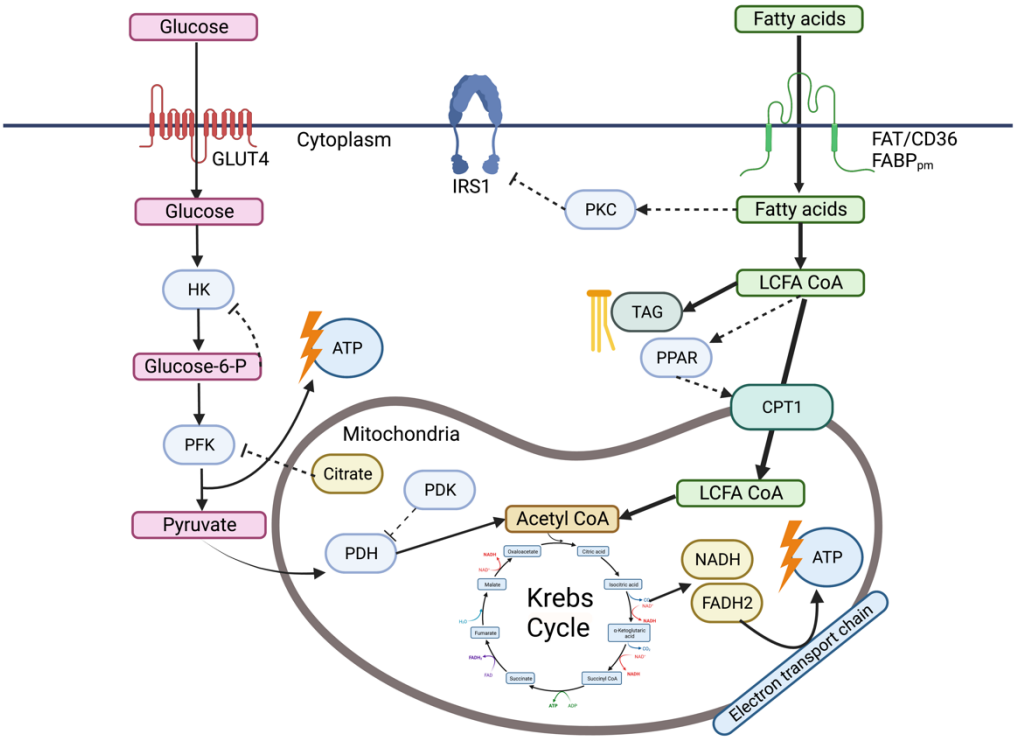


Figure 1.1 Cardiac metabolism of glucose and fatty acid in generating ATP

Illustrative images of glucose and fatty acid metabolism for energy generation. Glucose enters the sarcolemma through Glucose transporters (e.g., GLUT4) leading to production of pyruvate which is then converted to acetyl CoA to enter the Krebs Cycle. Fatty acids enter the sarcolemma through fat transporters (FAT/CD36 and FABPpm) and lead to increased LCFA CoA which inhibits pyruvate through inhibition of HK in combination with a feedback loop from glucose-6-P, PFK inhibition by citrate, and PDH inhibition by PDK to limit glycolytic flux. Increased in intracellular LCFA CoA leads to an increase in mitochondrial β-oxidation flux through CPT-1, activation of PPARα, and increased esterification to TAG. Increase fatty acid flux also leads to activation of PKC to inhibit IRS1 phosphorylation by insulin. Acetyl CoA enters the Krebs cycle to produce NADH and FADH2 and resulting in ATP production in the electron transport chain. Dashed lines represent regulatory effects. GLUT4: glucose transporter 4, HK: Hexokinase, PFK: Phosphofructokinase, Glucose-6-P: Glucose-6-phosphate, IRS1: insulin receptor 1, ATP: Adenosine triphosphate, PDH: pyruvate dehydrogenase, PDK: Pyruvate dehydrogenase kinase, LCFA CoA: long-chain fatty acid co-enzyme A, TAG: triacylglycerol, PKC: protein kinase C, CPT1: carnitine palmitoyl transferase 1.

The healthy heart is a metabolically flexible organ, able to choose the optimal substrate depending on the nutrient availability and energy status[14], for example, increasing

glycolysis when oxygen availability is low or utilising ketone bodies when fasting. This metabolic flexibility allows the heart to retain maximum ATP production in different conditions. There are key regulated steps that control the metabolic switch between fuels in the heart. For example, pyruvate dehydrogenase kinase (PDH) plays a major role in glucose metabolism by oxidative decarboxylation of pyruvate to acetyl-CoA for entry into the Krebs cycle. FAO increases the [acetyl-CoA]/[CoA] and [NADH]/[$NADH^+$] ratio which inhibit the PDH complex via PDH kinase activation[8,15,16]. Another example is cytosolic citrate, exported from the Krebs cycle, which is a major precursor of malonyl-CoA which inhibits CPT-1, thereby reducing fatty acid uptake into mitochondria and limiting β-oxidation.

1.3 Metabolism in the foetal heart

Although the adult heart has the ability to metabolise and generate energy from different substrates in the circulation, the foetal heart has a different pattern of substrate utilisation due to low levels of oxygen availability[17]. Therefore, in the foetal heart, the primary substrate preference is for carbohydrates, mainly glucose and lactate since the placenta is a rich source of lactate[18]. This environment results in glycolysis being the predominant method of energy production, with little contribution from FA β-oxidation[17]. Moreover, the lack of oxygen activates the glycolytic genes dependent of hypoxia-inducible factor 1α (HIF1α), a transcription factor (TF) which induces the expression of genes involved in glucose metabolism in order to increase the rate of glycolysis[19]. Fatty acid oxidation contributes towards energy generation in the foetal heart, albeit it is only up to 15% of total energy generated[20]. Mitochondrial activity is low in the foetal heart due to the hypoxic environment in the uterus[21]. Nonetheless, oxidative phosphorylation still occurs as it is needed for cardiac differentiation from stem cells[22,23]. The low utilisation of fatty acids for energy generation has been shown to inhibit the maturation of cardiomyocytes, but instead

favour cardiomyocyte proliferation through nucleotide biosynthesis and pentose phosphate pathway[24].

The pattern of metabolism in the heart changes after birth when glucose utilisation is reduced whilst fatty acid oxidation is elevated. This metabolic transition is triggered by changes in the substrate composition in the blood and oxygen availability. In contrast to the placenta that provides high levels of lactate, the first meals of the infant are maternal milk which is rich in lipids[25]. This metabolic transition is marked by the increase in mitochondrial number and the expression of mitochondrial proteins[26,27]. As the heart matures, it switches from a foetal metabolic programme, where glucose is the predominant fuel source, to a more adult programme. Increases in FAO results in inhibition of glycolysis via Randle cycle.

1.4 Diabetic cardiomyopathy

Diabetes is a global epidemic problem, affecting nearly half a billion people worldwide and projected to increase by 51%, surpassing 578 million and 700 million individuals by 2030 and 2045, respectively[1]. Diabetes mellitus (DM) is broadly classified into type 1 diabetes mellitus (T1DM) and type 2 diabetes mellitus (T2DM). T1DM, being a consequence of autoimmune β-cell destruction, results in hyperglycemia, with a relative absence of insulin production. In contrast, T2DM is characterized by systemic insulin resistance, hyperglycemia, hyperlipidemia and abnormal secretion of insulin. Diabetes not only increases vascular disease but also affects the cardiomyocytes themselves, as shown by Rubler and colleagues almost 40 years ago when they coined the term diabetic cardiomyopathy (DbCM)[28]. DM affects the heart by causing structural and functional alterations, activation of inflammatory processes and profound metabolic dysregulation.

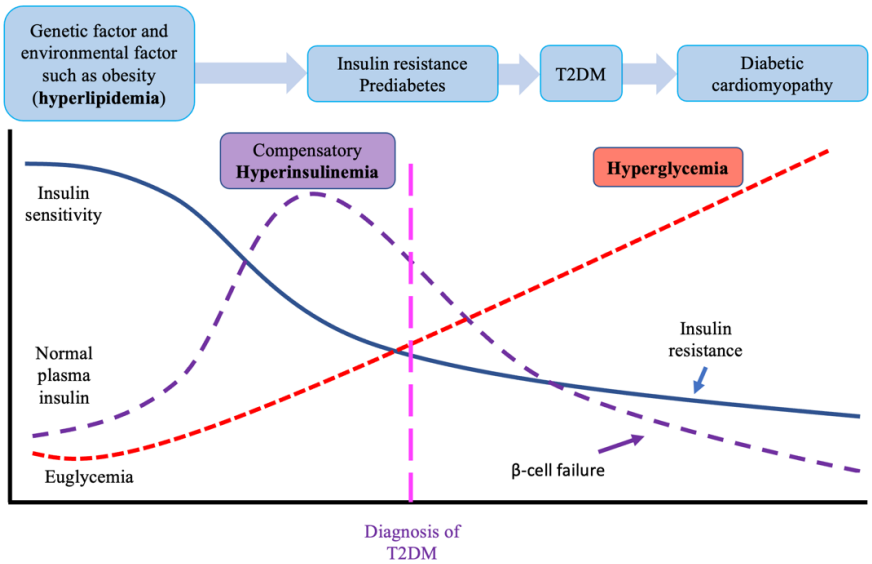


Figure 1.2 Typical sequence of insulin resistance during the development and progression of hyperlipidemia, hyperinsulinemia, and hyperglycemia in type 2 diabetes

Initiation of the disease process mostly involves interaction of genetic factors and environmental factor that disrupt nutrient homeostasis such as obesity and hyperlipidemia. During the prodromal period of insulin sensitivity deteriorates leading to insulin resistance and this is compensated by increased in insulin secretion (compensatory hyperinsulinemia). Pancreatic β-cells lose the ability to response to a rise in blood glucose and worsen by the insulin resistance leading to increase in blood glucose concentration (hyperglycemia). The illustration was adapted from Bailey, C, et al[29].

Genetic and environmental factors such as obesity are the risk factors of type 2 diabetes and initiated the disease process (**Figure 1.2**)[29]. High level of free fatty acids in the blood circulation, for example in the case of patients with obesity, leads to increase fatty acids uptake in the cells. Increase in fatty acid uptake causes inhibition of glucose uptake[14]. This phenomenon can be explained by the Randle cycle whereby increased levels of β-oxidation result in increased levels of acetyl-CoA in the mitochondria which induces phosphorylation and inactivation of pyruvate dehydrogenase (PDH) via the activation of PDH-kinase[14]. Acetyl-CoA increase also results in increased levels of mitochondrial citrate, which is exported into the cytoplasm, where allosterically inhibits phosphofructokinase (PFK). This results in accumulation of fructose 6-phosphate (F6P) which is converted back into glucose 6-phosphate (G6P) which allosterically inhibits hexokinase (**Figure 1.1**). Thus, increase availability of fatty acids and therefore increase levels of β-oxidation results in inhibition of glycolytic enzymes, causing a marked reduction in glycolysis[29].

Increase in fatty acid oxidation and inhibition of glycolysis via Randle Cycle causes decreased glucose transport into the muscle cells and increased fat breakdown, subsequently leading to elevated hepatic glucose production[14]. Insulin sensitivity starts to deteriorate due to multiple factors including lipotoxicity. To compensate the increase level of glucose in the blood circulation and insulin resistance, pancreatic β-cells produce high level of insulin (hyperinsulinemia)[29]. This phenomenon causes the 'stress' in the pancreatic β-cells and therefore lose their ability to responds to a prandial rise in blood glucose. The normal insulin secretory rhythm in pancreatic β-cells becomes disrupted and there is incomplete conversion of proinsulin to insulin, resulting in the secretion of more proinsulin which is less biologically active than insulin. The raise in insulin concentration is not sufficient to compensate the insulin resistance and blood glucose concentration rise, leading to a prediabetic condition. High level glucose in blood circulation (hyperglycemia) leads to glucotoxicity[29].

Diabetic cardiomyopathy affects the heart physiology such the systolic and diastolic function[30]. During systole, the ventricles contract and therefore ejecting blood out of the heart and arteries. Systolic function is related to the left ventricular ejection fraction (LVEF) which is the ratio of stroke volume and end-diastolic volume. Diastole begins when the ventricular muscles relax and therefore diastole refer to the relaxation phase of the heart. The abnormal stiffening of the ventricles and the resulting abnormal ventricular filling during diastole are referred to as diastolic dysfunction[31].

1.4.1 Metabolism in diabetic cardiomyopathy

The diabetic heart is bathed in an abnormal composition of substrates, due to the hyperglycemia, hyperlipidemia and circulating cytokines, which changes the fuel choice of the heart and has subsequent effects on intracellular processes. In the diabetic heart, metabolic preference for FAO increases, with the heart metabolising predominantly fatty

acids, and glucose metabolism only contributing a small amount to overall energy generation[32]. The flexibility of substrate metabolism is lost in part due to the high plasma fatty acid concentrations in the circulation[33]. Fatty acids are stored in the form of triacylglycerol (TAG) in the adipose tissue, however, when there is chronic excessive intake of fatty acids, the adipose tissue capacity may be overwhelmed leading to an increased level of free fatty acids (FFA) being delivered to peripheral tissues. Within the heart, increased expression, and localization of the fatty acid transporter FAT/CD36 to the sarcolemma results in increased cardiac fatty acid uptake, which fuels increased mitochondrial fatty acid oxidation and myocardial triglyceride esterification in diabetes. Increased fatty acid metabolism drives decreased metabolism of alternative substrates which, in combination with myocardial insulin resistance, decreases glucose uptake, glycolysis, and glucose oxidation within the diabetic heart. Moreover, the use of ketone bodies and certain amino acids and their derivatives showed enhanced metabolism in diabetic cardiomyocytes in both in vivo and in vitro diabetic models[34].

Insulin is vital to maintain the metabolic flexibility in the heart, and in diabetes the heart becomes insulin resistant. Insulin regulates signalling cascades starting from its interaction with the insulin sensitive receptor tyrosine kinase (RTK), leading to activation of intracellular phosphatidylinositol 3-kinase (PI3K) and mitogen-activated protein kinase (MAPK) signalling[35]. These signalling pathways stimulate glucose uptake and oxidation in the cardiac cells.

Upon loss of insulin response, GLUT4 is not translocated to the cell membrane and will remain in intracellular vesicles and therefore glucose uptake will be reduced. This results in the increase of blood glucose in the circulation, increasing the hyperglycaemic phenotype which is indicative of diabetes. The causes of insulin resistance are complex; however,

several studies have suggested that excess of glucose and fatty acids play a vital role in establishing insulin resistance[35].

1.4.2 Mechanisms implicated in the pathology of diabetic cardiomyopathy

A multitude of mechanisms have been reported in the pathogenesis of diabetic cardiomyopathy including alterations in cellular energy metabolism, increased lipid oxidation, intra-cellular accumulation of glycerides, mitochondrial dysfunction, abnormal calcium signaling, cardiomyocyte hypertrophy and apoptosis[36]. These trigger alterations in downstream transcription factors that lead to changes in gene expression, myocardial substrate utilization, myocyte growth, endothelial function, and myocardial compliance. As a consequence, diabetic cardiomyopathy is a complex and multifactorial disease. The clinical progression of DbCM is characterized by cardiac hypertrophy and diastolic dysfunction. This may increase the risk of pulmonary congestion and can progress to heart failure with preserved ejection fraction (HFpEF). If additional stressors are present, such as hypertension or ischemia, patients may go on to develop systolic dysfunction[37].

An understanding of the factors that drive changes within the myocardium in diabetes is important for understanding disease pathogenesis, and for identifying new targets for therapy.

1.4.2.1 Glucotoxicity

Hyperglycemia in DM occurs as a result of decreased glucose clearance and increased hepatic gluconeogenesis. Chronic exposure to hyperglycemia can result in cellular impairment and may become irreversible over time through a process called glucotoxity[38]. Several mechanisms play a role in DbCM due to hyperglycemia. The main mechanisms are the elevation of advanced glycation end products (AGEs), the increase in hexosamine and polyol flux, and the activation of protein kinase C (PKC), increase *O*-GlcNAcylation, epigenetic changes (e.g., acetylation methylation), and recently identified Sodium-

myoinositol cotransporter-1 (SMIT1) which mediates the production of reactive oxygen species induced by hyperglycemia in the heart shown in **Figure 1.3** and summarized in **Table 1.1**[39]. Battault, et al. described the mechanism of myocardial glucotoxicity in a comprehensive review[40].

AGEs are glucosamine formation produced through a non-enzymatic reaction between protein and lipids in the presence of reducing sugars and are found at high levels in the plasma of diabetic patients. They adversely affect cellular processes by directly trapping and cross-linking proteins or by binding to receptors for signaling pathways[41,42]. Advanced glycation end-product generation leads to the formation of reactive oxygen species (ROS), oxidative stress, and altered gene expression. Furthermore, increased polyol pathway flux leads to inhibition of glyceraldehyde-3-phosphate dehydrogenase (GAPDH), which modifies the pathway of glycolysis and eventually leads to glucotoxicity[43]. PKC can lead to activation of the pathways involved in p38 mitogen-activated protein kinase (MAPK) and c-Jun N-terminal kinase (JNK), which contribute to cardiac hypertrophy[44] .

The post-translational modification of serine and threonine residues of proteins by *O*-linked β-*N*-acetylglucosamine (*O*-GlcNAc) through *O*-GlcNAcylation has been found to be increased in the heart under hyperglycemic condition[45]. The increase of *O*-GlcNAcylation of nuclear proteins induces prolonged calcium transients which corresponding to delayed myocardial relaxation[46]. Increasing overall *O*-GlcNAcylation by hyperglycemia has been shown to have adverse effects on mitochondrial function and bioenergetics[47,48]. Recent studies also demonstrated that epigenetics (DNA methylation, histone modifications, and non-coding RNAs) directly or indirectly contribute to pathogenesis of diabetic cardiomyopathy[49]. Finally, Sodium-myoinositol cotransporter-1 (SMIT1) which expressed in the heart, was shown to trigger NADPH oxidase 2 (NOX2) activation and reactive oxygen species (ROS) production caused by hyperglycemia[50].

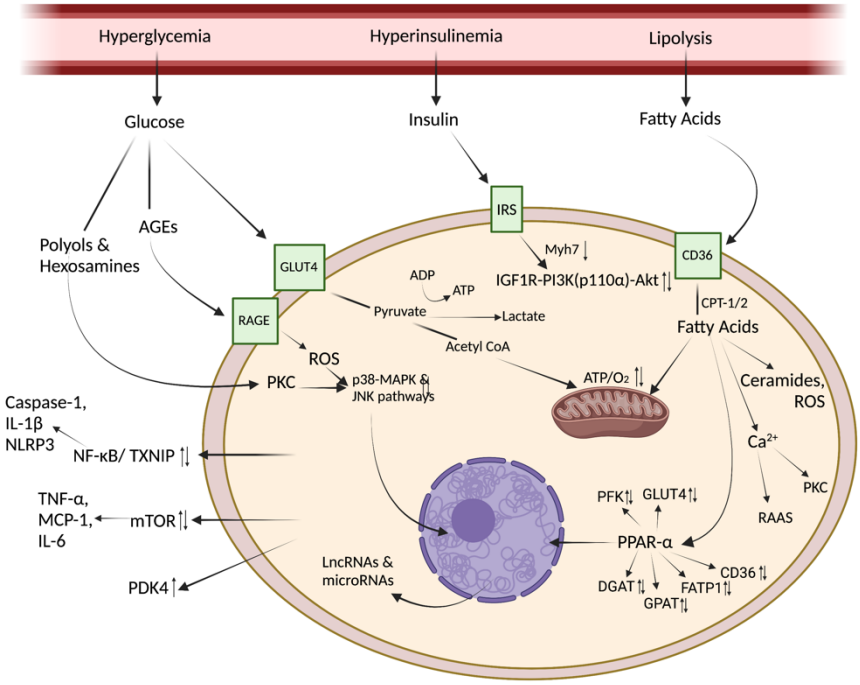


Figure 1.3 Molecular mechanism inducing diabetic cardiomyopathy, showing pathways activated in cardiomyocytes.

Elevated levels of plasma glucose and insulin in T2DM and increased lipolysis of fatty acids activates a number of adverse signalling pathways in cardiomyocytes. AGEs: advance glycation end products, RAGE: receptor for AGEs, GLUT4: glucose transporter 4, IL-1β: interleukin 1β, NLRP3: Nod-like receptor family pyrin domain containing 3, NF-kB: nuclear factor kappa B, TXNIP: thioredoxin interacting protein, TNFα: tumour necrosis factor α, MCP-1: monocyte chemoattractant protein-1, IL-6: interleukin-6, mTOR: mammalian target of rapamycin, PDK4: pyruvate dehydrogenase 4, ROS: reactive oxygen species, PKC: protein kinase C, p38-MAPK: p38 mitogen-activated protein kinase, JNK: c-Jun N-terminal kinase, IRS: insulin receptor, MYH7: myosin heavy chain 7, IGF1R: insulin-like growth factor 1 receptor, PI3K: phosphatidylinositol-3-kinase, CPT1/2: carnitine palmitoyl transferase 1 or 2, RAAS: renin-angiotensin-aldosterone-system, PFK: phosphofructokinase, PPARα: peroxisome proliferator-activated receptor α, DGAT: diglyceride acyltransferase, GPAT: glycerol-3-phosphate acyltransferase, FATP: fatty acid transport protein.

Table 1.1 Metabolic changes leading to diabetic cardiomyopathy

Triggers	Mediators and Mechanism of action	Consequences
Hyperglycemia (glucotoxicity)	Increase AGE[51], hexosamine flux[52], polyol flux[53], protein C kinase activation[54], increase O-GlcNAcylation[40,55], SMIT1[50]	Decreased myocytes contractility, increased ventricular stiffness, prolonged calcium transient, impaired relaxation, and increased myocytes apoptosis
Hyperlipidemia (lipotoxicity)	Enhanced PGC1/PPARα, increased secretion of cytokines (TNF-α, MCP-1, IL-6)[56,57], triggered p38α/MAPK pathway, upregulated c-fos, c-jun and caspase-8[58]	Hypertrophy, heart injury, cardiomyocytes apoptosis, cell death

1.4.2.2 Lipotoxicity

Excessive esterification of fatty acids into triglycerides and ceramides within the diabetic myocardium has been shown to stimulate oxidative stress, mitochondrial damage, and cardiomyocyte apoptosis[59,60]. Collectively, these studies suggested that increases in fatty acid supply in the presence of diabetes alter cardiac lipid homeostasis and result in lipotoxicity as seen in **Figure 1.3**. Excessive fatty acid oxidation leads to enhanced peroxisome proliferator-activated receptor-γ coactivator/peroxisome proliferator-activated receptor-α (PGC1/PPARα) activation, which drives fatty acid-mediated transcriptional regulation within the heart, contributing to cardiac hypertrophy and hypoxia. Sustained increase in the secretion of cytokines and chemokines like tumour necrosis factor-α (TNF-α), monocyte chemoattractant protein-1 (MCP-1), interleukin-6 (IL-6), as consequences of increased fatty acid oxidation, also exert autocrine/paracrine effects on cardiomyocytes, leading to cell apoptosis.

Palmitic and oleic acid account for more than half of the total plasma fatty acids released by adipose tissues into the bloodstream[61,62]. However, long-chain saturated fatty acids, such as

palmitate, exhibit several cytotoxic effects which are not seen with unsaturated fatty acids such as oleate. Dyntar et al. showed that palmitic acid induces apoptosis in adult rat cardiomyocytes via de novo formation of ceramides and activation of the mitochondrial apoptosis pathway[63]. Ceramide synthesis also inhibits mitochondrial β-oxidation of fatty acids and activates the Nod-like receptor family pyrin domain containing 3 (NLRP3) inflammasome initiating inflammatory mechanisms linked to nuclear factor kappa B (NF-κB) mediated by the secretion of IL-6 and TNF- α[56,57]. Similarly, Oh et al. showed that high concentrations of saturated fatty acids triggered the p38 mitogen-activated protein kinase (p38α/MAPK) pathway and mediated cardiomyocyte apoptosis. Enhanced palmitic acid levels also induce microRNAs such as miR-451, which suppress the Liver Kinase B1/AMP-activated protein kinase (LKB1/AMPK) pathway and drive mitochondrial ROS generation, leading to endoplasmic reticulum stress and apoptosis of cardiomyocytes[58]. In contrast, oleic acid has been shown to be beneficial to cardiovascular cells [57]. Pretreatment with oleate has been seen to nullify the activation by palmitate of the TNF-α mediated c-Jun N-terminal Kinase (JNK1/2) and NF-κB mediated pathways, thus providing an anti-inflammatory environment[57].

1.4.2.3 Oxidative stress and mitochondrial coupling

The metabolic changes induced by diabetes generate a redox imbalance in the cardiomyocytes which culminates in elevated ROS production and oxidative stress. It has been shown that hyperglycemia elevates levels of protein glycosylation and dyslipidemia, which upregulated NADPH oxidase activities and dramatically increased the ROS content in DbCM[64,65]. As a consequence of the increased use of NADPH to produce sorbitol by the reduction of glucose (increased polyol pathway flux), the NADPH/$NADP^+$ ratio declines, which depletes NAPDH availability to maintain glutathione in its reduced form[66], required for defence against ROS.

The increased β-oxidation rate in the mitochondria increases the delivery of electron donors (NADH and $FADH_2$) to the electron transport chain. The excess of these electrons interacts with molecular oxygen and culminates in superoxide formation, followed by ROS overproduction within the mitochondria[20,67,68], which finally drives mitochondrial and cardiac dysfunction[69,70]. It is also well known that the $FADH_2$-linked substrate succinate induced reverse electron flow to complex 1 of the electron transport chain and this process generates superoxide[71]. The increased fatty acid oxidation and ROS generation within the diabetic heart upregulate the expression and activity of the mitochondria uncoupling proteins (UCP), namely UCP2 and UCP3[72,73]. These proteins disrupt the proton gradient in the mitochondria, generating an increase in oxygen consumption which is accompanied by a reduction in the ATP/oxygen ratio, resulting in a decrease in cardiac efficiency[74,75]. Both oxidative stress and UCPs have been implicated in the development of diabetic complications at the cardiovascular level[76,77].

1.4.2.4 Impaired ion channel function and calcium homeostasis

T2DM patients and streptozocin (STZ) induced T2DM models show a series of deviations in the electrocardiogram. Characteristics like prolonged QT interval, atrial fibrillation, increased arrhythmogenic potential and an enhanced disparity in depolarisation-repolarisation were noted in such models. Elevated plasma glucose concentration has been associated with significant changes in particular sodium and potassium ion channels[72]. For example, an uneven decrease of I_K dysregulated several repolarisation procedures, thereby increasing the action potential duration and explaining the episodes of ventricular arrhythmia seen in some diabetic patients[78]. This increase in action potential duration, consistent with reduced expressions of Kcnd2, Kcnd3 and Kcnip2 (genes encoding for K^+ channel alpha-subunits), has also been associated with atrial fibrillation in diabetic db/db mice[79]. In diabetic cardiomyocytes, reduced Na^+ influx during contractions has been

associated with a reduction in the sodium current I_{Na} and an increased intracellular calcium concentration[80]. Calcium homeostasis is important in regulating mitochondrial function and responsible from the regulation of cell's energy supply to the control of the intrinsic pathway of apoptosis[81,82]. Depressions in repolarizing K^+ currents due to hyperglycaemia showed prolonged and increased temporal intervals of the repolarisation phase in myocytes, thus remodelling the electrical phenotype of the diabetic heart[83]. Myocyte alterations were also observed due to downregulation of HCN2 and HCN4, thus projecting an altered arrhythmogenic profile of the diabetic heart[84].

Impairment of Ca^{2+} handling, activation of RAAS (renin-angiotensin-aldosterone system), ER stress and other pathophysiological aberrations have been seen to promote the activation of protein kinase C (PKC). Isoforms of PKC (PKC α1 and PKC β2) have been seen to be involved in the development of cardiac hypertrophy. They induce a series of changes in cellular functions, enhance ECM, hypertrophy, and apoptosis in DbCMs, which ultimately leads to heart failure[85].

1.5 Cardiac insulin resistance due to Duchenne muscular dystrophy

Duchenne muscular dystrophy (DMD) is the most common type of muscular dystrophy. It results from a mutation in the X-linked recessive dystrophin gene and is characterised by progressive muscle disorder affecting approximately 1 in 3,500-6,000 live male births[86,87]. DMD symptoms appear as early as 2 – 3 years of age with typical symptoms such as muscle weakness, difficulty climbing stairs, and frequent falls[88]. Rapid symptom progression becomes more apparent at age 7 leading to loss of upper limb function, respiratory insufficiency, and cardiomyopathy at 12 years old[89]. Despite recent improvements in the current clinical care and the use of corticosteroids, the mean average survival is to 13-14 years old[90]. Heart failure due to dilated cardiomyopathy is now considered as the major cause of death in adult DMD patients[89,91–93].

The dystrophin gene is the largest gene located on the short arm of the X chromosome near the region Xp21 (**Figure 1.4**). The size of the Dystrophin gene is more than 2.5 megabases (Mb) containing at least 79 exons. Exons 1-8 encode the N-terminal domain, exons 9-63 encode the central 'rod' domain, exons 64-70 encode a cysteine-rich domain, and exons 71-79 encode the C-terminal domain. There are a variety of mutations of which 60-70% are large deletions, 20% are point mutations (small deletion or insertion), and 5-15% are duplications. This variety of mutations, including frameshift or nonsense mutations, results in premature truncation or production of a non-functional protein[94].

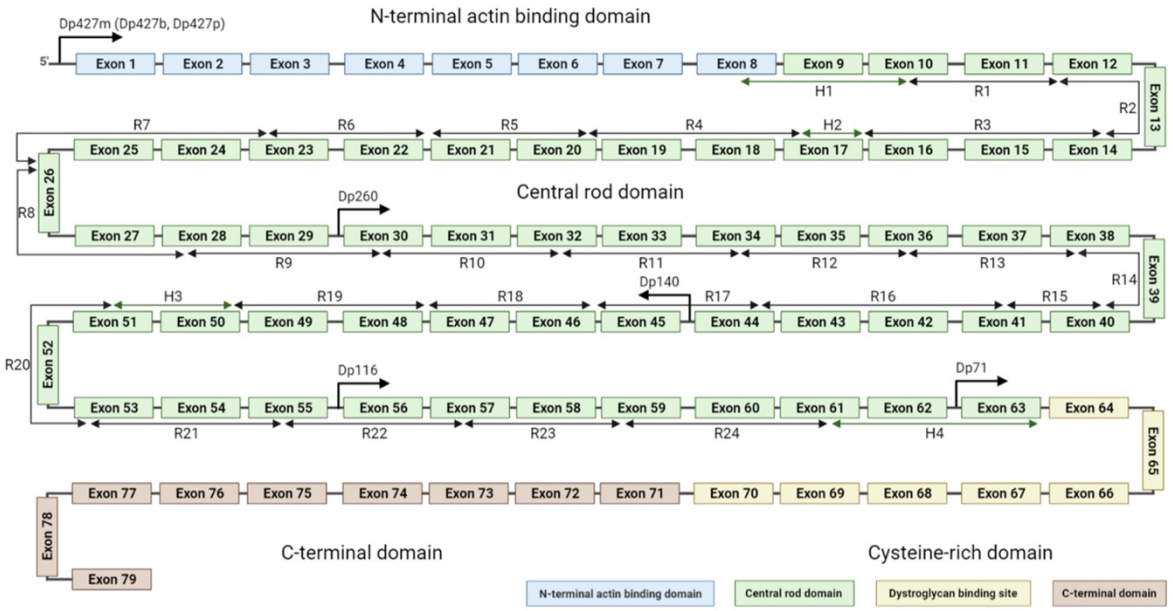


Figure 1.4 Dystrophin gene

Schematic representation of dystrophin gene organisation including locations of promoters for alternative isoforms regions encoding the hinges (H1-4) and spectrin-like repeats (R1- 24).

Dystrophin protein is mainly expressed in skeletal, cardiac, and smooth muscle cells, with smaller amounts expressed in the brain and retina. The mutation in the dystrophin gene causes loss of this full-length dystrophin protein (427 KDa) in the muscle cells which has a crucial role during muscle contraction. This is due to its location connecting extracellular matrix with the cytoskeleton, thereby preventing the stress caused by muscle contraction. This is due to its structure of triple replicate helix in the rod domain making it elastic and

flexible (**Figure 1.5**). The N-terminus of the protein binds into the cytoskeletal F-actin, and the C-terminus binds into the dystrophin-associated protein complex (DAPC) also known as dystrophin glycoprotein complex (DGC). The interaction between DGC and dystrophin provides a strong, stabilising connection between intracellular cytoskeleton and the extracellular matrix. The mutation in the dystrophin protein results in the inability to form DGC, which weakens the sarcolemma, making it prone to damage[94,95]. The effect of this damage can result in an increase in the concentration of calcium within the muscle cells and lead to a harmful increase in protein degradation. The long-term effect of this damage results in sarcolemma leakage, defective organelles (mitochondria and sarcoplasmic reticulum), inflammation and fibrosis[96]. The deficiency of dystrophin in the heart of DMD patients results in progressive dilated cardiomyopathy, cardiac fibrosis, conduction abnormalities, arrythmias, and cardiac insufficiency[86,96].

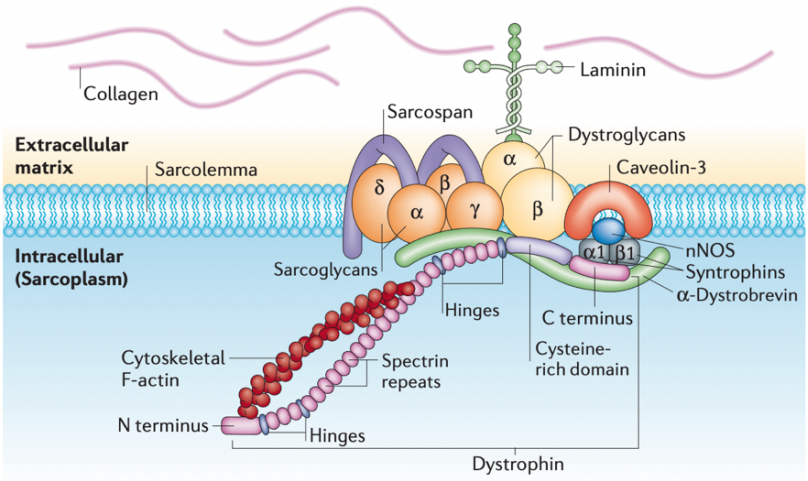


Figure 1.5 Dystrophin binds into DAPC in the sarcolemma
Schematic representation of dystrophin protein showing the N terminal binds into cytoskeletal F-actin and C terminal binding into the Dystrophin-Associated Protein Complex (DAPC).

Cardiomyopathy is the leading cause of death in DMD patients. Dystrophin deficiency in DMD leads towards progressive dilated cardiomyopathy, reduced systolic function, and cardiac arrhythmias, which can include both bradycardic and tachycardic rhythm disturbances[91,92,97]. These complications appear at a young age due to the increased muscle

strength and workload on the heart during development which leads towards early progression of cardiomyopathy[98].

1.6 Metabolism in the heart in Duchenne muscular dystrophy

Metabolic changes in DMD patients are a growing area of interest with the aim of finding a treatment to reduce the symptoms of DMD and increase the quality of life in these patients. Research on various DMD models suggests that there is a dysregulation in glucose and insulin metabolism[99–102]. Particularly, research suggested that insulin resistance may develop within the heart of DMD patients[101,103–105]. Some argue that the insulin resistance in DMD is linked to weight gain due to glucocorticosteroid treatment, but others reported that insulin resistance was observed in 27.3% of underweight DMD patients[96,106]. The isolated perfused mdx mouse heart was insulin resistant when compared with wild type control hearts[99]. Bioinformatic approaches found some alterations in metabolic protein expression, particularly the helix-loop-helix transcription factor sterol regulatory binding protein 1 (SREBP-1)[107]. Dysregulation in muscle lipid metabolism was also observed in both human patients and the mdx mouse, and associated with inefficient energy generation[100,108].

A recent study showed that DGC interacts with the insulin receptor that is stabilised by the plakoglobin protein interacting with β-dystroglycan. Competition between plakoglobin and autophagy protein LC3 leads to decreased binding of plakoglobin to β-dystroglycan. This reduces the stabilisation and leads to increased lysosomal degradation of the insulin receptor[109]. Hence, the lack of dystrophin may have a direct impact towards insulin resistance due to the degradation of insulin receptors[109].

1.7 Modelling cardiometabolic diseases

Experimental studies are an integral part of preclinical studies and are essential for early phase research to help identify disease mechanisms and potential therapeutic candidates. In vitro studies utilise isolated cells, biological molecules, cell culture systems, tissue slices

and isolated organs in optimised conditions performed outside the normal biological system. These are complemented by in vivo studies, and both are important to gain a full understanding of disease pathology.

Both in vitro and in vivo studies have been utilised for modelling cardiometabolic diseases. However, there are challenges for in vitro modelling of the heart, as access to human cardiac tissue is only feasible during highly invasive surgery and biopsies are often taken at the later stages of disease progression. Animal cardiac tissue is easily available however adult cardiomyocytes cannot be cultured in a dish for longer than a few days and neonatal cells cannot fully recapitulate the adult heart. Animal models have been very useful for the advancement in our understanding of these diseases, but questions remain regarding their translatability to humans[110]. Additionally, inborn cardiometabolic diseases are often difficult to study in animals because transgenic animal models of the disorder do not always fully recapitulate the human disease, for example as is seen with the mdx mouse model for DMD[111–113]. Here, I describe several in vitro and in vivo models used to study cardiometabolic diseases and discuss why human induced pluripotent stem cell derived cardiomyocytes fulfil an unmet need within the field.

1.7.1 Animal models and primary tissue

Animal models are a versatile research tool to increase our understanding of the mechanisms implicated in diabetic cardiomyopathy and are particularly valuable in exploring the complex interactions of insulin signaling on different organs of the body. Researchers have been modelling diabetic cardiomyopathy (DbCM) using large and small animal models. Due to ease of maintenance, short breeding cycles and the high homology between the human and rodent genome, small animal models have been widely used.

Animal models can be broadly divided into three groups: genetic models, chemically induced or diet-induced models. T1DM can be induced using high concentrations of

streptozotocin (STZ), which kills the pancreatic beta cells and results in a model of uncompensated T1DM[114]. T2DM is studied in the genetic ob/ob and db/db mice and the ZDF rat, which have mutations in leptin and leptin receptor genes[115]. However, there are concerns those cardiac effects may not result from the hyperphagia and obesity but instead from the changes in leptin signalling itself. Nevertheless, these animals are obese and have elevated plasma glucose and fatty acids and therefore do recapitulate many aspects of the T2DM phenotype. T2DM can also be induced using high fat or high fructose diets. Some mouse strains, such as the C57black6J mouse, are prone to insulin resistance when fed a high-fat diet[116]. Alternatively, a combination of high-fat feeding and a low dose STZ injection can induce a clinically relevant model of the early stages of T2DM[117].

Various in vitro models have been utilized to study the effect of diabetes in the heart. In vitro models of insulin-resistant cardiomyocytes have been developed using rodent cardiomyocytes, mouse neonatal cardiomyocytes, the H9C2 cell line or the HL-1 cell line cultured with high palmitate levels[118]. However, these cardiac myocytes cell lines have limitations such as lower expression and disorganization of contractile proteins compared to adult cardiomyocytes. Comparative transcriptomic analysis showed distinct phenotypes and alterations of gene expression pattern in these cell lines compared to adult cardiomyocytes[119]. Differences between these cell lines in metabolism and mitochondrial activity have also been reported[120]. Primary cardiomyocytes from adult rat and mouse heart do not survive for a long period of time in culture which limits their usage. Neonatal rat and mouse cardiomyocytes can be cultured for a longer time, but again expression of cardiac proteins differs from those in adult cardiomyocytes[119]. The immortalised human cell line, AC16, is another common resource to study heart disease. However, in terms of metabolism, hypoxic sensitivity, and even gene expression profiling, these cells differ from adult cardiomyocytes[119].

There are growing concerns that rodent cardiomyocytes and animal models do not recapitulate the human disease sufficiently, as many therapeutic compounds have shown promise during pre-clinical testing but do not perform as predicted in patients. Human induced pluripotent stem cell derived cardiomyocytes (hiPSC-CM) may provide a viable alternative to complement animal models and can be obtained in unlimited numbers. In addition, hiPSC-CM can be genetically modified and have been used to model several inherited cardiac disorders in vitro[121–123].

1.7.2 Human induced-pluripotent stem cell derived cardiomyocytes (hiPSC-CM)

The discovery of human induced pluripotent stem cells (hiPSC) by Yamanaka's group in 2006 was heralded as a major breakthrough as it generated stem cells that recapitulated human diseases[124–127]. Human iPSCs are embryonic-like cells which are reprogrammed from adult cells such as skin and blood[128–130]. They have great potential as tools for studying human disease because they are patient specific and have been shown to model several inherited diseases[129,130]. Reprogramming involves inducing (in somatic cells from the patients) ectopic expression of four genes which are *Oct3/4, Sox2, Klf4*, and *c-Myc* (Yamanaka factors)[124–127]. Due to their pluripotency, hiPSCs have the potential to be revolutionary in the world of disease modelling since they can be differentiated into many different types of cells, including lung tissue[131], kidney[132], liver[133], and heart[134]. We specifically use hiPSC to study the heart, hence we differentiate these cells to become cardiomyocytes. Therefore, human induced pluripotent stem cell derived cardiomyocytes (hiPSC-CM) may play a role as a viable alternative and can be obtained in unlimited numbers.

To successfully model the adult human heart and provide a suitable model to translate results seen in rodent models, it is necessary to confirm that hiPSC-CM recapitulate the structure and metabolism of the mature cardiomyocyte. When first differentiated, hiPSC-CM retain

an immature phenotype and differ from adult cardiomyocytes in gene expression[135,136], structural features[137], metabolism[138], and contractile function[139]. Immature hiPSC-CM have been shown to have low expression of GLUT4 and did not exhibit insulin-stimulated glucose uptake[140]. Therefore, strategies are needed to mature hiPSC-CM into a more adult phenotype.

The heart is among the earliest organs to develop and function in the embryo. Cardiogenesis starts from mesoderm formation in the primitive streak which involves the signalling molecules Bone morphogenetic protein 4 (BMP4), Activin and NODAL (member of transforming growth factor β - TGFβ family), fibroblast growth factor and the wnt/β-catenin pathway[141]. The study of cardiogenesis and its complexity helped to shed light on how to differentiate hiPSC into cardiomyocytes by providing developmental cues during differentiation, in particular, the role of the wnt/β-catenin pathway in differentiation and morphogenesis which is used in many protocols to direct hiPSCs into cardiomyocytes[142].

There are many approaches to induce the maturation of hiPSC-CM through biochemical factors, genetic manipulation, co-culture, electrical stimulation, substrate stiffness, mechanical stretch, and 3D culture. These strategies are often combined to increase the maturation of the hiPSC-CM. We and others have shown that addition of fatty acids to cell culture media induces structural and metabolic maturation of differentiated hiPSC-CM[143] and that culture of hiPSC-CM in 3D can recapitulate the physiological properties of the cells[144–149]. The 3D culture models fall into two categories, engineering the cells using a scaffold (typically hydrogel) as engineered heart tissue (EHT)[146,150–152] and self-assembly formation in 3D organoids without the addition of extracellular matrix/scaffolds[153–156]. Murine/hiPSC-derived 3D cardiac models, including spherical aggregates of cardiomyocytes, engineered heart tissues, cardiac organoids, vascularized microchambers etc., have been established to recapitulate cardiac-specific organization in vitro[157–162].

1.7.3 Organoids and Organ-on-a-chip

Organoid technology is one of the best and most popular approaches to study human cardiac diseases in the dish. Researchers have described that organoids are organ-like multicellular structures that self-assemble from stem cells, leading to differentiated organotypic structures and functionality[163] with minimal external intervention[164,165]. The advancement of human 3D cardiac organoids allows us to model complex diseases caused by genetic mutation and environmental factors. The human 3D organoids created by co-culturing different type of cells such as cardiomyocytes, fibroblasts, and endothelial cells have been shown to recapitulate the differences seen in genetic cardiomyopathies[154]. Furthermore, the complex structure of 3D cardiac organoids allows us to look at oxygen diffusion as a gradient through tissue which better recapitulates the hallmarks of the acute post-myocardial infarction state[155]. It should be remembered, however, that 3D models are limited by the inability to model the structural and functional complexity of the tissues and organs they intend to represent[166–173].

Another advanced system that researchers use is organ-on-a-chip. This system allows the organoids to be placed in a microdevice consisting of dynamic culture-based 3D cardiac microtissues and microelectromechanical system-based microfluidic chips. Organ-on-a-chip models can visualise the kinetics of cardiac microtissue and quantify physiological parameters such as fluidic output, pressure, and force[174].

1.7.4 Engineered heart tissue (EHT)

Engineered heart tissue is a 3D cell culture formed by directed assembly with addition of external factors such as extracellular matrix (e.g., hydrogel, collagen, etc)[175] using cardiomyocytes from either animal or human source (e.g., hiPSC-CM or primary rodent cardiac cells). Those cells were aggregated into a spherical structure producing what were known as cardiac spheroids[176,177]. Originally, EHT was created using isolated chicken or

neonatal rat heart cells inside collagen I or Matrigel hydrogels[178,]. More recently, fibrin/thrombin-based methods are preferred[179]. The EHT approach enables precise mechanical loading of the sarcomeres and there are a variety of loading regimes such as auxotonic mechanical loading and static stretching or phasic stretching[180].

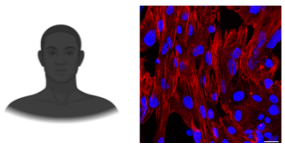
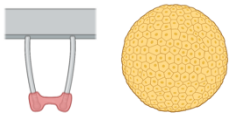
Engineered heart tissues are constructed using a range of methods which differ in the cell differentiation protocol, extracellular matrix, cardiac cell type and composition, culture media, size, potential application, and additional external stimuli. However, they are all the same in the utilization of biomaterials mixed with the cells and placed in a biocompatible format such as between silicone posts. The construct pioneered by Thomas Eschenhagen and Wolfram-Hubertus Zimmermann was generated by casting the cells in a gel template between two flexible silicon posts[181]. Those further developed by the Eschenhagen group are fibrin-based and referred to as engineered heart tissue (EHT) whereas the Zimmermann group use collagen-based engineered heart muscle (EHM).

EHT has been utilised for many applications such as for studying diseases, drug testing, and cardiac regeneration[182] and EHM has recently entered a clinical trial in Germany with identifier number NCT04396899. Another example is the heart dynamometer (Heart-Dyno) microtissue platform which is similar to EHTs but engineered in a 96-well plate format containing polydimethylsiloxane (PDMS) elastomeric posts spaced 1.0 mm apart[146,180]. Heart-Dyno has been used to study pro-regenerative molecules, including molecules that activate the cell cycle network and the mevalonate pathways for regeneration[183]. Another modification of EHT has been used to study cardiac injury by applying a dry ice probe to the surface of the tissue which led to localized cell death and reduced contractility[155]. Currently, EHTs are also used for studying the effect of COVID-19 infection in the heart[184]. The best model to use can depend on the research questions. Organoids are better to study heart development and EHTs are generally better to study cardiomyocyte-specific questions

and for drug testing. Both have pros and cons, including issues with cell heterogeneity, cell-cell interaction, functional analysis, etc[175].

Engineered heart tissue has been shown to increase the maturation of the cardiomyocytes compared to traditional 2D monolayer culture[145,148]. EHT has been used to model several diseases such as ischemic heart disease[151], however, there is little evidence of modelling metabolic diseases using EHT with human iPSC-CM.

Table 1.2 Different in vitro cell models to study insulin resistance in cardiomyocytes

Most used in vitro cell models	**Benefits**	**Limitations**
 H9C2, neonatal and adult rat cardiomyocytes HL-1 AC16	• Ease of maintenance • Relatively large commercial availability • Simple culturing protocol	• Loss of specific cardiac features • Resistance to hypoxic injury • Highly glycolytic and use high glucose for energy generation
Potential future in vitro models		
 Human iPSC-CM 	• Myocardial gene expression more closely resembles that in human adult cardiomyocytes • More responsive to hypoxic injury • More mature cells show increased fatty acid oxidation	• High degree of variability in some hiPSC-CM • Require extra steps to create more mature cardiomyocytes

H9C2: female embryonic BDIX rat ventricular tissue, HL-1: immortalized mouse atrial cardiomyocytes, AC16: immortalized human ventricular cardiomyocytes fused with transformed human fibroblast, hiPSC-CM: Human induced-pluripotent stem cells derived cardiomyocytes, EHT: Engineered heart tissue

1.8 Thesis aims

The work described in this thesis intends to explore the potential of human induced-pluripotent stem cell derived cardiomyocytes (hiPSC-CMs) in 2D and 3D (engineered heart tissue) as alternative models to study the effect of insulin resistance (IR) in diabetic cardiomyopathy and Duchenne muscular dystrophy, and to explore their potential use in drug discovery. Since hiPSC-CMs are structurally and metabolically immature when cultured in conventional 2D culture for a short period of time, advances are needed to mature these cells into a more adult-like cardiomyocyte phenotype. The aims of my thesis are to develop more mature hiPSC-CMs in engineered heart tissue (EHT), cultured in more physiologically relevant media containing relevant fatty acids. Furthermore, I explored how to use this model to study the effect of insulin resistance in the heart by using "diabetic-like" media and investigated whether Duchenne muscular dystrophy causes insulin resistance using patient-derived hiPSCs. Finally, I explored whether I could use these models to study potential treatments to improve function in the insulin resistant heart.

The outcomes of these aims are discussed in the following four result chapters:

1. Differentiating and characterising hiPSC-CM and comparing the maturity profile (structure, gene and protein expression, metabolism, function/contraction) of hiPSC-CM cultured in 2D monolayer and 3D as engineered heart tissue by modulating PPAR signalling and with addition of oleic acid. The hypothesis is that culturing the cells in 3D as engineered heart tissue with addition of oleic acid could improve the maturation of hiPSC-CM.
2. Characterising hiPSC-CM in 2D and 3D EHT for the study of insulin resistance in diabetic cardiomyopathy by developing "diabetic-like" media mimicking hyperlipidemia, hyperglycaemia, and hyperinsulinemia. The hypothesis is that

culturing hiPSC-CM in 2D and 3D EHT with “diabetic-like” media could mimic the effect of diabetes in the heart.

3. Exploring the potential of hiPSC-CMs in 2D and 3D EHT for testing known drugs for type-2 diabetes (perhexiline and metformin) to improve insulin response in IR cardiomyocytes and to validate the model. Testing the effect of the Prolyl Hydroxylase (PHD) inhibitor, molidustat, in the IR hiPSC-CMs to stabilise HIF in the heart and the potential of this drug to improve cardiac function following ischemia. The hypothesis is that hiPSC-CMs in 2D and 3D EHT with and without IR condition could be used to test drugs affecting the heart.
4. Characterising hiPSC-CM in 2D and 3D EHT for the study the effect of the dystrophin mutation in Duchenne muscular dystrophy (DMD) in the heart by using the hiPSCs developed from DMD patients. The hypothesis is that hiPSC-CM in 2D and 3D EHT could be used to study the effect of DMD in the heart.

2

Materials and methods

CHAPTER 2

2 MATERIALS AND METHODS

This chapter will cover general materials and methods, chapter-specific methods will be further described in the appropriate chapters. All reagents are listed in **Appendix C**.

2.1 Human induced pluripotent stem cells lines

2.1.1 Healthy cells

The healthy cell lines used for the experiments were IMR90, OX1-19 and M180. IMR90 was kindly provided by Prof. Sian Harding (Imperial College London) and was originally from Dr. James Thomson (WiCell, University of Wisconsin). The IMR90 iPSC cell line was generated from human lung fibroblasts derived from lung tissue of a 16-week-old female Caucasian foetus[185]. OX1-19 cell line was kindly provided by Dr. Sally Cowley (James Martin Stem Cell Facility, University of Oxford). The OX1-19 iPSC cell was derived from fibroblasts from a skin biopsy of a 36-year-old male patient after signed informed consent (Ethics committee: National Health Service, Health Research Authority, NRES Committee South Central – Berkshire, UK)[186]. The M180 cell line was provided by Emmanuelle Massourides (CECS/I-STEM, France) under a Material Transfer Agreement (MTA) and comprised human iPS cells obtained by reprogramming of adult human myoblasts using Yamanaka technology with ectotrophic retrovirus[187].

2.1.2 Duchene Muscular Dystrophy (DMD) cells

The DMD cell line used for the experiments was the M202 line with deletion in exons 8 to 43. The cells were provided by Emmanuelle Massourides (CECS/I-STEM, France) under a Material Transfer Agreement (MTA). As with the M180 line, these human iPS cells were obtained by reprogramming of adult human myoblasts using Yamanaka technology with ectotrophic retrovirus[187].

2.2 Human iPSC Cell culture

2.2.1 Maintenance of human iPSC cell culture

Human iPSCs were cultured and expanded according to the protocol of their lab of origin for cell banking purposes. All cell lines were cultured feeder free on Matrigel hESC-qualified matrix (Corning)-coated plates using chemically defined media TeSR-E8 or mTeSR1 (Stem Cell Technology). Matrigel hESC-qualified matrix was aliquoted in small tubes stored at -20°C. Prior to expanding the cells, Matrigel-coated plates were prepared using one aliquot of Matrigel hESC-qualified matrix in Dulbeccos's modified eagle medium: nutrient mixture F12 (DMEM/F-12) basal media (ratio 1:100; Fischer Scientific) and incubated at 37°C for at least 1 hour. Plates could be stored at 37°C for up to 14 days. The cells were maintained in either T25 or T75 flasks or a six-well plate.

2.2.2 Recovery of human iPSCs

Human iPSCs were passaged when they reached 90-95% confluency. The media was removed from the plates which were then washed twice with Dulbecco's Phosphate Buffered Saline (DPBS, Sigma Aldrich). The cells were dissociated using ReLeSR (Stem Cell Technologies) by adding 1 mL/well of six-well plates, 2 mL/T25 flask, 6 mL/T75 flask for 1-minute incubation at room temperature. The ReLeSR was then removed from the flask, leaving a thin layer remaining. The cells were then incubated in this layer for a further 6 minutes at 37°C. The plates were stripped with TeSR-E8 or mTeSR1, three times, and cells and media were collected in a 50 mL falcon tube. The cells were then re-plated to the flasks or plates ($5x10^5$ cells/well of 6-well plates, 1 million/T25 flask, 2 million/T75 flask) to complete the passaging.

2.2.3 Passaging protocol

The cells in the cryogenic vial stored in liquid nitrogen were removed and then placed in the 37°C water bath for 2 minutes until most of the ice had melted. The cells were then

immediately resuspended into 10 mL TeSR-E8, mTeSR1, or DPBS in a 15 mL falcon tube to dilute the dimethyl sulfoxide (DMSO) contained in the cryopreservation solution. The pellets were isolated by centrifugation for 4 mins at 1500 rpm. The supernatant was discarded, and the pellet was resuspended in TeSR-E8 or mTeSR1 media containing 10 μM ROCK inhibitor, Y-27632 (Tocris Bioscience) to enhance the viability of the cells[188]. The cells were placed in the Matrigel-coated 6-well plates, 1 million cells/2 mL media/one well of 6-well plates.

2.2.4 Freezing human iPSCs for long term storage

Cells for long-term storage were dissociated using ReLeSR as described above. The cells were then washed with DPBS and spun for 4 mins at 1500 rpm. The supernatant was discarded, and the pellet was resuspended in Cryostore CS10 media containing 10% DMSO (Stem Cell Technologies). The suspension was quickly pipetted into the prelabelled cryogenic vial (1 million cells/vial) and placed in the Mr. Frosty Freezing Container (Thermo Fischer Scientific) at -80°C for 24-48 hours before being placed into liquid nitrogen[189].

2.2.5 Human induced-pluripotent stem cell differentiation into cardiomyocytes

When hiPSCs reached 90% confluency, the cells were dissociated using ReLeSR as described above[190]. The cells (5 x 10^5 cells) were then transferred into Growth Factor Reduced (GFR) Matrigel-coated plates or flasks in the mTeSR or TeSR-E8 medium for differentiation into hiPSC-CM. The following day (day 0), Roswell Park Memorial Institute (RPMI) 1640 (Gibco), supplemented with 1% B27 minus insulin (Gibco) and 6 μM CHIR99201 (Tocris Bioscience) was added. The media was changed to RPMI with 1% B27 minus insulin with no additional factors at day 2. The following day, the media was changed to fresh RPMI with 1% B27 minus insulin with the addition of 2.5 μM Wnt-C59 (Tocris Bioscience). On day 5, 7 and 9 the medium was changed again to RPMI with 1% B27 minus

insulin with no additional factors. The glucose depletion method was performed at day 11 and day 13 by changing the media to RPMI containing no glucose with 1% B27 minus insulin[191,192]. The media was finally changed to RPMI 1640 containing 1% B27 Complete for maintenance culture for further use. The timeline of differentiation can be seen in **Figure 2.1**.

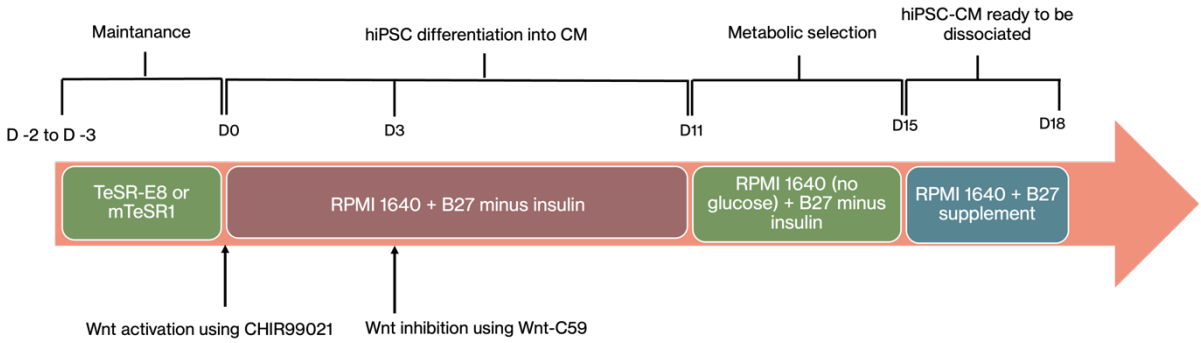


Figure 2.1 Protocol for human iPSC differentiation into cardiomyocytes.
The culture media are listed in the middle row with additional small molecules indicated with arrows on D0 and D3

2.2.6 Dissociation and replating of Human iPSC-CM

Human iPSC-CMs were dissociated using TrypLE Express enzyme (ThermoFisher). When the cells were ready to be re-plated, the media was removed, and the cells were washed twice with DPBS. TrypLE Express enzyme was added into the well (1 mL/well of a 6-well plate). The cells were incubated at 37°C for 8 minutes, washed with DPBS (ratio 1:5), collected into a 15 mL falcon tube and spun for 4 mins at 1500 rpm. The supernatant was discarded, and the pellet was resuspended in RPMI 1640 supplemented with B27 supplement. The cells were then replated to 96-well, 24-well, 12-well or 6-well plates, or used for engineered heart tissue (EHT).

For experiments requiring single cells, such as flow cytometry and the patch-clamp experiments, human iPSC-CMs were dissociated using collagenase II[193]. The dissociation solution was made from collagenase II (200 U/mL) in combination with HEPES, 10 μM

ROCK inhibitor, Y-27632 (Tocris Bioscience), and 30 μM N-Benzyl-p-toluenesulfonamide (BTS). Cells were incubated with 1.5 mL of dissociation solution per 9.5 cm^2 growth area for 3.5 hours at 37°C and for an additional 30 minutes if the cells had not fully dissociated. Cells were then neutralised with RPMI supplemented with DNAse (500:1), collected, and centrifuged at 800 rpm for 15 minutes.

2.3 Generating Engineered Heart Tissue

Engineered heart tissue was generated using the protocol adapted from previously described methods developed by the Eschenhagen group from University Medical Centre Hamburg-Eppendorf, Germany[179]. The gel template for casting EHT was made by dissolving 2% agarose (Invitrogen) in DPBS. This mixture was then autoclaved (121°C, 1 hour) and stored at 2 - 8°C for long term storage. On the day of EHT generation, the agarose template (**Figure 2.2 A**) was made by heating the sterile agarose using a microwave for 2 minutes. The molten agarose was mixed and left until slightly cooled, and then 1.6 – 1.8 mL was pipetted into each well of a 24 well-plate. A Teflon spacer was added to the wells to create the mould (**Figure 2.2 B**) and then removed after 1-hour of cooling at room temperature or 15 mins at 2-8°C. The silicon posts were placed in the gel template (**Figure 2.2 A and C**). Human iPSC-CMs were dissociated using TrypLE Express Enzyme at 37°C for 8 minutes as described above. A master mix of cells and media for EHT (normally 4 – 16 EHTs) was prepared as shown in **Table 2.1** and **Table 2.2**.

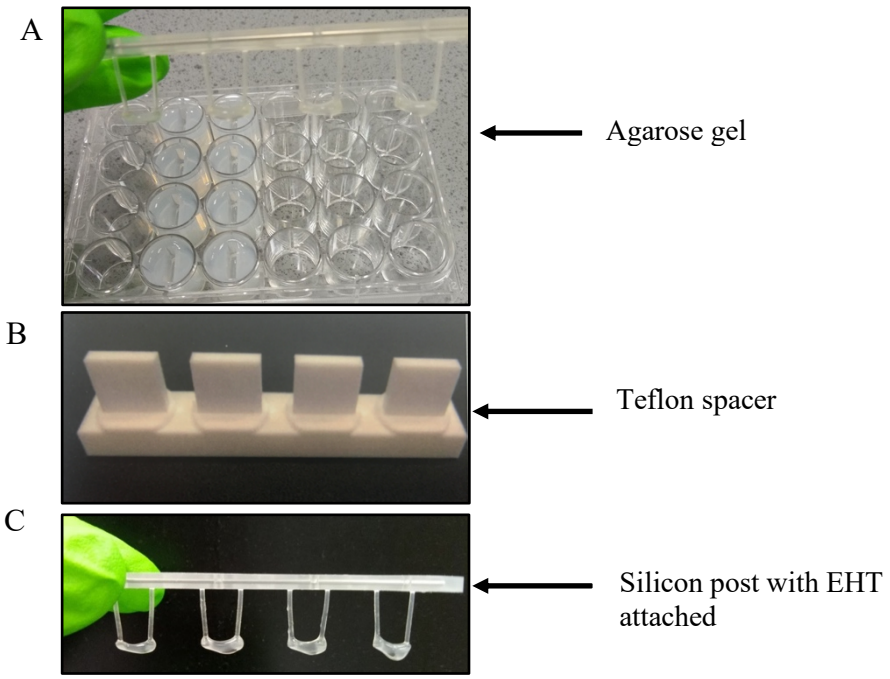


Figure 2.2 Apparatus for EHT generation

Agarose gel as a template (A), teflon spacer to create the mould (B), silicon posts to hold the EHTs (C).

Table 2.1 Reagents for EHT generation

Reagent name	Components
UltraPure Agarose (Life Technologies)	2 g UltraPure agarose + 100 mL sterile DPBS
10X DMEM (Life Technologies)	1.34 g DMEM powder + 10 mL sterile water
2X DMEM	1 mL 10X DMEM + 1 mL horse serum + 100 µl Penicillin/Streptomycin + 2.9 mL Water (TC sterile)
NKM Medium	100 mL DMEM + 10 mL Foetal Bovine Serum (FBS) + 1 mL Penicillin/Streptomycin + 1 mL L-glutamine
EHT medium	45 mL DMEM + 500 µl Penicillin/Streptomycin + 50 µl Insulin 10 mg/ml + 50 µl Aprotinin 33 mg/ml + 10 mL horse serum

The master mix was then pipetted to a well of 96-well plate containing 3.6 µl of thrombin (for single EHT) and transferred quickly into the agarose mould with the silicone posts. The EHTs were normally made in batches of 6 - 12 single EHT depending on the number of hiPSC-CMs. The EHTs were incubated for 90 mins in 37°C. Following the incubation, 500 µl NKM media was added to each EHT for hydration, and they were left for another 30

minutes. All EHTs were then transferred from the gel moulds into 24 well-plates containing 2 mL EHT media. EHTs were fed every two days with 1.5 mL fresh EHT media. Table 2.2 contains a list of the reagents used for EHT culture media:

Table 2.2 Master mix formula for EHT

	1x	**4.5x (for one column – 4 EHTs)**
NKM (containing the cells)	94.56 µl	425.5 µl
2X DMEM	6.68 µl	30.1 µl
Rock inhibitor	0.12 µl	0.5 µl
Matrigel	12 µl	54 µl
Fibrinogen + aprotinin	3.04 µl	13.7 µl

2.4 Quantitative PCR

2.4.1 Primer Design

The NCBI Primer-Blast online tool (*www.ncbi.nlm.nih.gov/tools/primer-blast/*) was used for designing primers. In order to get optimal primer design, the primers should have a GC content of 50-60%, a melting temperature of 65 - 75°C, and a length of 18-25 nucleotides. In addition, the primers must flank the exon-exon border of the gene to avoid genomic DNA amplification and primers ending in G or C. Some primers used were from published papers and validated in house.

The thermocycler (Senso Quest Gene Flow) run was designed by setting the denaturation time to 95°C for 5 minutes for the initial cycle and 30 seconds on the subsequent cycles. The annealing temperature was set to be 5°C below the Tm of the primers (no lower than 40°C) for 30 seconds. The extension was set to 72°C for 1 min/kb of expected products and 5 – 10 on the last cycle. The calculated cycle number was 30.

2.4.2 Total RNA extraction and purification

Human iPSC-CM were dissociated using the TrypLE Express Enzyme protocol described above and the pellets placed in the Eppendorf tubes and frozen in liquid nitrogen. EHTs

were carefully isolated using tweezers and scissors and freeze-clamped in liquid nitrogen. The frozen cell pellets and EHTs were stored at -80°C for further analysis. To extract RNA, DNA, and protein, the cells and EHTs were treated with Trizol reagent (ThermoFisher) and disrupted using a pellet disrupter.

Total RNA was isolated and purified from the extract solution using the RNeasy Mini Kit (Qiagen), according to the protocol. An equal amount of absolute ethanol (99% ethanol) was added to the Trizol reagent containing total RNA and mixed gently. The mixture was then placed in a RNeasy spin column placed in a 2 ml collection tube, spun at 10000 rpm for 15 seconds, and the flow-through was discarded. Buffer RW1 was added into the RNeasy spin column and centrifuged at 10000 rpm for 15 seconds and the flow-through was discarded. Next, buffer RPE was added into the RNeasy spin column and centrifuged at 10000 rpm for 15 seconds and the flow-through was discarded. Buffer RPE was added again onto the RNeasy spin column and centrifuged at 10000 rpm for 2 mins to wash the spin column membrane. The spin column was transferred to a new collection tube and further spun for 1 min. The RNeasy spin column was finally transferred to a new 1.5 mL collection tube and 20-30 µl of RNase free water was added to the spin column and centrifuged at 10000 rpm for 1 min. A Nanodrop spectrophotometer was used to determine RNA yield and purity, with a ratio of $A_{260/280}$ = 1.8 – 2.0 considered as acceptable[194].

2.4.3 Complementary DNA (cDNA) synthesis

RNA was converted into cDNA using the High-Capacity cDNA Reverse Transcription Kit (Life Technologies). The total volume of reaction was 20 µl consisting of 10 µg RNA, 2 µl RT random primers, 2 µl RT buffer, 1 µl MultiScribe Reverse Transcriptase enzyme, 0.8 µl deoxynucleotide triphosphate (dNTP) mix and 4.2 µl of ddH_2O. The solution was incubated in a SensoQuest Basic Thermal Labcycler (SensoQuestGeeneFlow) for 10 minutes at 25°C, 120 minutes at 37°C, and 5 minutes at 85°C.

2.4.4 Quantitative PCR reaction

An Applied Biosystems StepOnePlus Real-Time PCR System (Applied Biosystems, ThermoFisher) was used for performing the qPCR reaction. The genes of interest are listed in **Appendix B**. The reaction was performed using SYBR Green (ThermoFisher) as a detection system. The SYBR Green was mixed with the primers and the cDNA according to the formula listed in **Table 2.3**. The mixed solution and the cDNA were then loaded to a 96-well qPCR plate (MicroAmp Fast, Applied Biosystem). In order to prevent evaporation, the plate was sealed using a MicroAmp™ Optical Adhesive Film (Applied Biosystem, ThermoFisher) and centrifuged at 4400 rpm for minutes.

Table 2.3 Formula for the qRT-PCR reaction

Component	Volume (µl)
SYBR Green (2X mixture of SYBR Green 1 Dye, AmpliTaq Gold™ DNA Polymerase, dNTPs with dUTP, Passive Reference 1 (ROX), and optimized buffer components)	5
Forward primer	0.5
Reverse primer	0.5
RNase/DNase free water	1.5
Template cDNA (12.5 ng)	2.5
Total	10/reaction

The method used for the reaction was a two-step cycle with 40 cycles in total with the setting shown below:

Table 2.4 Method for qRT-PCR reaction

Stage	Time (s)	Temperature (°C)
Holding (polymerase activation)	600	95
Cycling (denaturation)	15	95/60
Melt Curve (annealing/extension)	30	60

2.4.5 Analysis of qPCR data

The relative mRNA expression was calculated using the ΔΔCt Livak method[195], plotting the data as $2^{-\Delta\Delta CT \pm SE}$. The analysis was done by comparing the experimental group to the control group. The number of cycles required by the fluorescent signal of a sample to exceed the background signal was measured as the cycle threshold (C_T). The mRNA expression was normalised to housekeeping gene (HKG). The C_T of each target (TG) was normalised twice, against the HKG and then against the control group, following the steps below:

1. Calculate the average C_T of the TG and of the HKG
2. Calculate ΔC_T: $\Delta C_T = C_T\,(TG) - C_T\,(HKG)$
3. Calculate $\Delta\Delta C_T$: $\Delta\Delta C_T = \Delta C_T\,(\text{experimental group}) - \Delta C_T\,(\text{control group})$
4. Calculate the relative fold change: $2^{-\Delta\Delta C_T}$
5. Use the fold change data for statistical analysis

2.5 Immunohistochemistry and immunocytochemistry

2.5.1 Tissue Cryo-sectioning

Engineered heart tissues were harvested using tweezers and scissors, rinsed with DPBS, and fixed in 4% paraformaldehyde (PFA) for 2 hours at RT. Fixed EHTs were then equilibrated in 30% sucrose in DPBS (pH 7.4) overnight at 4°C. Optimal cutting temperature compound (OCT; Sakura Tissue-Tek, 4583) for embedding tissue was prepared by pouring it to a plastic template (half full) and leaving it to harden. EHTs were placed in the middle of the OCT and covered with fresh OCT and stored at -80°C. Frozen EHTs were sliced into 10 µm cryo-sections using a cryostat (Bright 5040) at -20°C and placed on glass slides (Superfrost).

2.5.2 Sample preparation for immunostaining

The cells were seeded on Matrigel-coated glass coverslips in 24-well plates. Culture media was removed, and the cells were washed twice with DPBS prior to fixation with 4% PFA (Santa Cruz) for 10 mins at RT. After fixation, the cells were washed twice with DPBS and

stored at 4°C. For intracellular staining, cells were permeabilised with 0.5% Triton X-100 (Sigma, UK) for 10 mins at RT and washed twice with DPBS. The cells were then blocked with blocking solution containing 1% BSA, 10% serum from the species in which the secondary antibody was raised, ± 0.05% Triton X-100 for 1 hour in RT.

2.5.3 Immunostaining

Fixed cells were incubated with the primary antibody in blocking solution at 4°C overnight then washed with DPBS. The cells were then incubated with the secondary antibody (**Appendix A**) for 1 hour in the dark at RT and washed with DPBS. Nuclei were stained with DAPI (1µg/ml in DPBS) for 10 mins at RT and then washed with DPBS. Slides were mounted with 1:1 DPBS:Glycerol under glass coverslips and stored in the dark at 4°C. Sample imaging was carried out using an Inverted Olympus FV1000 Confocal system and the images were analysed using Fiji software.

2.5.4 Oil Red O staining

Lipid droplets in the cells were stained using an Oil Red O staining kit (Sigma Aldrich). The cells were washed twice with DPBS and fixed with 4% PFA for 10 minutes at RT and stored at 4°C after washing with DPBS. The cells were treated with 60% isopropanol for 5 mins and incubated with Oil Red O working solution for 10-20 mins after the isopropanol was discarded. Oil Red O was discarded, and the cells were washed 25 times with water until no excess stain was seen. Nuclei were stained using DAPI for 1 min and washed three times with water. The cells were scanned using an Inverted Olympus FV1000 Confocal system and acquired images were processed using Fiji software. At least three images were analyzed as technical replicates, within each biological replicate.

2.5.5 MitoTracker red CMXRos staining

Human iPSC-CMs were incubated with DMEM media containing 100 nM of MitoTracker Red CMXRos dye for 10 mins at 37°C. The cells were then washed twice with DPBS and

fixed with 4% PFA for 10 mins at RT and stored at 4°C after washing with DPBS. Nuclei were stained with DAPI (1μg/ml in DPBS) for 10 mins at RT and then washed with DPBS. Fixed cells were scanned using an Inverted Olympus FV1000 Confocal system and acquired images were processed using Fiji software. Fluorescence intensity was calculated by taking the intensity of each area divided by the cell number as determined from the DAPI stain.

2.6 Flow cytometry

Single cell human iPSC-CM were used for flow cytometry. The cells were dissociated using collagenase II solution described in cell dissociation protocol. Cell viability staining was done using Zombie Violet (ZV; 1:100, BioLegend, 405 nm wavelength) for 20 mins in the dark at RT. The supernatant was discarded after centrifuging the cells prior to fixation with 4% PFA for 20 mins at 4°C.

One million cells per mL of DPBS were incubated with blocking media (DPBS, 1% bovine serum albumin, 0.05% Triton) for 1 hour in the dark at RT. The samples were incubated with primary antibody (1:200 dilution) in blocking media for 1 hour at RT. The samples were then washed with DPBS containing 0.5% BSA by centrifugation (2000 rpm, 4 minutes). The samples were then incubated with a secondary antibody (1:200, 1 hour, at RT) and washed three times with DPBS containing 0.5% BSA.

For flow cytometry, each sample was resuspended in 600 μl – 1 mL of DPBS. Controls were used in each run consisting of fixed cells (negative control), fixed ZV-treated cells (ZV control), and secondary antibody stain only (secondary antibody control). Flow cytometry was performed by using a BD FACSAria III machine and analysed using FlowJo Software 10.0. The analysis was done using three plots. First, side scatter (SSC-A) vs forward scatter (FSC-A) for singlets. Second, ZV (405 nm) vs FSC for live cells. Third, ZV (405 nm) vs FITC (488 nm) to find the protein of interest. The graph was also presented as a histogram.

2.7 Assessing cell metabolism using radiolabelled compounds

2.7.1 Glycolytic flux (5-^{3}H-glucose)

The rate of glycolysis in the cells from the monolayer and engineered heart tissue (EHT) was measured using the rate of ^3H_2O produced from ^{3}H-glucose added to the cells. This well-established protocol was adapted from several previous publications[196–204]. The ^3H_2O was released as a by-product in the ninth step of glycolysis which is the conversion of 2-phosphoglycerate to phosphoenolpyruvate catalysed by enolase (**Figure 2.3**).

The experiment was started by preparing the cells either in 24-well plates (1.9 cm^2 growth area) as a monolayer with cell density 300K-500K cells per well or in EHT. The incubation media was made by mixing glucose-free DMEM (ThermoFisher) supplemented with 5 mM glucose and 0.2 µCi/mL of glucose, D-[5-^{3}H(N)] (PerkinElmer). The prepared samples were then incubated with incubation media (1 mL/well in 24-well plates or 1.5 mL/well for EHT) in the incubator (37°C, 5% CO_2, and 21% O_2) for 6 hours. After the incubation, the media was collected and frozen at -20°C for subsequent extraction. The cells were lysed with lysis buffer and frozen at -20°C for measurement of protein concentration.

^3H_2O was separated from 5-^{3}H-glucose using an ion-exchange chromatography separation (Dowex) method. Dowex was prepared by mixing 250 g Dowex 1 x 4 chloride form, 100-200 mesh (Sigma Aldrich) with 1.25 M NaOH and 1.61 M boric acid. The mixture was mixed gently and repeatedly washed with distilled H_2O until the mixture reached pH 7.5. Dowex was put in glass Pasteur pipettes (VWR 612-1701) that had glass wool in the bottom (**Figure 2.4**). 200 µl of the media was added to the Dowex column and incubated for 15 mins, allowing ^{3}H glucose to bind to the column. ^3H_2O was eluted into scintillation vials by washing twice with distilled water. Radioactivity was measured using Tri-Carb 2800TR liquid scintillation analyzer (PerkinElmer). 0.2 mL medium at time point 0 was used as a control to determine the specific activity of the buffer.

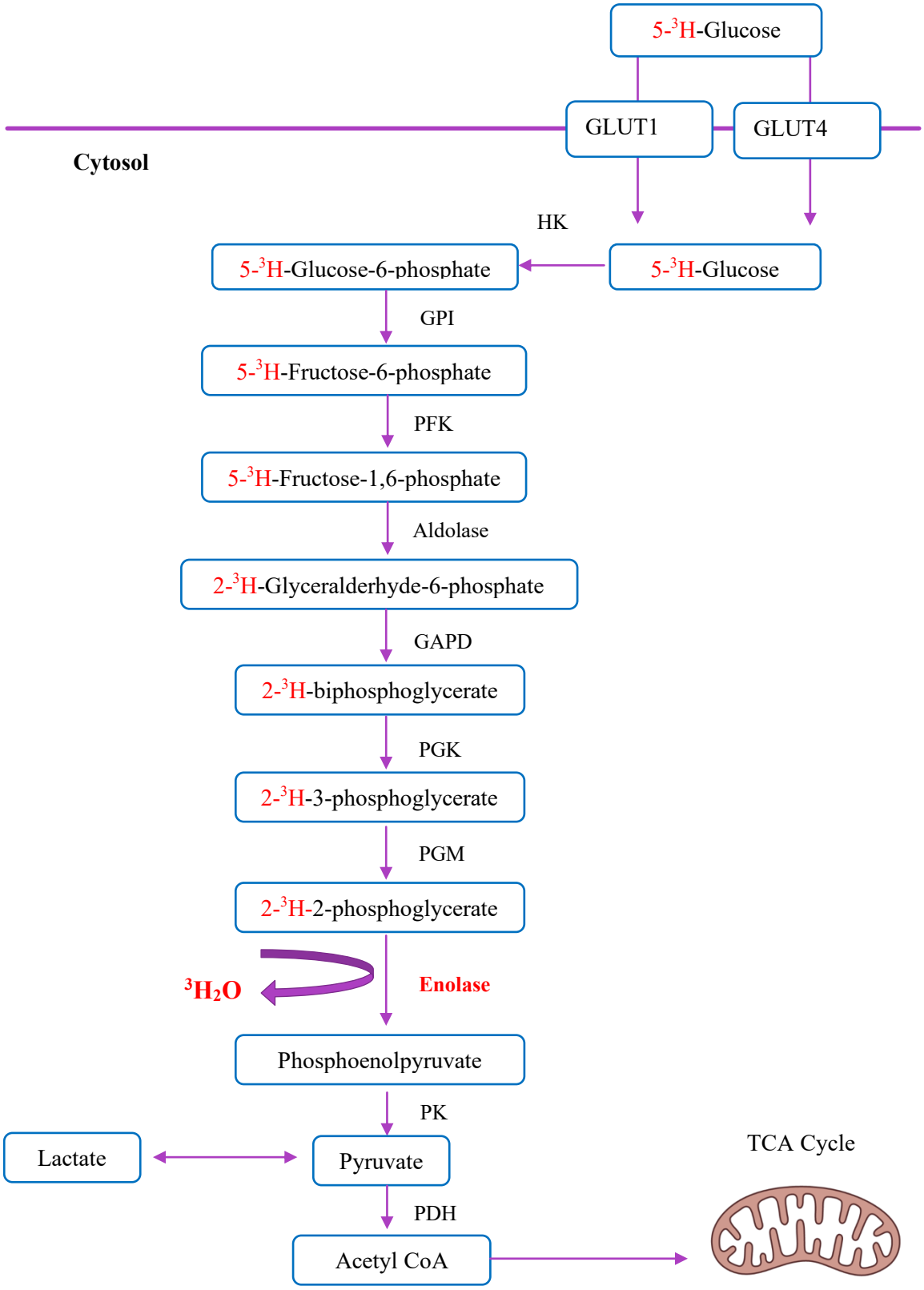


Figure 2.3 Schematic representation of uptake and utilisation of ^{3}H-glucose and its release as $^{3}H_2O$ facilitated by Enolase

HK: Hexokinase, GPI: Glucose-6-Phosphate Isomerase, PFK: Phosphofructokinase, GAPDH: Glyceraldehyde-3-phosphate dehydrogenase, PGK: Phosphoglycerate Kinase, PGM: Phosphoglycerate Mutase, PK: Pyruvate Kinase, LDH: Lactate Dehydrogenase, PDH: Pyruvate Dehydrogenase, TCA: Tricarboxylic Acid. The illustration was adapted from Barr, R and Lopaschuk, G, et al.[201]

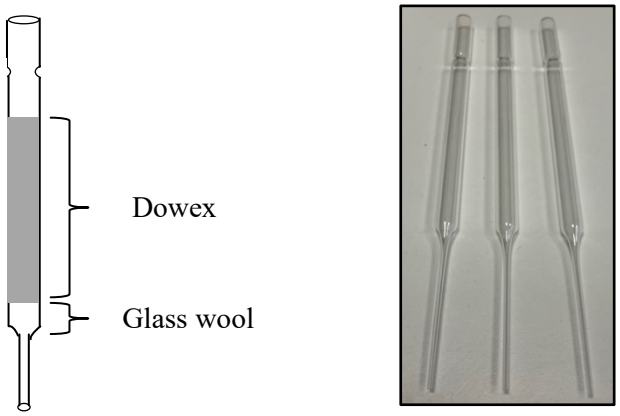


Figure 2.4 Pasteur glass pipette image representation

Pasteur glass pipette image representation and the proportion of Dowex for the ^{3}H-glucose and $^{3}H_2O$ separation

2.7.2 ^{3}H palmitate oxidation and ^{3}H oleate oxidation

Palmitate and oleate oxidation (**Figure 2.5**) were measured by determining the $^{3}H_2O$ production from ^{3}H palmitate or ^{3}H oleate via the electron transport chain[201,205–207]. The cells were cultured in 24-well plates. The reagent was made by mixing 2% BSA in no-glucose DMEM (ThermoFisher) with 0.3 mM palmitate or oleate and 0.2µCi/mL of palmitate or oleate, [9,10-3H(N): 1mCi-37MBq] (PerkinElmer). Palmitate and oleate were heated prior to conjugation with BSA, and the ^{3}H palmitate or ^{3}H oleate was added straight afterwards. 1.5 mL incubation media was added to the cells and incubated for 8 hours at 37°C, 5% CO_2, and 21% O_2.

$^{3}H_2O$ produced from the incubation was separated using the Folch extraction method[208] modified by Malandraki-Miller, S. et al[205]. 0.5 mL perfusate in 15 mL falcon tube was added to 1.88 mL of chloroform:methanol (1:2 v/v) solution, 625 µl chloroform and 625 µl KCL-HCl solution (2 M KCl, 0.4 M HCl). The solution was then rotated on a laboratory Stuart rotator SB3 at 40 rpm for 1 h before removing the top aqueous layer and discarding the organic layer. The top aqueous layer solution was added to a further 1 mL chloroform, 1 mL methanol and 0.9 mL KCL-HCL and rotated for 1 h at 40 rpm. 0.5 mL of the top aqueous layer was used to count the radioactivity. 0.5 mL medium at time point 0 was used as a control to determine the specific activity of the buffer.

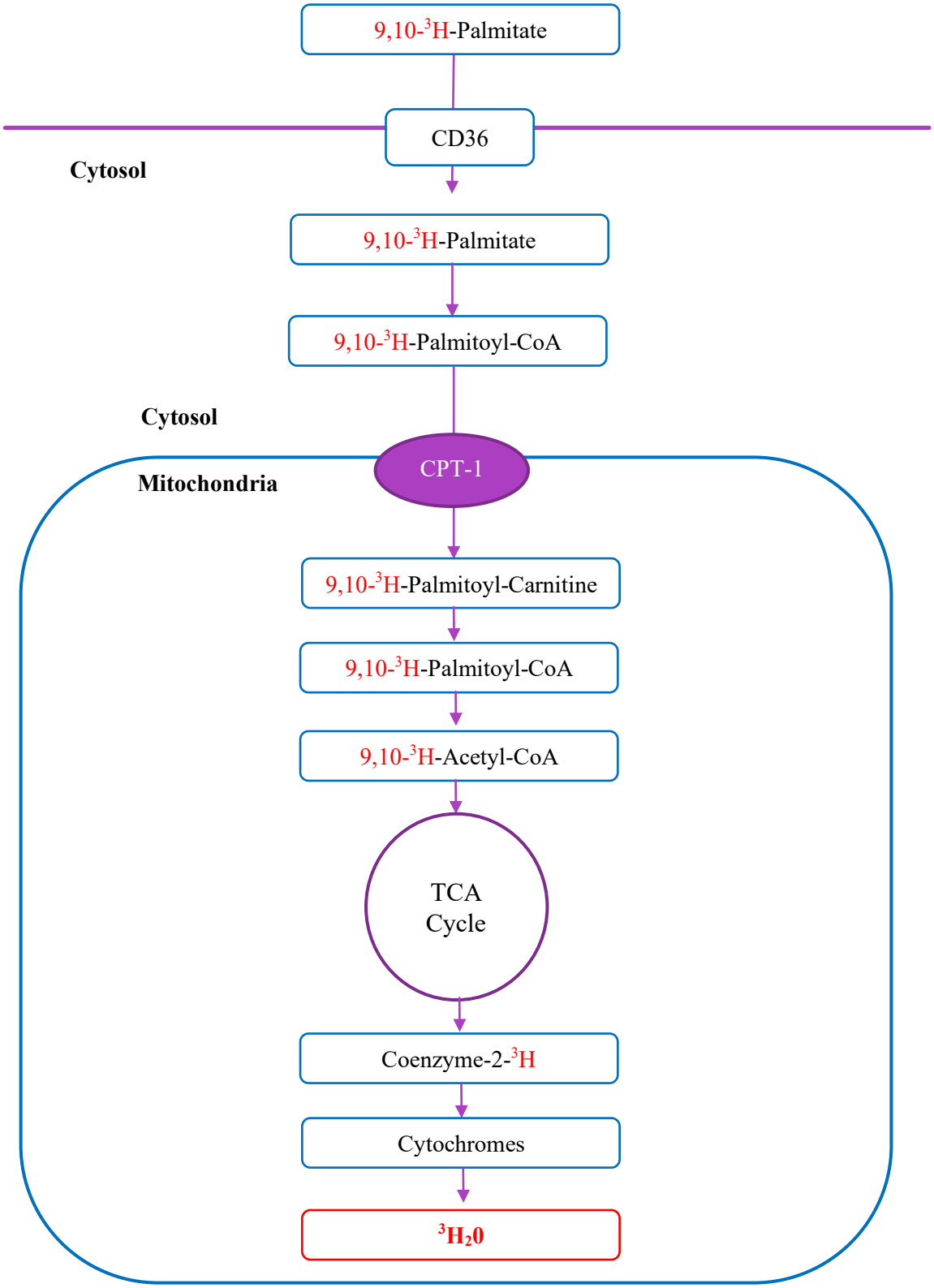


Figure 2.5 Schematic representation of uptake and utilisation of ^{3}H-palmitate and its release as $^{3}H_2O$ in the mitochondria

TCA: Tricarboxylic Acid, CoA: Coenzyme A. The illustration was adapted from Barr, R and Lopaschuk, G, et al.[201].

2.8 Assessing cell metabolism using enzymatic reaction and Pentra analysis

2.8.1 Lactate assay

The lactate assay measures the amount of NADH produced by the LDH-catalysed conversion of lactate + NAD^+ → pyruvate + NADH as an indicator of lactate in the sample. Lactate released from the cells was measured using L-lactic dehydrogenase from bovine heart (Sigma Aldrich) following manufacturer's instruction with the modified glycine buffer solution consisting of 0.6 M glycine, 1.3% of Hydrazine Hydrate (50-60% pure), and KOH to reach a final of pH 9.5. Sample media was mixed with the lactate assay buffer (containing 1.5 mM NAD^+) and L-lactic dehydrogenase. The mixture was incubated at 37°C for 20 mins before reading the absorbance at 340 nm. The lactate concentration of each well was determined against the standard curve.

The lactate assay was also performed using an ABX Pentra 400 Chemistry Analyser (Horiba). The culture medium from the cell experiments was analysed using the lactate reagent (Horiba). The reagent from the manufacturer containing lactate oxidase reacts with the lactate molecules in the media and triggers the release of hydrogen peroxide. The reagent also contains 4-aminoantipyrine and ESPAS which, with the help of peroxidase, reacts with hydrogen peroxide to produce a coloured complex. The intensity of the colour is proportional to the amount of lactate present in the sample.

2.8.2 Glucose assay

Glucose was measured in the media before and after culturing with the cells. This was carried out using the glucose assay reagent (Sigma Aldrich) following manufacturer's instruction. Sample media was mixed with the glucose assay reagent and incubated at 37°C for 15 mins before reading the A_{340}.

The glucose assay was also performed using the ABX Pentra 400. The glucose PAP CP reagent from the manufacturer contains glucose oxidase which would react with glucose in the media and with oxygen to produce hydrogen peroxide which was detected as above.

2.8.3 Lactate dehydrogenase (LDH) Assay

The lactate dehydrogenase (LDH) assay was performed using the ABX Pentra 400 using the LDH CP reagent (Horiba) and analysed as above.

2.9 Assessing cell viability

2.9.1 Alamar Blue assay

The Alamar Blue (ABA) assay is a non-destructive assay to quantify the viability of the cells in the same population over time. The viability of the cells is measured by the reduction of Alamar Blue. Initially, 1.5 mL resazurin (blue and low fluorescence) was added to each well of a 24 well-plate containing cells or EHT and incubated for 4 hours at 37°C. The same amount of resazurin solution was put in the fridge as a negative control and at 90°C as a positive control for 4 hours. Resazurin was converted to resorufin (magenta and high fluorescence) in the mitochondria. The measurement was done by putting 200 µl of this media into flat bottom 96-well plates and the absorbance was measured at 550 nm.

2.9.2 Cell counting kit-8 (CCK-8)

The cell counting kit-8 (CCK-8 – Sigma Aldrich) is a colorimetric assay to determine the viability of the cells and measure cytotoxicity in the cells. This assay uses WST-8 (2-(2-methoxy-4-nitrophenyl) – 3 – (4-nitrophenyl) – 5 – (2,4-disulfophenyl) – 2H – tetrazolium, monosodium salt). This compound is reduced by NADH/NADPH in the presence of 1-Methoxy-5-methylphenazinium methyl sulphate to become Formazan, a water-soluble compound which is directly proportional to the number of living cells. CCK-8 kit is stable and has low toxicity to the cells. The CCK-8 solution was added directly into each well of designed plates or 24-well plates for EHT and incubated at 37°C for 4 hours. The absorbance

was read at 550 nm. The number of living cells was calculated by using standard curve from CCK-8 assay from cells with different density.

2.9.3 Automated cell counting

Cell number and viability was counted by using a Countess Automated Cell Counter (ThermoFisher). The cells were mixed with 0.4% Trypan Blue solution (ThermoFisher), ratio of 1:1, only cells with intact membranes can effectively exclude the dye, so dead cells with compromised membranes become stained.

2.10 Western blot

Cells were washed twice with DPBS and then lysed with lysis buffer (**Table 2.5)**. EHTs were snap frozen with liquid nitrogen, crushed, and lysed with lysis buffer (**Table 2.5**). The protein concentration was measured using a BCA assay (Sigma Aldrich) following the manufacturer's protocol. Protein (10 μg) was loaded onto SDS-PAGE gels and separated by electrophoresis at a fixed voltage (200-volt, 1 hour). The proteins in the gels were then transferred onto nitrocellulose paper by electrophoresis at a fixed current (0.18 A, 1 hour). The protein transfer was confirmed by Ponceau staining. The blots were incubated with blocking solution (5% Milk or BSA) and then incubated with primary antibodies followed by secondary antibodies. Bands were quantified using LI-COR C-Digit chemiluminescent detection system (LI-COR Biotechnology, Lincoln, Nebraska) and Image Studio software version 5-2-5 (LI-COR) or ChemiDoc XRS+ (Bio-Rad) and Image Lab software (Bio-Rad).

Table 2.5 Composition of lysis buffer for protein extraction

Component	Quantity
Tris-hydrochloric acid (Tris-HCL)	75 mM
Sodium dodecyl sulphate (SDS)	3.8%
Urea	4M
Glycerol	20%
Triton X-100	0.1%
Water	

Note: Protease inhibitor cocktail (Roche) and Phosphatase inhibitor cocktail (Roche) were added to every 10 mL lysis buffer or according to the manufacturing instruction.

2.11 Musclemotion

The video of contracting 2D culture cells and EHT were taken at 60x magnification for 15-30 seconds duration using either a Canon EOS 100D camera or an iPhone 11 with macro lenses (120/240 frames per second) using the in-house designed box as shown in **Figure 2.6**. The videos were then converted into 50 frames per second tiff sequence images using a terminal in MacOS with the code *for I in *.*; do ffmpeg -I "$i" -pix_fmt nv12 -f avi -c:v rawvideo "${i%.*}.avi "; done.* The videos were then processed using Musclemotion software v.1[209–211] as a macro plug in FIJI/ImageJ software. The data generated could be used to calculate contraction amplitude, peak-to-peak time, time to peak, relaxation time, and peak amplitude as shown in **Figure 2.7**.

2.12 Multielectrode array

Human iPSC-CM were dissociated and replated onto the 8 x 8 or 6 x 10 electrodes of a multielectrode array chip. The optimum cell number for the replating was 10.000 – 20.000 cells per chip. Prior to cell plating, the chip was sterilised using 100% ethanol and coated with Matrigel overnight. This step was necessary to promote the cellular adhesion and to increase the hydrophilicity of the chip surface. The voltage changes in the cells were then measured using the Maxwell Biosystem software[193].

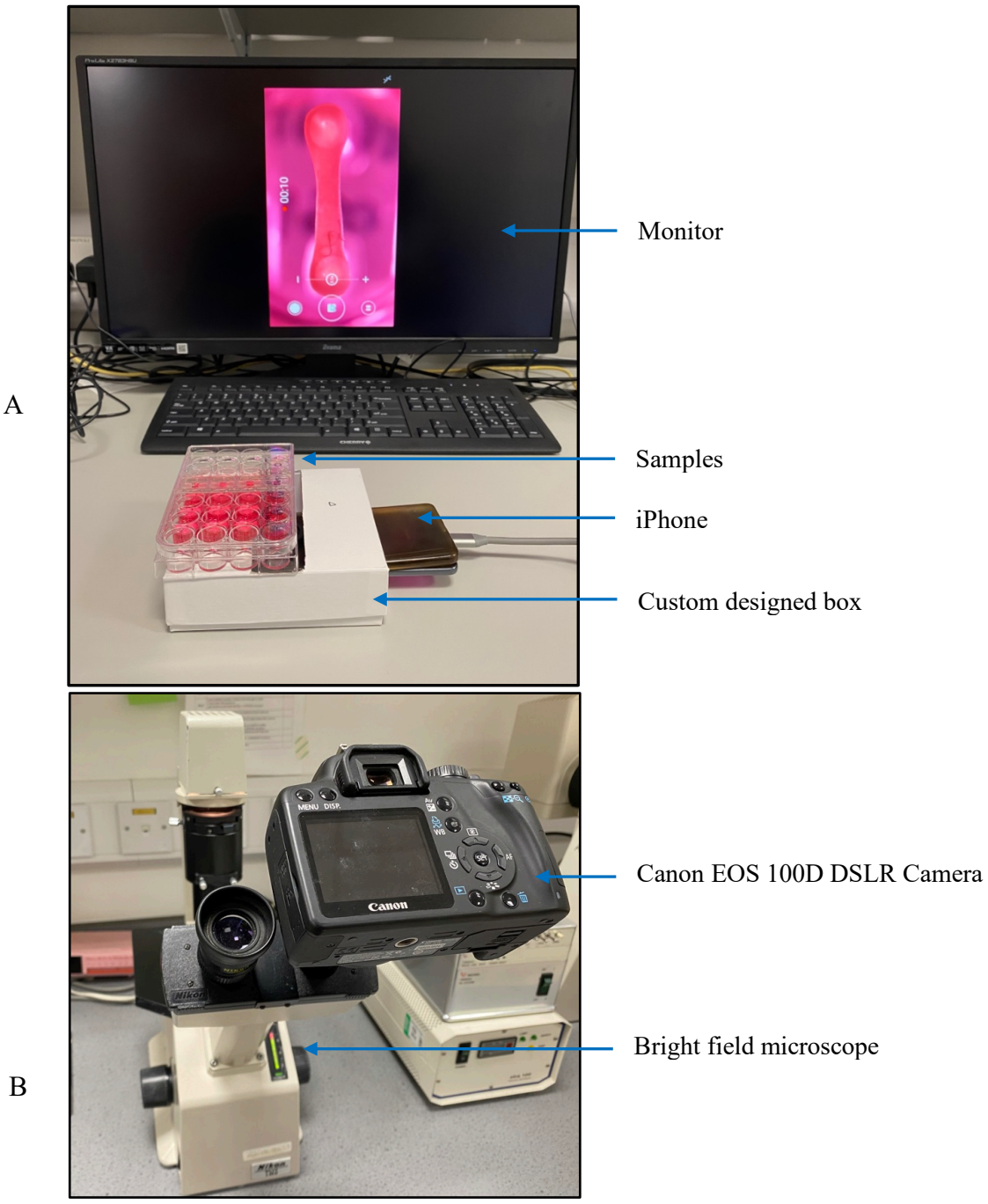


Figure 2.6 Custom designed instrument to measure contractility of EHT

The custom designed box was used to hold the samples and iPhone camera and connected to the monitor to observe the EHT contractility in real time (A) or using brightfield microscope connected to DSL camera (B). The videos were used for measuring EHT contractility using Musclemotion.

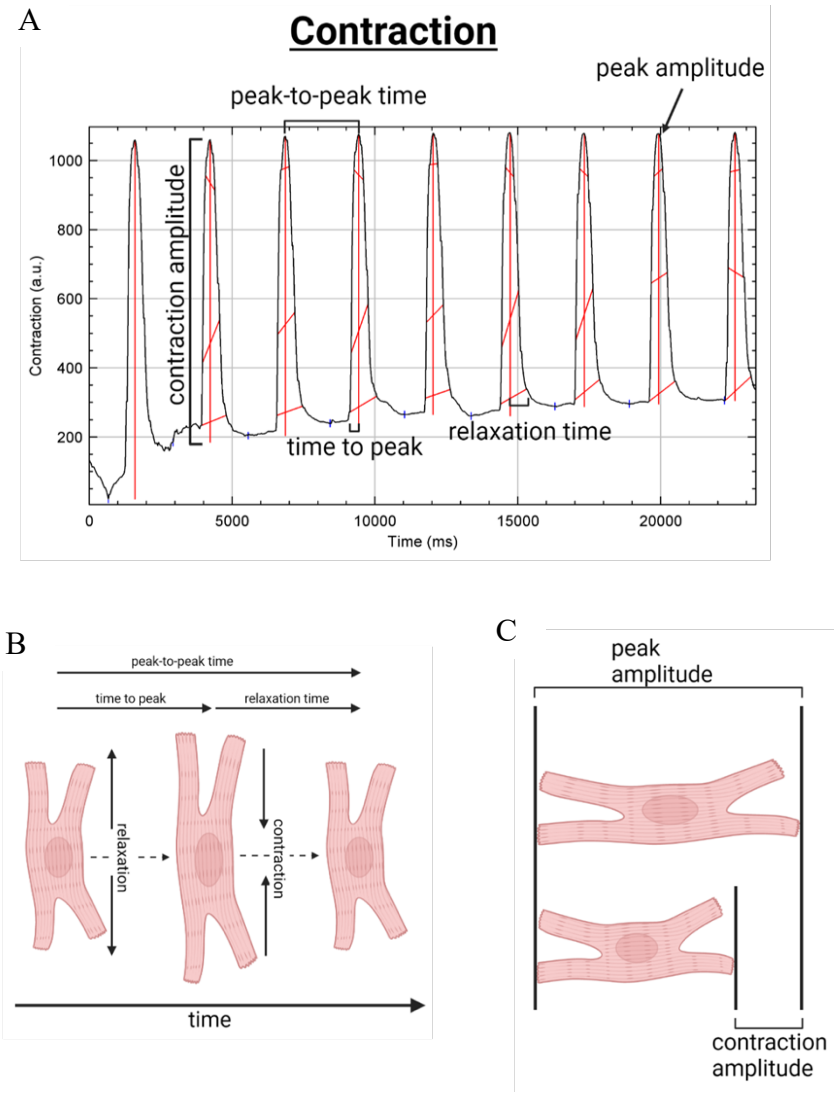


Figure 2.7 Schematic representation of Musclemotion parameters

Contraction graph generated from Musclemotion indicating peak amplitude, which is the highest value for each peak, contraction amplitude which is the different between peak amplitude and baseline correlated to the force of CM contraction (A). Schematic representation of the time parameters as measured in single cardiomyocytes (B). Schematic representation of the peak and contraction amplitude, where peak amplitude corresponds to the pixels of the CMs in the relaxed state and the contraction amplitude corresponds to the difference in pixels of the CMs in the relaxed and contracted state.

2.13 Patch clamp

Human iPSC-CMs were dissociated into single cells using the collagenase II protocol described in the cell dissociation protocol. Engineered heart tissue was dissociated into patchable single cells using modified protocol previously described[212]. EHTs were incubated for 15 mins with activated papain solution containing 20 U/ml papain from Carica papaya (Sigma Aldrich), 1.1 mM EDTA, 67 µM 2-mercaptoethanol (Sigma Aldrich), 5.5 mM l-

Cysteine-HCl (Sigma Aldrich) in 1 x EBSS (Thermo Scientific). The enzymatic reaction was terminated using DMEM/F-12 supplemented with 10% FBS. Whole patch clamp recording was performed using a patch clamp amplifier. Current-clamp recording for action potential measurements was conducted in normal Tyrode's solution containing 140 mM NaCl, 5.4 mM KCl, 1 mM MgCl2, 10 mM glucose, 1.8 mM CaCl2 and 10 mM HEPES (pH 7.4 with NaOH at 25°C) using the pipette solution 120 mM K d-gluconate, 25 mM KCl, 4 mM MgATP, 2 mM NaGTP, 4 mM Na2-phospho-creatine, 10 mM EGTA, 1 mM CaCl2 and 10 mM HEPES (pH 7.4 with KCl at 25 °C)[193]. Patch clamp measurement and data analysis was done with the help of Dr. Taiyi Wang, a postdoc in the Cardiac Metabolism Research Group.

2.14 Proteomics and transcriptomics analysis

EHTs were washed with DPBS and quickly frozen using liquid nitrogen and stored at -80°C. For transcriptomic analysis, the total RNA was prepared for each sample using the RNEasy mini kit (Qiagen) to generate 500 ng RNA in 5 µL RNAse free water. Proteomics and transcriptomics analysis were performed in collaboration with the Novo Nordisk Research Centre Oxford (NNRCO), Old Road Campus, Roosevelt Drive, Oxford, OX3 7FZ, UK. The data was analysed by a Dphil student from Prof. Lisa Heather's group, Ryan Carter.

2.15 Transmission electron microscopy (TEM)

The 2D culture hiPSC-CM samples for TEM were prepared by culturing the cells on polycarbonate filters in a 6 well 24 mm Transwell, with a 0.4 µm polycarbonate membrane insert (Corning). The EHTs were removed from the posts. All cell samples were immersed in fresh 2% paraformaldehyde/2.5% glutaraldehyde for 1 hour in their plates, and EHT sections were immersed for 2 hours in Eppendorf tubes. After that, the samples were kept in a 10% fixative solution until they were processed. The samples were washed in 0.1 M phosphate buffer (PB) before being post-fixed in 1 percent w/v osmium tetroxide (in 0.1 M

PB) and stained with 2 percent w/v uranyl acetate (in distilled water). Before embedding the samples in Spurr's resin, they were dehydrated with increasing concentrations of ethanol (70-100 percent) and then acetone (Agar Scientific). Using a Reichert ultra-cut S-microtome (Riechert-Leica), 50-80 nm sections were cut and mounted on 200 mesh nickel grids (Agar Scientific) by a technician at the Dunn School of Pathology, University of Oxford. The sections were examined with a JEM 1010 JEOL transmission electron microscope, and images were taken with a GANTAN Orius digital camera. Ms. Kirsti Brisk, a MRes student in Prof Carolyn Carr's group, prepared the samples for sectioning, acquired the images with the assistance of Professor Helen Christian and performed the data analysis.

2.16 Statistic and data analysis

The data were obtained from duplicate or triplicate technical repeats with at least three biological repeats. Results are presented as mean ± standard error. GraphPad Prism version 8 (GraphPad Software, La Jolla, California) was used for statistical tests, and results were considered significant at $p < 0.05$ and represented as * = $p<0.05$, **= $p< 0.01$, *** = $p<0.001$, **** = $P<0.0001$, or # = $p<0.05$, ## = $p<0.01$, ### = $p<0.001$, #### = $P<0.0001$. Data set containing two groups were analysed with a two-tailed parametric unpaired t-test with Welch correction. Data sets containing multiple groups were analysed with one-way ANOVA, with Tukey post hoc correction for multiple comparison. Data sets with two groups and two variables were analysed with two-way ANOVA, with Dunnett or Tukey post hoc correction for multiple comparisons. For the statistical analysis, normality test was not performed.

3

Metabolic maturation of human induced pluripotent stem cells derived cardiomyocytes in 2D and engineered heart tissue

CHAPTER 3

3 METABOLIC MATURATION OF HUMAN INDUCED PLURIPOTENT STEM CELLS DERIVED CARDIOMYOCYTES IN 2D AND ENGINEERED HEART TISSUE

3.1 Abstract

Cardiac metabolism and function are linked, as substrate metabolism generates the energy which enables the heart to beat. Human heart cells can be studied in vitro using human induced pluripotent stem cell-derived cardiomyocytes (hiPSC-CM). However, when cultured in normal media, hiPSC-CM use glucose as the primary substrate whereas adult cardiomyocytes generate energy predominantly through fatty acid oxidation (FAO). Here I have explored the impact on maturation when combining stimulation of FAO and the use of 3D engineered heart tissue (EHT) cultures. I investigated substrate metabolism in hiPSC-CMs grown as 2D monolayer and by culture in EHT, by measuring rate of glycolysis and FAO), changes in gene expression, sarcomere actinin and mitochondrial expression and structure, electrophysiological properties, and mitochondrial activity. FAO was stimulated by peroxisome proliferator-activated receptor α (PPAR-α) activation, using oleate and the PPAR-α agonist WY-14643, which induced an increase in FAO in hiPSC-CMs. Culturing the hiPSC-CM in media containing oleate and WY-14643 in 2D monolayer induced an increase in FAO. In EHT, FAO was significantly higher than in 2D monolayer cells and could be further increased by culturing with oleate and WY-14643. In conclusion, a more mature metabolic phenotype can be induced firstly by stimulating FAO though pharmacological stimulation, then by culturing in 3D.

3.2 Introduction

3.2.1 Differentiation of human iPSCs into cardiomyocytes

Human induced-pluripotent stem cells (hiPSC) have a great potential as tools for studying human disease because they are patient specific and have been shown to model several inherited diseases[129,130]. These cells provide an infinite supply and can be differentiated into any type of cell, including cardiomyocytes, because they are pluripotent. There have been several approaches for cardiac differentiation in vitro, based around methods such as inductive coculture[213], embryoid body (EB) formation[214–216] and monolayer-based methods[216–219]. Currently, monolayer-based is the most efficient method for hiPSC differentiation into cardiomyocytes[220].

Researchers have identified defined factors to direct differentiation of the hiPSCs into cardiomyocytes and which enabled the differentiation to be done in a monolayer setting. The serum-free monolayer protocol using stage specific activation and inhibition of the Activin/NODAL and BMP4 signalling pathways generated more than 30% beating CMs[221]. However, there was high variability between cell lines and experimental repeats[222]. The exploration of Wnt/β-catenin signalling resulted in a more reproducible protocol involving activation and inhibition of the Wnt signalling pathway[220]. Furthermore, removing insulin during the differentiation process was shown to enhance the differentiation as insulin inhibits the formation of the cardiac mesoderm[223].

Human iPSCs can also be differentiated to a very specific cardiac cell type such as atrial and ventricular cardiomyocytes [224]. This can be done since atrial and ventricle cells develop from distinct mesoderm populations[225]. Most differentiation protocols that have been reported predominantly produce ventricular-like cardiomyocytes[226].

3.2.2 Maturation of human iPSC-CM

The great potential of hiPSC-CM is limited by the fact that the cells have an immature phenotype, resembling foetal cardiomyocytes[227,228]. Adult cardiomyocytes (CMs) are large and cylindrical, bi- or polynucleated, with an extensive t-tubule network, aligned and striated sarcomeres, a low resting membrane potential and long action potential duration (**Figure 3.1 A**). In contrast, hiPSC-CMs are smaller with a round or slightly oblong morphology, no apparent t-tubules, sarcomere disarray, and a high resting potential and short action potential duration[229] (**Figure 3.1 B**). Prolonging the time in culture enhances maturation but does not fully recapitulate the properties of adult heart[229,230]. This is partly due to the fact that hiPSC-CM are routinely cultured in 2D with non-physiological media[231]. Despite a number of successful studies in disease modelling, hiPSC-CMs are still not the same as adult CMs and the interest in driving hiPSC-CM to be more mature is growing. For drug testing it is important to know that the expression of necessary ion channels and receptors matches that in the adult heart. For example, it has been reported that monolayer hiPSC-CM do not necessarily exhibit an α-adrenergic hypertrophic response which casts doubt on their use to model adrenergic signalling[232].

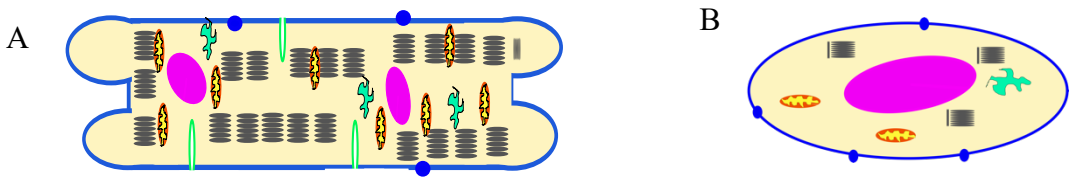


Figure 3.1 Illustrative images of adult cardiomyoctes versus immature hiPSC-CM

Representative illustration of adult cardiomyocytes (A) and immature hiPSC-CM in 2D monolayer culture (B) showing illustration of organelles such as nucleus, sarcomeric actinin, mitochondria, t-tubules.

During heart development, there is a switch in energy utilisation from glycolysis to FAO, to accommodate the increase in energy generation needed for contraction[233,234]. However, most differentiation and maintenance media contain a high glucose concentration, around 11 mM,

with little or no addition of fatty acids. There are several approaches to metabolically mature hiPSC-CM using addition of fatty acids or other small molecules previously described[156,235–237]. Previous studies have shown that when cultured as monolayers, hiPSC-CM have a highly glycolytic metabolism and do not have the choice to upregulate the pathway associated with fatty acid oxidation[180]. Addition of oleic acid was found to increase rates of FAO, but glycolysis remained the predominant route for ATP production[149].

Changing the composition of the culture medium has previously been shown to improve cardiac metabolic maturation. Depletion of glucose from the media forced the hiPSC-CMs to upregulate maturation-related genes, such as those in the tricarboxylic acid cycle and mitochondrial electron transport chain, and the addition of free fatty acids (FFAs) to the culture medium appears to promote further maturation[236]. Yang et al. found upregulation of genes involved in the oxidation pathway when hiPSC-CMs were grown in medium containing glucose and a cocktail of palmitate, oleate, and linoleate, at levels comparable to those in breast milk[236]. Ramachandra et al. supplemented hiPSC-CM culture with a 1:1 palmitate/oleate mixture, which significantly improved mitochondrial remodelling and oxidative metabolism[235].

The engineered heart tissue (EHT) model pioneered by Thomas Eschenhagen and Wolfram-Hubertus Zimmermann is arguably one of the most advanced 3D in vitro models of the heart and one of the strategies used to mature hiPSC-CMs[147,238]. EHTs are generated by casting cells in a gel template generating a construct that contracts between two flexible posts, enhancing maturation and providing a system to measure the effect of drugs on contraction frequency and force[239]. EHTs have been used to model several diseases such as ischemic heart disease[151] and diabetic myocardium using isolated rat cells[240]. However, previously, modelling metabolic diseases using EHT with hiPSC-CM has not been reported. With appropriate conditions, these will better recapitulate the human disease and can be used as

alternative disease model and/or to support the data found in disease modelling using animal model.

One of the advanced methods to measure the maturation of hiPSC-CM in 2D monolayer is by using vibration spectroscopy. Fourier transform infrared (FTIR) spectroscopy has become a well-established tool in biophysics for analysis of the structure and interactions of proteins, lipids, carbohydrates, and nucleic acids. These molecules have characteristic and well-defined infrared (IR) vibrational modes and can be used as markers for the biochemical response of cells and tissues to different treatments and pathologies[241–245].FTIR spectroscopy allows the detection of vibrational characteristics of a sample without external labels or laborious sample preparation, while providing comprehensive information on the biochemical composition of the sample and its macromolecular structure. Synchrotron based micro-FTIR spectroscopy applied to stem cells can both fingerprint and indicate general changes in the molecular composition of stem cells in a label-free, non-invasive, non-destructive manner[246–249]. More recently synchrotron infrared spectro-microscopy has been applied to track the changing biochemistry and protein phosphorylation of single nerve cell during differentiation[250,251].

We were approached by Dr Gianfelice Cinque of the Diamond Light Source to ask if we were interested in exploring the potential of synchrotron based micro-FTIR absorption spectroscopy in our work. We suggested that it would be interesting to see if it could be used to detect structural changes during the differentiation and maturation of hiPSC-CM.

3.3 Chapter aims

The work described in this chapter was a continuation of studies started by previous DPhil students in the lab, to complement their data for publication. This chapter aims to investigate ways to stimulate the maturation of hiPSC-CM using the interplay between stimulation of fatty acid oxidation (FAO) and by culture in 3D in engineered heart tissue (EHT). In summary, this chapter investigates:

1. The optimum method for culturing and differentiating hiPSC into cardiomyocytes, as well as ways to characterise them
2. The effect of oleic acid and WY14643 treatment on the activation of PPARα and maturation in hiPSC-CMs, by measuring gene and protein expression, changes in structure, metabolism, and action potential.
3. The maturation of hiPSC-CM in engineered heart tissue and the effect of oleic acid and WY-14643 treatment on further maturing the cells

3.4 Materials and Methods

3.4.1 Human iPSCs differentiation into cardiomyocyte

The method for differentiation of hiPSCs into cardiomyocytes was described in chapter 2.

3.4.2 Reagent preparation and treatment

3.4.2.1 Oleic acid bound with BSA

Powdered 2.825 grams oleic acid (Sigma Aldrich) was weighed and dissolved in 2 mL ethanol on the water bath before being mixed with 100 mM aqueous solution of anhydrous potassium carbonate. This mixture was then transferred to 0.9% sodium chloride solution to make a 100 mM oleate solution, which was stored in the fridge for later use. In order to bind the oleate with BSA (ratio 2:1), oleate was slowly added into warm ultrapure fatty acid free BSA (Sigma Aldrich) 165.5 μM solution while stirring. This solution was filtered using 0.22 μm filter before adding into maturation media for the cell culture.

3.4.2.2 Maturation media

Maturation media was made by mixing low glucose DMEM containing 5.5 mM glucose, vitamin C, vitamin B12, biotin, insulin, non-essential amino acid, and oleate:BSA. The full recipe is listed below:

Table 3.1 Composition of maturation media

Component	Concentration
DMEM	-
Glucose (in the DMEM)	5.5 mM
Oleate:BSA	400 μM
Insulin	50 nM
Vitamin B12	5 μg/mL
Vitamin C	0.5 mM
Biotin	0.82 μM

3.4.2.3 Fatty acid and WY-14643 treatment

The cells were treated with oleic acid (OA) and WY-14643 (PPARα agonist) to induce further maturation of the cells. The maturation media was mixed with 120 μM WY-14643 and used for the cell culture for 7 days. The media was changed every 2 days.

3.4.3 Sample preparation for infra-red (IR) spectroscopy

Human iPSCs (IMR90) were cultured in mTeSR1 media on Vitronectin-coated plates and were dissociated using ReLeSR. The cells were then transferred onto twenty-four Vitronectin-coated 13 mm diameter x 1 mm CaF_2 (UV grade, Crystran, UK) windows for differentiation (twelve slides – Day -1, Day 3, Day 7, Day 15 all-time points in triplicate) into hiPSC-CM for 15 days and matured using maturation media for another 15 days (further twelve slides, Day 22, Day 22OA, Day 30, Day 30OA also in triplicate). The cells were fixed at each time point using 4% Paraformaldehyde (PFA) for 10 minutes at RT, washed with distilled water, and dried overnight at RT.

3.4.3.1 Single cell measurement on micro-FTIR spectroscopy

The spectral acquisition and analysis by SR-FTIR micro-spectroscopy were carried out by Ms. Magda Wolna at MIRIAM beamline B22 at Diamond (Diamond Light Source, UK). A Vertex 80 V FTIR spectrometer (Bruker Optics, Germany) coupled to a Hyperion 3000 IR microscope (Bruker) equipped with high sensitivity MCT detector (Infrared Associates) within the extended mid-IR fingerprint region between 4000cm^{-1} and 900 cm^{-1} and fitted with a 36x magnification objective/condenser (0.5 NA) optics was used. All measurements were performed in transmission mode. Other parameters were 256 scans at 4 cm^{-1} spectral resolution. Background measurements were taken from areas of the vitronectin coated CaF_2 substrates that were free of any sample material. A minimum of 50 cells per time point were measured and repeated in triplicate to have statistically relevant data for a proof of principle, by focusing the beam at aperture 15µm x 15µm on each cell.

3.4.4 Engineered heart tissue

Engineered heart tissues were generated as described in the chapter 2. In order to further enhance the maturation of EHT, the EHT were cultured in maturation media for 7 days. The EHTs were also treated with WY-14643 in maturation media to test further the maturation.

3.5 Results

3.5.1 Differentiating iPSC into cardiomyocytes using modified GiWi protocol

Prior to differentiation, hiPSC from different sources were cultured in Matrigel coated 6-well plates using mTeSR or TeSR-E8 media (Stem Cell Technologies). A previous study found that mTeSR and TeSR-E8 can be used interchangeably with similar results in the iPSC culture[252]. In our cells, the cells cultured in mTeSR and TeSR-E8 appeared to have the same colony formation and morphology with defined edges for all the cell lines used (**Figure 3.2 A-B**). During the early attempts of hiPSC culture in the lab, some cells were found to spontaneously differentiate, forming a branched cell (**Figure 3.2C**). To overcome this issue, the techniques were modified to include more gentle cell dissociation and targeted dissociation. It was much easier to culture the cells in open plates, such as 6-well plates, rather than flasks, but careful attention needed to be given as this increased the possibility for contamination.

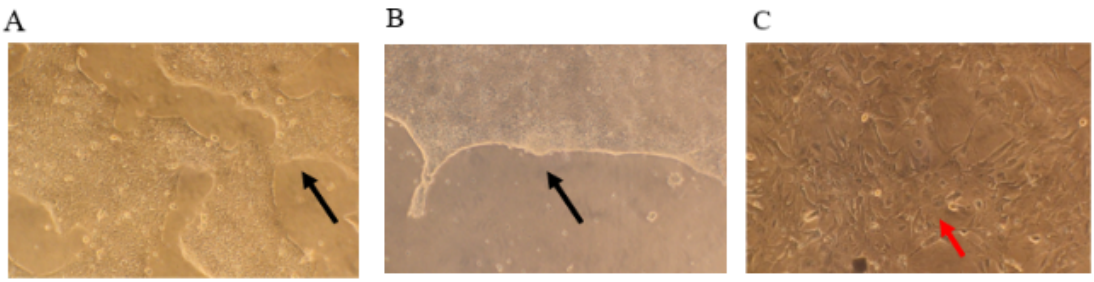


Figure 3.2 Human induced pluripotent stem cells (hiPSCs) colonies

Images of iPSC cell line IMR90 in mTeSR media (A) and in TeSR-E8 media (B), showing packed cells with well-defined edges indicated by black arrows. Spontaneously differentiating IMR90 cells in mTeSR media formed large cells and loss of defined edges shown by the red arrow (C).

After reaching 90 – 100% confluency, hiPSCs were dissociated and plated onto Growth-Factor Reduced Matrigel (GFR Matrigel) in 6-well plates for differentiation. A variety of protocols were optimised for hiPSCs dissociation, including enzyme-based protocols using TrypLE Express and Accutase, and enzyme-free protocols using Versene solution and ReLeSR. Although all the reagents mentioned worked well on hiPSCs, the enzyme-based

protocol produced single cells (**Figure 3.3 A**), with the addition of a ROCK-inhibitor to prevent cell death. The enzyme-free protocol produced cells in clumps (**Figure 3.3 B**), but the ROCK-inhibitor was not needed as the survival rate was much higher. Both protocols worked similarly, but I used enzyme-free protocol using ReLeSR most of the time as it did not require the use of ROCK-inhibitor.

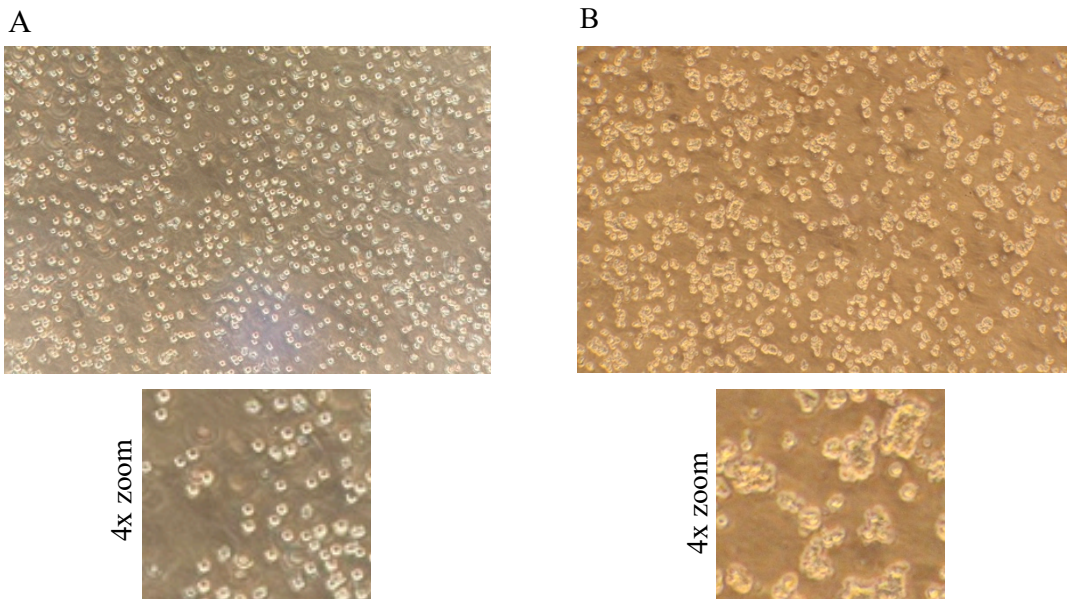


Figure 3.3 Human induced pluripotent stem cells (hiPSCs) after cell dissociation
Images of human iPSC cell line IMR90 under brightfield microscopy with the 40x objective magnification after dissociation with an enzyme-based protocol which generated mostly single cells (A) and with enzyme-free protocol which generated cells which were mostly formed as clumps (B).

Human iPSCs were differentiated using the GiWi protocol modified from Lian, et al and Buridge, et al[220,224,253,254] as presented in **Figure 3.4**. This modified protocol successfully generated 75-90% of cells positive for sarcomeric α-actinin when characterised by using flow cytometry (**Figure 3.5A**). The differentiation protocol involved activation and inhibition of the Wnt pathway using the small molecules CHIR99021 and wnt-C59. This protocol was successfully developed and modified after trials of different compounds such as CHIR99021 in salt and base-form and IWP4. I found that base-form CHIR99021 and wnt-C59 were the best small molecules to produce cardiomyocytes – this combination

resulted in the highest number of successful differentiations from hiPSC to hiPSC-CM and minimal cell death. To produce pure cardiomyocytes and eliminate non-cardiomyocytes from the population, the protocol included a metabolic selection process by glucose deprivation.

There were many factors affecting the success of differentiation such as time in culture, cell dissociation, and the cell culture handling. Moreover, the confluency of the cells influenced the outcome of differentiation process. I found that the best confluency for differentiation was between 90 – 100%. When the cells were plated at too high a density, they became detached from the plates, but when plated at less than 90% confluent the efficiency of differentiation was poor. This indicates that determining the best confluency prior to the differentiation process is critical.

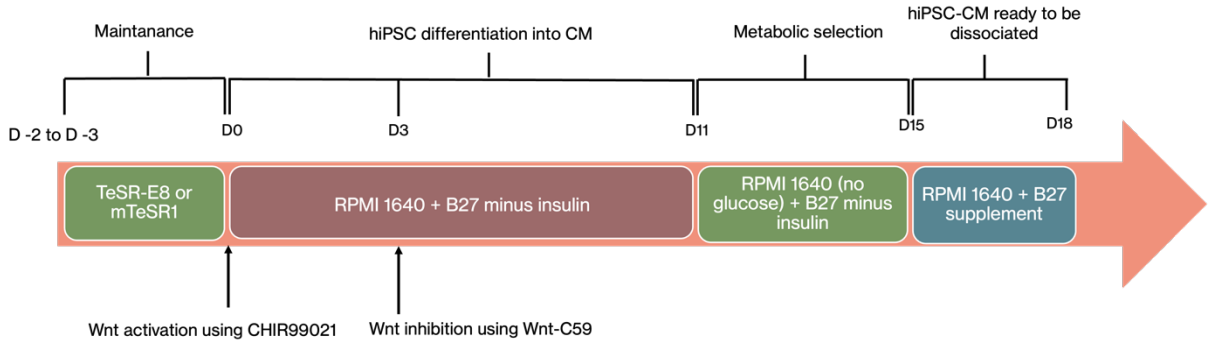


Figure 3.4 Protocol for differentiation of human iPSC into cardiomyocytes

The culture media are listed in the middle row with additional small molecules indicated with arrows on D0 and D3.

Immunofluorescence was used to characterise the cardiomyocytes in the population and to indicate that the protocol was successfully differentiating hiPSC to cardiomyocytes. Sarcomeric α-actinin staining confirmed that the cells produced from the differentiation protocol were truly cardiomyocytes. The immunofluorescence showed that the cells appeared to have irregular sarcomeres and were mostly mononucleated suggesting immature

CMs (**Figure 3.5B**), although a few cells appeared to have undergone binucleated division (**Figure 3.5C**).

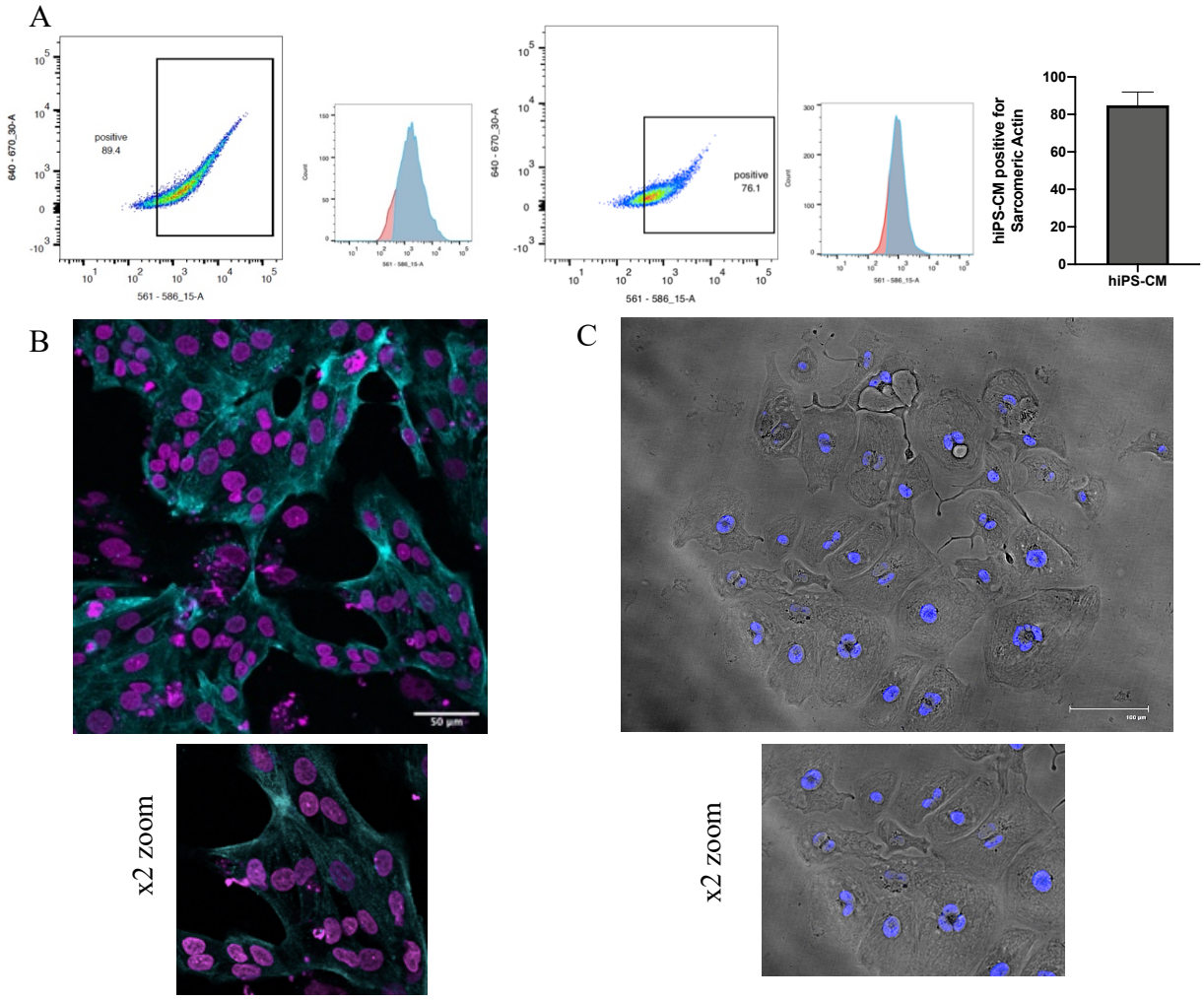


Figure 3.5 Flow cytometry analysis
Flow cytometry analysis showing quantification of three differentiations (A) and immunostaining for sarcomeric α-actinin (α-actinin-cyan, DAPI-magenta), live nucleus imaging under bright field microscope showing binucleated division (nucleus-blue).

Further characterisation was performed by a collaborating group using our protocol to investigate whether the protocol produced chamber-specific cells such as atrial, ventricular, and nodal-like cardiomyocytes. Ni Li, a DPhil student from the Patterson Group, found that 80.0% out of 1020 live cells produced using our protocol on the IMR90 cell line were double positive for the ventricular cardiomyocytes marker, myosin light chain 2v (MLC2v) and the cardiomyocytes marker, troponin T2 (TNNT2). Moreover, when the protocol was used for

differentiating hiPSC obtained from a patient with catecholaminergic polymorphic ventricular tachycardia (CVPT) hiPSC-CM obtained from the patient, 97.9% out of 4888 live cells were positive for MLC2V and TNNT2. This data indicated that more than 80% of those cells were ventricular-like cardiomyocytes (**Figure 3.6A**). Consistent with the flow cytometry and immunofluorescence data, patch clamp analysis performed by Dr. Taiyi Wang showed that the hiPSC-CM had L-type calcium channel and sodium channel currents (**Figure 3.6B-C**), indicating that the cells were cardiomyocytes with a more ventricular-like phenotype.

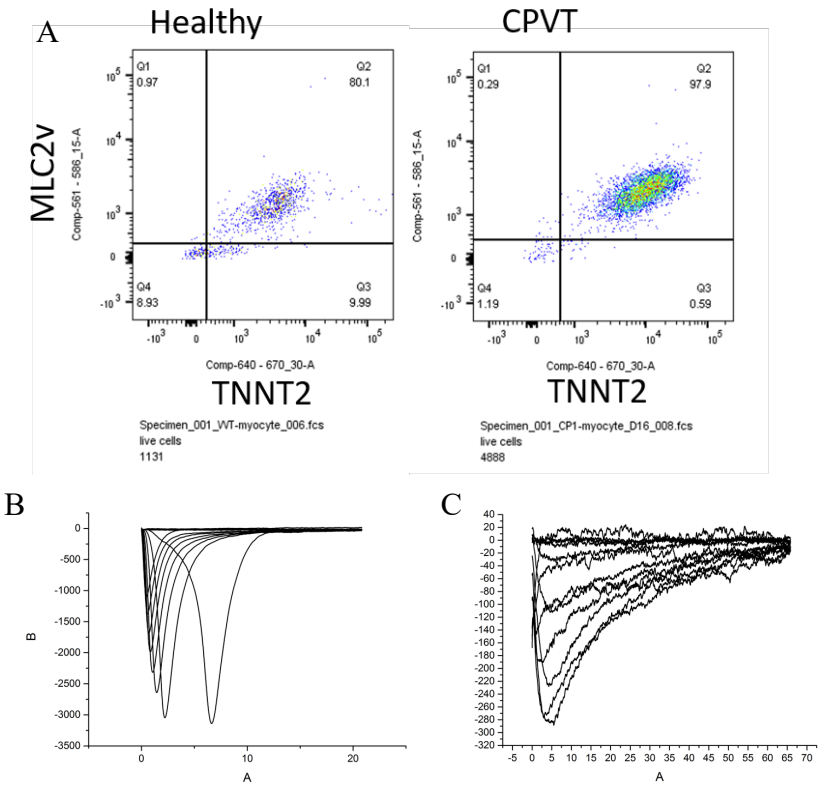


Figure 3.6 Flow cytometry analysis for TNNT2 and MLC2V and current recording of ion channels

Flow cytometry analysis for troponin T2 (TNNT2) and myosin light chain 2v (MLC2v) for healthy IMR90 cells and catecholaminergic polymorphic ventricular tachycardia (CVPT) cells (A), current recordings obtained during depolarising voltage-clamp showing L-type calcium (B) and sodium channel (C). Data provide by Ms. Ni Li and Dr. Taiyi Wang.

The protocol for hiPSC differentiation was routinely used to produce cardiomyocytes for all experiments in this thesis. Moreover, this protocol has also been shared with other research groups who have used it to model cardiac diseases as well as investigating the effect of external factors such as toxic compounds, drugs, and SARS-CoV-2.

3.5.2 The effect of oleic acid and PPAR agonist on iPSC-CM maturation

Experiments to investigate the effect of palmitic and oleic acid supplementation to the cells were carried out, to determine the effect on maturation of the hiPSC-CM.

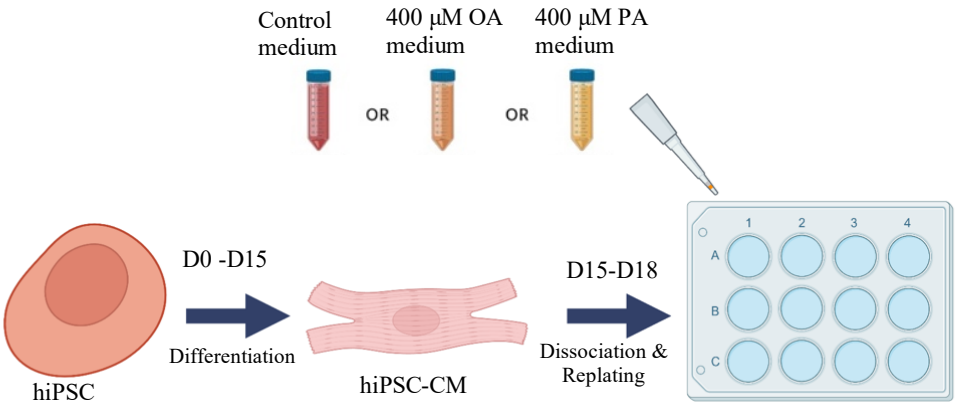


Figure 3.7 Schematic illustration of differentiation
Schematic illustration of differentiation of hiPSC-CMs and culturing the cells in 12-well plates with fatty acids supplementation for 7 days in monolayer culture.

To investigate the effects of the two fatty acids on cell maturation and the potential for toxicity, 1 million hiPSC-CMs were seeded in 12-well plates and cultured in media containing 5.5 mM glucose supplemented with either 400 µM oleate (OA) or palmitate (PA) for a week (**Figure 3.7**). The effect of different fatty acid supplementation on gene expression was quantified using qPCR. There was no change in gene expression of myosin heavy chain 6 (MYH6). Expression of insulin receptor substrate-1 (IRS1) decreased in the cells with PA supplementation, suggesting a change in insulin signalling, however this did not happen in the cells with OA supplementation. Addition of OA significantly increased expression of GLUT1 mRNA this was decreased with PA addition. Addition of OA also

significantly increased mRNA expression for GLUT4 and peroxisome proliferator-activated receptor gamma co-activator 1α (PGC1α) whilst no changes were observed after PA supplementation (**Figure 3.8**). Hence, OA but not PA supplementation had a significant effect on the metabolic maturation-associated gene expression.

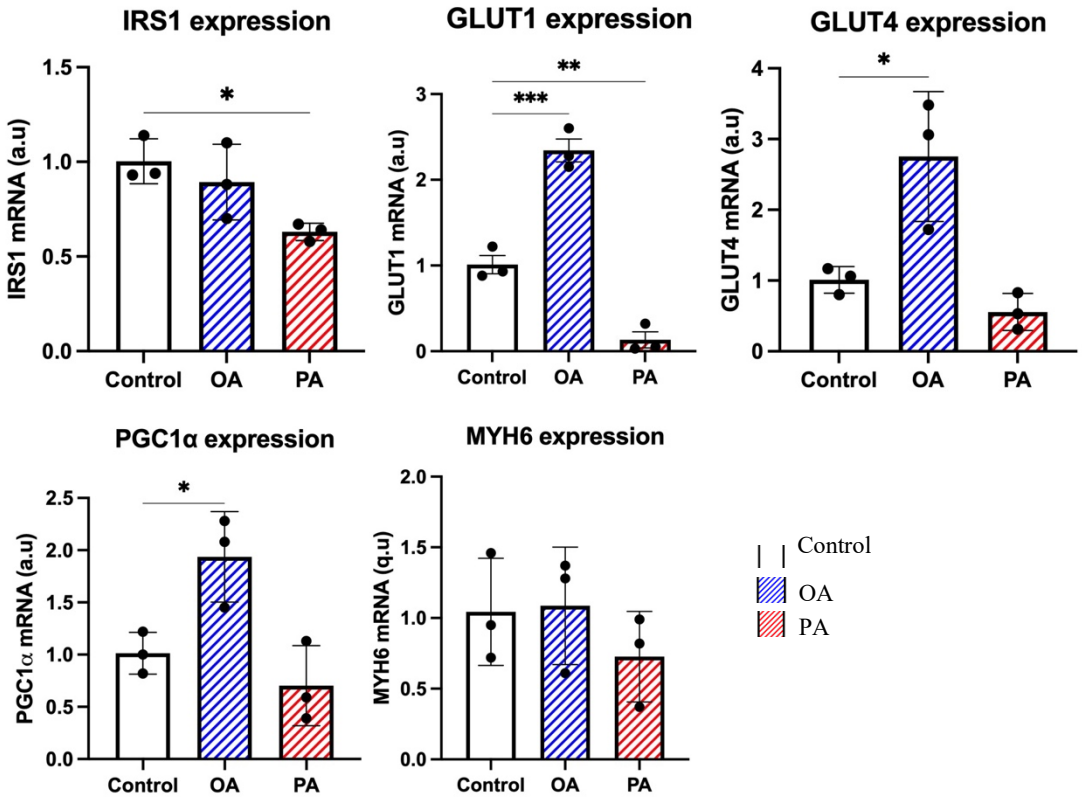


Figure 3.8 The relative gene expression of metabolic and structural genes in hiPSC-CMs with or without OA- and PA- treatment using qPCR.
Insulin receptor substrate 1 (IRS1), glucose transporter 1 (GLUT1), glucose transporter 4 (GLUT4), peroxisome proliferator-activated receptor gamma co-activator 1 alpha (PGC1α), and myosin heavy chain 6 (MYH6) relative expression in hiPSC-CM of IMR90 cell line. Data represent the mean ± SEM and statistical significance was assessed by one-way ANOVA followed by Dunnett's test with a *, **, *** $p < 0.05, 0.01, 0.005$ compared with control hiPSC-CMs (n=3).

It was hypothesized that fatty acid supplementation may cause lipid accumulation in hiPSC-CMs, and lead to lipotoxicity and lipoapoptosis[255]. Oil Red O (ORO), a lysochrome diazo dye that stains neutral lipid droplets within tissue sections, was used to determine the degree of lipid accumulation in fatty acid-supplemented hiPSC-CMs in monolayer (normalized to cell number counted from DAPI-stained nuclei). The lipid accumulation in OA-supplemented hiPSC-CMs was comparable to control, while there was significantly higher

lipid accumulation in PA-supplemented hiPSC-CMs (**Figure 3.9 A-B**). Excess accumulation after PA supplementation was consistent with previous findings in HL-1 cells[256]. Across the samples, the number of cells per slide in OA-supplemented culture was seen to be consistently higher than in control or PA-supplemented culture.

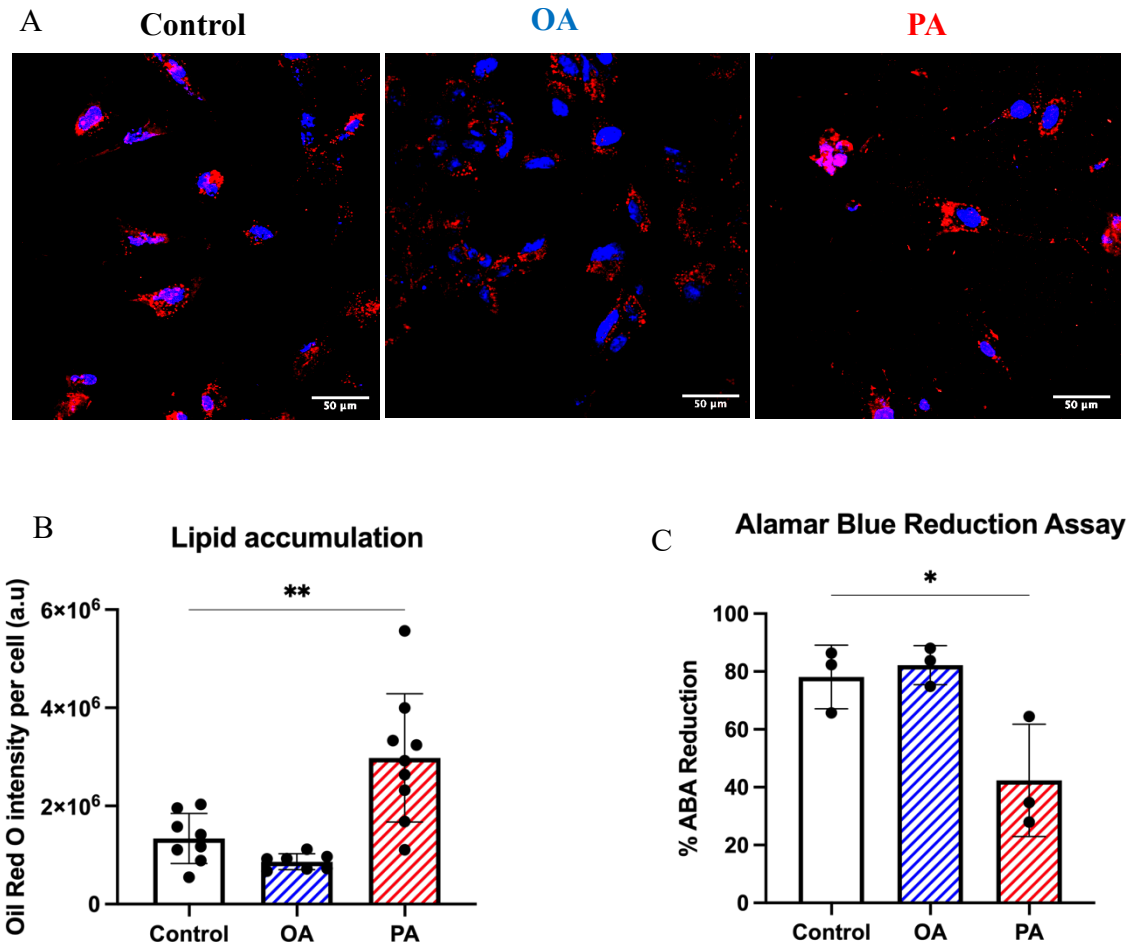


Figure 3.9 Oil red O staining and Alamar Blue reduction assay to assess lipid accumulation and cell viability in hiPSC-CM cultured in fatty acid supplementation media
Representative images from confocal microscopy of the lipid accumulation of control OA- and PA-treated groups stained with ORO (A) (neutral lipid-red, DAPI-blue), scale bar is 50µm. ORO intensity per cell for control, OA- and PA-treated groups was calculated by dividing total ORO intensity by the number of nuclei (B). Data of Alamar Blue reduction percentage, calculated and adjusted to positive and negative controls (C). Data represent the mean ± SEM and statistical significance was assessed by one-way ANOVA followed by Dunnett's test with a *, ** $p < 0.05, 0.01$ compared with control hiPSC-CMs, n= 8-9 for (B) and n=3 for (C).

A non-invasive Alamar Blue assay was then used to see if adding fatty acids to the hiPSC-CMs cultured in monolayer impaired cell viability. There was no significant difference in cell viability between the control and OA-supplemented groups. In comparison to the control

and OA-treated groups, PA-supplemented culture showed a significant reduction in cell number with higher variability between samples (**Figure 3.9C**). This impairment in cell viability when cells were cultured in PA was consistent with the hypothesis that PA supplementation caused lipotoxicity due to excess lipid accumulation.

Since OA supplementation increased the expression of some metabolic maturation genes and showed less lipid accumulation and less toxicity compared to PA supplementation, OA was used for maturation of the hiPSC-CMs. To stimulate fatty acid metabolism further, differentiated hiPSC-CM were treated with OA alone or with OA plus the PPARα agonist WY-14643 at concentrations of 60, 120, 180 and 240 μM for 24 h (**Figure 3.10A**) and 7 days, and the cell number counted using a CCK-8 assay (**Figure 3.10B**). Treatment with WY-14643 caused a dose-dependent decrease in cell number after 24 h and 7 days. PDK4 expression, indicative of PPARα activation, was measured after 24 h (**Figure 3.10C**), and addition of both 120 and 180 μM significantly increased PDK4 expression. Protein levels of sarcomeric α-actinin trended upwards but were not significant with doses up to 180 μM, most likely due to the large error bars (**Figure 3.10D**). This validated the dose of 120 μM WY-14643 which had been used in previous work[205] and was therefore continued for further experiments.

The effects of OA and OA+WY-14643 (120 μM) on the sarcomeric α-actinin levels were further investigated using immunostaining. Expression of the protein was shown to increase after the addition of OA, with a further increase on addition of WY-14643 (**Figure 3.11**). the immunostaining for sarcomeric α-actinin generated more homogenous data than the Western blotting.

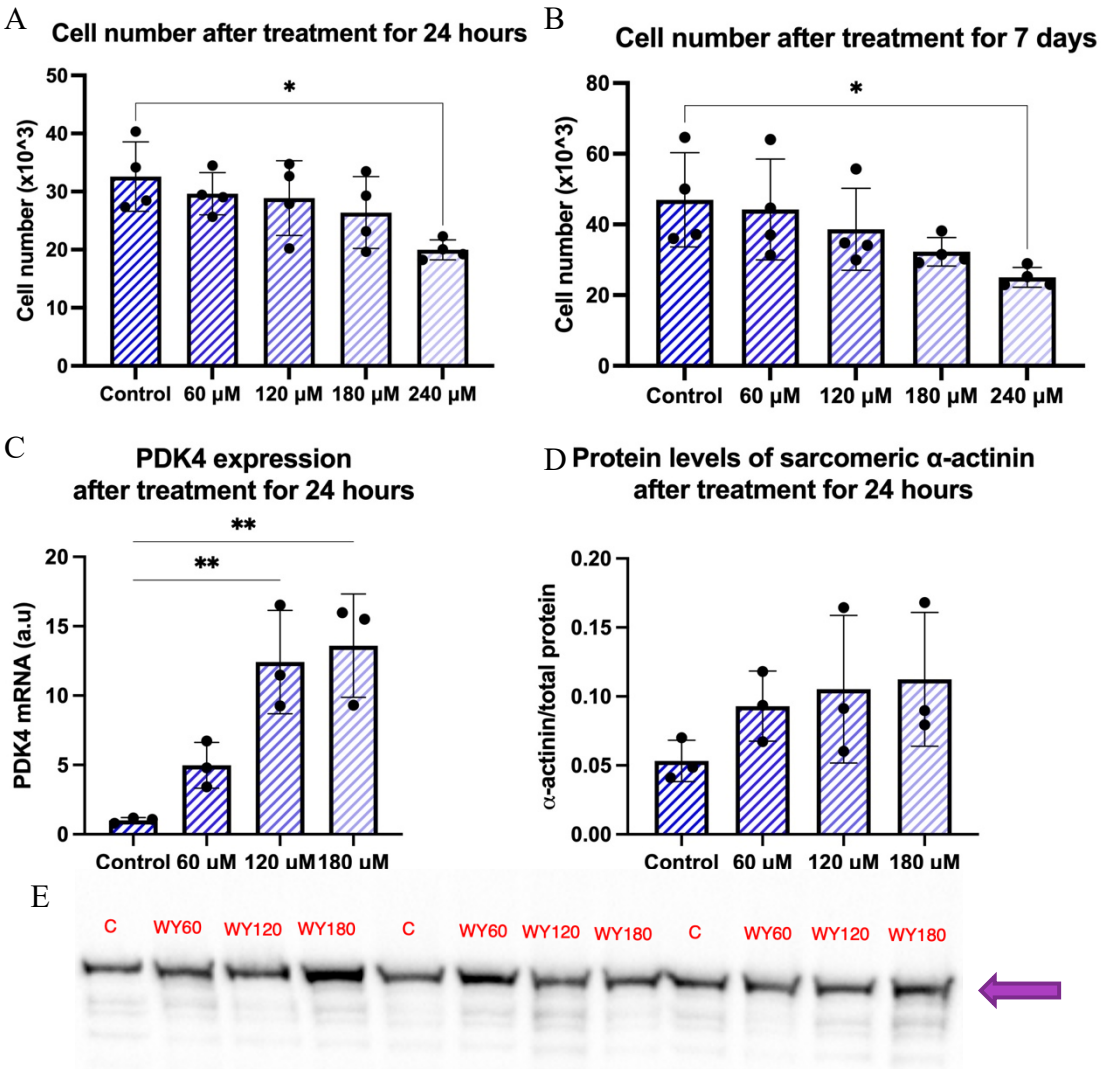


Figure 3.10 Dose response in hiPSC-CM to WY-14643

Human iPSC-CM were treated with 400 µM OA alone (control) or with 60, 120, 180 or 240 µM WY-14643 for 24 hours (A) and 7 days (B). PDK4 mRNA expression was tested after treatment with OA ± 60, 120 or 180 µM WY14643 for 24 hours (C), expression of sarcomeric α-actinin protein after treatment for 7 days was assessed using Western blotting and quantified by Image Lab software from Bio-Rad (D) with a representative image shown in (E). Data represent the mean ± SEM and statistical significance was assessed by one-way ANOVA followed by Dunnett's test with *, ** $p < 0.05$ and 0.01, compared with control OA-treated cells (n = 3 or 4 as indicated).

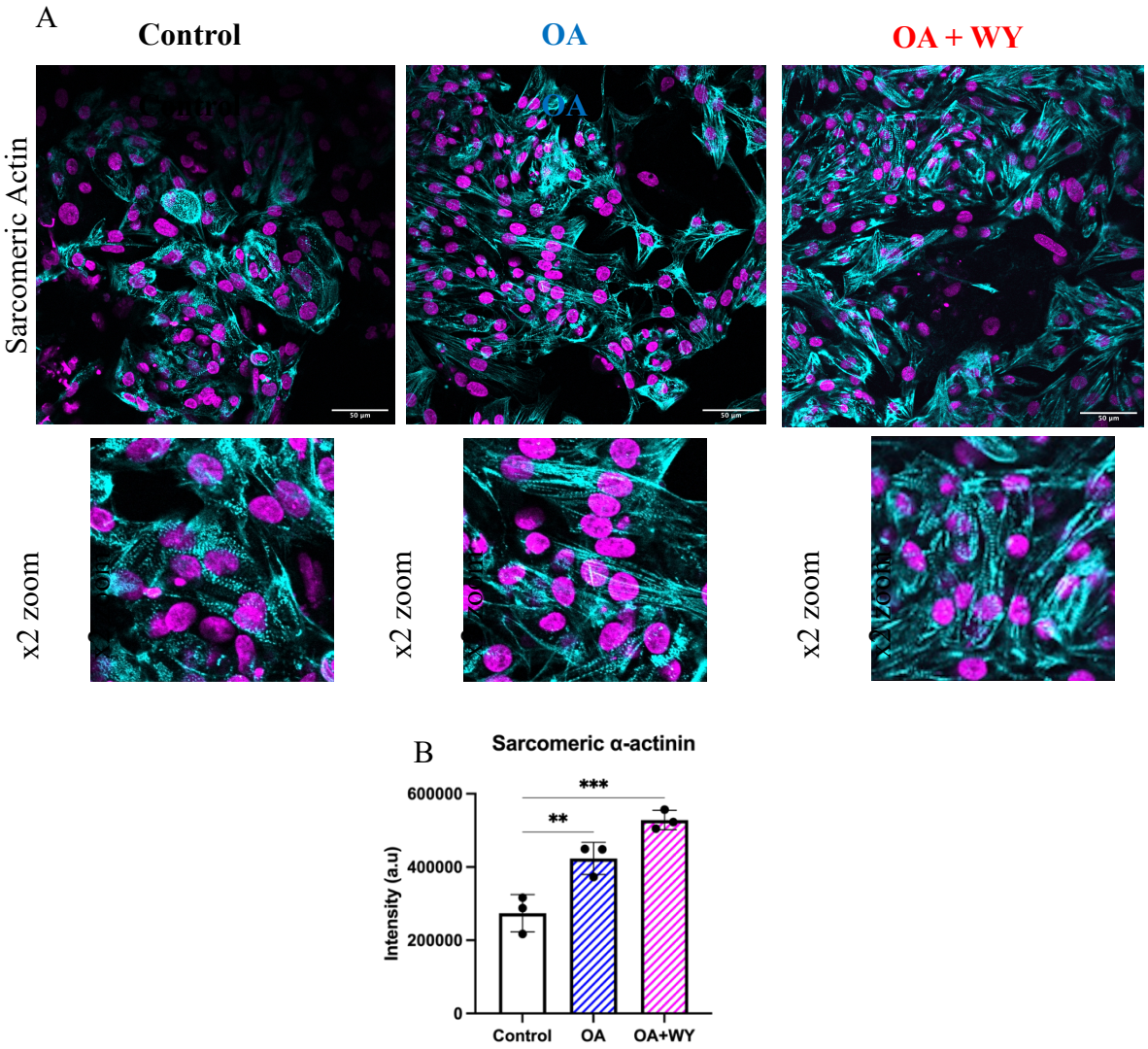


Figure 3.11 Confocal microscopy images for Sarcomeric α-Actinin

Immunostaining for sarcomeric α-actinin (cyan) with DAPI (magenta), as control or after treatment for 1 week with OA ± WY-14643; scale bar is 50 μM with ×2 zoom below (A); signal intensity is quantified in (B). Data represent the mean ± SEM and statistical significance was assessed by one-way ANOVA followed by Dunnett's test with **, *** $p < 0.01, 0.005$ compared with control hiPSC-CMs (n = 3).

Cardiac maturation is associated with a shift in ATP generation from cytoplasmic glycolysis to mitochondrial oxidative phosphorylation. MitoTrackerTM Red CMXRos was used to measure mitochondrial membrane potential and network formation, a marker of metabolic maturity. OA-supplemented and OA+WY-14643 hiPSC-CMs exhibited significantly higher fluorescence intensity per cell compared to control (**Figure 3.12**). There was no significant

change when comparing OA to OA+WY-14643. This suggested increased formation of the mitochondrial network after treatment with OA.

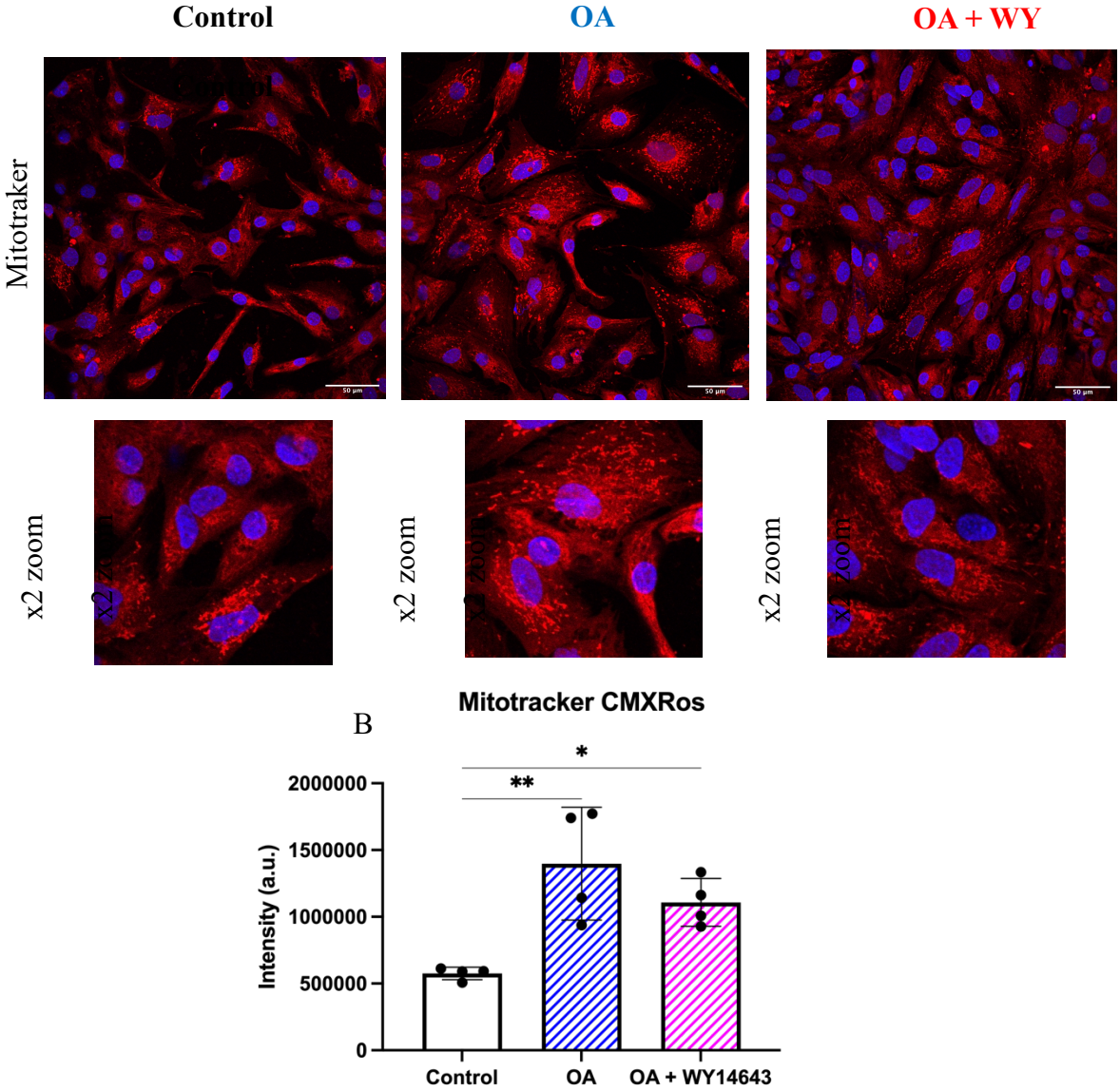


Figure 3.12 Confocal microscopy images for MitoTracker Red CMXRos

Immunostaining for MitoTracker Red CMXRos (red) with DAPI (blue), as control or after treatment for 1 week with OA ± WY-14643; scale bar is 50 µm with ×2 zoom below (A); signal intensity is quantified in (B) and normalised to cell number. Data represent the mean ± SEM and statistical significance was assessed by one-way ANOVA followed by Dunnett's test with *, ** $p<0.05$, 0.01 compared with control hiPSC-CMs (n = 4).

Rates of glycolysis were quantified after treatment for 1 week with OA and OA + WY-14643 and shown to be significantly decreased by both treatments (**Figure 3.13A**). Treating hiPSC-CMs with OA alone decreased glycolysis by 49% ± 6.4% while with OA+WY-14643 decreased glycolysis by 17% ± 6.4%. Interestingly, rate of glycolysis in OA+WY-14643

treated hiPSC-CMs was significantly higher compared to OA treated hiPSCC-CMs by 63% ± 15.9% (**Figure 3.13A**). Culture with OA for 1 week was sufficient to increase palmitate oxidation, with a further increase after addition of WY-14643 (**Figure 3.13B**). Culture with OA for 1 week induced an increase in oleate oxidation with a further increase in cells treated with OA + WY-14643 (**Figure 3.13C**).

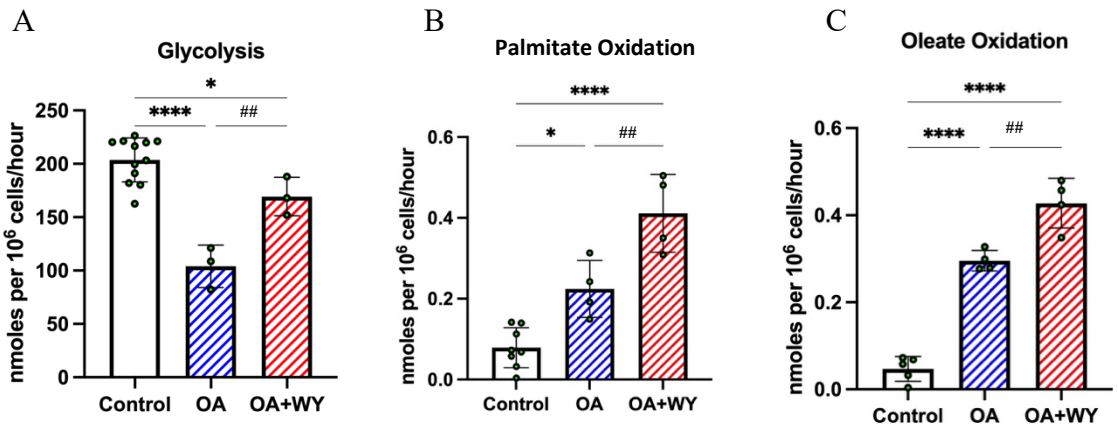


Figure 3.13 Glycolytic and fatty acid oxidative flux measured by radiolabelled measurement

Rates of glycolysis (A), oxidation of palmitate (B) and oleate (C) were measured in hiPSC-CMs after culture for 1 week with OA ± WY-14643. Data represent the mean ± SEM and statistical significance was assessed by one-way ANOVA followed by Dunnett's test with *, **** $p < 0.05$, 0.001 compared with control hiPSC-CMs, #, ## $p < 0.05$, 0.01 compared with OA-treated hiPSC-CMs

3.5.3 Synchrotron-based micro-FTIR absorption spectroscopy for characterising oleate enhancement of maturation of cardiomyocytes

The assessment of cardiomyocytes maturation using synchrotron based micro-FTIR was performed in collaboration with Magda Wolna, Mark D Frogley, Taiyi Wang, Ioannis Lekkas and Gianfelice Cinque at the Diamond Light Source Limited, Harwell Science and Innovation Campus. I prepared all the samples, Magda Wolna and I took the measurements at Diamond Light Source Ltd. The detailed results and analysis of the spectroscopic data performed by Ms Wolna are presented in **Appendix D**.

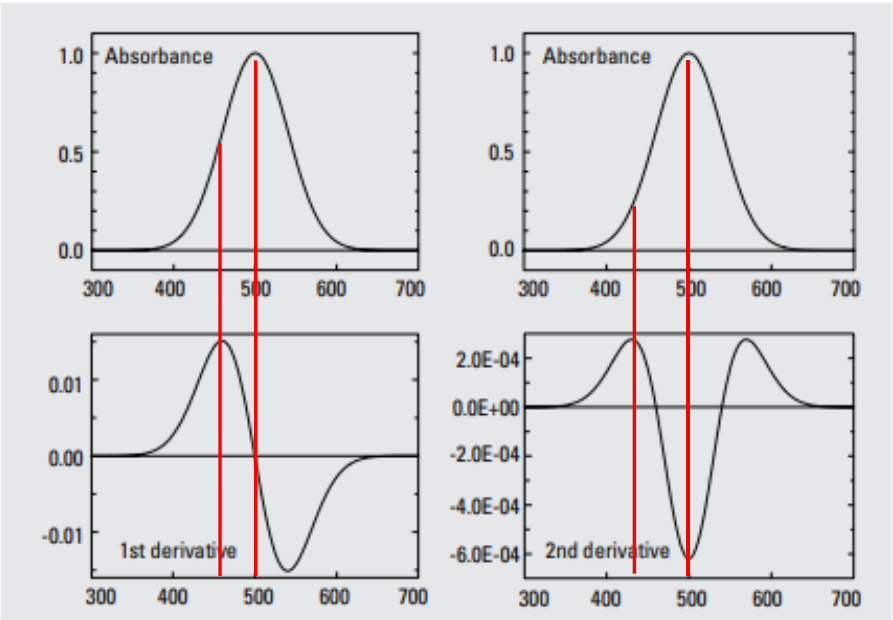
Firstly, the effect of coating agent or extracellular matrix used for cell culture was assessed to avoid any effect of the spectra measurement. As Matrigel can form a thick layer, vitronectin was explored as an alternative coating. Vitronectin (VN) is a fully chemically defined recombinant human protein that is suitable for clinical application and is an effective alternative to Matrigel. It is a multifunctional glycoprotein that binds to various biological ligands and plays a key role in tissue remodeling by regulating cell adhesion through binding to different types of integrins, mainly via the Arginylglycylaspartic acid (RGD) sequence. We found that a coating with Vitronectin did not impede the acquisition of the spectra and that it was a good fit for the experiment.

The first round of analysis was performed using samples prepared in our lab by Dr Taiyi Wang. When the cells were taken to Diamond, it was found that the natural tendency of the hiPSCs and hiPSC-CMs to grow in clumps meant that it was very hard to acquire clean spectra from individual cells. To ease the measurement on single cell, I dissociated the hiPSC-CM and replated on the vitronectin coated CaF_2 substrates about 24 hours before cell fixation. During FTIR measurement, I selected the cells that appear as single layer on the colony.

The power of the micro FTIR technique is that it provides a vast amount of data (**see appendix D**). However, this relates to changes in vibration of bonds in molecules within the cells and therefore interpretation of the data requires an understanding of what each different vibration peak refers to and then how this might provide information about what is happening to the cells. The data was provided to us as the absorbance spectra and also as the second derivative of the absorbance (**Figure 3.14 A**). The second derivative highlights peaks of intensity as sharp negative peaks and is able to detect small peaks that may be masked in the absorbance spectrum by neighbouring larger peaks[257].

Figure 3.14 B-C shows absorbance and second derivative spectra acquired in the lipid region and demonstrates that even in the second derivative, the data is complex and quite variable. However, a clear change can be seen between the spectra from the day 30 cells (pink) and the day 30 cells with OA (orange). Full analysis of the data from this experiment has been delayed by accessibility issues due to COVID-19 pandemic, but there are some interesting findings in the amide and lipid regions which can be seen more clearly when Ms Wolna performed PCA analysis (**Figure 3.15**). In the amide region (**Figure 3.15 A**), there are clear changes between the cells at days 1, 3 and 7. This is not unexpected as changes in the amide region largely correspond to changes in protein structure, and there are obvious changes in PC-1 occurring during differentiation from hiPSCs to hiPSC-CMs. Once the cells have differentiated, there are no clear differences between the populations at day 15, day 22 and day 30 or after the addition of OA. In contrast, in the lipid region (**Figure 3.15 B**) there are no differences seen during the early stages of differentiation but a clear shift in PC-2 at day 30 and in PC-1 with addition of OA.

A



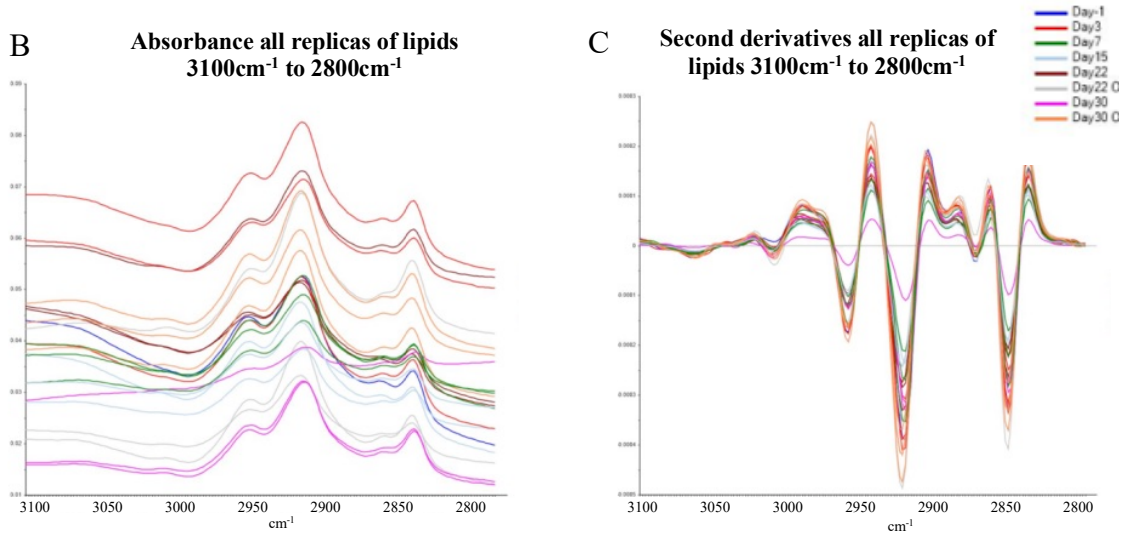


Figure 3.14 The average absorbance and second derivative absorbance spectra of hiPSC-CMs in the lipid region

The illustrative image of average absorbance and second derivative absorbance (A). The average absorbance and its second derivative spectra during hiPSCs differentiation into cardiomyocytes with fatty acid stimulation at day -1, 3, 7, 15, 22, 22OA, 30, 30OA in the lipid region (3100cm^{-1} to 2800cm^{-1}) (B-C).

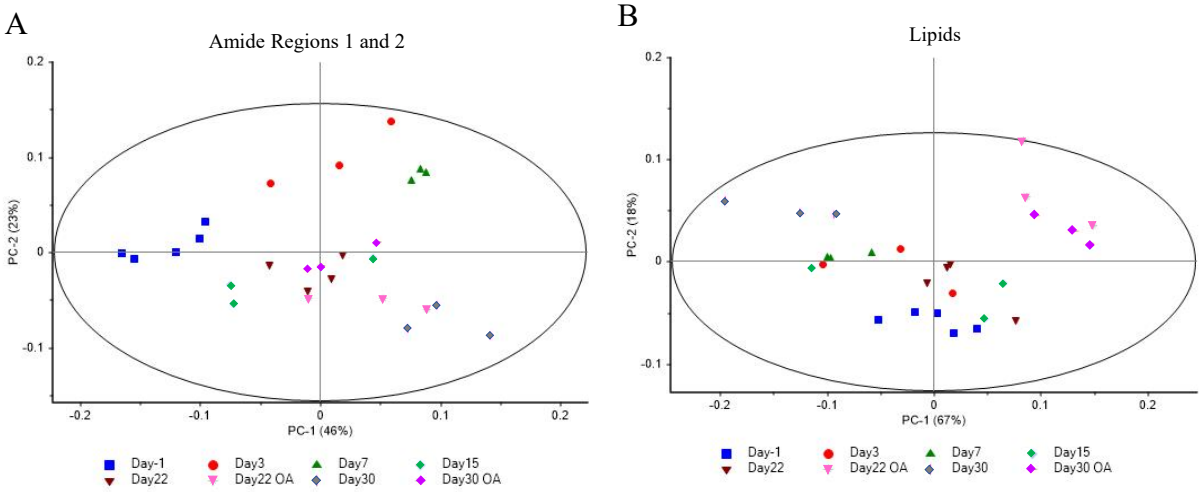


Figure 3.15 Score plots obtained for the first two principal components after PCA with the second derivative spectra of hiPSC during differentiation and FA stimulation

Principal component analysis (PCA) of all spectra of amide region (A) and lipids region (B) of hiPSC during differentiation and FA stimulation at day -1, 3, 7, 15, 22, 22OA, 30, 30OA.

3.5.4 Engineered heart tissue increases cell maturation

To further increase the maturation of hiPSC-CMs, the cells were cultured in three-dimensional engineered heart tissue (EHT), generated using the protocol developed by Hansen et al[179]. Human iPSC-CM (1.2 x 10^6 cells) were suspended in a fibrinogen and thrombin gel mixture across two flexible silicone posts (**Figure 3.16**).

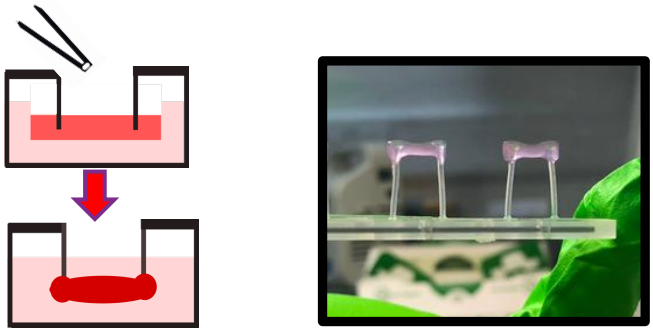


Figure 3.16 Solid hydrogel form in between silicon posts

The cells were mixed with master mix solution described in the method chapter 2 to form the EHT.

Cell dissociation prior to adding the cells to the gel was a critical step in the EHT generation process because it affected the cell viability, total number of cells, and cell/colony distribution to achieve homogeneity. There were two protocols for dissociation being optimised, using collagenase II or TrypLE express. The collagenase II protocol produced more single cardiomyocytes (**Figure 3.17A**) while TrypLE express produced some single cells but also some colonies, albeit homogeneous (**Figure 3.17B**). The collagenase II protocol is more suitable for experiments requiring single cells, such as patch clamp, however the process takes 4 hours which could have an adverse effect on the cells during the incubation process. Therefore, the TrypLE express dissociation protocol was more frequently used.

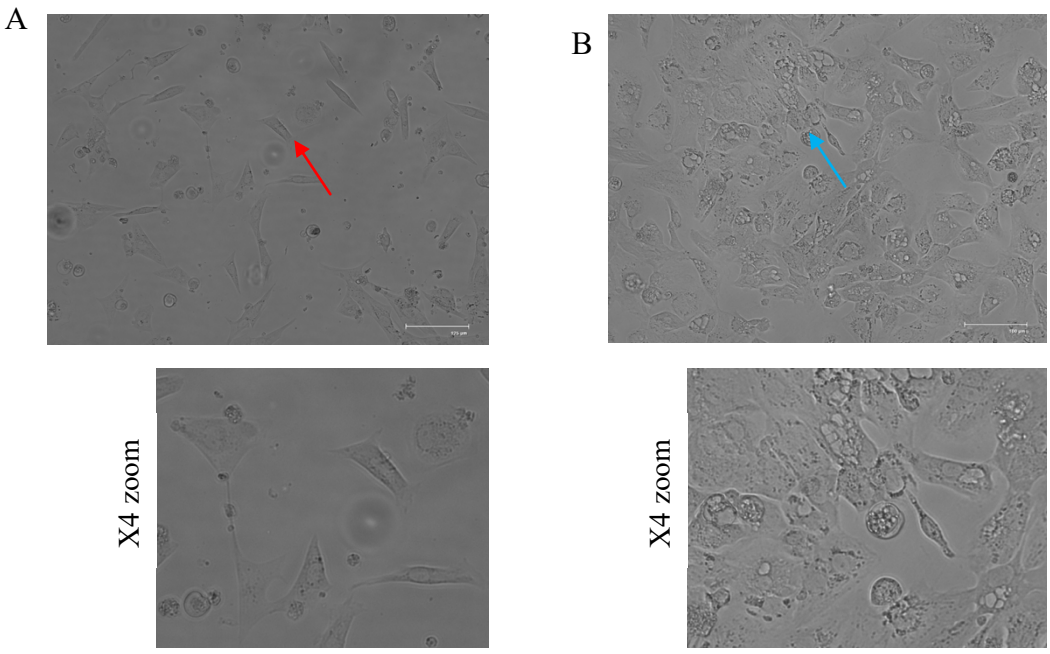


Figure 3.17 Bright field microscopy images for hiPSC-CM after dissociation

The hiPSC-CMs were dissociated using collagenase II protocol producing mostly single cells shown by the red arrow (A) and TrypLE Express producing more cell colony shown by the blue arrow (B) and detailed images in 4 times zoom underneath it.

Human iPSC-CM survival in EHT was assessed using the Alamar Blue (ABA) assay the day after casting. The 15-20% ABA reduction was consistent from the three batches of EHT over the same period of time (**Figure 3.18 A-B**). The result confirmed that hiPSC-CMs were viable and metabolically active and had comparable viability from batch to batch. The homogeneity of cells across the EHT was investigated under a microscope, showing that the hiPSC-CM were evenly distributed (**Figure 3.18 C**).

The cells cultured in EHT appeared bigger than those in 2D and appeared to include more binucleated cells and better sarcomere actinin alignment, (**Figure 3.19A**). In addition, the sarcomeric α-actinin expression was much higher in control EHT (without OA or OA+WY-14643 treatment) compared to 2D culture (**Figure 3.19B**). qRT-PCR analysis showed that the cells culture in EHT had significantly higher mRNA for PDK4, PGC1α, and PPARα, but did not have any effect on IRS1, MYH6, and TNNT2 gene expression (**Figure 3.20**).

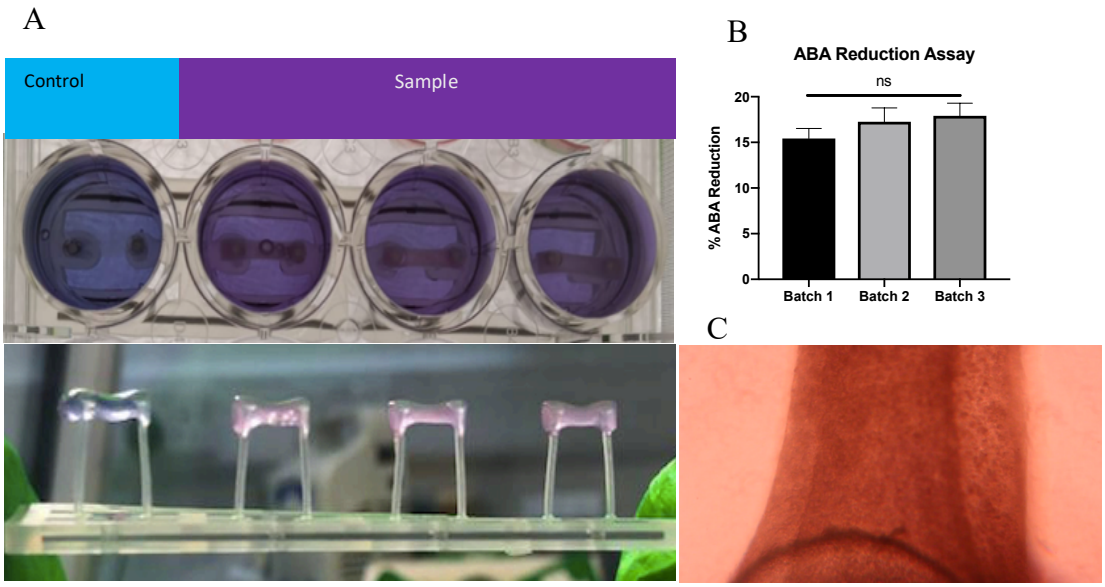


Figure 3.18 Alamar Blue reduction assay and image of EHT under bright field microscope

Alamar Blue reduction reagent was used to analyse the viability of the cells shown by colour change from blue to purple (A) which was quantified using spectrophotometry (B). Image of EHT under bright field microscope showing cell distribution in EHT (C).

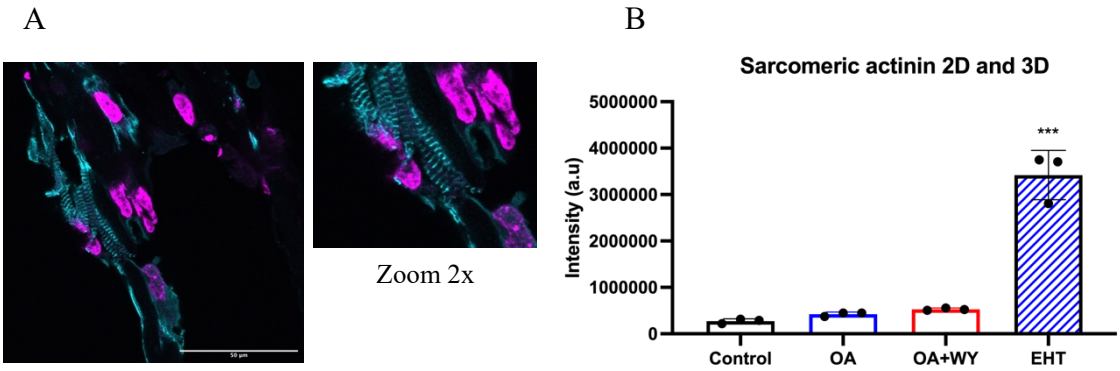


Figure 3.19 Immunostaining for sarcomeric α-actinin using confocal microscopy

Immunostaining for sarcomeric α-actinin (actinin-cyan, DAPI-magenta) in a section through an EHT, scale bar is 50 µm with ×2 zoom to the right (A); signal intensity is quantified in (B) compared with that for cells in 2D shown in Figure 3.11, indicated as open bars. Data represent the mean ± SEM and statistical significance was assessed by one-way ANOVA followed by Dunnett's multiple comparison test with a *** $p < 0.005$ (n=3).

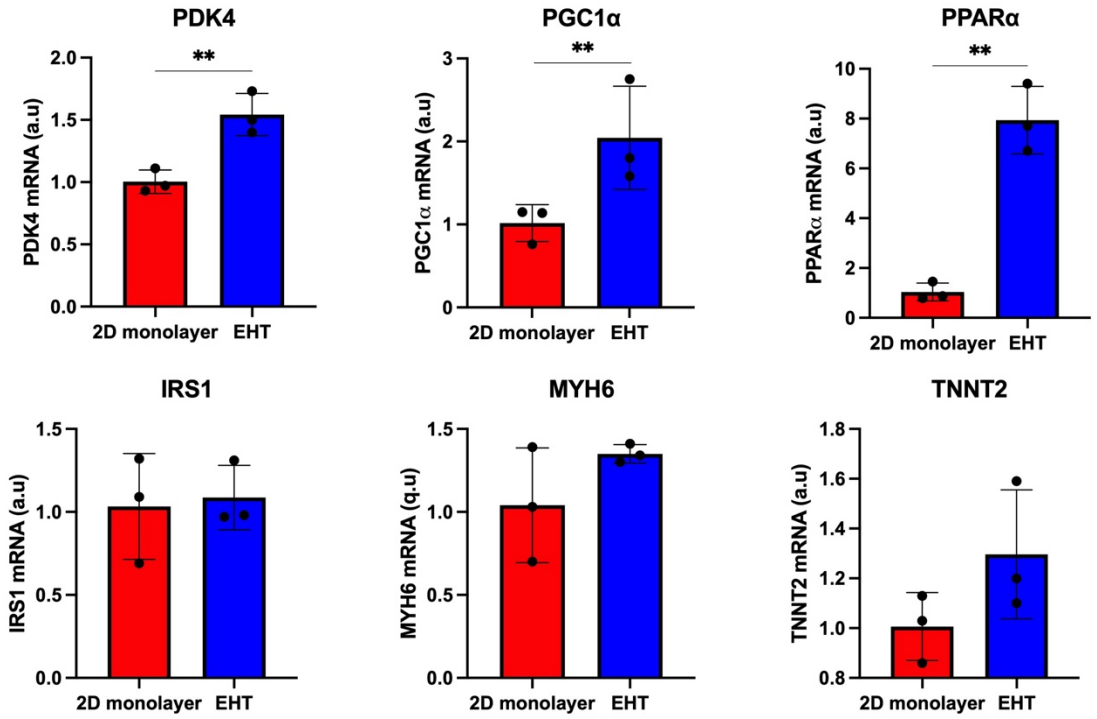


Figure 3.20 The relative expression of metabolic and structural genes of hiPSC-CMs in 2D and EHT

PDK4, PGC1α, PPARα, IRS1, MYH6, and TNNT2 relative expression in hiPSC-CM of IMR90 cell line in 2D monolayer and EHT. Data represent the mean ± SEM and statistical significance was assessed by t-test with a ** $p < 0.01$ compared with 2D monolayer hiPSC-CMs, n=3.

3.5.5 Combination of engineered heart tissue and metabolic maturation further increased cell maturation

3.5.5.1 Gene expression in engineered heart tissue cultured in maturation media

Knowing that oleic acid (OA) and WY-14643 addition to 2D monolayers increased FAO and mitochondrial activity, they were introduced to EHT for 7 days. Following treatment of EHTs with OA and OA±WY-14643 for 1 week, changes in mRNA expression were investigated. Treatment with OA alone induced an increase in pyruvate dehydrogenase kinase 4 (PDK4), peroxisome proliferator-activated receptor gamma co-activator 1α (PGC1α), peroxisome proliferator-activated receptor α (PPARα), and myosin heavy chain (MYH6) expression compared to control EHT (no treatment) (**Figure 3.21**). Treatment of EHTs with OA+WY-14643 further increased PGC1α from that observed in treatment with OA alone. Interestingly, PDK4 and PPARα went back down to the level observed in the

control EHT while MYH6 was the same level found in OA alone. Addition of OA alone or OA+WY-14643 did not change expression of IRS1 and TNNT2.

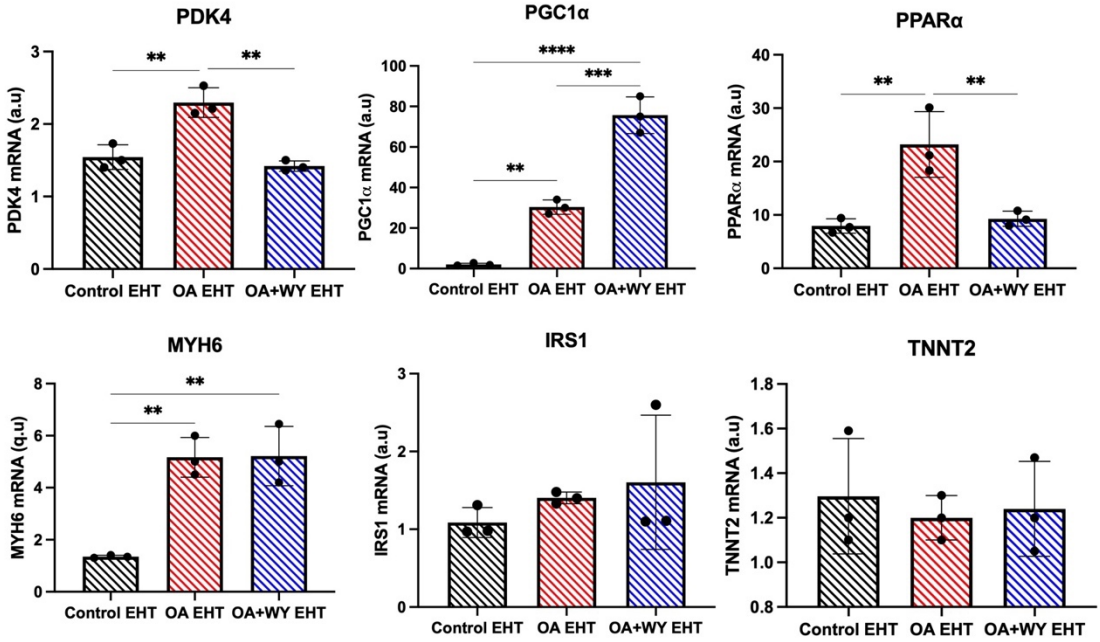


Figure 3.21 The relative expression of metabolic and structural genes of hiPSC-CMs in EHT and treatment with OA and OA+WY-14643 using qRT-PCR

PDK4, PGC1α, PPARα, IRS1, MYH6, and TNNT2 relative expression in hiPSC-CM of IMR90 cell line in EHT with treatment of OA and OA+WY-14643. Data represent the mean ± SEM and statistical significance was assessed by one-way ANOVA followed by Dunnett's test with a **, ***, **** $p < 0.01, 0.005, 0.001$ compared with control EHT, n=3.

3.5.5.2 Metabolic switch

To measure the metabolic flux in the EHT, radiolabelled experiments were performed. Human iPSC-CM in EHT had a significantly increased rate of FAO (both palmitate and oleate oxidation) and a substantial decrease in glycolysis compared to that of cells in the 2D monolayer (**Figure 3.22**). Addition of OA+WY-14643 in EHT significantly increased palmitate oxidation compared to control EHT. However, addition of OA±WY-14643 had no effect on the rate of oleate oxidation compared to control EHT.

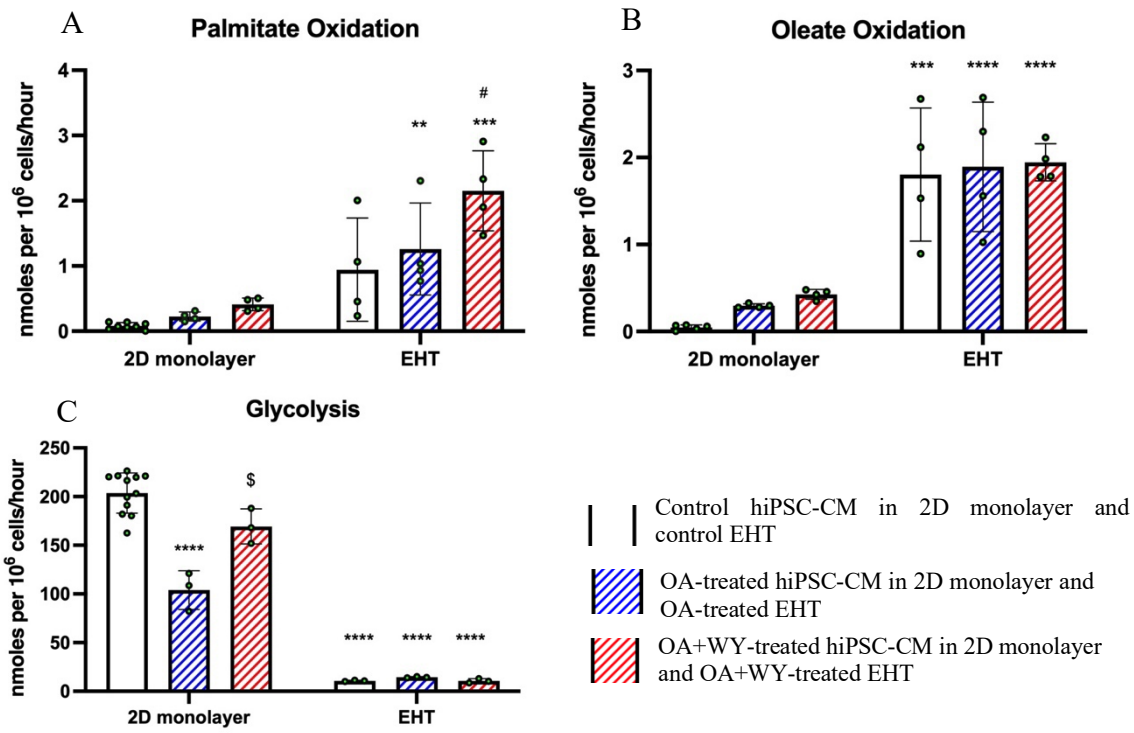


Figure 3.22 Fatty acid oxidative and glycolytic flux in hiPSC-CM in 2D and EHTmeasured by radiolabelled measurement

Rates of oxidation of palmitate (A), oleate (B) and glycolysis (C) were measured after culture in 2D monolayer and EHT for 1 week with OA ± WY-14643. Data represent the mean ± SEM and statistical significance was assessed by two-way ANOVA followed by Tukey's multiple comparison test with *, **, ***, **** $p<0.05$, 0.01, 0.005, 0.001 respectively compared with control hiPSC-CMs in 2D monolayer; # $p<0.05$ compared with control EHT; $ $p<0.05$ compared with OA-treated hiPSC-CM in 2D monolayer.

3.5.5.3 Structural changes

Although hiPSC-CMs grown in EHT showed higher sarcomeric actinin expression and clearer striation than the cells cultured in 2D, we did not observe a further increase in levels of sarcomeric actinin after addition of OA±WY-14643 (**Figure 3.23C**). Similarly, no changes in mitochondrial membrane potential were observed in EHT after treatment (**Figure 3.23B**).

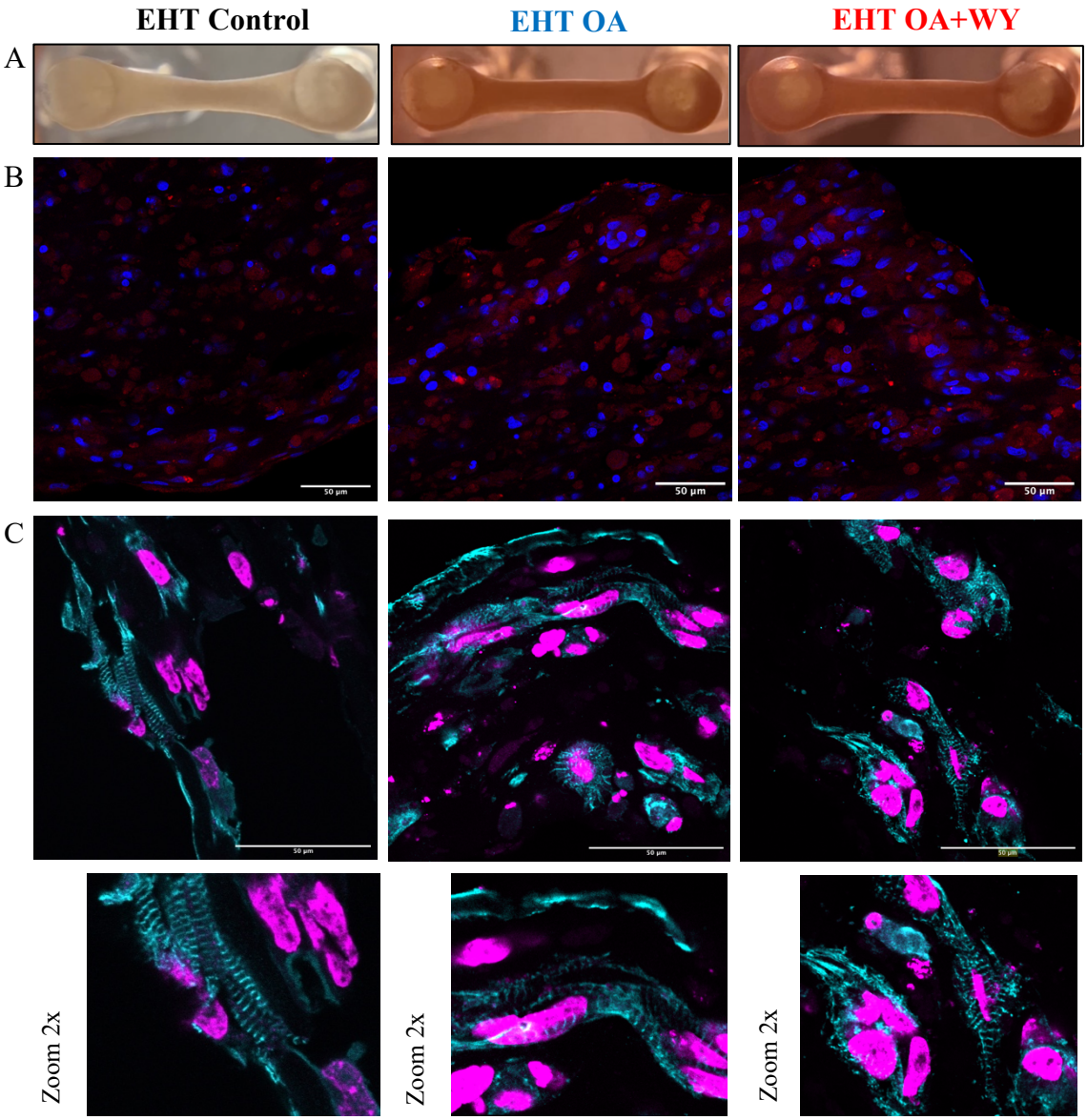


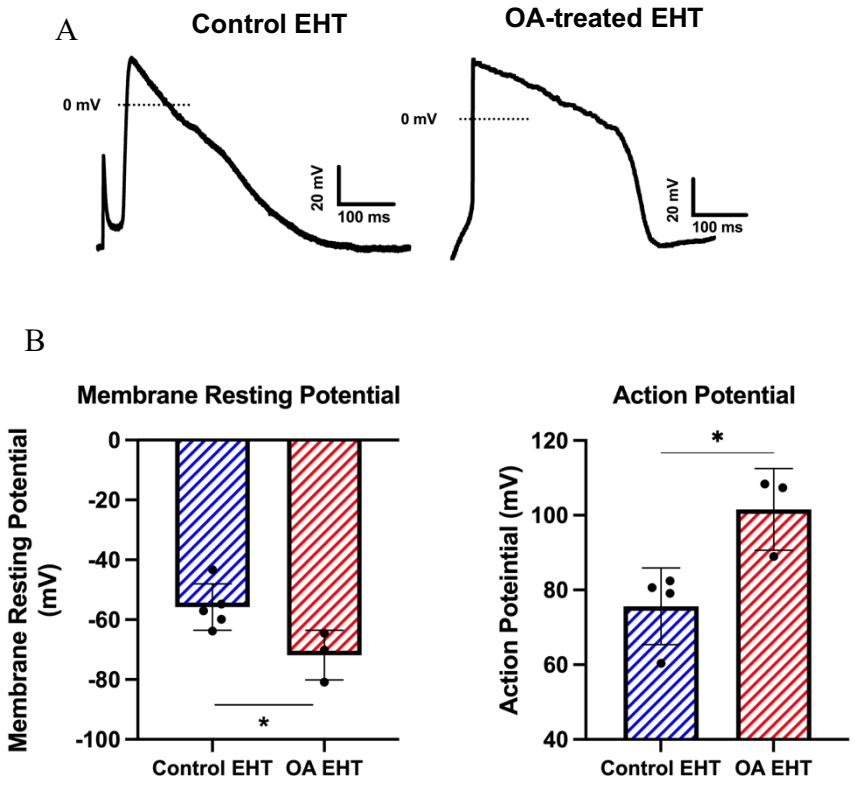
Figure 3.23 EHT images taken using brightfield microscope and immunostaining using confocal microscopy

Images of whole EHTs taken using macro lenses on brightfield microscope (A) and a confocal microscopy z-stack of control and treated EHT, after 1 week of treatment with OA +/- WY-14643, stained with MitoTracker Red CMXRos dye to show mitochondrial membrane potential (B) and an antibody for sarcomeric α-actinin showing sarcomeres in the cardiomyocytes (C). Scale bars in (B) and (C) are 50 μm, with a x2 zoom in (C) shown below. Red: MitoTracker, cyan: sarcomeric actinin, blue and magenta: DAPI

3.5.5.4 Contraction profile

Action potential traces of OA-treated EHT resembled more adult ventricular-like cardiomyocytes compared to control EHT (**Figure 3.24A**). Moreover, electrophysiological analysis showed lower resting potential and higher action potential in cells from OA-treated

EHT (**Figure 3.24B**). Moreover, the effect of OA and OA+WY-14643 on EHT contractility was quantified using Musclemotion and shown different contraction profile between control, OA-, and OA+WY-14643 treated EHTs (**Figure 3.25A**). When comparing the OA and OA+WY-14643 treatment on EHT to control EHT, there was no significant difference in the peak amplitude (**Figure 3.25E)**. However, OA-treated EHT showed significantly higher contraction duration, time to peak, relaxation time, contraction amplitude, and peak to peak time (**Figure 3.25B, C, D, F, G**), showing that OA-treated EHT contracted more strongly and more slowly than control. EHT with OA+WY-14643 treatment showed significantly higher contraction amplitude and peak-to-peak time compared to control EHT, but no significant effect was observed on contraction duration, time to peak, and relaxation time as shown in **Figure 3.25 B, C, D**.



.

Figure 3.24 Electrophysiology properties of hiPSC-CMs in EHT and OA-treated EHT
Action potential traces of control and OA-treated EHT (A); Quantification of membrane resting potential and action potential (B). Data represent the mean ± SEM and statistical significance was assessed by unpaired t-test with * $p < 0.05$ compared with hiPSC-CM in control EHT, analysed by Dr. Taiyi Wang, n=3

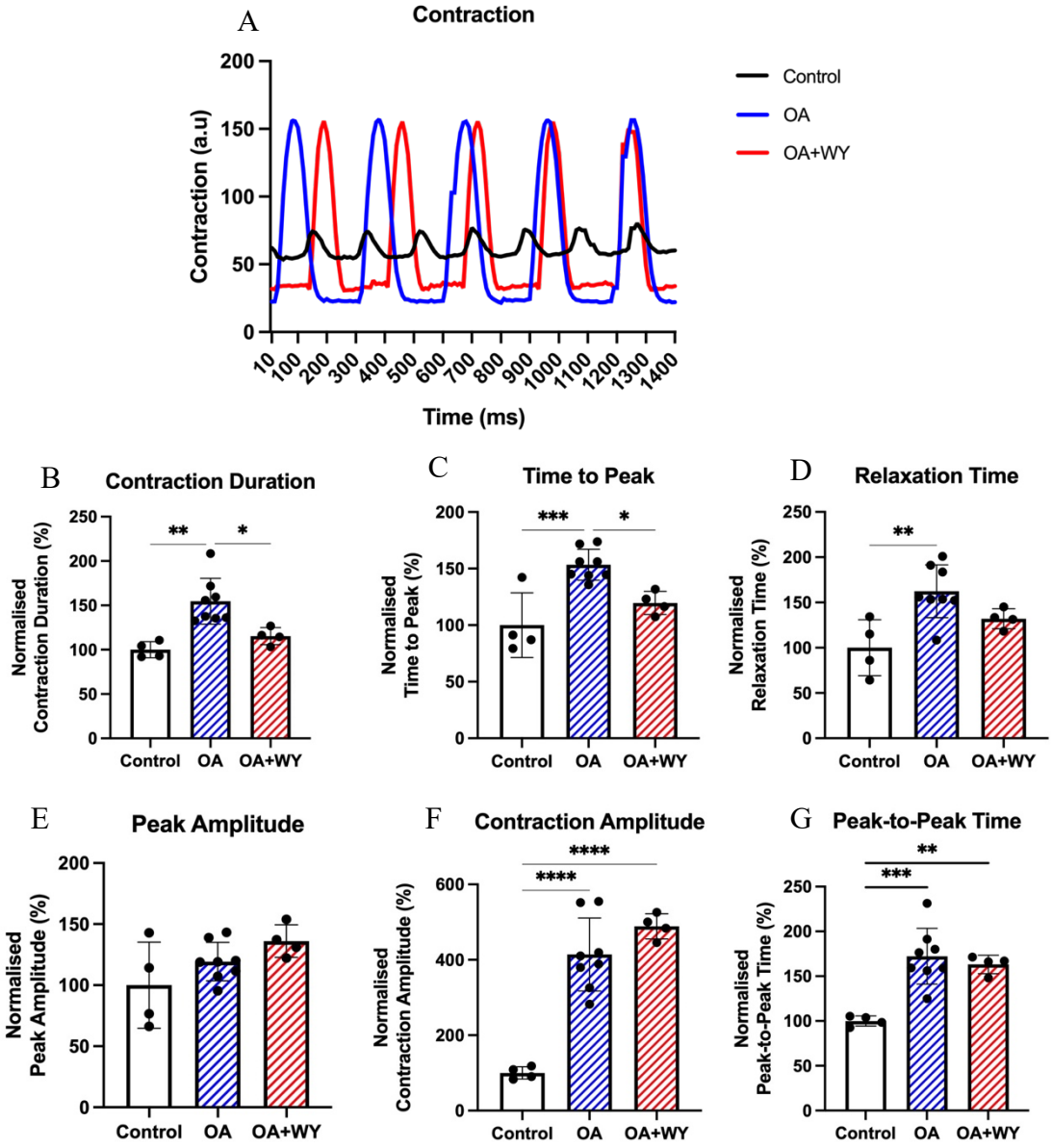


Figure 3.25 The effect of OA and OA+WY-14643 on the contraction of the EHT

Representative graph of contraction in the control, OA, and OA+WY-14643 treated EHT (A). Contraction parameters including contraction duration (B), time to peak (C), relaxation time (D), peak amplitude (E), contraction amplitude (F), and peak-to-peak time (G) of hiPSC-CMs in EHTs cultured in RB+ media (control), media supplemented with OA (OA), and media supplemented with OA and 120 µM WY-14643 (OA+WY). Data represent the mean ± SEM and statistical significance was assessed by one-way ANOVA followed by Tukey's multiple comparison with a *, **, ***, **** $p<0.05$, 0.01, 0.005, 0.001 compared with control hiPSC-CMs (n=4 for control and OA+WY-14643 and n=8 for OA).

3.5.5.5 Lipid accumulation

Oil red O staining did not show a significant difference in fatty acid accumulation in OA treated EHT when compared with control EHTs (**Figure 3.26 B-D**). The Alamar Blue reduction assay showed that the cell viability (or metabolic activity) was significantly enhanced in OA-supplemented EHTs compared with control (**Figure 3.26E**).

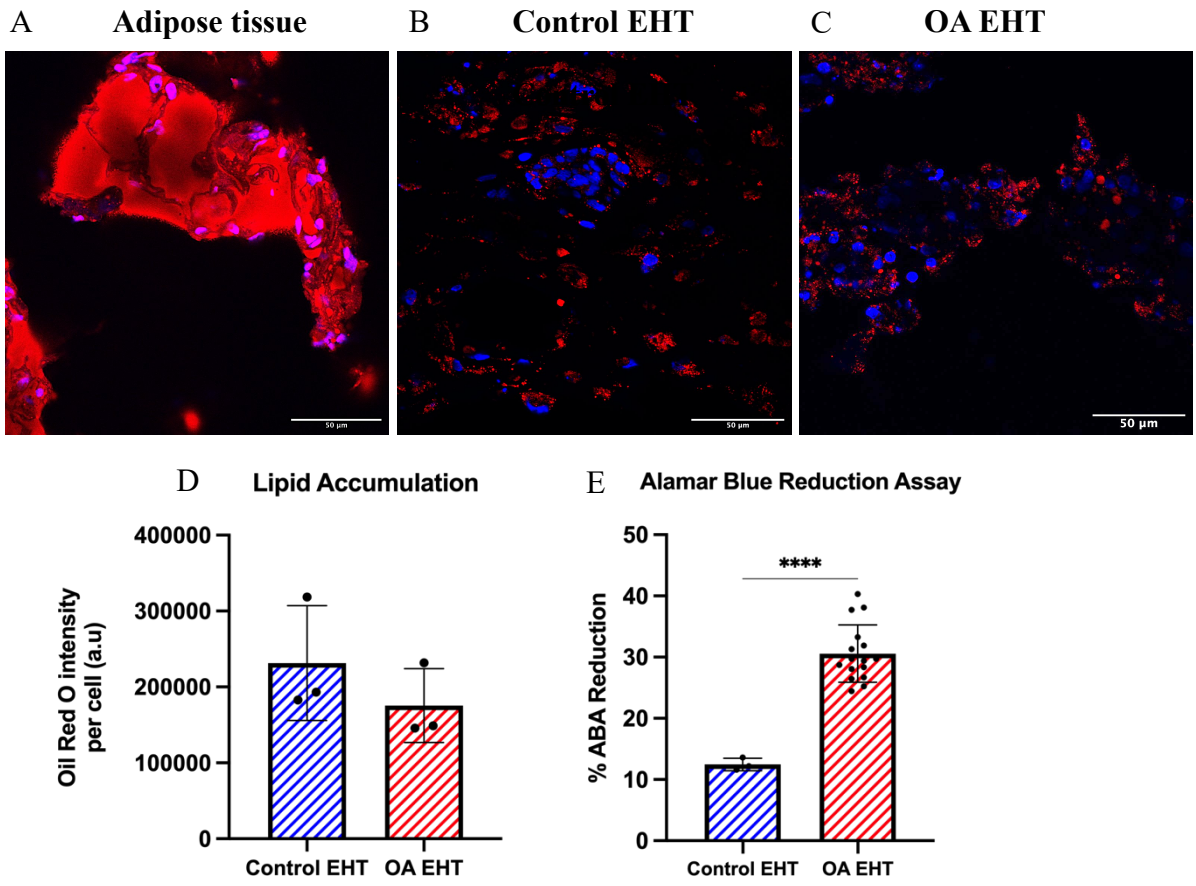


Figure 3.26 Oil red O staining and Alamar Blue reduction assay to assess lipid accumulation and viability in EHTs cultured with and without fatty acid supplementation. Oil Red O staining of adipose tissue is shown as a comparison.
Representative images from confocal microscopy of the lipid accumulation of adipose tissue (A), control EHT (B), and EHT cultured in OA supplementation (C) stained with ORO (neutral lipid-red, DAPI-blue), scale bar is 50µm. ORO intensity per cell for control and OA-treated EHT groups was calculated by dividing total ORO intensity by the number of nuclei (D). Data of Alamar Blue reduction percentage, calculated and adjusted to positive and negative controls (E). Data represent the mean ± SEM and statistical significance was assessed by unpaired t-test with a **** $p<0.001$ compared with control EHT (n=3 for lipid accumulation and control EHT on ABA assay, n=16 for OA EHT on ABA assay.

3.5.5.6 Ultrastructure

Ultrastructure analysis was performed using Transmission Electron Microscopy (TEM) by a MRes student, Kirsti Brisk. I prepared the samples to investigate the different between 2D and EHT with or without maturation media containing oleic acid. The experimental design had two variables to be investigated, tissue types (2D vs EHT) and treatment with OA. The samples were prepared as described in chapter 2. The ultrastructure of the cells was qualitatively observed to investigate the presence of sarcomeric striation, mitochondrial networks, and muscle area.

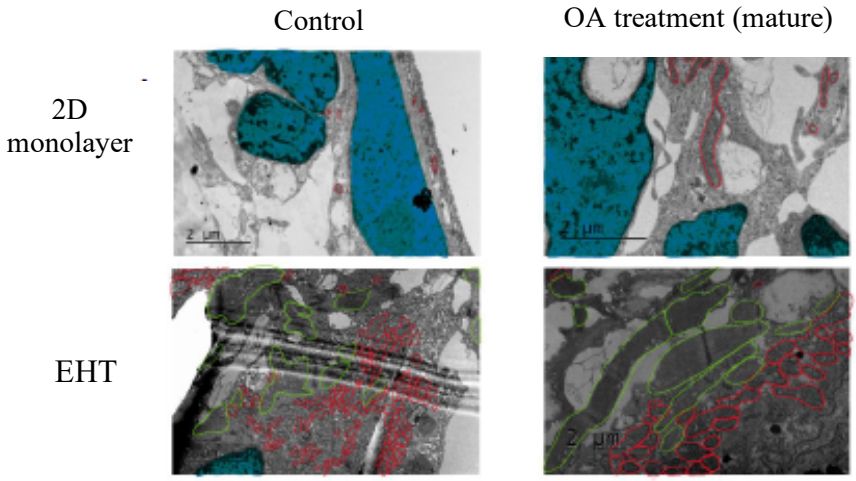


Figure 3.27 TEM images showing maturation of hiPSC-CMs in 2D and EHT (with or without maturation media)

Nuclei are shown in blue, and mitochondria and muscle are outlined in red and green, respectively.

Overall, qualitative observation showed that control EHT has more mitochondria number compared to both control and mature hiPSC-CM in 2D (**Figure 3.27**). EHT in maturation media showed a similar number of mitochondria to controls, although the mitochondria appeared bigger (**Figure 3.27**, shown in red). Additionally, there were more observable sarcomeric striations and gap junctions in EHT cultured in maturation media (**Figure 3.27**, shown in green). More detailed analysis of the TEM data will follow in chapter 4.

3.6 Discussion

3.6.1 GiWi Protocol by activating and inhibiting Wnt pathway with Wnt-c59 molecules improves differentiation outcomes

Human iPSC-CMs have been shown to have numerous applications including modelling human diseases, drug testing, and as a potential cell source for cardiac regeneration. Researchers have been differentiating hiPSCs into cardiomyocytes (CMs) using different protocols recapitulating the key stages of heart development[258]. It has been suggested that the early differentiation protocols such as embryoid body formation protocol were not efficient and produced a small number of cardiomyocytes[259]. Therefore, the more efficient differentiation protocol using monolayer culture was adopted in our lab. This protocol allowed the cells to differentiate hiPSCs to CMs and cultured as a monolayer in serum free media, with activation of pathways that are known to regulate primitive streak (PS) formation and mesoderm induction[260].

In this project, I modified the existing protocols used in the lab to increase the number of hiPSC-CM produced and the consistency of the procedure. The GSK-3β inhibitor, CHIR99021, activates the Wnt pathway and can be used as a salt or as the free base form. I found that addition of the base form of CHIR99021 for 2 days was more efficient to allow mesoderm formation. This may be because the base form of CHIR99021 is less polar than the salt, the molecule may penetrate across the cell membrane more easily. Two small molecule inhibitors of Wnt signalling, IWP4 and C59 were compared and C59 was found to be more effective. Both molecules inhibit Wnt signalling by inactivating Porcupine, a membrane-bound O-acyltransferase responsible for palmitoylating Wnt proteins which is essential for Wnt signalling ability and secretion[261]. I added a metabolic selection step by depriving the cells of glucose in the cell culture media for 4 days, changing the media every 2 days. This cardiomyocytes purification has been used extensively to increase the

percentage of cardiomyocytes as non-myocytes do not survive well without glucose, as compared to the more metabolically flexible cardiomyocytes[192]. However, the implication of the metabolic selection towards cardiomyocytes functionality has not been extensively studied.

The modified protocol successfully generated 75-90% cardiomyocytes shown by the number of cells that were α-actinin positive using flow cytometry. This quantitative analysis was supported by the structural analysis using immunostaining. Furthermore, this protocol also produced hiPSC-CMs that were more than 80% ventricular-like cardiomyocytes. It has been reported that GiWi protocol produces an heterogenous population of cardiomyocytes consisting atrial, ventricular, and nodal-like cardiomyocytes[220]. Since this protocol has been shown to be robust, it was then used extensively throughout the project.

3.6.2 Addition of oleic acid and PPAR agonist enhances hiPSC-CM maturation

Human iPSC-CMs are immature and reflect a fetal phenotype rather than that of adult cardiomyocytes. There have been many attempts for maturation including long term culture, applied mechanical and electrical stimulation, genetic approaches, substrate stiffness, addition of small molecules, and 3D culture[149,262–265]. However, these approaches have not yet generated fully adult CMs[263,264,266]. Nonetheless, the strategy of maturation keeps growing and there is a rise of attention in the field. Palmitic acid (PA, saturated fatty acid) and oleic acid (OA, mono-unsaturated fatty acid) are the two common fatty acid circulating in the human body[61,62]. When comparing the two fatty acids it was found that OA was better for maturation, as it increased expression of PGC1α and the glucose transporters, which was not seen with PA. Instead, PA reduced cell viability and increased the accumulation of lipid deposits. Others have shown that PA downregulates PGC1α in skeletal muscle cells[267]. The metabolic changes induced by modulating the culture medium have been investigated by others. Horikoshi et al. grew 2D hiPSC-CMs in a glucose-free maturation medium

containing linoleic acid and OA for 3 to 7 days and observed structural maturation as well as increased glycolysis and PA oxidation whereas I saw a decrease in glycolysis when OA was added into a glucose-containing media[268]. Yang et al. found that adding physiological amounts of PA, OA, and linoleic acids to 2D hiPSC-CM increased structural maturation, glucose oxidation, and calcium handling, but did not directly measure FAO[236].

PPARα has been shown to be an important factor in driving metabolic maturation of the heart after birth[269,270]. PPARα expression peaks twice during mouse embryonic stem cell differentiation to CMs[269,270]. Treatment with PPARα agonists increased the number of spontaneously contracting embryoid bodies, as well as the expression of cardiac genes, during differentiation[269,270]. Although addition of OA+WY-14643 gave some added effect on the hiPSC-CMs such as higher PA and OA oxidation, higher PDK4 and sarcomeric α-actinin expression assessed by immunocytochemistry compared to controls, addition OA alone was sufficient to elevate the changes in the cells indicating more mature hiPSC-CMs in 2D monolayer (**Table 3.2**). Moreover, there is a concern over toxicity of WY-14643 addition into the cells over longer period in a dose-dependent manner. Therefore, it was decided to use OA alone to enhance maturation of the hiPSC-CMs.

Table 3.2 Parameters indicating maturation of hiPSC-CM

Parameters	OA	OA+WY-14643	Better maturation agent
PDK4 expression	⇑	⇧	OA+WY-14643
Toxicity	No observable toxicity	Decreased cell number on the dose-dependent manner and unknown toxicity for longer period.	OA
Sarcomeric α-actinin (immunocytochemistry)	⇑	⇧	OA+WY-14643
Mitotracker CMXRos	⇧	⇑	OA
Glycolysis	⇩	⇓	OA
Palmitate oxidation	⇑	⇧	OA+WY-14643
Oleate oxidation	⇑	⇧	OA+WY-14643

Note: The data presented above was compared to control hiPSC-CMs in 2D monolayer

3.6.3 Combination of engineered heart tissue and metabolic maturation further increase cell maturation

Tissue engineering has been used in recent years as an attractive maturation approach providing a more physiological environment to better mimic cells in vivo. However, the effect on metabolism in engineered tissue is rarely studied. The frequently used technique to quantify the substrate metabolism, Seahorse Bioanalyzer, cannot be used for complex 3D construct such as engineered heart tissue. Therefore, in addition to other characterisation approaches such as immunohistochemistry, Western blot, and qPCR, metabolic flux in the EHT was quantified using radiolabelled substrates to investigate the effect of OA in the EHT.

Growing the cells in EHT led to enhanced metabolic maturation, exemplified by a significant

metabolic switch from glycolysis to FAO, increasing gene expression of metabolic and structural genes, and increased mitochondrial number compared to 2D culture. This agrees with Ulmer et al[239], who recently demonstrated that culture of hiPSC-CMs in EHTs resulted in the maturation of energy metabolism when compared to 2D culture. The findings back up the theory that contractile work aided in the metabolic maturation of hiPSC-CMs.

The addition of OA alone on EHT was sufficient to increase the metabolic and structural gene expression compared to control EHT. In contrast, addition of OA with the PPARα agonist did not significantly affect metabolic and structural genes expression and even downregulated some genes compared to addition of OA alone. A recent study showed that although PPARα is the most active isoform protein in hiPSC-CM, it is PPARdelta (PPARδ) activation that efficiently upregulates the gene regulatory networks underlying FAO[271].

The addition of OA alone increased the rate of PA oxidation 1.5-fold higher than control EHT. The addition of OA and WY-14643 for 1-week increased the rate of PA oxidation to the point where the cells oxidised twice of the amount of PA used in control EHT and 20 times the amount of PA used by the untreated hiPSC-CMs grown in 2D. The addition of OA alone is sufficient to increase the contraction parameters including contraction duration, time to peak, relaxation time, contraction amplitude and peak-to-peak time (**Figure 3.25**). This is supported by the data in the improvement in the membrane resting potential and action potential, recapitulating that of more adult cardiomyocytes (**Figure 3.24**). However, addition of OA and PPARα agonist only increased contraction amplitude and peak to peak time but not contraction duration, time to peak and relaxation time compared to control (**Figure 3.25**). The improvement in the contraction parameters due to OA addition is likely to be the result of the upregulation in the gene expression underlying FAO and the increase in PA oxidation. This improvement in the metabolism drives the contraction of EHT via ATP production. This was not seen with the addition of OA with the PPARα agonist as this

only increased contraction amplitude and peak to peak time, despite a greater increase in PA oxidation than seen with OA alone. However, contraction duration, time to peak and relaxation time did not change compared to control which is likely due to the toxicity effect of PPARα agonist on longer period exposure as shown in 2D monolayer data. Therefore, OA addition alone was chosen for the disease modelling and drug testing described in the next chapters.

3.7 Conclusion

I have directly compared the effects of OA and PA supplementation on maturation and cellular health of hiPSC-CMs in 2D monolayer. OA enhances oxidative metabolism without lipid accumulation or impairing cell viability; hence, OA supplementation was further investigated on the project onwards. I have contributed to a study that explored the potential of SR-FTIR to detect changes in the macromolecules in the hiPSC-CM during differentiation and maturation. The multimolecular sensitivity of this technique provides complex data, which shows that changes are occurring in the cells during differentiation.

Culture in 3D can induce a switch to a more metabolic phenotype in hiPSC-CMs, with increased FAO, and pharmacological stimulation of the PPARα pathway. Because the cells in EHT are working harder, they can benefit from more FAO-dependent ATP production.

4

Modelling the effect of diabetes on human iPSC-CM in 2D and EHT

CHAPTER 4

4 MODELLING THE EFFECT OF DIABETES ON HUMAN IPSC-CM IN 2D AND EHT

4.1 Abstract

Cardiovascular disease is the leading cause of mortality in patients with diabetes. Elucidating and understanding early stages of the disease is vital for seeking possible therapeutic targets for diabetes. Despite numerous studies using in vitro and animal models, current preclinical models do not recapitulate the adult human heart. Moreover, there are multiple differences between rodent and human physiology providing a challenge when studying the effect of cardiometabolic diseases such as the effect of diabetes in the heart. Therefore, there is a pressing need for an in vitro model to bridge the gap and aid understanding of the factors of the diabetic phenotype that are harmful to cardiac tissue. Human induced-pluripotent stem cell-derived cardiomyocytes (hiPSC-CMs) have potential as a predictive tool. Here I show for the first time how to modulate media in the hiPSC-CMs in 2D monolayer and engineered heart tissue (EHT) to induce the cells to become insulin resistant. I developed a “diabetic-like” medium by modulating concentrations of glucose, insulin, and palmitate. Culture in the diabetic media resulted in an increase in fatty acid metabolism, decrease in glucose metabolism, and a blunted insulin signalling pathway in hiPSC-CM in 2D monolayer and EHT. This protocol demonstrates that hiPSC-CMs had become insulin resistant, providing an in vitro human model for studying the diabetic heart.

4.2 Introduction

In the previous chapter, I showed that culturing cells with the addition of oleic acid in 2D monolayer can drive the cells to become metabolically more mature, and that additionally culturing the cells as EHT can promote this further. In this chapter, I explored the utilisation of hiPSC-CM to model the effect of insulin resistance in the heart.

4.2.1 Insulin resistance in diabetic cardiomyopathy

Insulin resistance contributes towards the early development of the pathophysiology in Type-2 diabetes (T2DM). Insulin resistance is characterised by reduced insulin signalling in normally insulin-responsive tissues including the heart, and has been reported to result from factors including increased ceramides or diacylglycerol (DAG), endoplasmic reticulum stress, altered mitochondrial function and increased reactive oxygen species (ROS)[272]. In addition to hyperglycaemia and insulin resistance, it is currently hypothesised that high lipid uptake and lipid accumulation (hyperlipidaemia) in the adipose and non-adipose tissue (heart, muscle, and liver) lead to insulin resistance.

Cardiac insulin resistance has been shown to contribute to contractile dysfunction in T2DM, even at the early stages, due to metabolic derangement[273]. Some evidence from animal models showed that hyperglycaemia and hyperlipidaemia cause reduced contractility, specifically affecting diastolic function[274,275]. Hyperglycaemia induces defects in intracellular calcium and its homeostasis, leading to impaired mechanical performance in diabetic heart[276–278]. Increased substrate metabolism of lipids drives reactive oxygen species production and stimulates inflammatory signalling, which results in impairment of mitochondrial energetics and contractile dysfunction[279].

4.2.2 Modelling diabetic cardiomyopathy using hiPSC-CM

There have been numerous reviews about the benefit of hiPSC-CM as a versatile tool for disease modelling and drug targeting[280]. However, unlike other monogenic diseases that

have been successfully studied in vitro using iPSC-CM, diabetic cardiomyopathy (DbCM) is a multifactorial and lifestyle-related disease, and therefore caution must be taken in establishing what can be deduced from studying a cell-based model. Previous studies have suggested that to model DbCM using iPSC-CM, the cells should meet the minimum requirement of DbCM etiology and show insulin resistance, a metabolic shift, lipotoxicity, hypertrophy, and altered cardiac function[281]. These changes can be induced by culturing the cells in the extracellular milieu found in the diabetic state. Drawnel et al. used media containing fatty acids (FA) in the absence of glucose to induce a metabolic shift towards more fatty acid oxidation (FAO)[282]. The cells were then cultured in media consisting of intermediate glucose levels, endothelin 1, and cortisol. Subsequently, the cells started showing hallmarks of their diabetic counterpart, with glucose-restriction-induced cellular distortion, lipid accumulation and peroxidation, decreased frequency of calcium transients, cellular hypertrophy, and loss of sarcomere integrity.

The use of hiPSC-CM from patients with insulin resistance concluded that it is the insulin resistance that drives the impairment in energy homeostasis and increased oxidative stress. Iovino et al. further supported this when they showed that insulin-resistant iPSC-derived myotubes, when differentiated from cells from patients with mutations in the insulin receptor, also showed impaired insulin signaling and aberrant glycogen synthesis[283,284]. Geraets et al cultured embryonic stem cell-derived cardiomyocytes with high palmitate and insulin and saw lipid-induced insulin resistance[285], although they commented that the cells were structurally and functionally immature.

Advanced 3D culture has been used to study metabolic disorders in some tissues. However, there are few approaches to study the effect of insulin resistance in the heart. Modelling the effects of pre-gestational diabetes was performed by exposing a healthy heart organoid to diabetic levels of glucose and insulin[286]. Structural and metabolic changes including cardiac

hypertrophy, reduction in mitochondrial number, aberrant lipid metabolism, and increased glycolysis were seen, thus encompassing several of the factors of diabetic cardiomyopathy[286]: Lewis-Israeli et al. have developed the most complex model of the developing heart, using differentiating iPSCs, which contain multi-lineage cardiac cell types and internal chambers. They modelled the effects of pre-gestational diabetes by exposing a pre-prepared heart organoid to diabetic levels of glucose and insulin[151].

The availability of nutrients/oxygen in the centre of the 3D structure is important to ensure the physiological relevance of the model. The diabetic heart has impaired vascular function, accelerated atherosclerosis and an impaired hypoxic signaling[287–293]. Diabetic rats and diabetic mouse cells have decreased recovery when exposed to hypoxia and ischemia[256]. Katare, et al. used engineered heart tissue from rat cardiomyocytes to assess the ischemic changes of the heart in vitro. Using culture under hypoxia, they found that their model showed similar changes in cell survival signaling to those seen in the adult rat heart under hypoxic stress[151]. Therefore, it is also important to assess the 3D cell culture under hypoxic conditions, particularly for studying ischemia.

4.3 Chapter Aims

This chapter aims to investigate the utilisation of hiPSCs in 2D and EHT for modelling insulin resistance in diabetic cardiomyopathy. In summary, this chapter investigates the optimum method to induce insulin resistance in hiPSC-CM in 2D and EHT to show the major characteristics of insulin resistance including attenuation of intracellular insulin signalling, changes in gene expression, a metabolic shift to increased fatty acid oxidation and mitochondrial dysfunction, while maintaining sufficient viability of the cells.

4.4 Materials and methods

4.4.1 Protocol to induce insulin resistance in hiPSC-CM in 2D and EHT

Palmitic acid (PA) was used to induce insulin resistance in the hiPSC-CM. Palmitic acid:BSA (bound 6:1) was prepared using the same conjugation technique for oleic acid:BSA (2:1) described in the method section of chapter 3. Powdered palmitic acid (2.56g; Sigma Aldrich) was weighed and dissolved in 2 mL ethanol in the water bath at 70^{o}C before mixing with 100 mM aqueous solution of anhydrous potassium carbonate. This mixture was then transferred to 0.9% sodium chloride solution and stored in the fridge for later use. In order to bind the palmitate with BSA (ratio 6:1), palmitate was slowly added into warm ultrapure fatty acid free BSA (Sigma Aldrich) 165.5 μM solution while stirring. This solution was filtered using 0.22 μm filter before adding it to the DMEM containing 5.5 mM glucose for the cell culture.

To test the different concentrations of PA in the hiPSC-CMs in 2D monolayer and EHTs, cells were cultured in either control media or media containing 50 nM insulin and either 100 μM, 300 μM, or 500 μM of PA for 24-, 48- and 72-hours following maturation. In the final protocol, insulin resistance was induced by culturing mature hiPSC-CM for three days in 'glucose-free IR-media,' which included DMEM without glucose, 0.3 mM palmitic acid:BSA (bound 6:1), and 50 nM insulin. On day 4, the media was changed to the 'IR media' which is the same media as above but with the addition of 12 mM glucose for another three days. The detailed media composition is listed in **Table 4.1** and **Table 4.2,** schematic representation of the established protocol is shown in **Figure 4.6** , and a full reagent for the media is listed in **Appendix C**.

To test insulin response in hiPSC-CM, the hiPSC-CMs in 2D monolayer were cultured for 7 days in maturation media followed by insulin resistance induction for 6 days. At day 6, the hiPSC-CM in 2D monolayer were incubated with basal media for 4 hours and then

washed twice with DPBS. The hiPSC-CMs in 2D monolayer were cultured in 1 g/L glucose DMEM with or without 50 nM insulin for 30 mins in the incubator (5% CO_2 at 37°C), then used for Western blotting.

Table 4.1 Glucose-free IR media

Reagent	Volume (%)
DMEM, no glucose	87.30
Insulin solution human	0.10
Horse serum	10.00
Palmitic acid-BSA (300 µM)	2.10
Vitamin B12	0.20
Vitamin C	0.10
Biotin	0.20

Table 4.2 IR media

Reagent	Volume (%)
DMEM, low glucose	58.45
DMEM, high glucose	28.75
Insulin solution human	0.20
Horse serum	10.0
Palmitic acid-BSA (300 µM)	2.10
Vitamin B12	0.20
Vitamin C	0.10
Biotin	0.20

4.4.2 Insulin resistance in hiPSC-CMs analysis using qPCR, Western blot, radiolabelled experiment, muscle motion, proteomic and transcriptomic analysis

Insulin resistance in the hiPSC-CMs was analysed using protocols described previously in the general method chapter 2. The insulin resistant hiPSC-CMs were compared to control hiPSC-CMs cultured in maturation media.

4.4.3 Cell viability assay

Cell viability was assessed using the CCK-8 and Alamar Blue reduction assay, described in chapter 2 general methods, and ReadyProbes® (ThermoFischer Scienific) according to the manufacturing protocol. ReadyProbes® consists of NucBlue® Live reagent (Hoechst 33342) and NucGreen® Dead reagent and labelled cells are imaged using fluorescence microscopy

using the DAPI and GFP filter respectively. NucBlue® Live reagent stains all the nuclei and NucGreen® Dead reagent only stains the nuclei from the cells that have lost their integrity.

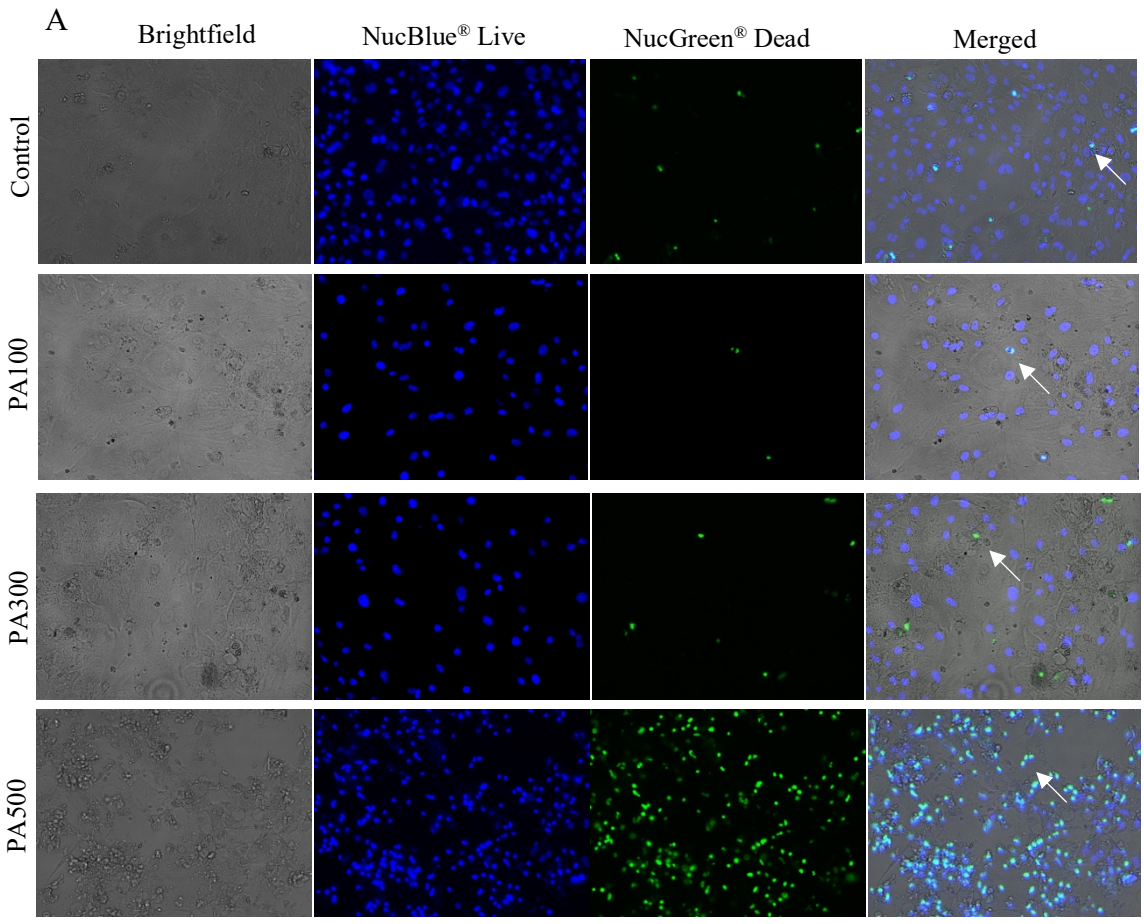
4.4.4 Proteomics and transcriptomics

The cell preparation for proteomics and transcriptomics was performed described in the general method chapter 2. Proteomic and transcriptomic analysis were performed in collaboration with Novo Nordisk Research Centre Oxford (NNRCO), Old Road Campus, Roosevelt Drive, Oxford, OX3 7FZ, UK. The data was analysed by a Dphil student from Prof. Lisa Heather's group, Ryan Carter.

4.5 Results

4.5.1 Human iPSC-CM in 2D and EHT treatment with palmitic acid

Palmitate (PA) has previously been shown to induce insulin resistance in HL-1 cells and primary cardiomyocytes from neonatal mouse hearts[118,294]. Therefore, hiPSC-CMs were treated with PA acutely for 24 hours or chronically for longer periods of exposure in both 2D and 3D EHT. I have shown previously in chapter 3 that treatment with 500 µM of PA for 24 hours was toxic and did not induce maturation in 2D monolayer hiPSC-CMs. Therefore, the first experiment was to investigate a range of PA concentrations (0 µM, 100 µM, 300 µM, 500 µM) across a range of time points (24 – 72 hours).



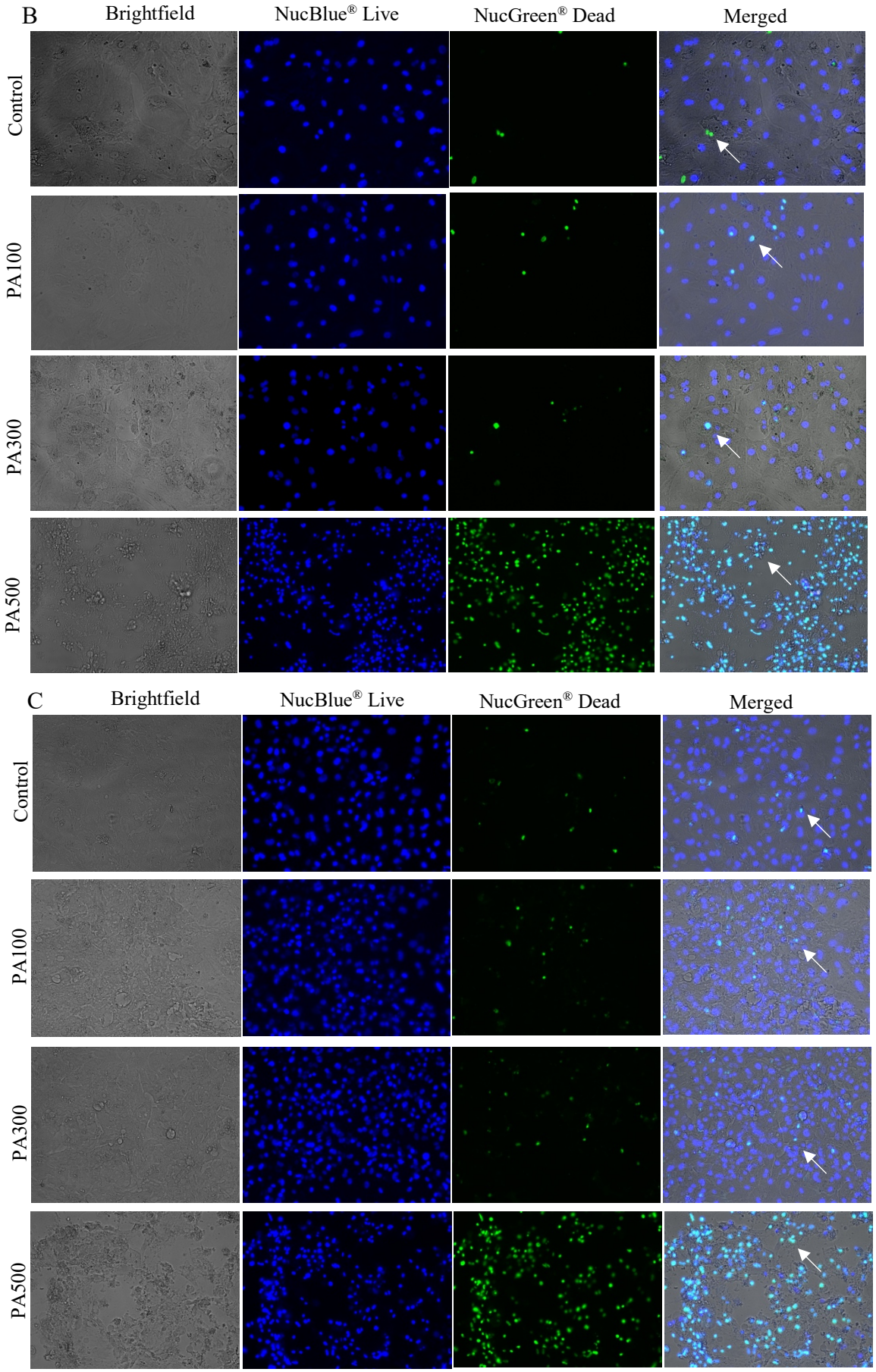


Figure 4.1 Assessment of toxicity of different concentrations of palmitate on hiPSC-CM in 2D
Cell death staining using ReadyProbes was performed after one day (A), two days (B), and three days (C) of palmitate treatment and imaged using fluorescence microscopy. PA100: Palmitate 100 µM, PA300: Palmitate 300 µM, PA500: Palmitate 500 µM. White arrows showed dead cells.

The effect of different PA concentrations on cell viability in 2D monolayer was assessed using a live/dead staining procedure (ReadyProbes). Qualitative image analysis showed that there were no obvious differences when the cells were exposed to 100 μM and 300 μM PA across three days. However, there was an obvious increase in the number of nuclei stained by green dye when the cells were exposed with 500 μM PA across three days indicating that there were more dead cells at all time point (**Figure 4.1).**

Next, PA toxicity was assessed by the Alamar Blue (ABA) assay in the 3D EHT. The addition of 500 μM PA for 24 hours decreased the red fluorescent signal from ABA suggesting that PA toxicity resulted in a lower number of cells or blunted cell metabolism in the EHT. In contrast, there was no significant difference in ABA reduction in the EHT groups after addition of 100 μM PA compared to control EHTs (**Figure 4.2**). Interestingly, unlike in 2D monolayer, addition of 300 μM of PA to the EHT significantly reduced cell viability. A concentration of 300 μM of PA was used in further studies of the effect of PA on insulin resistance in EHTs. This concentration reduced cell viability in EHTs but did not increase cell death in the 2D monolayer. We were concerned that a lower concentration may not be sufficient to induce a significant metabolic change in the cells so selected this concentration that was on the borderline of toxicity. I then assessed the effect of PA addition for three days, to analyse a longer period of exposure. EHTs were matured for seven days using OA and then were cultured with either control media or PA media at the concentration of 300 μM. The ABA assay was performed on the EHTs after 24-, 48-, and 72-hours treatment with control media or 300 μM PA media. There was no significant drop in ABA reduction between the control EHT over time. However, there was a significant decrease in ABA reduction in PA-treated EHTs compared to untreated EHTs at each timepoint (**Figure 4.2B**). Interestingly, ABA reduction was significantly higher after 48 hours PA treatment compared to 24 hours PA treatment and then decreased again after 72 hours PA treatment.

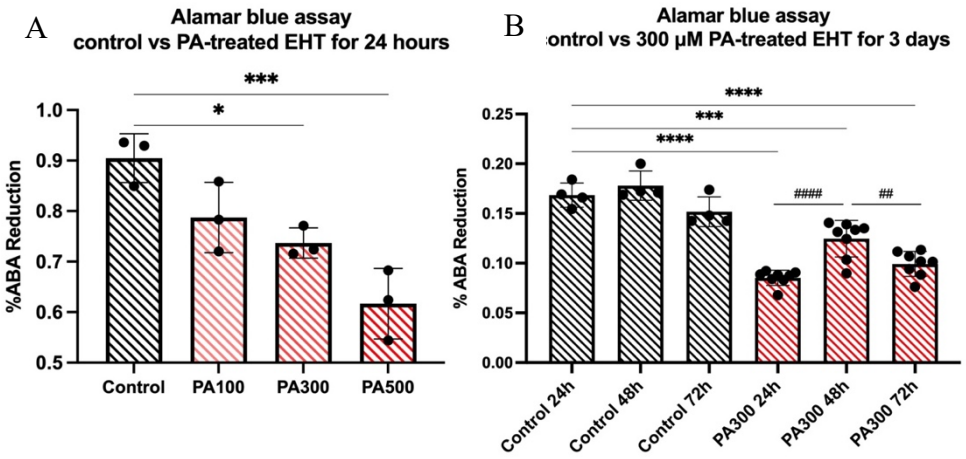


Figure 4.2 Alamar Blue (ABA) reduction assay on the EHT to assess the effect of palmitate on cell viability

ABA assay was performed to assess the effect of different concentrations of palmitate for 24 hours (A) and the effect of of longer-term palmitate exposure (B). Data is presented as mean value ± SEM and was analysed using a one-way ANOVA followed by a Tukey's multiple comparisons test with *, **, **** $p < 0.05, 0.01, 0.001$ compared with control EHT, ##, #### $p < 0.01, 0.001$ compared with PA300 24h, n=3-8

Lactate production was measured to assess if the cells undergo metabolic remodelling from oxidative phosphorylation to aerobic glycolysis after treatment with different palmitate concentration. A lactate assay was performed on media from the matured EHTs after 24 hours of treatment with either control media or different concentrations of PA. This showed that that there was no significant difference in the lactate production in the EHTs following 24 hours treatment with PA when normalised to either cell number (**Figure 4.3A**) or protein

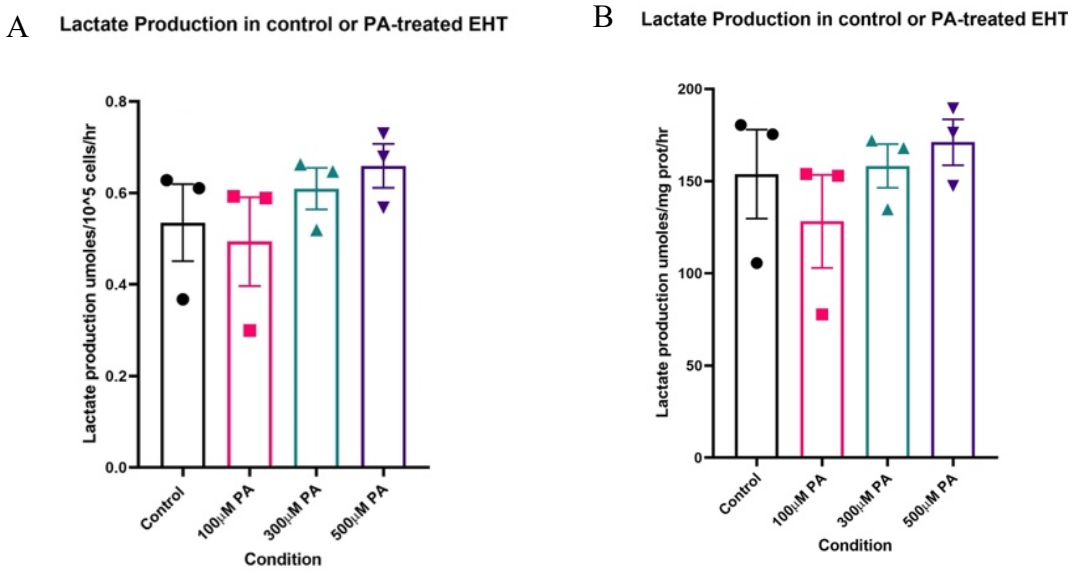


Figure 4.3 PA treatment on the EHTs did not influence lactate production

Lactate production in control EHTs compared to PA-treated EHTs normalised to the cell number (A) and protein quantity (B). EHT media was collected from either control or PA-treated EHT batches after 24 hours and lactate concentration measured using enzymatic reaction described in chapter 2. Data is presented as mean value ± SEM and was analysed using a one-way ANOVA followed by a Tukey's multiple comparisons test, n=3.

The effect of 300 µM PA on the contractility of the EHT was assessed by using Musclemotion. EHTs were matured for seven days followed by PA treatment for 24, 48, 72, and 96 hours. There were no significant changes in contraction duration or relaxation time in the control group over time. There was a significant increase in contraction duration and relaxation time between control and PA-treated EHT after 24 hours of treatment. There were no significant changes in contractile duration or relaxation time between control and PA-treated EHT after 48, 72 and 96 hours of treatment (**Figure 4.4**).

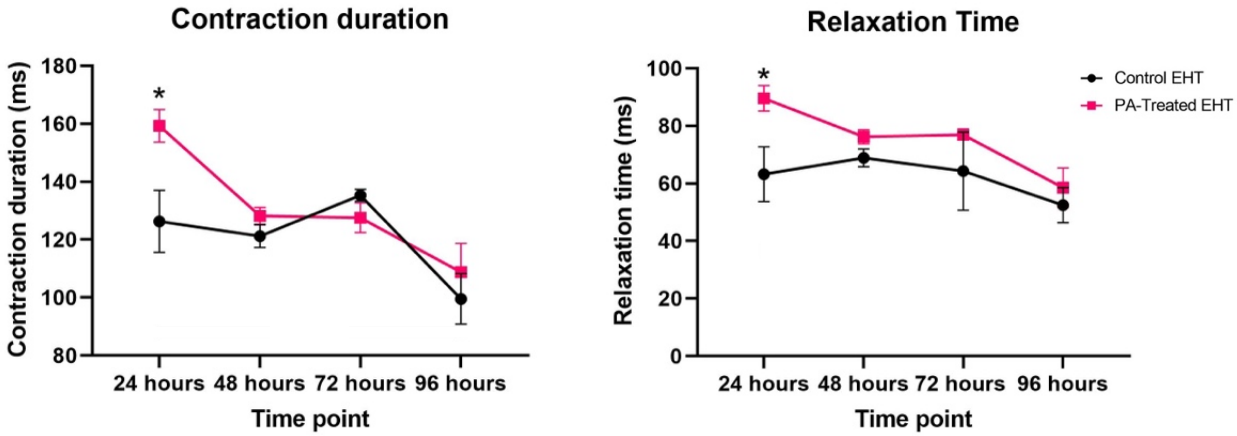


Figure 4.4 Long-term effect of PA treatment on EHT for contraction duration and relaxation time

Videos were taken of beating EHT after 24, 48, 72 and 96 hours of treatment which were then analysed using Musclemotion software to investigate the contractile properties. Data is presented as mean ± SEM and was analysed using a two-way ANOVA followed by a Dunnett's multiple comparisons test with * $p < 0.05$ compared to control 24hrs, n= 5 for Control 24hr and PA300 72hr, n=4 for control 48hr and control 96hr, n=3 for control 72hr, n=14 for PA300 24hr, n=7 for PA300 48hr and PA300 96hr.

4.5.2 Further optimisations of the protocol to induce insulin resistance in human iPSC-CMs in 2D and EHT

In the previous experiment, I tested different concentrations (100, 300, and 500 µM) of palmitate (PA) in media that contained 5.5 mM glucose. Although the level of glucose in the media is within the physiological concentration of blood glucose, I wanted to investigate the impact of manipulating glucose concentrations in addition to PA. In monolayer cells, I

tested two experimental designs: addition of 300 μM PA and 50 nM insulin (hyperinsulimia condition) in the media without glucose for six days (protocol A), and addition of 300 μM PA and 50 nM insulin in the media without glucose for three days followed by addition of 300 μM PA in the media with hyperglycaemia (12 mM glucose) for another three days (protocol B). I then tested glucose consumption at the end of six days to determine which protocol inducing insulin resistance. Protocol A and protocol B showed similar rates of glucose consumption and significantly lower than the control as shown in **Figure 4.5**.

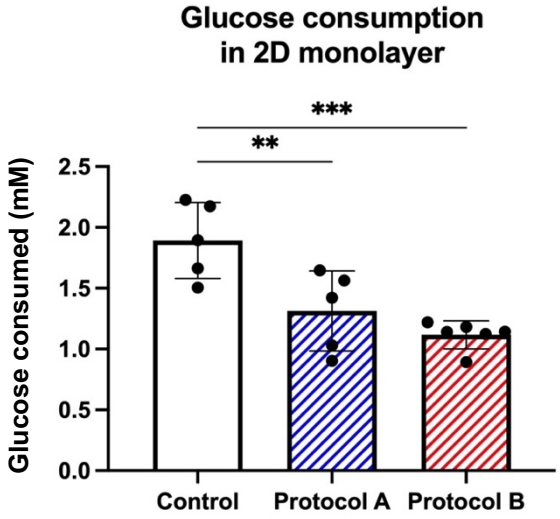


Figure 4.5 Protocol A and B induced reduction in glucose consumption of hiPSC-CMs
Glucose consumption in 2D monolayer hiPSC-CMs exposed to protocol A (6 days with media containing no glucose, 300 μM PA, 50 nM insulin) and protocol B (3 days with media containing no glucose, 300 μM PA, 50 nM insulin, followed by 3 days with media containing 12 mM glucose, 300 μM PA, 50 nM insulin). Data is presented as mean ± SEM and analysed by one-way ANOVA followed by Dunnett's multiple comparison test with ** $P<0.01$ compared to control, n=6

As there was no difference between the two protocols, it was protocol B that was taken forward for further investigation as it included the hyperlipidaemia, hyperglycaemia, and hyperinsulinemia – all three of which are circulating factors found in patients with insulin resistance. The finalised insulin resistance protocol was further tested in the 2D monolayer culture and described going forward as "IR-media" (**Figure 4.6**).

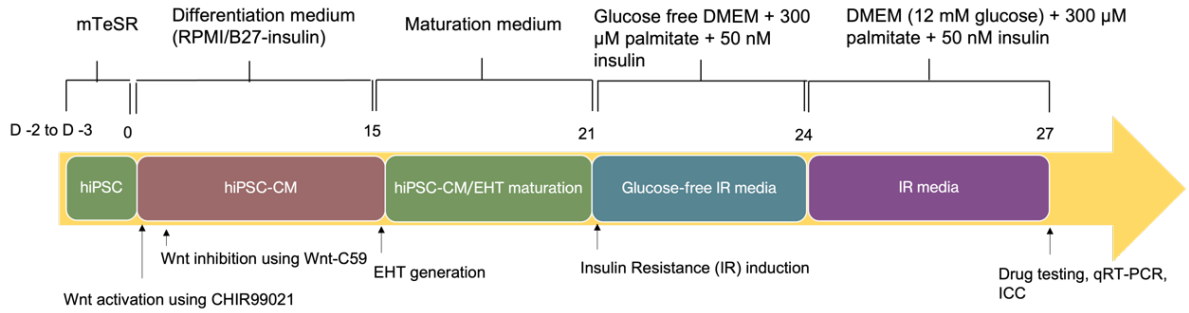


Figure 4.6 Schematic overview of the established protocol to induce insulin resistant

The IR media did not affect the viability of the cells after 7 days of induction. There was no obvious difference in the green stain of NucGreen in IR-media indicating that the established insulin resistance media did not affect the viability of the cell (**Figure 4.7**).

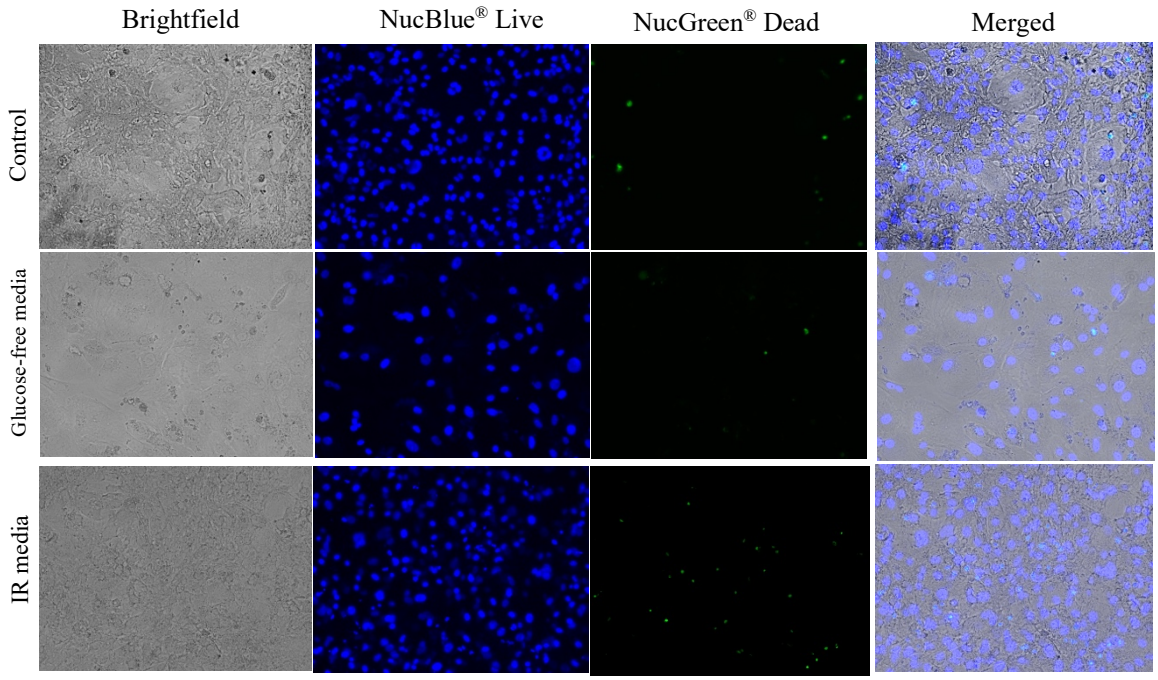


Figure 4.7 Human iPSC-CM in 2D monolayer cultured in the glucose-free media and insulin resistance media

Cell death staining on hiPSC-CMs after culturing in "IR media" which consisted of 3 days culturing in the glucose-free media (media containing no glucose, 300 µM PA, and 50 nM insulin) followed by insulin resistance media (media containing 12 mM glucose, 300 µM PA, and 50 nM insulin) for another 3 days.

4.5.3 Characterising the effect of insulin resistance on hiPSC-CM in 2D and EHTs

To test the insulin response of the hiPSC-CM in 2D monolayer towards insulin stimulation, the phosphorylation of the Akt, a key step in the insulin signalling cascade, was measured following insulin stimulation. In control cells, acute insulin stimulation increased phosphorylation of Akt (**Figure 4.8)**. In contrast, there was no significant difference in pAkt in IR cells with or without insulin exposure, suggesting that the cells had become unresponsive towards insulin stimulatio

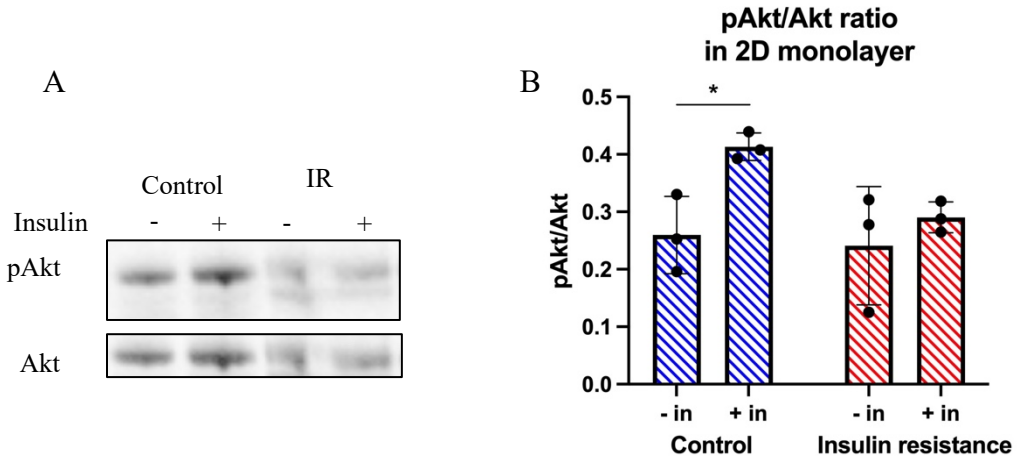


Figure 4.8 Insulin response testing using acute insulin stimulation assessment in control and IR hiPSC-CMS
Representative Western blot image for pAkt and Akt protein expression in hiPSC-CMs cultured in 2D monolayer with or without insulin (A), quantitative analysis of pAkt/Akt ratio (B), * P<0.05, using two-way ANOVA followed by Tukey's multiple comparison test, n=3.

The change in Akt phosphorylation was also assessed in EHTs following insulin stimulation, and a similar profile was found. Control EHTs displayed an increase in pAkt following insulin stimulation, which was absent in the IR media cultured EHTs (**Figure 4.9)**. Although IR hiPSC-CMs showed similar result in 2D monolayer and EHTs, the results were much more striking in the EHTs by looking at the blots. Moreover, total Akt expression in the EHTs were similar in all of the samples, whereas there was a drop in total Akt expression in IR hiPSC-CM in 2D monolayer.

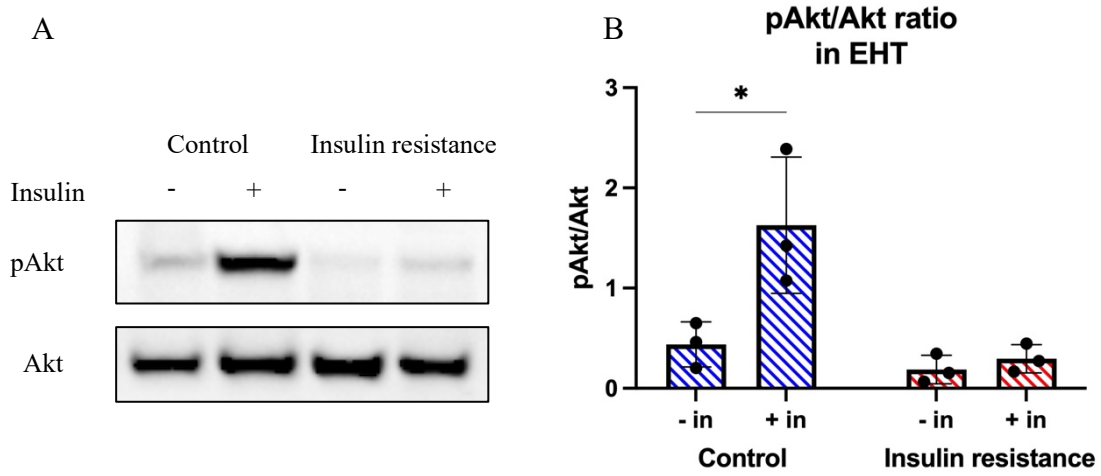


Figure 4.9 Insulin response testing using acute insulin stimulation assessment in EHT

Western blot image representative of pAkt and Akt protein expression in hiPSC-CMs cultured EHT with or without insulin (A), quantitative analysis of pAkt/Akt ratio (B), * P<0.05, using two-way ANOVA followed by Tukey's multiple comparison test (n=3).

It was previously described in chapter 3 that PA caused intracellular fat accumulation which might lead to the lipotoxicity. Oil red O staining of control and IR EHTs showed that there was a higher oil red O intensity in the insulin resistant EHT, confirming that there was a significantly higher fat accumulation in the cells as seen in **Figure 4.10**.

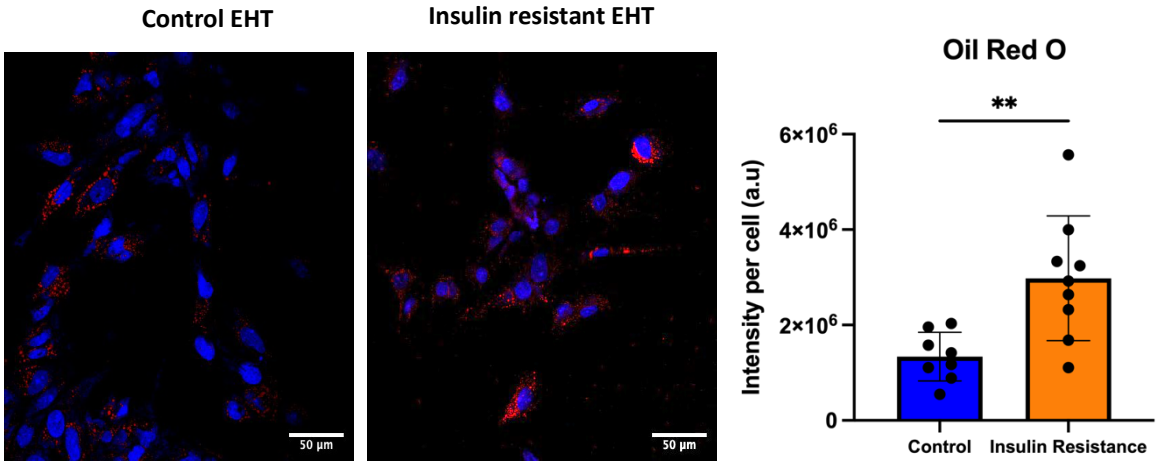


Figure 4.10 Fat accumulation assessment using oil red O

Control and insulin resistant EHTs were treated with oil red O to stain free fatty acid inside the cells. Data represent the mean ± SEM and statistical significance was assessed by t-test, with a ** $p < 0.01$, n=8.

4.5.4 Metabolic changes in hiPSC-CM in 2D monolayer and EHT using the IR media

Changes in metabolism are one of the major characteristics of the heart in T2DM. Therefore, I performed several experiments to assess metabolism in the insulin resistance model, including measuring lactate production and glucose consumption via enzymatic assays, and radiolabelled experiments to measure glycolysis and fatty acid oxidation in the cells.

I cultured the hiPSC-CMs in 2D monolayer in maturation media for 7 days followed by insulin resistance induction for 6 days (using the protocol detailed in **Figure 4.6**). At the end of day 6, I collected the control and IR media that had been bathing the cells for the previous 24 hours. The isolated media was then analysed for the glucose concentration and compared to the starting media of previous 24 hours. To gain a more detailed understanding of glucose metabolism in these cells, I performed radiolabelled measurements of glycolytic flux in the absence and presence of insulin.

In 2D monolayer hiPSC-CM, there was significantly lower glucose consumption in the IR hiPSC-CMs compared with controls over the period of 24 hours **(Figure 4.11A)**. There was a significantly higher glycolytic flux when culturing the control cells with insulin compared to control cells without insulin. However, this insulin-stimulated increase in glycolysis did not happen in insulin resistant cells, confirming an impaired response to insulin (**Figure 4.11B)**. Fatty acid oxidation rates were measured in the cells using ^{3}H-oleic acid. There was no significant difference in oleic acid oxidation between control and IR hiPSC-CM in 2D monolayer ($p < 0.0961$) when normalising the result to cell number. However, oleic acid oxidation was significantly higher in IR hiPSC-CMs compared to the control when normalised to protein concentration as seen in **Figure 4.11D**.

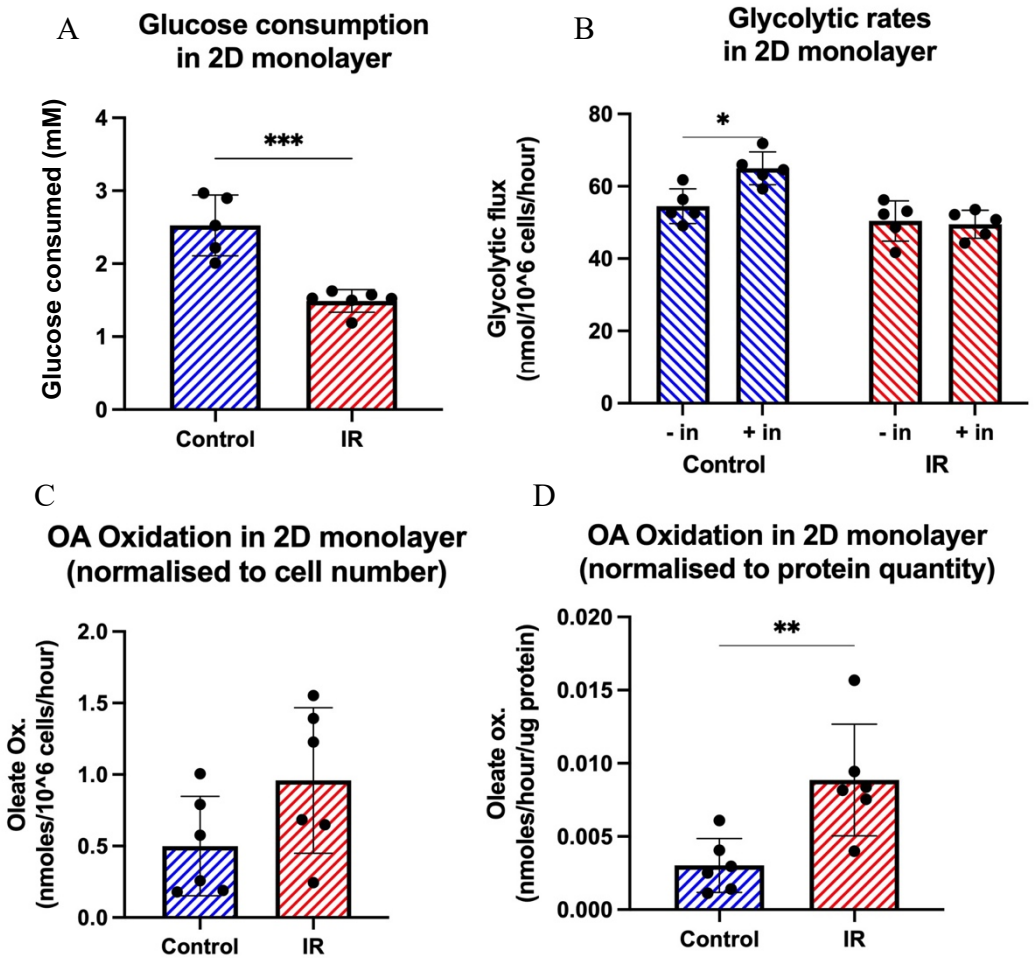


Figure 4.11 Metabolic flux in 2D monolayer measured using enzymatic and radiolabelled assay

Glucose consumption in the control vs IR hiPSC-CMs (per 1.5 million cells) measured by enzymatic assay after 24 hours (A), glycolytic flux in the control vs IR hiPSC-CMs with and without addition of insulin (B), oleic acid oxidation in the control vs IR hiPSC-CMs normalised to the total number of the cells (C) and to the total protein concentration (D). Data represent the mean ± SEM and statistical significance was assessed by t-test, with a *, **, *** $p < 0.05$, 0.01, 0.005 compared with control cells, n=6.

Substrate metabolism was also measured in the cells cultured in EHT. There was a significantly lower glucose consumption and lactate release in the IR EHT compared to control EHT, indicating that the IR EHT consumed less glucose during the period of incubation (**Figure 4.12 A-B**). Control EHTs had significantly higher glycolytic flux when cultured with insulin compared with the absence of insulin (**Figure 4.12 C**), confirming that the EHTs were responsive to insulin stimulation. Although, the increase was not doubled as normally observed in insulin adult heart. In contrast, there was no significant difference in the glycolytic flux in the IR EHT after addition of insulin (**Figure 4.12 C**). Moreover, IR EHT had significantly lower insulin-stimulated glycolytic flux compared with control EHT.

This was accompanied by significantly higher oleic acid oxidation rates in IR EHT compared with control EHT (**Figure 4.12 D**). As seen before, the EHT had relatively lower glycolytic flux and higher oleic acid oxidation compared to 2D monolayer both in control and insulin resistance condition (**Figure 4.13**).

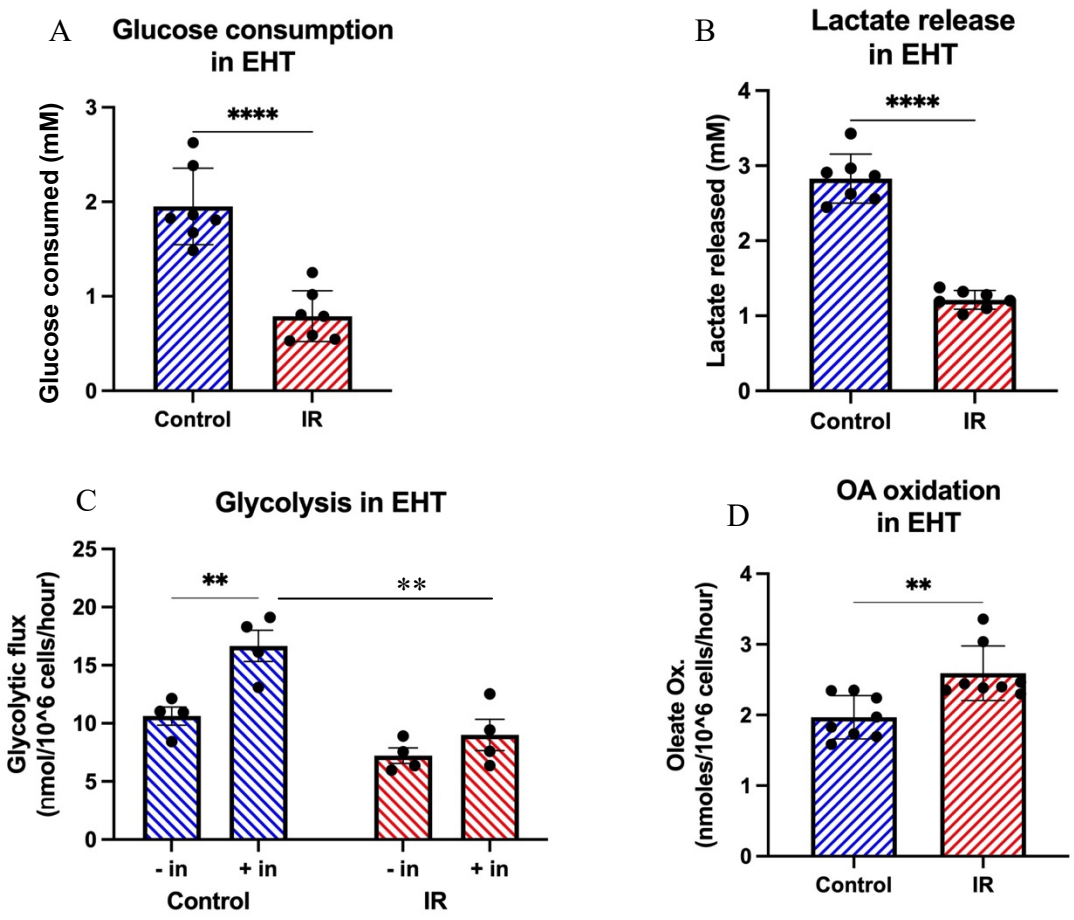


Figure 4.12 Metabolic flux in EHT measured using enzymatic and radiolabelled assay

Glucose consumption (A) and lactate release (B) in the control vs IR EHT (1.5 million cells) measured by enzymatic assay after 24 hours, glycolytic flux in the control vs IR EHT with and without addition of insulin (C), oleic acid oxidation in the control vs IR normalised to the total cell number (D). Data represent the mean ± SEM and statistical significance was assessed by t-test for A, B, D and two-way ANOVA followed by Tukey's multiple comparison test for C with a **, **** $p < 0.01$, 0.001 compared to control cells, n=4-8.

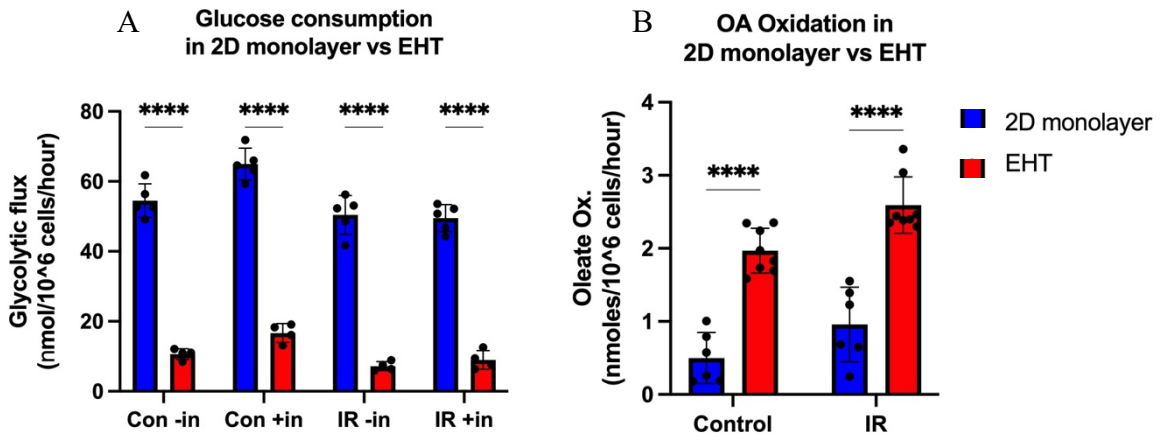


Figure 4.13 Metabolic Flux in 2D monolayer versus EHT measured using radiolabelled assay
Glucose consumption (A) and oleic acid oxidation (B) in the control vs IR normalised to the total cell number. Data represent the mean ± SEM and statistical significance was assessed by two-way ANOVA followed by Tukey's multiple comparison test with **** $p < 0.001$ compared to control cells, n=4-8.

4.5.5 Assessing the effect of insulin resistance in 2D and EHT during hypoxia

Hypoxia is a key component of myocardial ischemia; therefore, I investigated the response to hypoxia in insulin resistant hiPSC-CM in 2D monolayer. Human iPSC-CMs were replated into 24-well plates (750.000 cells/plate) after 15 days of differentiation. The cells were then cultured in maturation media for 2 weeks before exposure to the IR protocol in **Figure 4.6** for 6 days. At the end of insulin resistance induction, the healthy (control) and IR cells were cultured in either normoxia (5% CO_2, 16% O_2) or hypoxia (5% CO_2, 2% O_2) for 16 hours. The total RNA and protein were harvested for gene expression analysis using qPCR or protein expression analysis using Western blot.

Exposure of control hiPSC-CM in 2D monolayer to hypoxia stabilised HIF1α protein (**Figure 4.14 J-K**) and induced transcription of downstream HIF target genes including bcl2/adenovirus E1B 19kDa-interacting protein 3 (BNIP3), GLUT1, adolase A, and prolyl hydroxylase 2 (PHD2) (**Figure 4.14 A-B, D-E**). Hypoxia reduced expression of the factor

inhibiting HIF (FIH), HIF1α mRNA, and fatty acid regulatory transcription factor PPARα in control hiPSC-CM (**Figure 4.14 F, G, and I**). In contrast, when insulin-resistant hiPSC-CMs in 2D monolayer were exposed to the same hypoxic challenge, stabilization of HIF1α protein and induction of downstream gene targets were suppressed, demonstrating a blunted adaptive response to hypoxia in insulin resistance (**Figure 4.14 A-D**). In insulin resistant cells, hypoxia induced a significant reduction in expression of PHD2 and PGC1α, but not PPARα (**Figure 4.14 E, H, and I).**

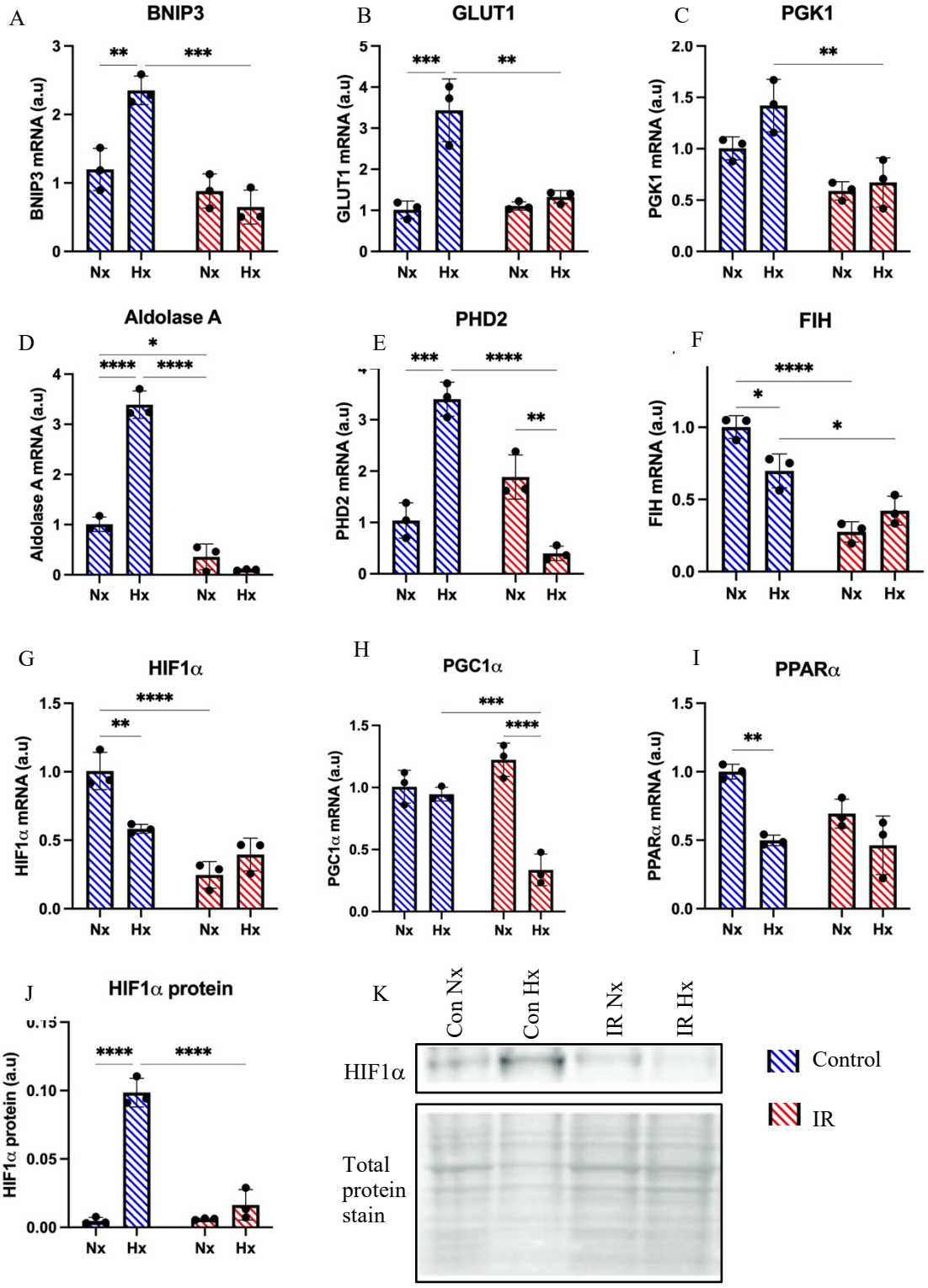


Figure 4.14 Gene and protein expression in control and IR hiPSC-CM in 2D monolayer and EHT under normoxic and hypoxic condition

Expression of HIF1α target genes in control and IR hiPSC-CM under normoxia (Nx) or hypoxia (Hx), including bcl2/adenovirus E1B 19kDa-interacting protein 3 (BNIP3), GLUT1, phosphoglycerate kinase 1 (PGK1), aldolase A, prolyl hydroxylase domain (PHD)2, factor inhibiting HIF (FIH), and HIF1α (**A-G**), expression of mitochondrial related target gene including PGC1α and PPARα (**H-I**), and expression of HIF1α protein (**J-K**). Data represent the mean ± SEM and statistical significance was assessed by two-way ANOVA test, with a *, **, ***, **** p < 0.05, 0.01, 0.005, 0.001, n=3.

Unlike the 2D monolayer, EHT is about 2 mm thick, so there was a concern that oxygen may not diffuse as efficiently through the full thickness. Therefore, I performed immunohistochemistry for HIF1α protein, using EHT kept under normoxia or hypoxia for 16 hours (2% oxygen). There was more HIF1α protein surrounding the nucleus of the cells at the core of EHTs grown under hypoxia indicating that EHTs are responsive towards hypoxic stimulation. In contrast, the EHTs grown under normoxia had little or no HIF1α protein in the cells from the core of the tissue, indicating that the oxygen was able to diffuse to the core of EHTs (**Figure 4.15**).

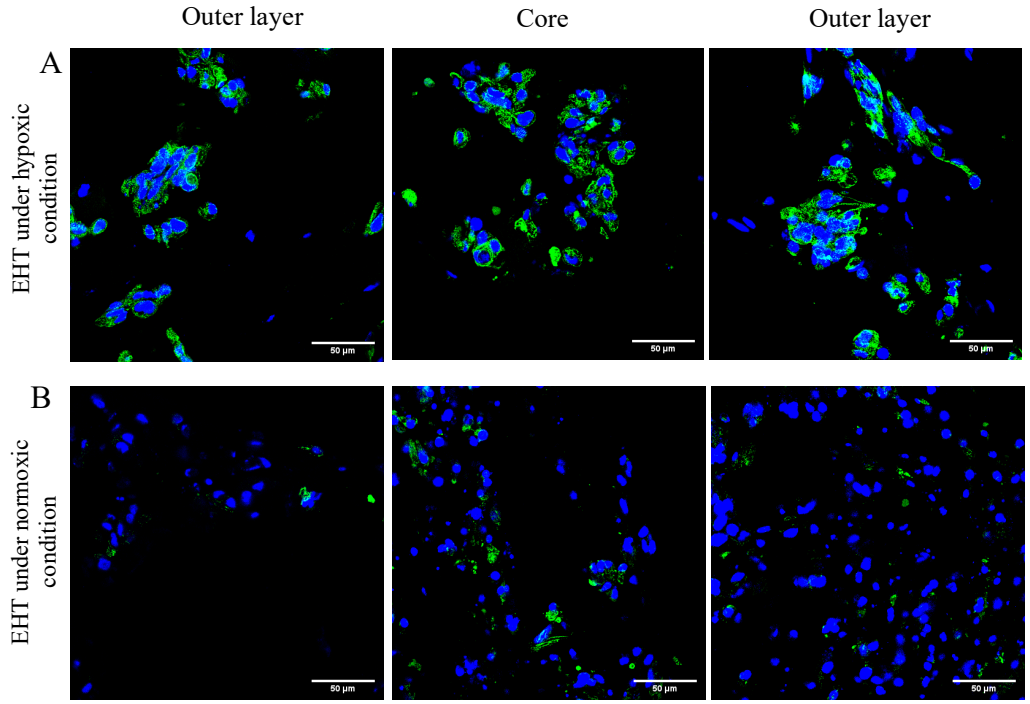


Figure 4.15 Immunohistochemistry of EHTs shown HIF1α protein in the cells under normoxic and hypoxic condition

EHTs were cultured under hypoxia (2% Oxygen) and showed high levels of HIF1α protein (A) whilst EHTs cultured under normoxia (16% oxygen) showed low HIF1α protein expression (B). HIFα (green) and DAPI (blue).

It has previously been shown that insulin resistance affects blunted HIF1α stabilisation in the cardiomyocytes and hiPSC-CM in 2D monolayer. Therefore, I examined HIF1α stabilisation in the insulin resistant EHTs under hypoxia and observed that the insulin resistant EHTs had reduced HIF1α protein compared with control EHTs (**Figure 4.16**).

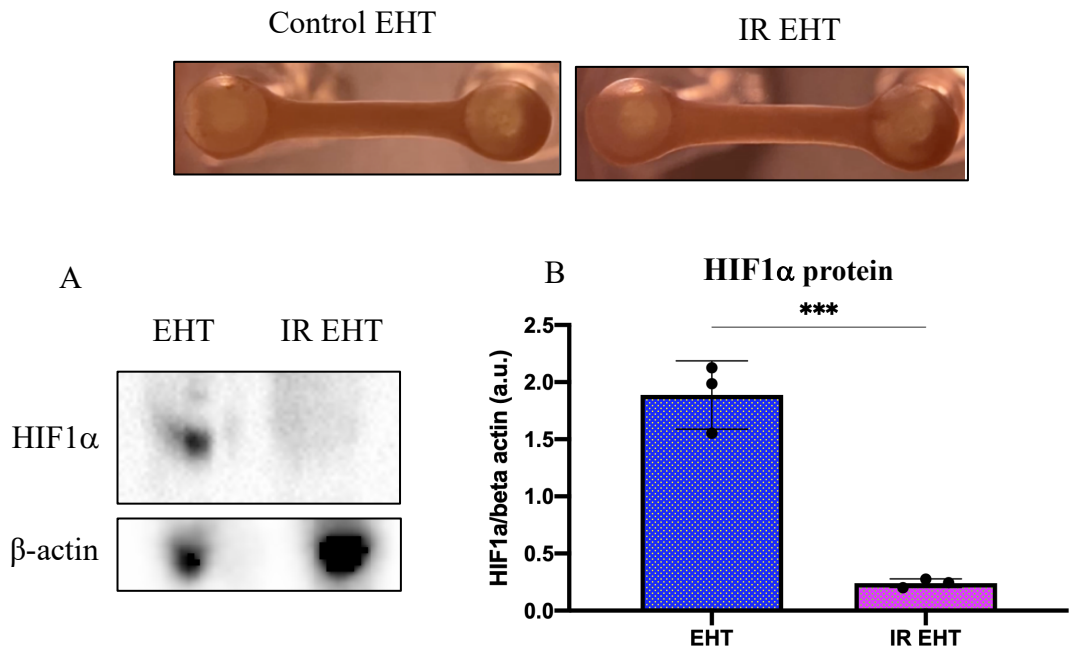


Figure 4.16 HIF1α protein expression in control and IR EHT under hypoxia

Western blot showed HIF1α and β -actin expression on control and IR EHT under hypoxia (A) and protein quantification of HIF1α protein normalised to β-actin as housekeeping protein under hypoxia (B). Data represent the mean ± SEM and statistical significance was assessed by t-test with a *** $p < 0.005$, n=3.

4.5.6 Assessing the effect of insulin resistance on subcellular structure of hiPSC-CM in 2D and EHTs using Transmission electron microscopy

To explore the difference between cells in 2D monolayer or EHT that had not been exposed to maturation media (control), those that had been exposed to maturation media for 7 days (mature) and those that had been exposed to the IR protocol (IR) at the organelle level, transmission electron microscopy (TEM) was used, and then qualitative and quantitative analysis was performed. I cultured the cells for these experiments which were performed and analysed by master's student, Kirsti Brisk, and imaging was performed at the Dunn School of Pathology as described in chapter 3. The induction of insulin resistance had effects at the organelle level both in 2D monolayer and EHT. Qualitatively, mitochondria number was seen to increase in mature 2D monolayer compared to control 2D monolayer (**Figure 4.17**). However, the mitochondria were seen more fragmented in insulin resistance 2D

monolayer. A similar pattern also observed in EHT but with more mitochondria observed in EHT compared to 2D monolayer.

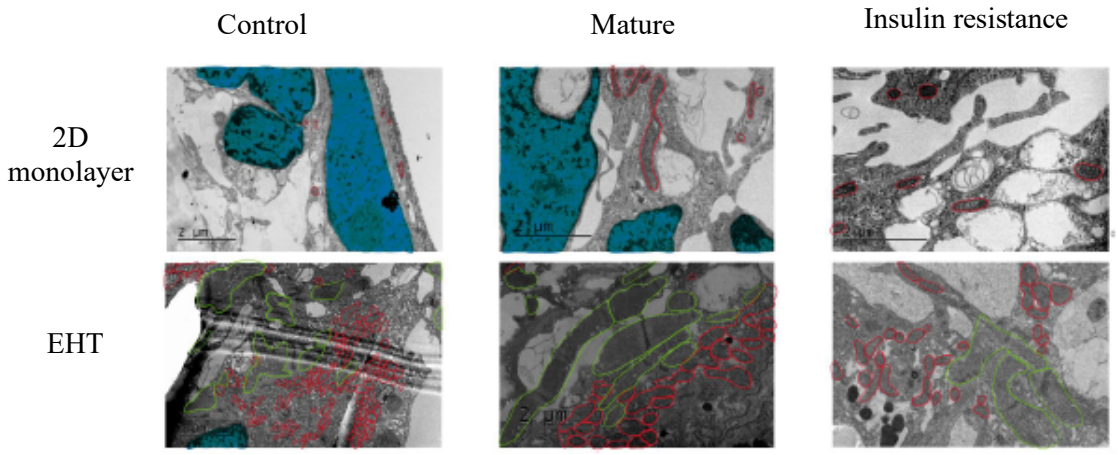


Figure 4.17 Representative Transmission electron microscopy (TEM) images of hiPSC-CMs in 2D and EHT exposed to control and IR media

Control and insulin resistant 2D hiPSC-CMs and EHTs were imaged using transmission electron microscopy (TEM), nuclei in blue, mitochondria in red and muscle in green.

Average muscle area was significantly increased as the EHT exposed to maturation media and the muscle appeared structurally more mature. Interestingly, there was decrease in average muscle area in the IR EHT compared to mature EHT (**Figure 4.18**), suggesting that there was an adverse effect on muscle size of inducing insulin resistance in the cells. This was not seen in the 2D monolayer cells as they did not show any muscle area.

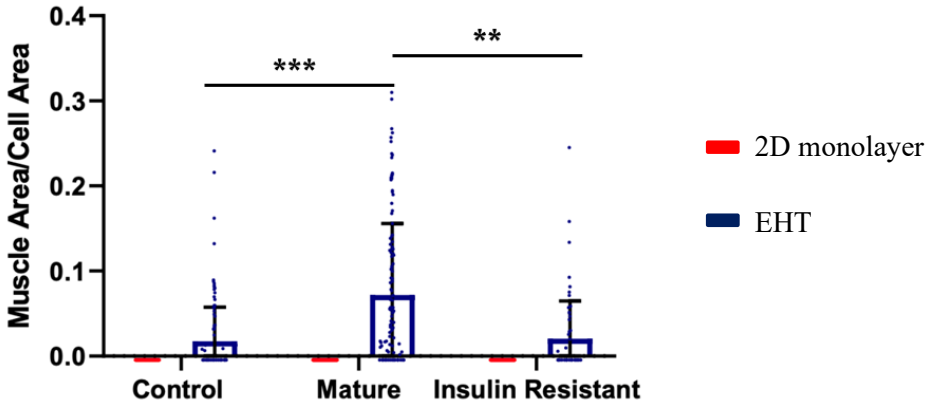


Figure 4.18 Quantification of muscle area of hiPSC-CMs in 2D and EHT exposed to control and IR media using Transmission Electron Microscopy (TEM)

Control and insulin resistant 2D hiPSC-CMs and EHTs were imaged using TEM and muscle area was measured by delineating areas of striation. Statistical analysis was performed by Kirsti Brisk using R studio, ** $p < 0.01$, *** $p < 0.001$ in an estimated marginal means pairwise equality test with a Tukey P-value adjustment.

4.5.7 Assessing the effect of insulin resistance on contractility using Musclemotion

The effect of insulin resistance on the cell contractility in 2D monolayer and EHT was quantified using Musclemotion at days 3 and 6 of induction **(Figure 4.19)**.

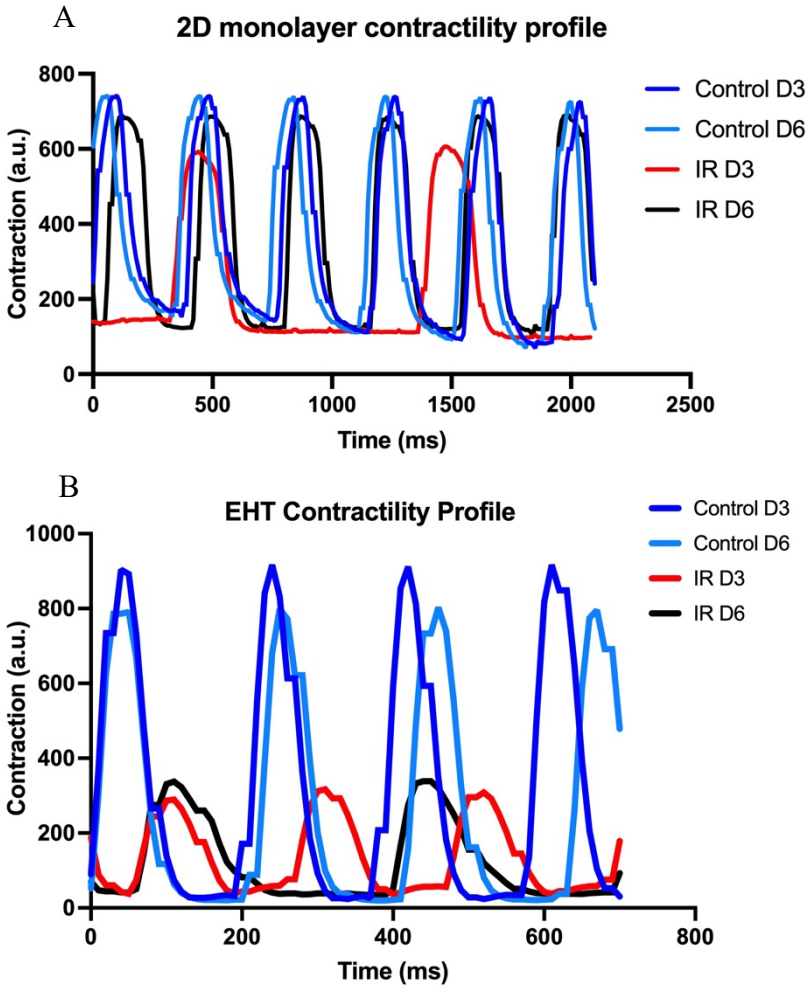


Figure 4.19 Contractility profile of the hiPSC-CMs in 2D monolayer and EHT

Representative images of the contraction of the hiPSC-CMs in 2D monolayer and EHT cultured in control maturation media and IR media. The videos were taken and analysed using Musclemotion software.

The insulin-resistant hiPSC-CMs in 2D monolayer had longer contraction duration and peak to peak time **(Figure 4.20)** at 3 days after exposure to the IR media. However, by day 6 of exposure these parameters had returned to control values, suggesting that the cells had adapted to the IR media.

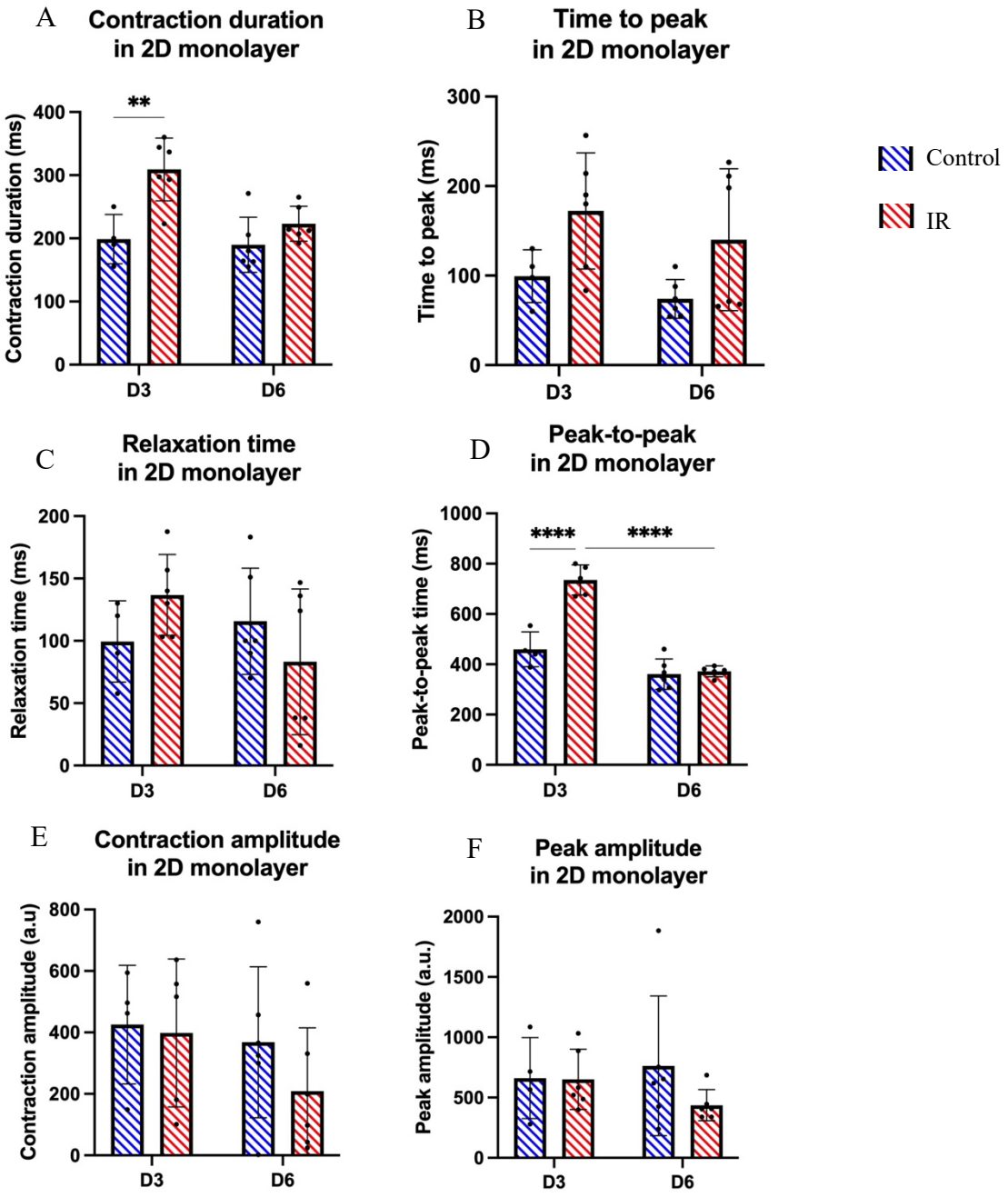


Figure 4.20 Contraction parameters of hiPSC-CMs in 2D monolayer determined by Musclemotion

Contraction parameters including contraction duration (A), time to peak (B), relaxation time (C), peak-to-peak time (D), contraction amplitude (E), and peak amplitude (F) of hiPSC-CMs in 2D monolayer cultured with control maturation media and insulin resistance media. The videos were taken on D3 and D6 of incubation. Data represent the mean ± SEM and statistical significance was assessed by two-way ANOVA followed by Tukey's multiple comparison test with a *, **** $p < 0.05, 0.001$ compared with hiPSC-CMs cultured in control maturation media; ns = non-significant

When muscle motion was used to assess changes in contractility in the EHT, the insulin resistant EHT showed a significantly increased contraction duration, relaxation time and peak-to peak time **(Figure 4.21)**. In contrast to the cells grown in 2D, in the insulin resistant

EHT, the relaxation time returned to control values by day 6, but the increase in contraction duration was maintained at day 6, whilst there was a further increase in peak-to peak time compared with the measurement at day 3.

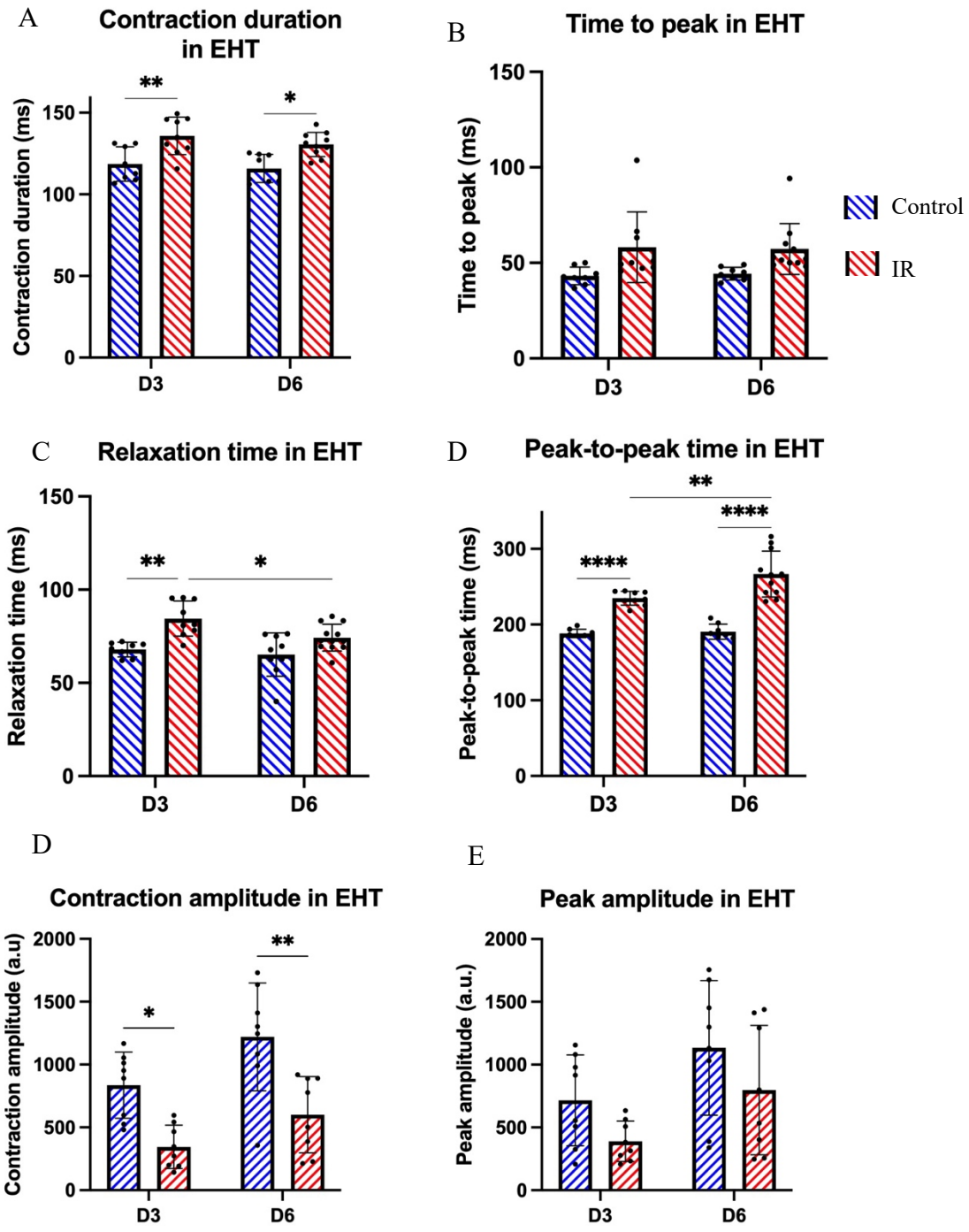


Figure 4.21 Contraction parameters of hiPSC-CMs in EHT determined by Musclemotion

Contraction parameter including contraction duration (A), time to peak (C), relaxation time (C), peak-to-peak time (D), contraction amplitude (E), and peak amplitude (F) of hiPSC-CMs in EHT cultured with control maturation media and IR media. The videos were taken on D3 and D6 of incubation. Data represent the mean ± SEM and statistical significance was assessed by two-way ANOVA followed by Tukey's multiple comparison test with a **, **** $p < 0.01$, 0.001 compared with EHT cultured in control maturation media (n= 8).

4.5.8 Assessing the effect of insulin resistance on the inflammatory cytokines

To investigate the effect of insulin resistance on the immune response of cardiomyocytes, I performed qPCR analysis to determine the expression of IL-6 and IL-1β in control and IR EHT cultured under normoxia or hypoxia **(Figure 4.22)**. There was a significant decrease in expression of IL-6 in IR EHT when cultured in normoxia compared with controls. However, the expression of IL-6 was significantly higher in IR EHT compared with control when cultured under hypoxia. IL-1β expression did not significantly change between groups. The data showed that IL-6 is affected by insulin resistance in hiPSC-CM. However, more cytokines are required to assess to draw clear conclusion.

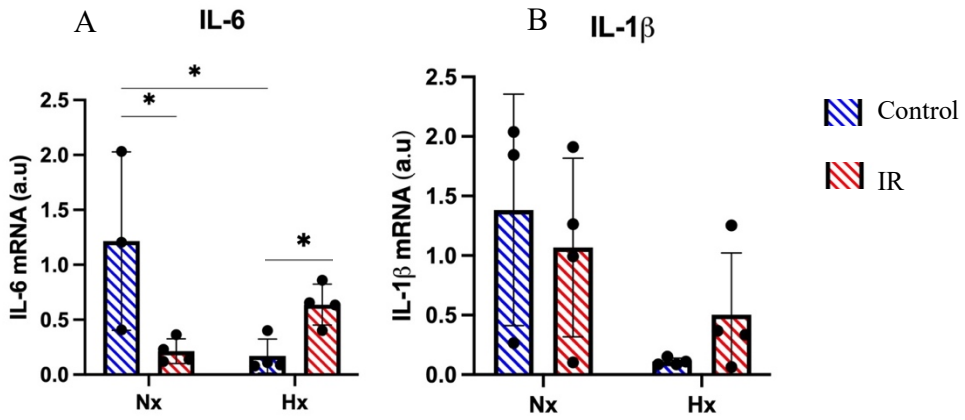


Figure 4.22 Inflammatory cytokines gene expression using qPCR

The expression of inflammatory cytokines genes IL-6 (A) and IL-1β (B). Data represent the mean ± SEM and statistical significance was assessed by two-way ANOVA followed by Tukey's multiple comparison test, with a * $p < 0.05$ n=3-4.

4.5.9 Assessing protein and gene expression using proteomic and transcriptomic analysis

Proteomic and transcriptomic analysis were performed to gain a more global understanding of the effect of insulin resistance on EHT. The data was analysed by DPhil student, Ryan Carter from Prof. Lisa Heather's Group. As the generation of the data by Novo Nordisk was delayed by the pandemic, Ryan has only been able to undertake a preliminary analysis so far.

Differential enrichment analysis of proteomic data (DEP) showed that there were differences in several metabolic proteins in IR EHT compared with control EHT. Unbiased analysis flagged up three key metabolic protein: subunit of NADH dehydrogenase – complex 1 (A0A024R6G6 or NDUFB1) and NAD-dependent deacetylase located in the mitochondrial matrix (E9PM75 or SIRT3) were upregulated in control EHT and downregulated in IR EHT, whereas cytochrome c oxidase 1 – complex 1 (A0A059QX78 or COX1) was downregulated in control EHT and upregulated in IR EHT (**Figure 4.23**).

RNA-sequencing data with DESeq2 showed a marked differences between control and IR EHT, and there were more genes downregulated in IR EHT than upregulated (**Figure 4.24A**). Further downstream analysis using fast preranked gene set enrichment analysis (FGSEA) revealed that genes involved in the PI3K/Akt/mTOR pathway were downregulated in IR EHT, supporting the argument that the IR EHTs are insulin resistant (**Figure 4.24 B**). The leading-edge subset in the gene enrichment analysis (GSEA) showed that most of the genes in the PI3K/Akt/mTOR pathway were downregulated compared to control (**Figure 4.24 C and D**)

KEGG pathway analysis of differentially expressed genes and proteins showed that the transcriptomics and proteomics did not always agree. For example, the expression of genes involving in insulin signalling pathway showed a marked downregulation in IR EHT compared to control EHT. However, the distinction was less clear in the proteomic data (**Figure 4.25**).

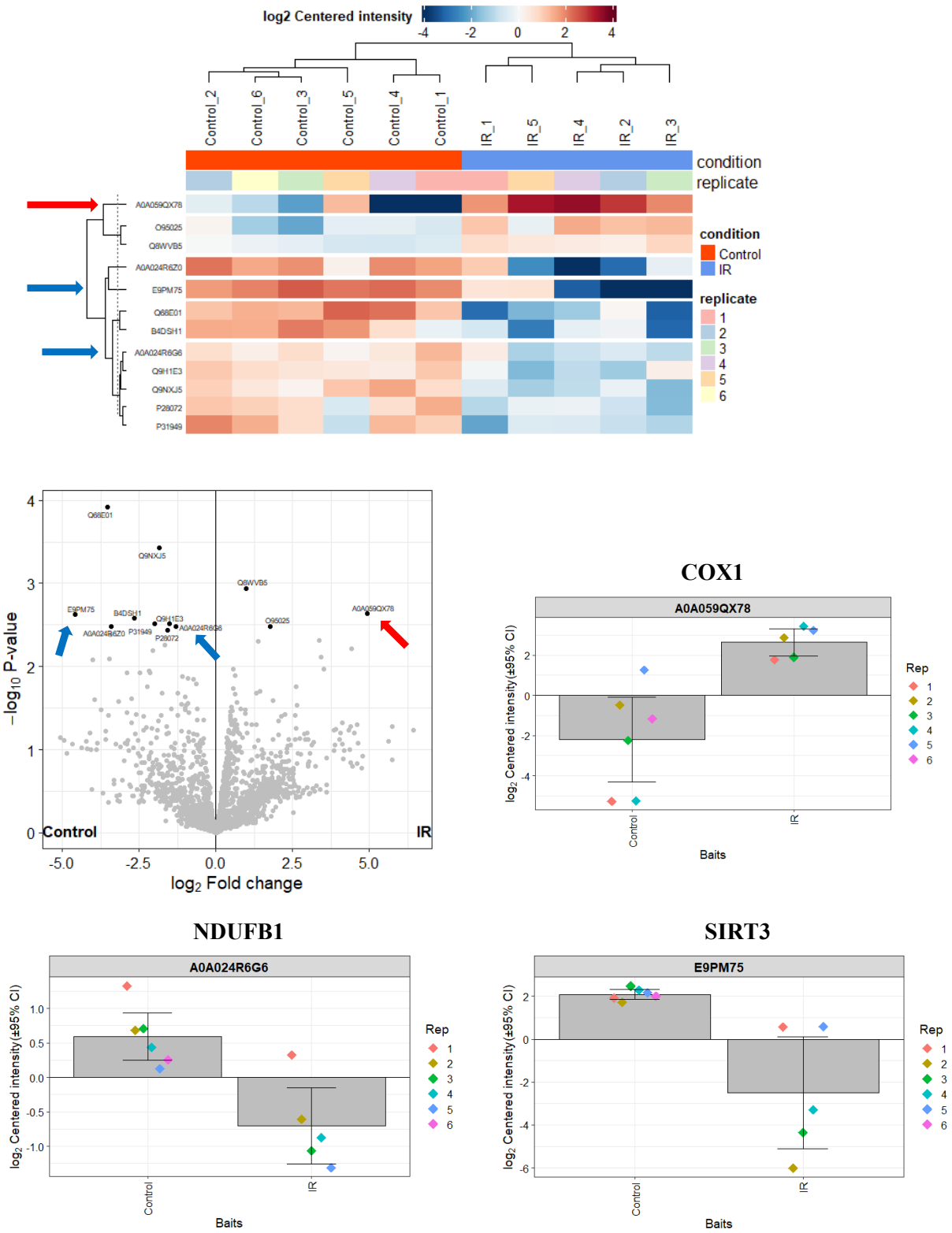


Figure 4.23 Key protein changes in control and IR EHT analysed by differential enrichment of proteomic data (DEP)

Analysis of the proteomic data using DEP included three key metabolic proteins amongst those showing significant differences in expression. Red arrow showed cytochrome c oxidase 1 – complex 1 (accession number: A0A059QX78 or COX1) and blue arrows showed NADH dehydrogenase – complex 1 (accession number A0A024R6G6 or NDUFB1) and NAD-dependent deacetylase located in the mitochondrial matrix (accession number E9PM75 or SIRT3).

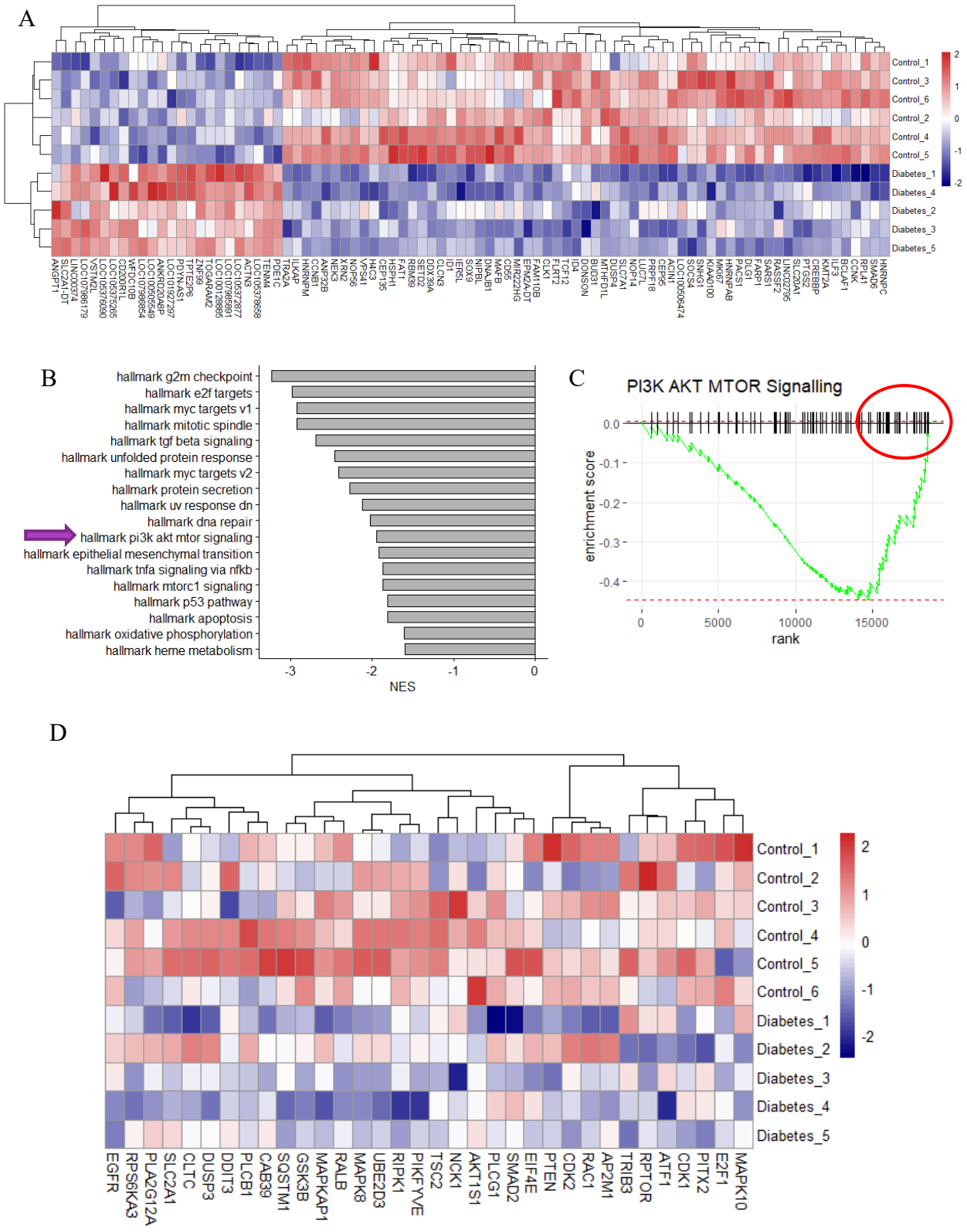


Figure 4.24 Gene expression changes in control and IR EHT from RNA-seq data analysed with DESeq2 and fast preranked gene set enrichment analysis (FPGSEA)

Analysis of RNA-seq data showed changes in gene expression between control and IR EHT for a wide range of genes (A), pathway analysis (B) with changes in PI3K-Akt-mTOR signalling shown in more detail (C, D).

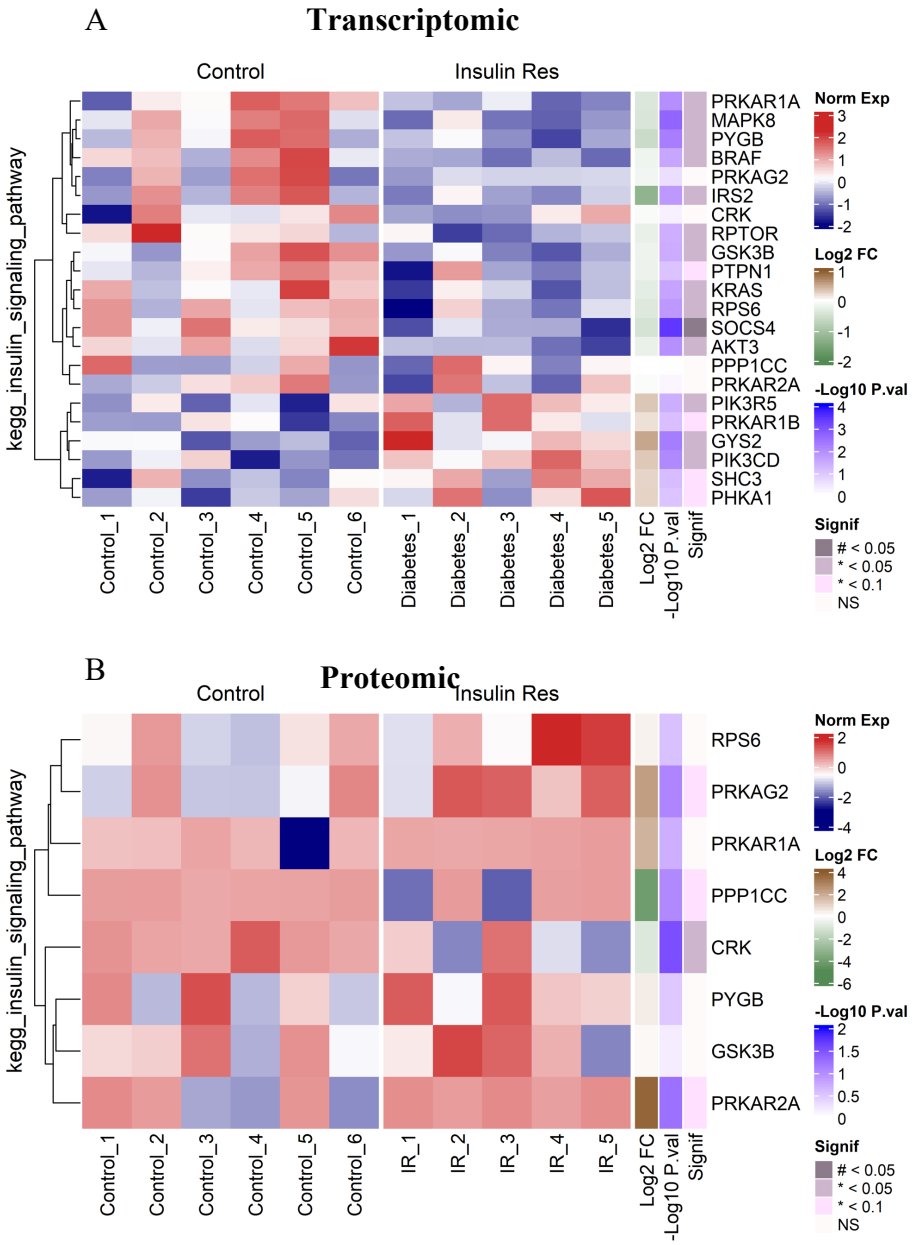


Figure 4.25 Transcriptomic and proteomic analysis of the insulin signalling pathway

The differential expression of genes (A) and proteins (B) involved in the insulin signalling pathway, identified using transcriptomics and proteomics, respectively.

4.6 Discussion

Diabetes involves a chronic pathogenic process which is influenced by high circulating fatty acids and glucose. The palmitate (PA) concentration in the plasma of patients with diabetes is 1.5-fold higher than that in healthy patients, at around 300 – 500 μM[295–297]. In addition, patients with type II diabetes often have a high level of insulin in their blood due to the overproduction of insulin by the β-cells in order to compensate for the insulin resistance[298]. It is important that diabetes-related pathogenic factors in a cellular model should mimic this change in circulating metabolites, should not be cytotoxic in a significant or acute manner, but rather should cause chronic oxidative stress and cell hypertrophy, tissue fibrosis, inflammatory responses, and eventually cardiac dysfunction[281].

Palmitate (PA) has been shown to cause inflammation, ceramide accumulation, mitochondrial dysfunction and eventually insulin resistance[294], many facets found in the diabetic heart. However, the cytotoxic effect of PA can be detrimental for the cells causing apoptosis before a study can be performed. Therefore, creating a formula to induce insulin resistance while maintaining cell viability in hiPSC-CMs was key towards successful disease modelling. Although previous experiments on insulin resistant cardiomyocytes have been performed in cell lines[294,299,300], to our knowledge there are no published studies using hiPSC-CMs in EHTs. I first determined the optimum dose of PA to create a relevant in vitro model in both 2D and 3D, which could be cultured for multiple days to allow for intervention studies post-insulin resistance induction. PA at 500 μM decreased the viability of the cells after 24 hours, making this concentration unsuitable for studying more chronic effects or insulin resistance.

Prolonging the PA treatment while reducing its concentration was shown to increase the viability in 2D monolayer. Data from both cell viability assays and Musclemotion showed that 300 μM PA caused an initial adverse reaction in CMs for the first 24 hours, after which

the cells stabilised. To further optimise the protocol to induce insulin resistance, I added a step comprising incubating the cells with glucose-free media containing 300 μM PA and 50 nM insulin for three days to ensure that the cells could only use PA and with the hope that this would induce a more profound metabolic switch. After three days of incubation, I changed to the diabetic milieu found in diabetic patients comprising hyperlipidaemia, hyperglycaemia, and hyperinsulinemia by adding 12 mM glucose. This established protocol successfully maintained the cell viability over 6 days in 2D monolayers and could also be used for EHTs.

It has been shown that at the molecular level in insulin-resistant cells, there is an impairment in the IR/IRS-PI3K-Akt pathway which is responsible for the suppressed insulin-induced glucose uptake in insulin-sensitive organs such as the heart[301,302]. Through the acute insulin stimulation experiment, I showed that Akt phosphorylation was blunted in IR 2D monolayer hiPSC-CM and EHT. This impairment likely led to decreased GLUT4 translocation, causing the reduced glucose consumption and glycolytic flux in the cells. In a mouse model of diabetes, an increase in circulating lipids and concomitant increase in fatty acid metabolism has been seen before the presence of hyperglycaemia[303], suggesting that, at the onset of T2DM, lipotoxicity is of greater concern than glucotoxicity. The early effects of lipotoxicity result in symptoms of diastolic dysfunction and impaired response to cardiac stress[304]. Here I showed that there was a significantly higher oleic acid (OA) oxidation in IR hiPSC-CMs in 2D monolayer and EHT but also increased lipid accumulation in IR EHT when assessed using Oil Red O, matching that seen in rodent models. Hence, exposing the hiPSC-CMs, especially EHTs, to the insulin resistance media containing hyperlypidaemia, hyperglycemia, and hyperinsulinemia has successfully altered the metabolism, providing a good model to study the metabolism of the diabetic heart.

Diabetic cardiomyopathy is one of the leading causes of mortality in patients with diabetes, and their prognosis is poor in the event of a myocardial infarction or heart failure[305–307]. Heart metabolism becomes inflexible and HIF1α signalling is not properly activated during ischemia[308]. Our group has shown previously that the diabetic heart has an abnormal response during ischemia or hypoxia. The increasing amount of fatty acid in diabetes suppressed succinate accumulation during hypoxia which led to an inhibitory effect on HIF1α stabilization [256]. However, these experiments were performed using a mouse cell line or animal models. Hence, to confirm this finding in human cells and demonstrate the translation to the human disease, I explored the response to hypoxia in insulin resistant hiPSC-CM in 2D monolayer and EHT. Here I demonstrated impaired HIF stabilization and hypoxic signaling in the human insulin resistant iPSC-CM in 2D and 3D culture.

To further explore the ability of hiPSC-CMs in 2D monolayer and EHT to model diabetic cardiomyopathy profile of hiPSC-CMs over time, I used Musclemotion to measure the contractility profile of hiPSC-CMs in 2D monolayer and EHT over time. In this experiment different profiles of contractility were seen between the IR cells in 2D vs in the 3D EHT. The 2D insulin resistant cells demonstrated impaired contractility at day 3 but recovered by day 6. In contrast the insulin resistant EHTs remained dysfunctional through to day 6. The different profile can be explained by the different maturation stage of hiPSC-CM in 2D and EHTs. As the hiPSC-CMs in 2D monolayer use more glucose for energy generation, the switch to glucose-free media is likely to affect them more substantially than the more mature EHT. When they are exposed to a high concentration of glucose on day 4 to 6, they start to utilise glucose again and this results in a restoration of contractility to the basal state. The more long-term changes in the contractility of the EHT are supported by the decrease in muscle size seen in the EM images.

Differential enrichment of proteomic data (DEP) flagged up large changes in three key metabolic proteins. Levels of complex I and SIRT3 were significantly lower in the IR EHT, as has also been seen in the diabetic heart from animal modelss[309–311]. SIRT3 deficiency was shown to accelerate the development of metabolic syndrome[311] and targeting SIRT3 by pharmacological approaches to decrease the hyperacetylation has been shown to rescue the myocardial energetic dysfunction in diabetic heart[309]. Complex I is critical for electron transport chain activity at the start of the chain, accepting electrons from NADH, thus a decrease in NDUFB1 protein would limit production of the membrane potential. In contrast, COX1 was seen to increase in our proteomic data which supported the previous finding that COX1 is increased in diabetes patients[312,313]. Thus, the proteomic analysis provided further validation of our IR EHT, recapitulating changes seen in diabetic animal models and patients.

RNA-seq data showed a number of genes that were downregulated in IR compared to control EHT. Further gene set enrichment analysis showed that PI3K/Akt/mTOR signalling pathway was downregulated in IR EHT. This data confirmed previous findings in animal models where transcriptomics showed that hyperglycemia or diabetes in maternal rodents induced changes in developing hearts of the pups, including changes in PPAR, PGC1α, HIF1α, PI3K/Akt/mTOR and gene-sets that are related to calcium signalling, contraction pathways, oxidative phosphorylation, and glycolysis [314,315]. Other transcriptomic analysis in the heart of diabetic animal models showed alteration in structural genes (e.g., MYH6, TNNT2) and metabolic genes (e.g., GLUT1 and GLUT4)[316,317]. Overall, this data suggests the validity of IR EHT providing insulin resistance in the heart model. Evaluation of insulin pathway elements and phosphoproteomic could be useful as several technics has been shown by others to be useful to elucidate robust data beyond qPCR analysis[318–320].

4.7 Conclusion

I have shown that treatment of hiPSC-CMs with media containing increased lipid, glucose, and insulin induces insulin resistance in hiPSC-CMs in 2D monolayer and EHT, without causing significant cell death. The insulin resistance media successfully induced molecular and functional changes in the cells mimicking the insulin resistant condition in the heart. The changes include a metabolic shift towards more fatty acid oxidation, mitochondrial dysfunction, change in gene expression, and lipid accumulation. Insulin-resistant hiPSC-CMs in 2D monolayer showed a similar phenotype to that of the IR-EHT, except in several parameters of contractility. Transcriptomic and proteomic analysis revealed that the insulin resistant EHT showed some expected changes in gene expression and protein level.

5

Drug testing on healthy and insulin resistant human induced-pluripotent stem cell derived cardiomyocytes in 2D and EHT

CHAPTER 5

5 DRUG TESTING ON HEALTHY AND INSULIN RESISTANT HUMAN INDUCED PLURIPOTENT STEM CELL DERIVED CARDIOMYOCYTES IN 2D AND EHT

5.1 Abstract

Drug development faces many challenges such as unknown disease pathologies, inadequate models, human complexity, and patient heterogeneity. These contribute to a costly process that burdens both researchers and patients. Since cardiovascular disease is a leading cause of death, we urgently need to improve predictivity of preclinical models and clinical translatability. Human induced-pluripotent stem cell-derived cardiomyocytes have potential as a valuable predictive tool to speed up the drug discovery process and improve candidate drug success in clinical trials. Here, I aimed to utilise the diabetic heart model described in chapter 4 to investigate the response to a selection of drugs thought to have a beneficial effect in the diabetic heart. I treated control and insulin resistant cells in 2D and EHT with metformin and perhexiline, which increased insulin response and increased glucose consumption and lactate production. I also treated IR hiPSC-CM with molidustat (BAY85-3934), a prolyl hydroxylase domain (PHD) inhibitor, to rescue the impaired response to hypoxia. I found that molidustat can stabilise hypoxia-inducible factor (HIF) 1α signalling in hiPSC-CMs and increase glycolysis. The results show that insulin resistant hiPSC-CM can be a valuable predictive tool which may speed up the drug discovery process and improve candidate drug success in clinical trials.

5.2 Introduction

The immaturity of hiPSC-CMs limits their potential for drug testing, with concerns raised by their aberrant response towards α-adrenergic stimulation suggesting they may not respond appropriately towards cardiotoxic drugs[232]. Moreover, it has been reported that immature hiPSC-CMs do not exhibit insulin-stimulated glucose uptake caused by low expression of GLUT4 which limits the study of the drugs for metabolism related diseases such as diabetic cardiomyopathy[140]. Therefore, a matured human cell model that responds to metabolic challenges and therapy is needed.

There are many pharmacological treatments that can potentially be used to treat insulin resistance in the heart by modulating metabolism. Current therapies that increase insulin sensitivity, such as metformin, are beneficial for cardiovascular outcomes[321]. However, their mechanism of action is still unknown. New therapies in the developmental pipeline have been proposed that inhibit fatty acid oxidation and promote glucose metabolism in the heart, such as perhexiline, however, these are not approved for use in Europe or the US. In addition to improving insulin sensitivity, treatment is needed to improve cardiac function during ischaemia in the insulin resistant heart, for example using hypoxia inducible factor (HIF) stabilisers (e.g., molidustat). The current challenge is that drug development is a costly and time-consuming process due to poorly characterised disease pathologies, inadequate models, human complexity, and patient heterogeneity[322–325].

Investigation of the mode of action of these drugs has largely been performed using animal models and rarely have these studies used human cardiac cells[325–327]. Therefore, I used control and IR hiPSC-CMs that I developed and discussed in previous chapters, for testing drugs to improve cell response to insulin, improve metabolism, and improve IR hiPSC-CM flexibility in hypoxia. We chose three drugs at various stages of the developmental and approval pipeline: metformin which has been used for decades in patients, perhexiline which

is used selectively in some regions of the world, and molidustat which is currently completing phase 3 clinical trials for anaemia. This chapter outlines the utilisation of healthy and insulin resistant (IR) human induced pluripotent stem cell derived cardiomyocytes (hiPSC-CM) in 2D and EHT for drug testing. Part of the content of this chapter has been published, in a paper where I was joint first author[328].

5.2.1 Isoprenaline and isoliquiritigenin

Isoprenaline is a dual β1-β2-adrenergic receptor agonist that has acute positive chronotropic (increases the rate of contraction) and inotropic effects (increases the force of contraction) on the heart[329]. The effect of isoprenaline has been studied in the heart in several diabetic animal models, showing an impaired response of the diabetic heart towards isoprenaline stimulation[329–331]. Isoliquiritigenin is a component of liquorice extract which showed to be a potent inhibitor of the voltage-dependent K^+ channel[332]. Isoliquiritigenin has been shown to have anti-inflammatory activity and has been suggested to be a potential drug for treating diabetes. In addition, isoliquiritigenin can prolong the potential duration thereby reducing heart rate, and thus may be beneficial to treat chronic atrial fibrillation. Isoliquiritigenin can be used to assess the hiPSC-CMs response to potassium channel inhibition and can be a valuable tool for validating hiPSC-CMs.

5.2.2 Metformin

Metformin, a member of the biguanide family, is a first-class medication being widely prescribed for patients with type-2 diabetes due to its profound blood glucose lowering effect. It is considered as essential drug by World Health Organisation[333]. Numerous clinical studies have been performed showing that metformin has a remarkable safety profile and effectively controls the blood glucose concentration in T2DM patient[334,335]. Metformin's effect on lowering blood glucose level is primarily through inhibition of gluconeogenesis in the liver, but its exact mechanism of action is still on debate. Recent studies have shown that

metformin may have a cardioprotective effect which may reduce the cardiovascular events in the patients[336]. The effect of metformin on the cellular metabolism is believed to be related to the inhibition of the complex I activity, which affects several mechanisms including 5' adenosine monophosphate-activated protein kinase (AMPK) activation[337,338]. In contrast, some studies showed that the inhibition of complex I is independent from AMPK activation, with recent studies in hiPSC-CM showing that metformin has a biphasic effect as it can inhibit complex I and/or activate AMPK signalling pathway depending on the concentration[339,340].

Previous studies have been performed to understand the effect of metformin on the heart to answer questions such as whether metformin has a protective effect on the heart and what are the mechanism by which metformin acts on the heart. Furthermore, the question whether metformin can be a potential therapeutic for diabetic cardiomyopathy remains unanswered. It has also been shown that metformin can restore the sensitivity of insulin-resistant cardiomyocytes via AMPK activation[13]. However, it has been acknowledged that current insulin-resistant models, either animal models or in vitro from animal cells, may limit the study. Moreover, most of the studies have been performed under acute conditions consisting of either hyperlipidaemia[294], hyperinsulinemia[294], or hyperglycaemia[61], but not all the factors. Therefore, utilisation of insulin-resistant model using hiPSC-CM in either 2D monolayer or EHT can shed the light of our understanding of the effect of metformin in metabolic syndrome disease such as in diabetic cardiomyopathy.

5.2.3 Perhexiline

Perhexiline is a prophylactic anti-anginal agent that is currently being used primarily in Australia and New Zealand. A double-blind, placebo-controlled clinical trial in 56 heart failure patients in the US showed that perhexiline treatment resulted in improvements in left ventricular ejection fraction, VO_{2max}, and quality of life[341]. Perhexiline shifts metabolism

towards more glucose metabolism by inhibiting long-chain fatty acid oxidation, as it inhibits carnitine palmitoyl transferase (CPT)[342]. Principally, when CPT-1 is inhibited, fatty acid transport into mitochondria and its oxidation is reduced, promoting glycolysis via reduced acetyl-CoA production via Randle cycle[343].

Perhexiline has been proven to be highly efficacious for some cardiac diseases such as angina pectoris[344]. Metabolomic analysis revealed that perhexiline was shown to partially improve the hypertrophic phenotype in the hypertrophic cardiomyopathy animal model, and that the improvement may be linked to metabolic changes in the heart[345]. There is only anecdotal evidence of the benefit of perhexiline on diabetic heart, therefore there is no study the effect of perhexiline on the diabetic heart. Therefore, utilisation of insulin-resistant hiPSC-CM in 2D monolayer and EHT to assess the effect of perhexiline can help us to understand its effect on the diabetic heart.

5.2.4 Molidustat (HIF stabilisator)

Hypoxia inducible factor (HIF) is a transcription factor considered as a master regulator for oxygen homeostasis in the cells and its role is crucial in the heart in response to low oxygen availability[346–348]. HIF regulates hundreds of genes involved in metabolism, cell growth, angiogenesis, and erythropoiesis, allowing the tissue/organism to survive during hypoxia[349]. HIF stabilisation is essential for the heart to maintain its contractile function especially during ischemia after myocardial infarction and pressure-overload hypertrophy[350,351]. The discovery of HIF was recognised by the Nobel Prize award to William Kaelin Jr., Peter Ratcliff, and Greg Semenza in 2019. HIF1α regulation is oxygen dependent and in normoxia, it will be degraded by the proteosome[352,353] (**Figure 5.1**).

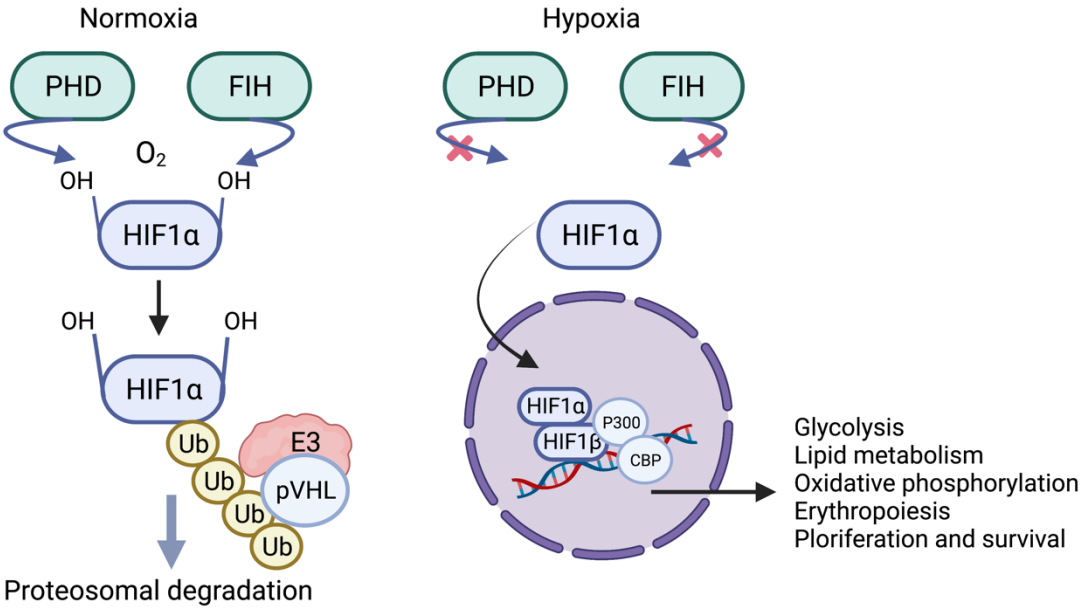


Figure 5.1 HIF1α regulation and signalling

Under normoxia, HIF1α is constantly synthesised, hydroxylated, and degraded by the proteosome via hydroxylation of proline residues, mediated by the oxygen-dependent prolyl hydroxylase domain (PHD) family enzymes and factor inhibiting HIF (FIH) which results in HIF1α being poly-ubiquitinated by von Hippel-Lindau (pVHL)-E3 ligase complex. Under hypoxia, HIF1α is stabilised and escapes to the nucleus where it binds to HIF1β and recruites co-activators of transcription p300 and CBP which influence many transcriptions of many HIF target genes.

As discussed in the previous chapter, insulin resistance in diabetic hearts suppresses HIF1α stabilization and downstream hypoxic adaptation[256]. This is due to elevated fatty acids in diabetes suppressing myocardial succinate concentrations, as succinate and fumarate inhibit the PHD enzymes necessary to promote HIF stabilization[256]. Therefore, investigating whether pharmacological HIF stabilisation in the heart provides benefit for the heart in diabetes may open up a new therapeutic approach to treat patients. Molidustat (BAY85-3934) is an orally bioavailable PHD inhibitor that successfully stabilizes HIF1α and is undergoing phase III clinical trials to treat anaemia in patients with chronic kidney disease[354–356]. However, the effect of molidustat in the heart, specifically in human cardiomyocytes has not been extensively explored.

5.3 Chapter aims

This chapter aims to investigate the utilisation of healthy and insulin resistant hiPSC-CMs in 2D and EHT for drug testing. In summary, this chapter investigates:

1. The effect of metformin to reverse the effect of insulin resistance in hiPSC-CM in 2D monolayer and EHT
2. The effect of perhexiline to reverse the effect of insulin resistance in hiPSC-CM in 2D monolayer and EHT
3. Whether molidustat could be repurposed for use in the heart to overcome the blunted HIF activation and correct the abnormal cardiac metabolism induced by diabetes

5.4 Materials and methods

5.4.1 Preparation of the drugs used for the experiments

5.4.1.1 Preparing isoliquiritigenin and isoprenaline

Isoliquritigenin (cat. No. I3766, Merck) was dissolved in DMSO according to the manufacturer's direction as a stock solution. Isoprenaline hydrochloride (cat. No. I5627, Merck) was dissolved in water according to the manufacture's direction as stock solution. In each case the stock solution was then mixed with the media to the intended concentration. Isoliquiritigenin and isoprenaline were used in serial dilutions for multielectrode array and Musclemotion analysis. Prior to data recording, hiPSC-CMs in 2D and EHT were incubated with either isoliquiritigenin or isoprenaline at 37ºC and 5% CO_2 for 10 minutes.

5.4.1.2 Preparing metformin

Metformin hydrochloride (cat no. 0215169105, MP Biomedical) was dissolved in water as a stock solution according to manufacturer's direction. The stock solution of metformin was then mixed with media to give the intended concentration. For Musclemotion experiments, EHTs were incubated with media containing metformin for 24 hours before video recording. For enzymatic assays, the media was collected at the end of experiment for further analysis.

Control and IR EHT were cultured in the untreated media or media containing 0.5 mM metformin for 24 hours. At the end of the incubation, the media was changed to new untreated media and media containing metformin for 30 mins and the cells were lysed and protein was analysed using Western blot.

5.4.1.3 Preparing perhexiline

Perhexiline maleate (cat no. SML0120, Merck) was dissolved in DMSO as a stock solution according to manufacturer's direction. The stock solution of perhexiline was then mixed with media to give the intended concentration. Control and IR EHT were cultured in untreated media or media containing 3 μM perhexiline for 24 hours and the cells were lysed, and total RNA was analysed using qRT-PCR.

5.4.1.4 Preparing molidustat

Molidustat (cat. No. ADV465750852, Merck, and R16009, Advanced Chem Blocks) was dissolved in DMSO as a stock solution. The stock solution was mixed with media to give the intended concentration. Human iPSC-CMs were cultured in the presence or absence of 50 μmol/L molidustat for 16 h. A subgroup of control and insulin-resistant hiPSC-CMs were exposed to hypoxia (2% O2, 5% CO2) for 16h, with molidustat added just prior to the insulin-resistant cells entering the hypoxic incubator. Cell media was collected and assayed spectrophotometrically for glucose and lactate concentrations, with measurement of the change in absorbance following incubation with glucose assay reagent (Merck) for the former or lactate dehydrogenase and NAD for the latter. Glucose consumption rates and lactate production rates were normalized to cell number.

5.5 Results

To determine whether the hiPSC-CM reacted to stimulation by known drugs in the same way as adult human cardiomyocytes, hiPSC-CMs were treated with increasing concentrations of isoprenaline and isoliquiritigenin (ILG). I used a multielectrode array (MEA) to analyse the effect of ILG on hiPSC-CM in 2D monolayer and video analysis using Musclemotion to study the effect of ILG and Isoprenaline on EHT.

5.5.1 Assessing the effect of isoliquiritigenin and isoprenaline on healthy human iPSC-CM in 2D monolayer and EHT

After differentiation and maturation, hiPSC-CMs were dissociated and cultured on the 8 x 8 or 6 x 10 electrodes MEA chips and the voltage changes in the cells were then measured using the Maxwell Biosystem software. The change of field potential with 9 different concentrations of ILG is shown in **Figure 5.2**. No obvious changes were seen in the coloured map, which displayed the propagation of each heartbeat across the MEA. Interestingly, the field potential recording showed continuous signal, but the heartbeat became sparse, and the amplitude of the signal decreased at the highest concentration (25 μM) of ILG suggesting that high concentrations had an adverse effect on the cells. ILG did not prolong field potential duration or reduce the amplitude of T-wave, even at the highest concentration, as shown in **Figure 5.3**.

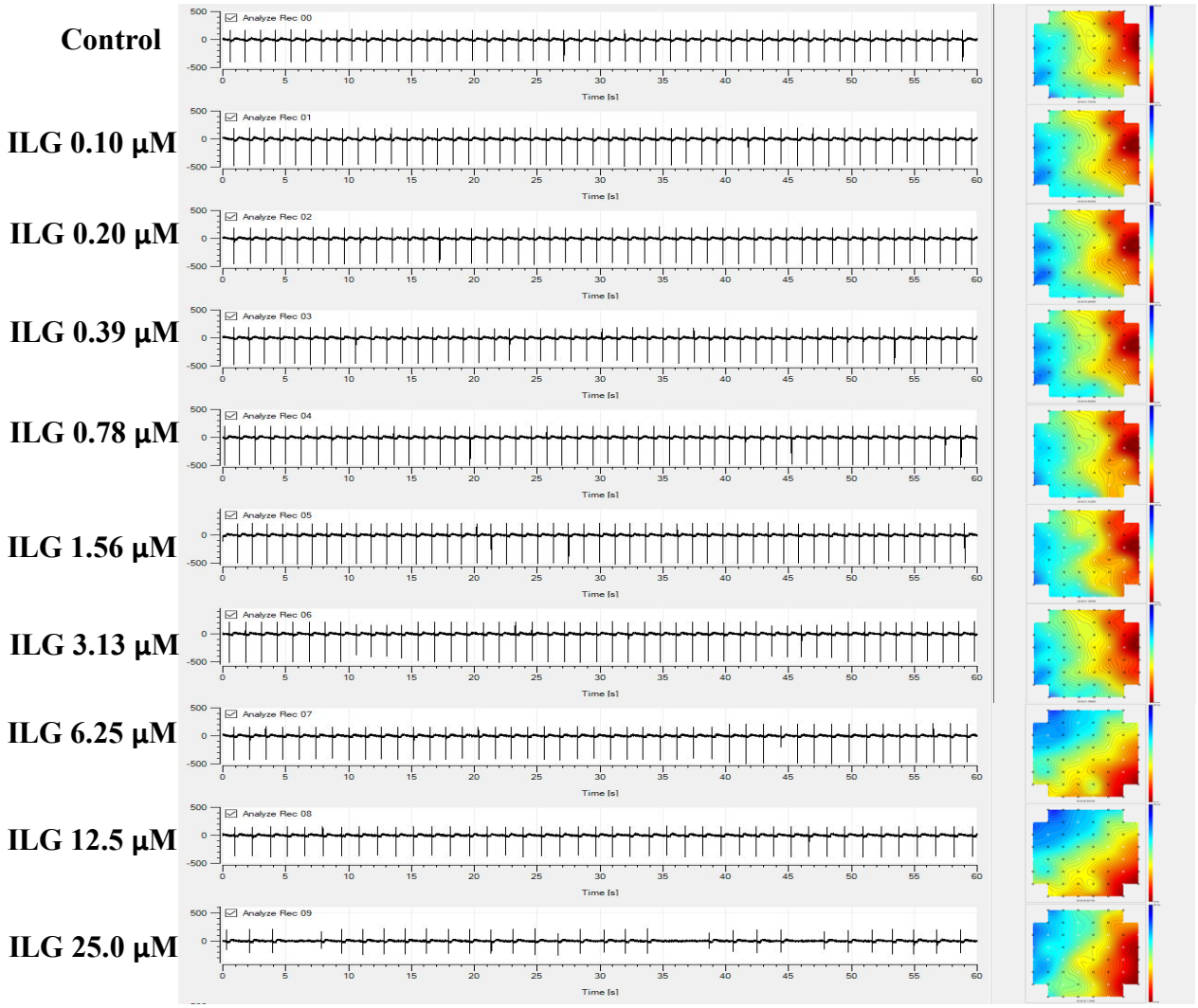


Figure 5.2 The effect of Isoliquiritigenin on field potential of hiPSC-CM in 2D monolayer measured using Multielectrode array

The field potential data of hiPSC-CMs in 2D monolayer showing continuous reading of field potential and heat map of heartbeat propagation through the cells after exposure to increasing concentrations of isoliquiritigenin.

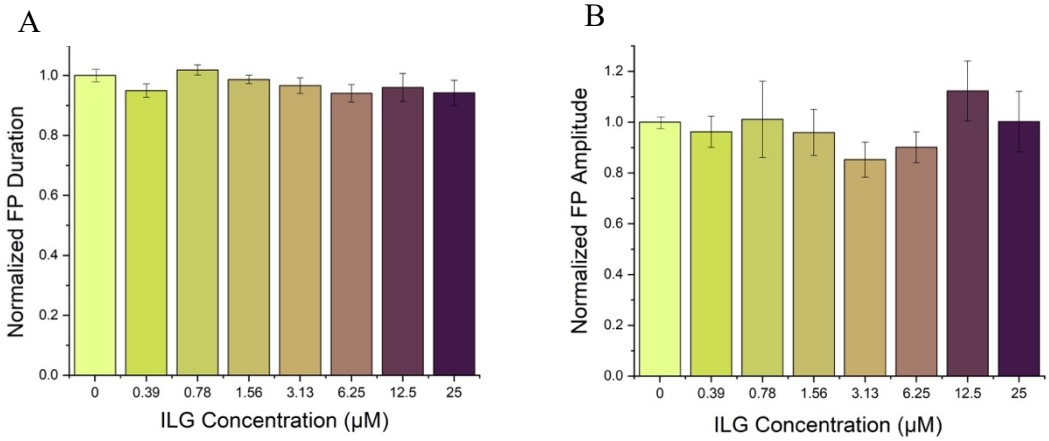


Figure 5.3 The effect of isoliquiritigenin on T-wave

The effect of different concentration of Isoliquiritigenin on field potential (FP) duration (A) and FP amplitude (B).

Low concentrations of ILG increased the sodium (Na) peak amplitude but this then decreased at concentrations above 1.56 µM and was significantly lower than control at 12.5 and 25 µM. The Na peak duration increased at concentrations about 6.25 µM as shown in **Figure 5.4**. Both the Na peak slope and max slope reduced at higher concentrations because of the sodium and potassium channel blockage effect. The two highest doses of ILG lowered the heart rate and increased the heartbeat interval, but only small changes in the conductance were seen, with no obvious pattern, as shown in **Figure 5.5**.

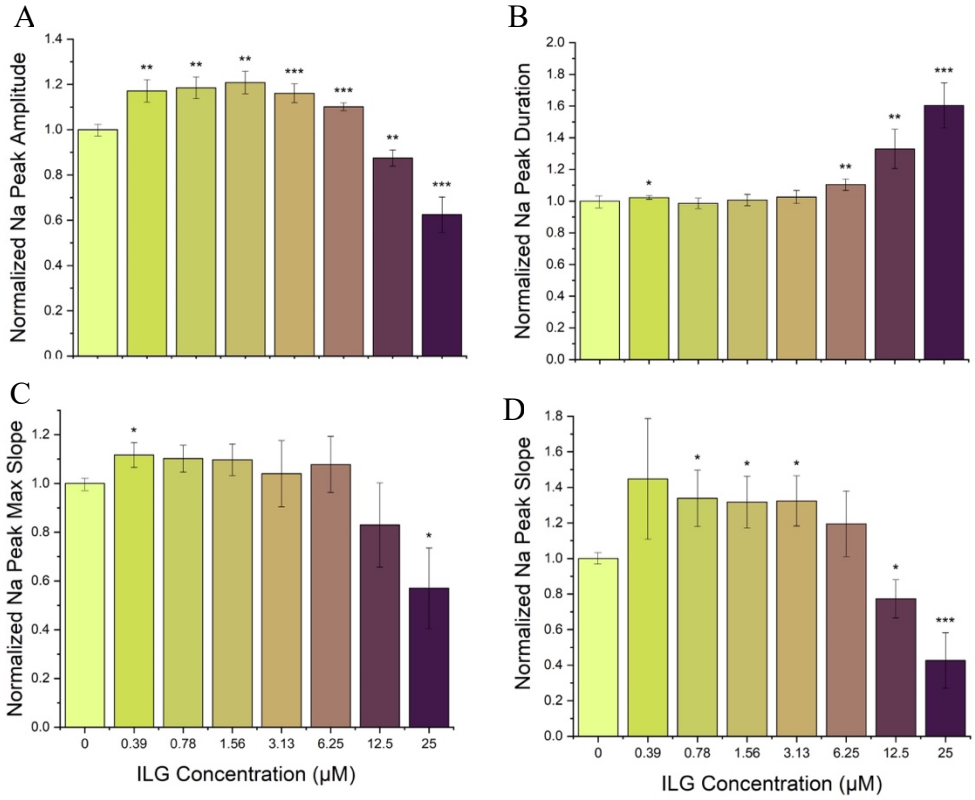


Figure 5.4 The effect of isoliquiritigenin on Na (sodium) peak

The effect of increasing doses of Isoliquiritigenin on Na peak amplitude (A), Na peak duration (B), Na peak max slope (C), and Na peak slope (D) of hiPSC-CMs in 2D monolayer measured using a multielectrode array (MEA). Data represents mean value and SEM analysed using one-way repeated measures ANOVA with a *, **, *** $p < 0.05, 0.01, 0.005$ compared to control, n=7-8.

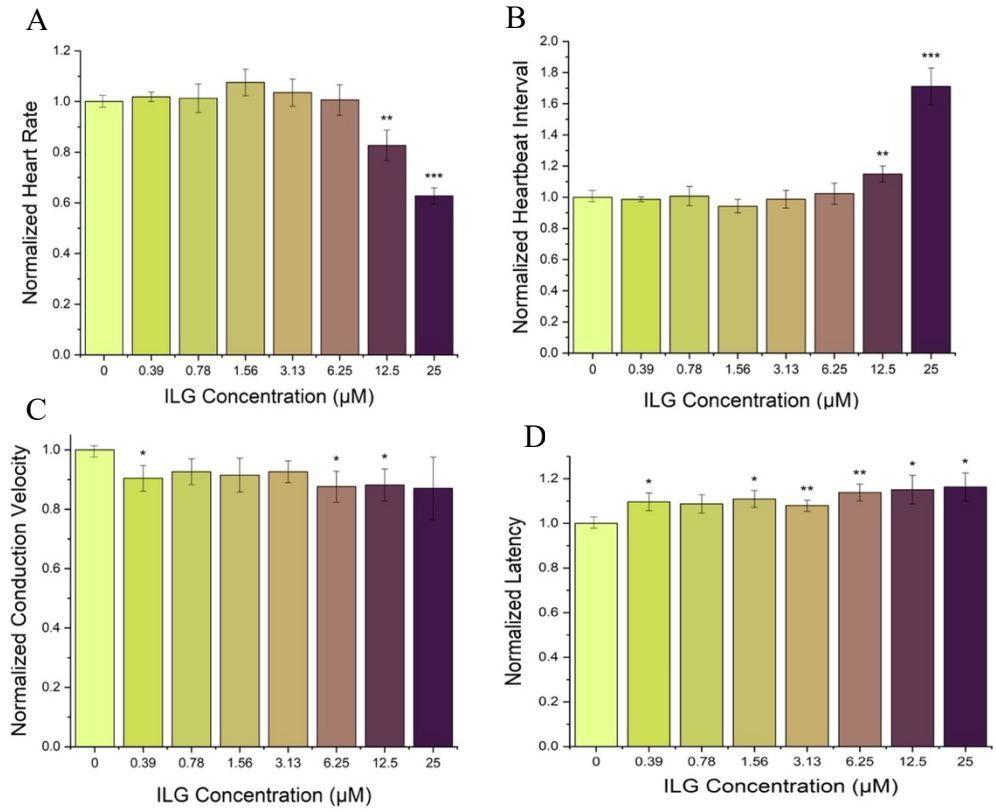


Figure 5.5 The effect of isoliquiritigenin on heart rate and conduction

The effect of increasing doses of isoliquiritigenin on the heart rate (A), heartbeat interval (B), conduction velocity (C), and latency (D) of hiPSC-CMs in 2D monolayer measured using a multielectrode array (MEA). Data represents mean value and SEM analysed using one-way repeated measures ANOVA with a *, **, *** $p < 0.05, 0.01, 0.005$ compared to control, n=7-8.

MEAs have been widely used by researchers worldwide to study the contraction of hiPSC-CMs in monolayer culture[357]. However, the technique is not useful for 3D culture and so I used Musclemotion to assess the effect of Isoprenaline and ILG on the cells in the EHT. I used 5 different concentrations of ILG with the same range of concentration to those in 2D monolayers. As seen in the monolayer, the EHTs beat more slowly at the highest concentrations shown by increasing contraction duration and relaxation time (**Figure 5.6 B-D**). There was no change in the peak amplitude. Interestingly, the contraction duration was significantly higher at a concentration of 6.25 μM of ILG which is half the value needed to induce a significant difference in the 2D monolayer.

To investigate the effect of isoprenaline (Iso) on the cells in the EHT I used 6 concentrations in a range selected from the literature[358,359]. Peak amplitude in EHTs did not change with

Iso treatment, but the contraction duration decreased in a concentration dependent manner. The contraction duration and relaxation time were significantly lower in EHTs treated with concentrations above 500 nM as seen in **Figure 5.6 E-G**. This suggested that hiPSC-CMs in EHTs are responsive towards β-adrenergic stimulation on positive chronotropic effect. However, Iso did not have positive inotropic effect in EHT showed by no effect in the peak amplitude.

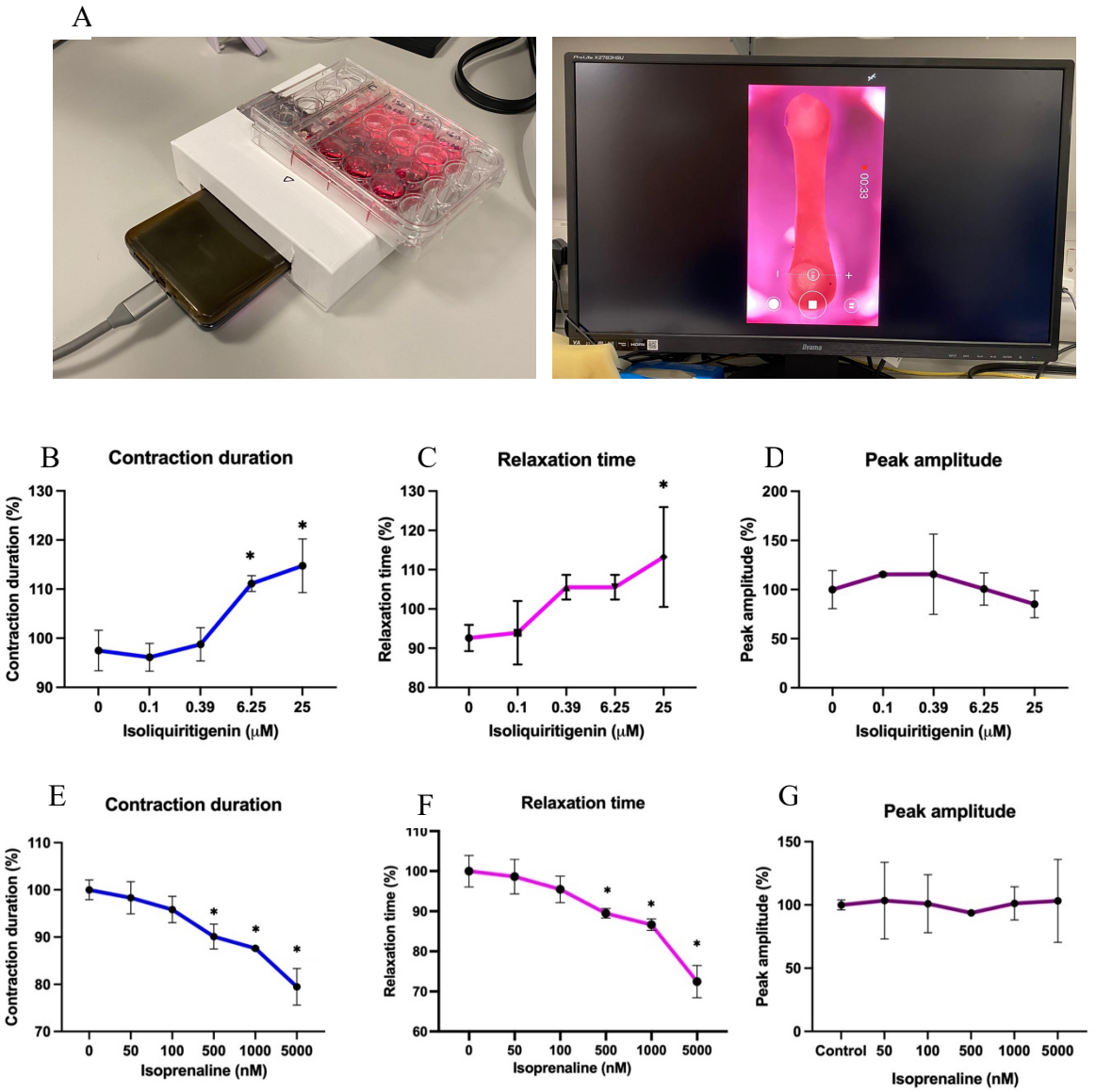


Figure 5.6 The effect of isoliquiritigenin and isoprenaline on the EHT measured by Musclemotion

The effect of different dose of isoliquiritigenin and isoprenaline on the contraction duration (B, E), relaxation time (C, F), peak amplitude (D, G) on EHT measures by Musclemotion. Data represents mean value and SEM analysed using one-way repeated measures ANOVA with a * $p<0.05$ compared with control, n=4.

5.5.2 Assessing the effect of isoprenaline on IR EHT

As the healthy hiPSC-CM in EHT gave the expected response to isoprenaline, I assessed the response of IR EHT to β-adrenergic stimulation. In contrast to the data shown in **Figure 5.6**, there was no significant decrease in contraction duration in control EHT in this experiment. At baseline, contraction duration and time to peak of IR EHT was significantly higher compared with control EHT. However, contraction duration decreased with increasing concentrations of isoprenaline and was significantly lower after isoprenaline exposure at concentration 500, 1000 and 5000 nM in IR EHT (**Figure 5.7 A**). Interestingly, the effect of isoprenaline on contraction duration was greater in IR EHT than in the control EHT, suggesting that IR EHTs were more sensitive to isoprenaline exposure. However, the effect of isoprenaline on the relaxation time of IR EHT showed more variability whereas control EHT showed downward trend and significantly decreased after exposure to 50000 nM (5 μM) of isoprenaline (**Figure 5.7B**). Isoprenaline did not affect the time to peak at any of the concentrations used in control EHT but significantly decreased that in IR EHT after exposure to 5000 nM isoprenaline (**Figure 5.7 C**).

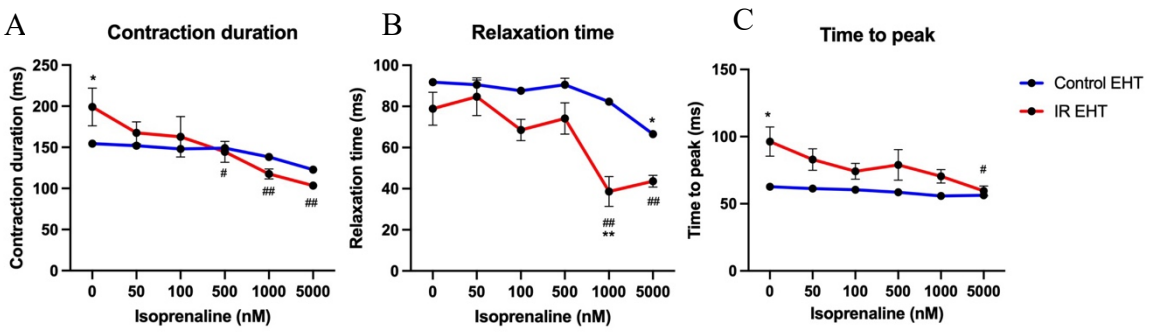


Figure 5.7 The effect of isoprenaline on the contraction in control and IR EHT measured by Musclemotion

The effect of increasing doses of isoprenaline on the contraction duration (A), relaxation time (B), time to peak (C) in control and IR EHT measured by Musclemotion. Data represents mean value and SEM analysed using two-way repeated measures ANOVA followed by Tukey's test with a * $p<0.05$ compared with control EHT, #, ##, ###, #### $p < 0.05$, 0.01, 0.005, 0.001 compared with 0 nM isoprenaline IR EHT, n=3-4.

5.5.3 Assessing the effect of metformin on healthy and insulin resistant hiPSC-CM in 2D monolayer and EHT

In order to determine the effective concentration of metformin to have an effect on hiPSC-CM, control, and IR cardiomyocytes (CMs) were exposed to media containing no metformin as control and media containing a range of concentrations from 0.1-5 mM for 24 hours. Glucose consumption and lactate release were quantified and showed that 5 mM increased glucose consumption in IR hiPSC-CM but not control hiPSC-CM (**Figure 5.8A**). Lactate release was significantly increased in both control and IR hiPSC-CM at 5 mM metformin exposure (**Figure 5.8B**). Lower concentrations of metformin (0.1 and 0.5 mM) did not significantly change glucose consumption in either control or IR hiPSC-CM, but lactate release was significantly increased in control hiPSC-CM after treatment with 0.5 mM metformin.

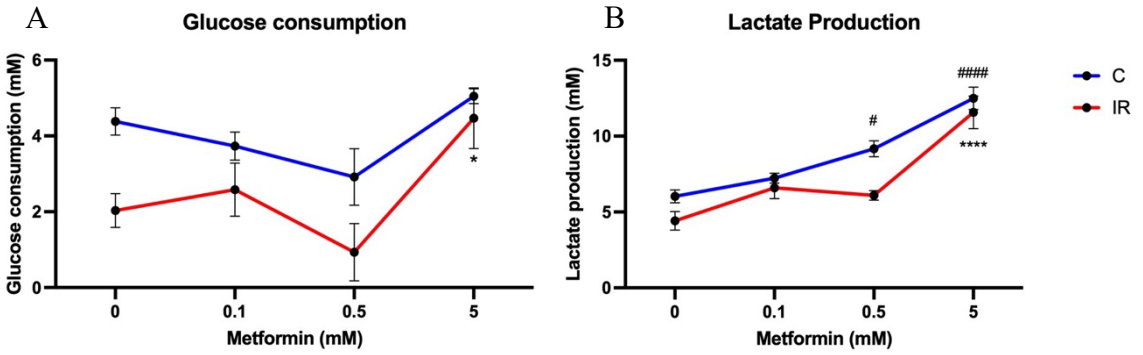


Figure 5.8 The effect of different concentrations of metformin on the metabolism of hiPSC-CM in 2D monolayer

Glucose consumption (A) and lactate release (B) in control and IR hiPSC-CM in 2D monolayer (1.5 million cells) were measured after 24 hours of exposure to 0.1-, 0.5-, and 5-mM metformin compared to untreated cells. #, #### $p < 0.05$, 0.001 compared with untreated control cell, *, **** $p < 0.05$, 0.001 compared to untreated IR cells, analysed using one-way ANOVA, n=4

Next, expression of the metabolic genes GLUT1, GLUT4, and PGC1α was assessed after exposure to three different concentrations of metformin. The highest concentration of metformin, 5 mM, significantly downregulated GLUT1 and upregulated GLUT4 and

PGC1α in both control and IR hiPSC-CM (**Figure 5.9A-F**). With 0.5 mM metformin, GLUT1 was downregulated significantly in control, but not in IR hiPSC-CM (**Figure 5.9 A and D)** and GLUT4 was upregulated significantly in control, but not in IR hiPSC-CM (**Figure 5.9 B and E**). PGC1α was downregulated to a small extent after 0.1 mM metformin in control hiPSC-CM, but then upregulated in both control and IR cells at 5 mM (**Figure 5.9**).

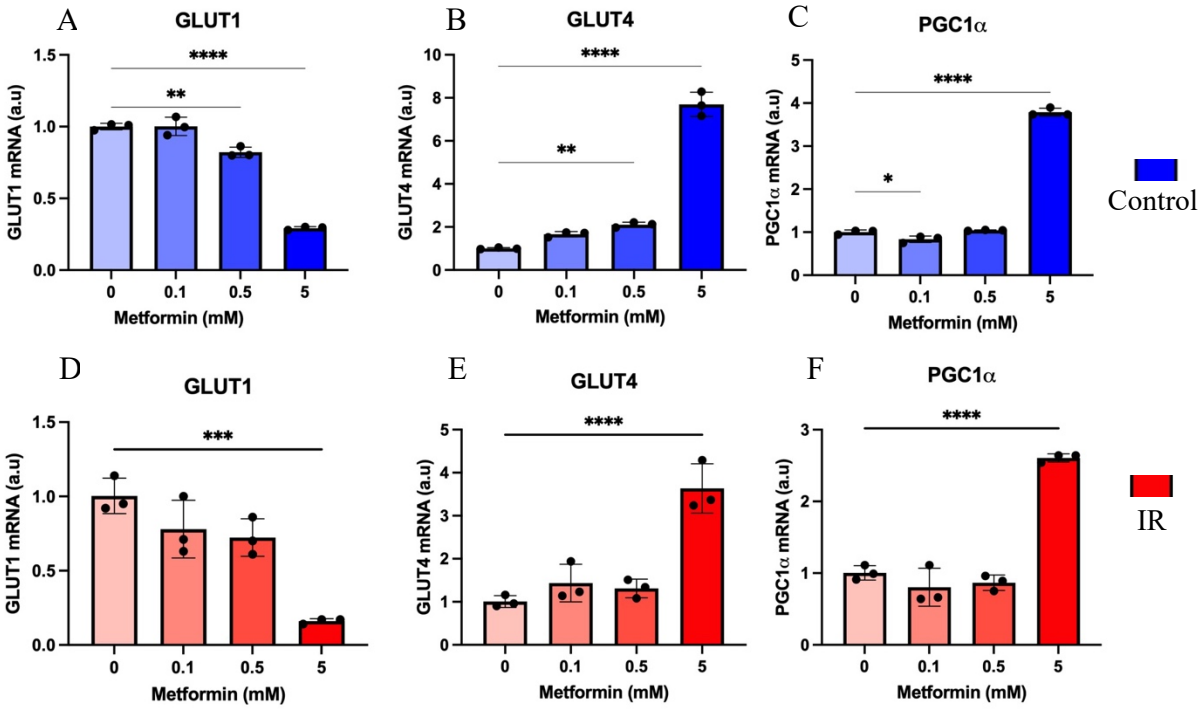


Figure 5.9 The effect of different doses of metformin on gene expression in hiPSC-CM in 2D monolayer

The expression of GLUT1, GLUT4, PGC1α in hiPSC-CM 2D monolayer of control (A, B, C) and insulin resistance (D, E, F). The data represents mean and SEM, analysed by one-way ANOVA followed by Dunnett's test with *, **, ****, P<0.05, 0.01, 0.001, (n=3).

Studies to assess the effect of metformin on other cell types such as liver, muscle, and cancers cells have found that a concentration of 5 mM metformin affects the metabolism of the cells but that it is substantially higher than physiological concentrations[360–362]. As treatment with 0.5 mM metformin for 24 hours induced significant changes in expression of GLUT1 and GLUT4, this was used in further experiments to assess the effect of metformin on Akt phosphorylation in hiPSC-CM.

The effect of metformin was further explored in EHTs. The analysis was started by assessing the effect of 0.5 mM metformin for 24 hours on the expression of the metabolic genes GLUT1, GLUT4, PGC1α, inhibitor of nuclear factor kappa-B kinase subunit β (IKK-β), forkhead box protein O1 (FOXO1), and BNIP3 in control and IR EHT. GLUT4 expression was significantly lower in IR EHT than in control but metformin significantly increased GLUT4 expression in both control and IR EHT (**Figure 5.10B**). PGC1α, IKK-β, and BNIP3 were not affected significantly by metformin treatment (**Figure 5.10 C, D, F**). Interestingly, metformin significantly decreased FOXO1 expression in control EHT but increased it in IR EHT.

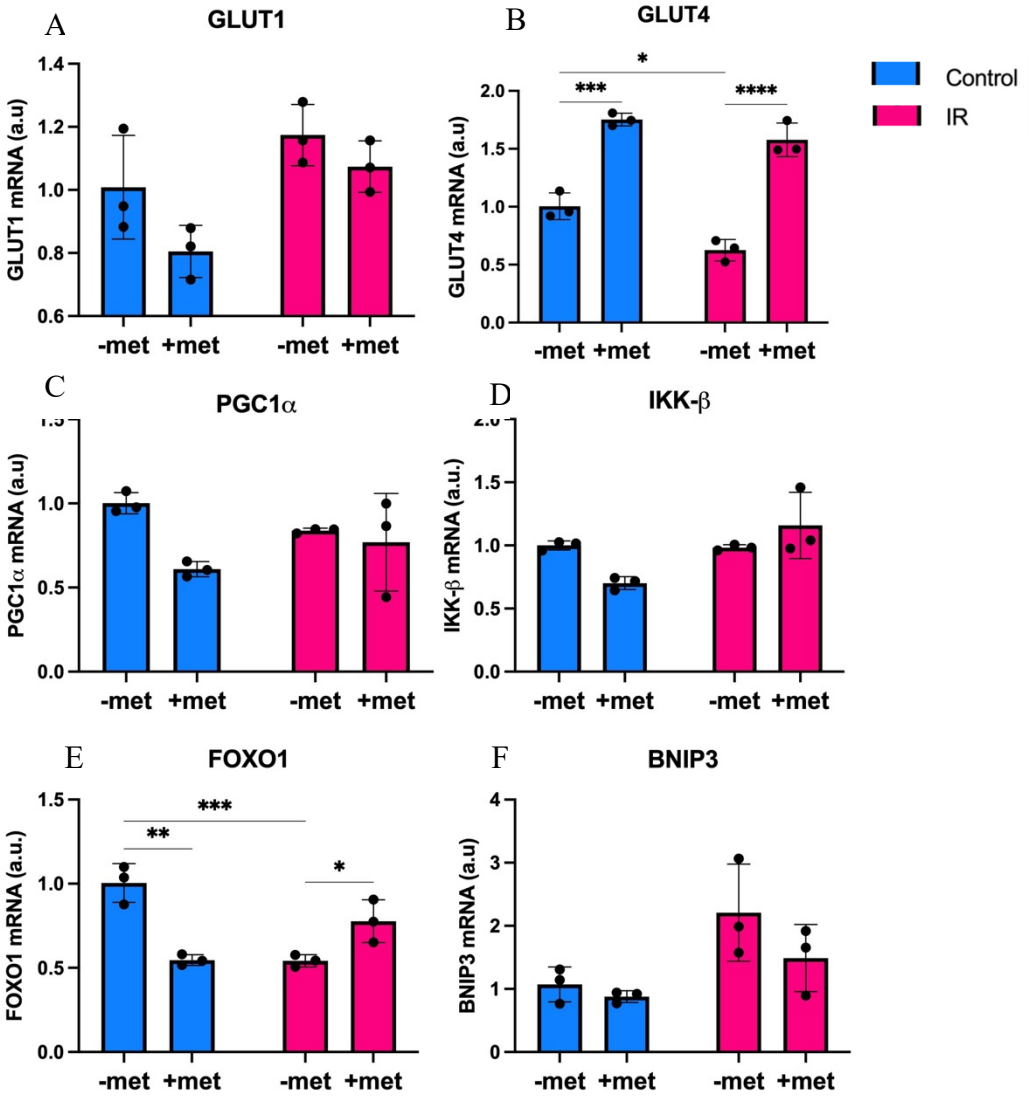


Figure 5.10 The effect of metformin treatment on control and insulin resistant EHT

Gene expression of GLUT1 (A), GLUT4 (B). PGC1α (C), IKK-β (D), FOXO1 (E), and BNIP3 (F) in control and IR EHT after exposure to 0.5 mM metformin for 24 hours. *, **, ***, **** $p < 0.05$, 0.01, 0.005, 0.001, analysed using two-way ANOVA followed by Tukey's test, n=3.

Western blot analysis showed that insulin stimulation increased levels of pAkt in control cells and this was further increased in metformin-treated cells, suggesting that metformin had an effect on sensitising the insulin response in control cardiomyocytes. Although there was no significant change in pAkt levels in IR hiPSC-CM, there was a trend towards a higher level of pAKT after treatment with metformin and insulin as shown in **Figure 5.11**.

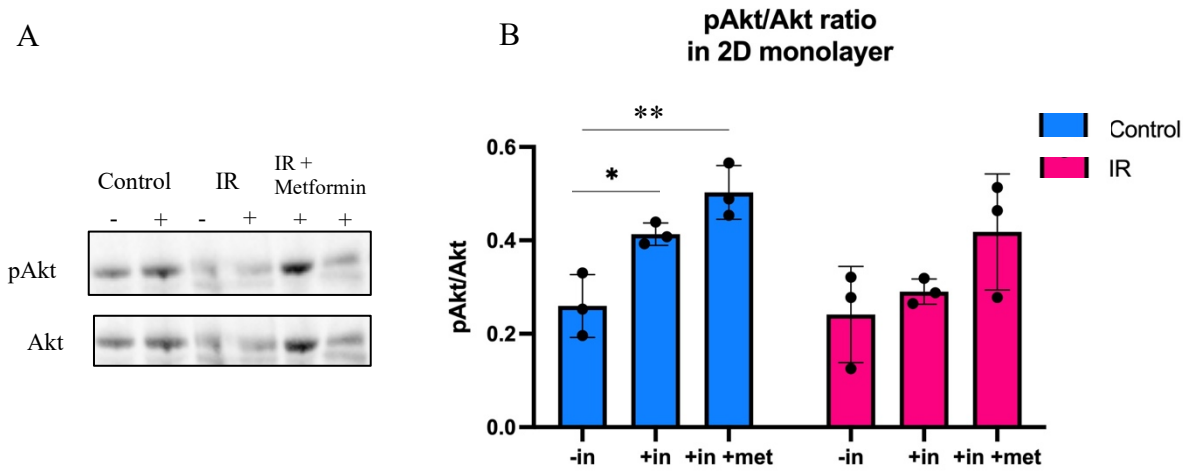


Figure 5.11 The effect of metformin on insulin response in control and IR 2D monolayer hiPSC-CM

Western blot image representative of pAkt and Akt protein expression in hiPSC-CMs cultured in 2D monolayer with or without insulin stimulation and treatment with 0.5 mM metformin for 24 hours, quantitative analysis of pAkt/Akt ratio (B), *, ** $P<0.05$, 0.01, analysed using two-way ANOVA followed by Tukey's test, n=3.

To understand the effect of metformin on glycolytic flux, the radiolabelled experiment using ^{3}H-glucose was performed as described in the methods chapter 2. Glycolytic flux was significantly higher in control hiPSC-CM in monolayer after metformin treatment, but no significant increase was found in control EHT with metformin (**Figure 5.12**). Glycolytic flux was significantly lower in IR hiPSC-CM in both 2D monolayer and EHT which agreed with the result described in **chapter 5**. Interestingly, metformin increased the glycolytic flux significantly in IR hiPSC-CM 2D monolayer and EHT.

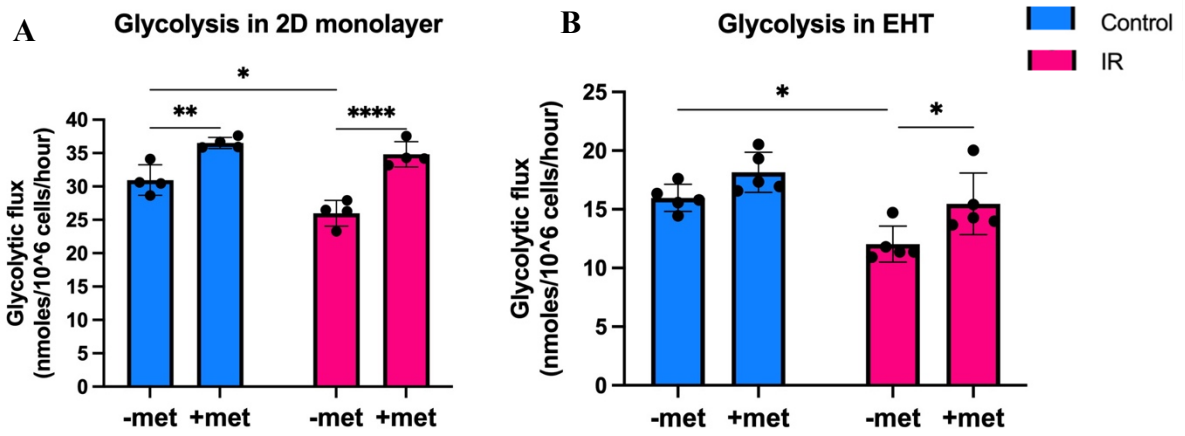


Figure 5.12 The effect of metformin on glycolytic flux in control and IR hiPSC-CM

The effect of metformin to glycolysis in control and IR hiPSC-CM in 2D monolayer (A) and EHT (B), *, **, **** P<0.05, 0.01, 0.001 analysed using two-way ANOVA followed by Tukey's multiple comparison test, (n=4-5).

It has been reported that metformin might increase glucose uptake and sensitise the insulin receptor via inhibition of complex 1 and activation of the AMPK pathway[363,364]. To understand the effect of metformin on the AMPK signalling pathway, the phosphorylation of AMPK at Thr172 was assessed. There was significantly higher AMPK phosphorylation in control EHT compared with IR EHT. Interestingly, metformin significantly increased the AMPK phosphorylation in control and IR EHT, suggesting that metformin acted on AMPK signalling (**Figure 5.13A-B**).

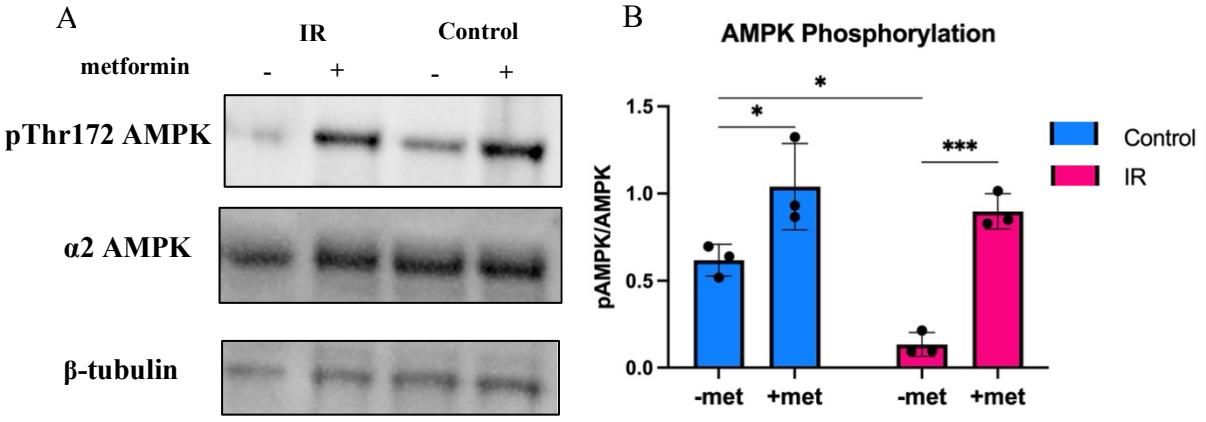
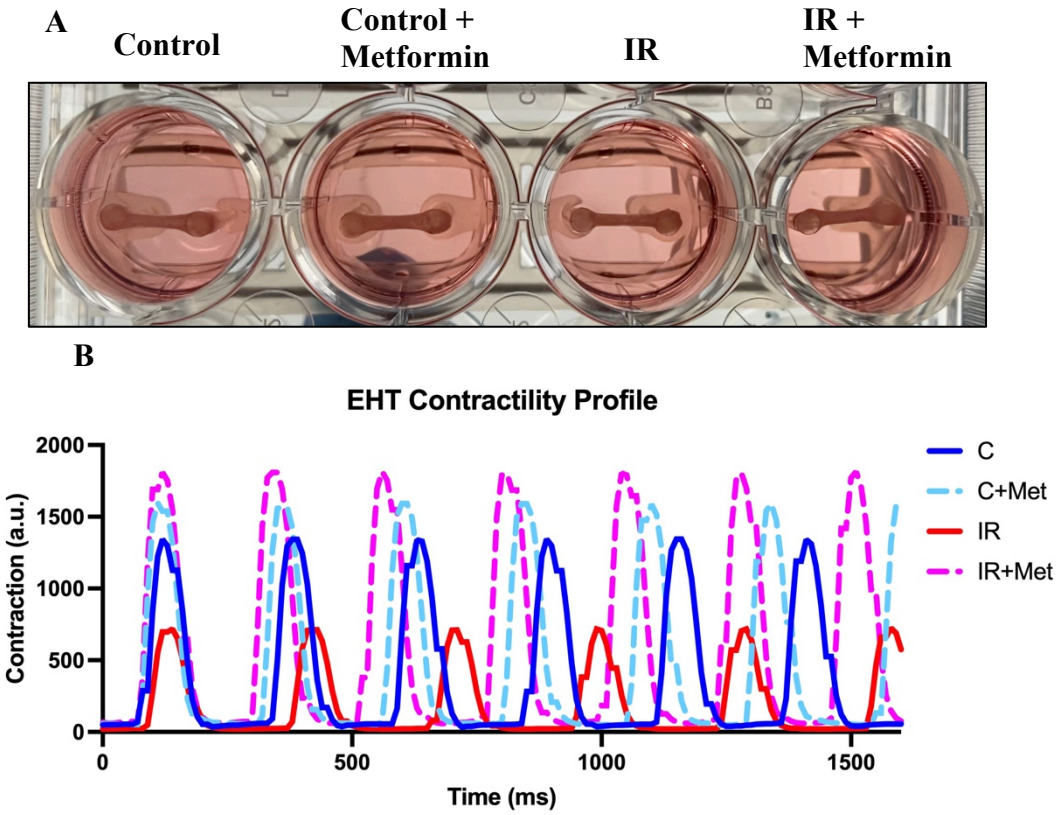


Figure 5.13 The effect of metformin on AMPK phosphorylation in EHT

The effect of 0.5 mM metformin on the AMPK phosphorylation of Thr172, α2 AMPK, and β-tubulin as housekeeping protein (A) and quantification of the protein as ratio of pAMPK/AMPK (B) in the control and insulin resistant EHT. *, *** p < 0.05, 0.005 analysed using two-way ANOVA followed by Tukey's test, n=3.

The effect of metformin treatment was further explored in the contractility profile of hiPSC-CM in EHT. Contraction in EHTs were shown to be regular and no arrythmia was observed in the samples. As shown in the previous chapter, the contraction amplitude of IR EHT was lower compared to control. Metformin treatment increased the contraction amplitude in IR EHT (**Figure 5.14 B**). There was no significant difference observed in relaxation time (**Figure 5.14 C**), suggesting that relaxation time was not influenced by IR or metformin treatment. Metformin did not significantly alter contraction duration, time to peak, and peak-to-peak time in control EHT. IR EHT had significantly higher contraction duration and peak-to-peak time compared to control EHT, and metformin significantly decreased those measurements to similar levels as in control EHT (**Figure 5.14 E-F**). Time to peak was also significantly lowered in IR EHT after metformin treatment.



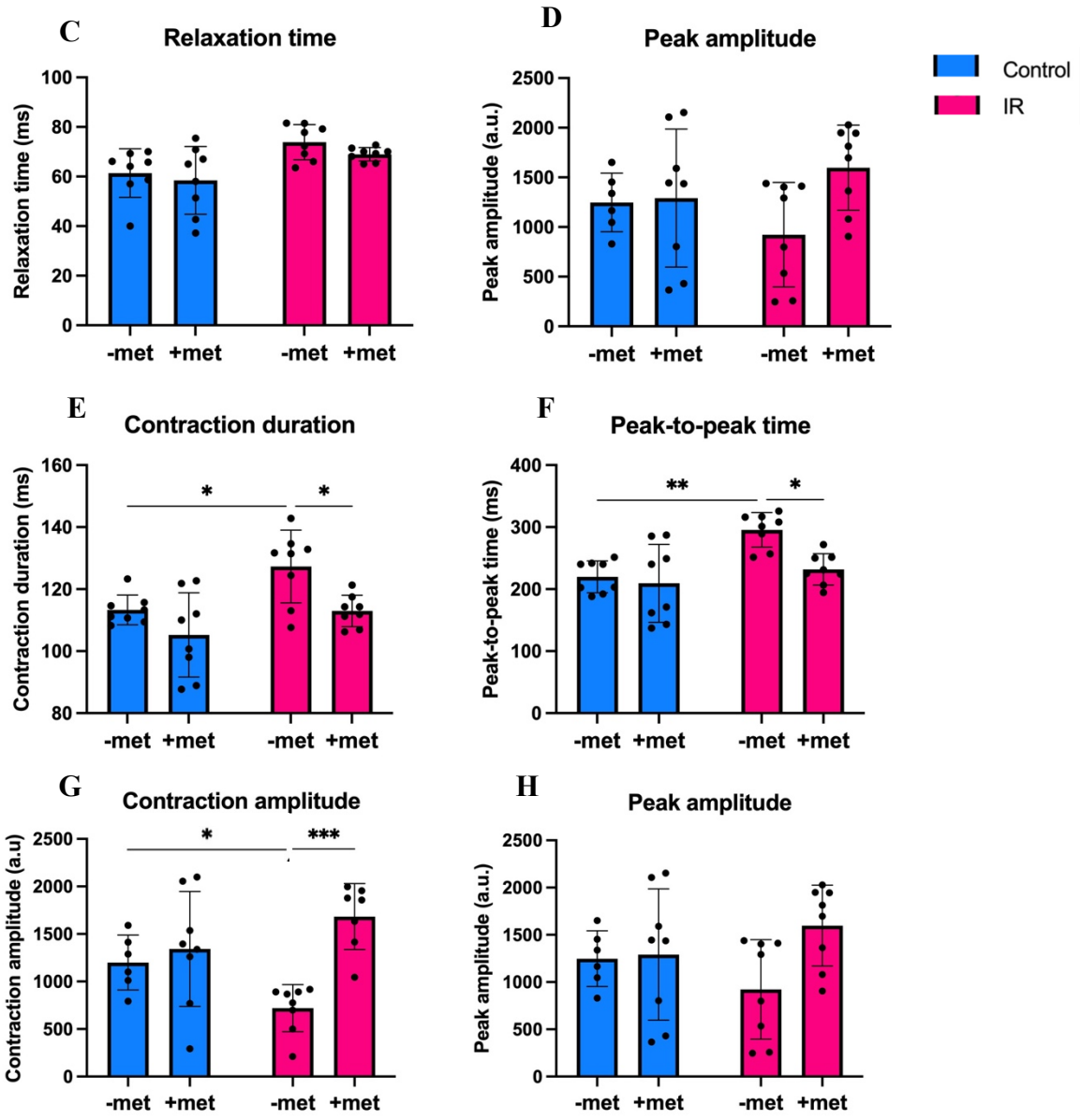


Figure 5.14 The effect of metformin on the contraction of control and IR EHT

Representative images of EHT in 24-well plates (A), traces of contraction of control and IR EHT with and without metformin (B), relaxation time (C), time to peak (D), contraction duration (E), peak-to-peak time (F), contraction amplitude (G), and peak amplitude (H) of control and IR EHT with and without metformin treatment. *, ** $p < 0.05$, 0.01 compared to untreated control or IR EHT, analysed using two-way ANOVA followed by Tukey's test, n=8.

5.5.4 Assessing the effect of perhexiline on healthy and insulin resistant hiPSC-CM in 2D monolayer and EHT

The experiment was started by determining the effective concentration of perhexiline for the hiPSC-CMs. A range of perhexiline concentrations (0 – 15 μM) was tested by assessing lactate dehydrogenase (LDH) release into the media (as a marker of cell death), glucose consumption, and lactate release. LDH levels were higher in IR than control hiPSC-CM. There was no significant difference in the LDH level when control and IR cells were incubated with 1 and 3 μM perhexiline, but the level of LDH dropped significantly when the cells were exposed to 5 – 15 μM perhexiline, indicating that there was less cell death if the cells were exposed to higher concentrations of perhexiline (**Figure 5.15A**). Glucose consumption and lactate production in control cells were not affected by treatment with perhexiline. In contrast, glucose consumption and lactate production were significantly increased compared to untreated IR hiPSC-CM when the IR hiPSC-CMs were treated with 3 μM perhexiline. Glucose consumption was significantly lower in IR hiPSC-CMs after treatment with 10 μM perhexiline compared with control treated with the same concentration of perhexiline. Lactate release was significantly lower in IR hiPSC-CMs after treatment with 7.5 μM perhexiline compared with control treated with the same concentration of perhexiline. There was a non-significant decrease in glucose consumption and lactate release after treatment with 5 – 10 μM perhexiline, but a significant increase in lactate release, compared to baseline, at the concentration of 15 μM (**Figure 5.15 B-C**).

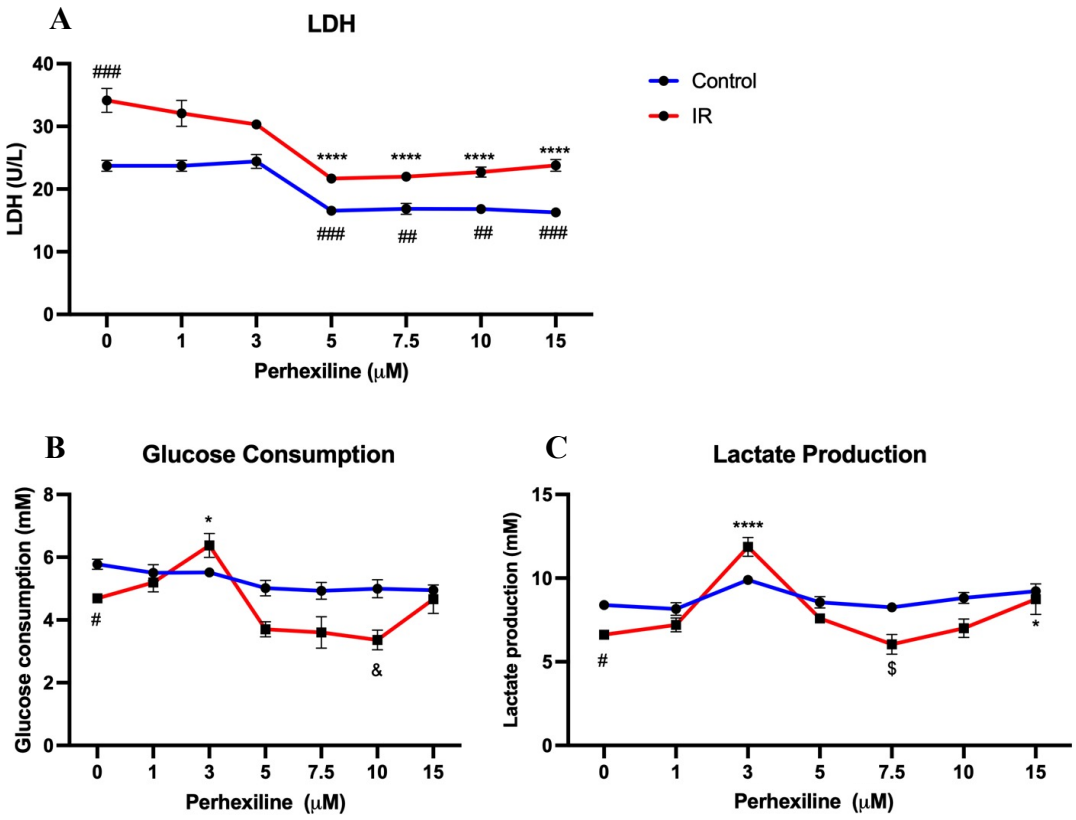


Figure 5.15 The effect of different concentration of perhexiline on the metabolism of hiPSC-CM in 2D monolayer

LDH (A), glucose consumption (B) and lactate release (C) in control and IR hiPSC-CM in 2D monolayer (per 1.5 million cells) after exposure into 1, 3, 5, 7.5, 10 and 15-μM perhexiline for 24 hours. #, ##, ### $p<0.05$, 0.01, 0.005 compared with untreated control cell, *, **** $p < 0.05$, 0.001 compared with untreated IR cells, & $p<0.05$ compared with control exposed to 10 μM perhexiline, $ $p<0.05$ compared with control exposed to 7.5 μM perhexiline, analysed using two-way ANOVA, n=5.

The expression of PGC1α mRNA was assessed in control and IR hiPSC-CM after treatment with 1 – 15 μM of perhexiline. PGC1α expression was not changed by treatment with 1-5 μM perhexiline in both control and IR EHT, apart from a small increase in expression in IR hiPSC-CM with 3 μM of perhexiline (**Figure 5.16 A-B**). The expression of PGC1α was significantly increased in the control hiPSC-CM after treatment with 10 μM perhexiline whereas a significant increase in IR hiPSC-CM was seen at 7.5 and 10 μM. Interestingly, PGC1α expression was significantly reduced in control hiPSC-CM after treatment with 15 μM perhexiline, and a small, but not significant, decrease was seen in IR hiPSC-CM compared with 0 μM perhexiline (**Figure 5.16 A-B)**. When all the data was taken together,

these experiments suggested that 3 μM would be an effective concentration to use for the further experiments to investigate the effect of perhexiline on improving the metabolism in insulin resistant heart.

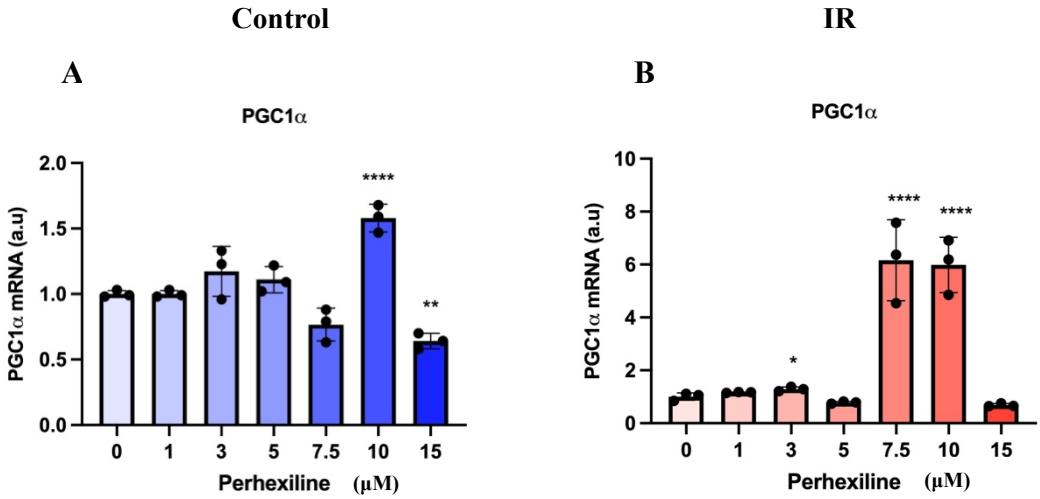


Figure 5.16 The effect of different doses of perhexiline on PGC1α expression in control and IR hiPSC-CM, analysed by qPCR

PGC1α expression on control (A) and IR (B) hiPSC-CMs in 2D monolayer treated with various concentration of perhexiline for 24 hours. *, **, **** $p < 0.05, 0.01, 0.001$ compared to untreated control and IR EHT, analysed using one-way ANOVA, n=3

To understand the effect of perhexiline on the insulin resistant heart, the EHT model was used. Expression of GLUT4, PDK4 and IRS2 were measured using qPCR and found to be significantly upregulated in both control and IR EHT treated with perhexiline, suggesting that the inhibition of CPT-1 led to an increase in glucose metabolism. PGC1α expression was significantly increased in control EHT, but not in IR EHT. There was no significant difference observed in GLUT1 and FOXO1 expression. (**Figure 5.17**).

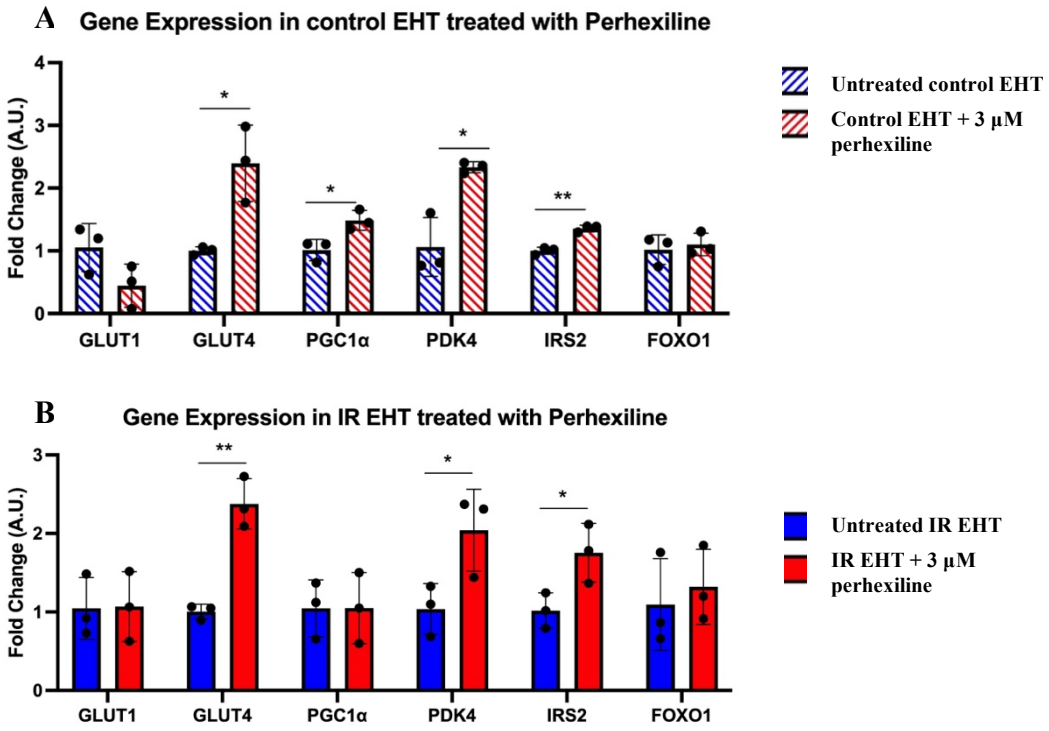


Figure 5.17 The effect of perhexiline on the expression of genes related to metabolism and insulin signalling in control and IR hiPSC-CM in EHT treated with 3 µM perhexiline for 24 hours

The gene expression of GLUT1, GLUT4, PGC1α, PDK4, IRS2, and FOXO1 in control EHT (A) and IR EHT (B). *, ** $p < 0.05, 0.01$ compared to untreated control or IR EHT, analysed using t-test, n=3.

The analysis of gene expression was expanded by presenting the data in groups, analysed by two-way ANOVA. GLUT4 was significantly upregulated in both control and IR EHT treated with perhexiline (Px). However, PDK4 was only significantly upregulated in control EHT treated with Px, while IRS2 was significantly upregulated in IR EHT treated with Px (**Figure 5.18**).

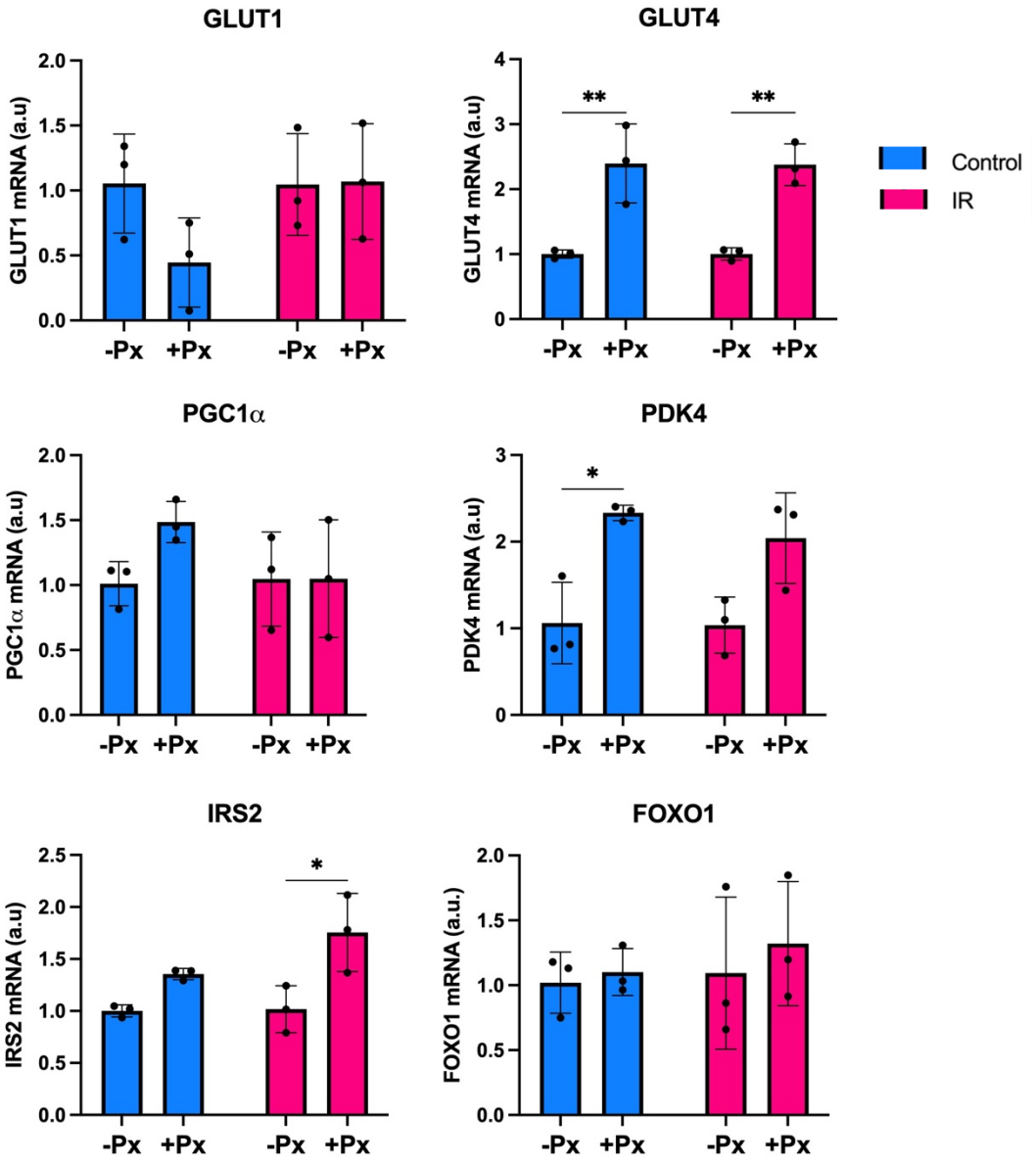


Figure 5.18 The effect of perhexiline on the expression of genes related to metabolism and insulin signalling in control and IR hiPSC-CM in EHT treated with perhexiline

The gene expression of GLUT1, GLUT4, PGC1α, PDK4, IRS2, and FOXO1 in control hiPSC-CMs in control EHT (normalised to untreated control EHT) and IR EHT (normalised to untreated IR EHT). *, ** $p < 0.05$, 0.01 analysed using two-way ANOVA followed by Tukey's test, n=3.

5.5.5 Molidustat activates HIF1α signalling and downstream metabolic adaptation in human cardiomyocytes

To determine whether molidustat could regulate HIF-dependent pathways in hiPSC-CMs, I tested the effect of two different concentration of molidustat (10 μM and 50 μM) on the

glucose consumption and lactate release in the cells. Untreated cells were incubated in normoxia (37ºC, 5% CO_2, 16% O_2) or hypoxia (37ºC, 5% CO_2, 2% O_2) for 16 hours and compared with molidustat-treated cells in normoxia. As before, there was substantial cell death seen in the hiPSC-CM under hypoxia. This was not seen with the molidustat-treated cells. Both concentrations of molidustat (10 µM and 50 µM) increased glucose consumption in hiPSC-CMs to the same level as that in hypoxia as shown in **Figure 5.19 (**Because of the degree of cell death, data are presented per mg of protein at the end of the experiment rather than per cell). Lactate release was also significantly higher after treatment with both concentrations of molidustat. This suggested that there was a stimulation of glycolysis as a result of PHD inhibition and HIF1α stabilisation.

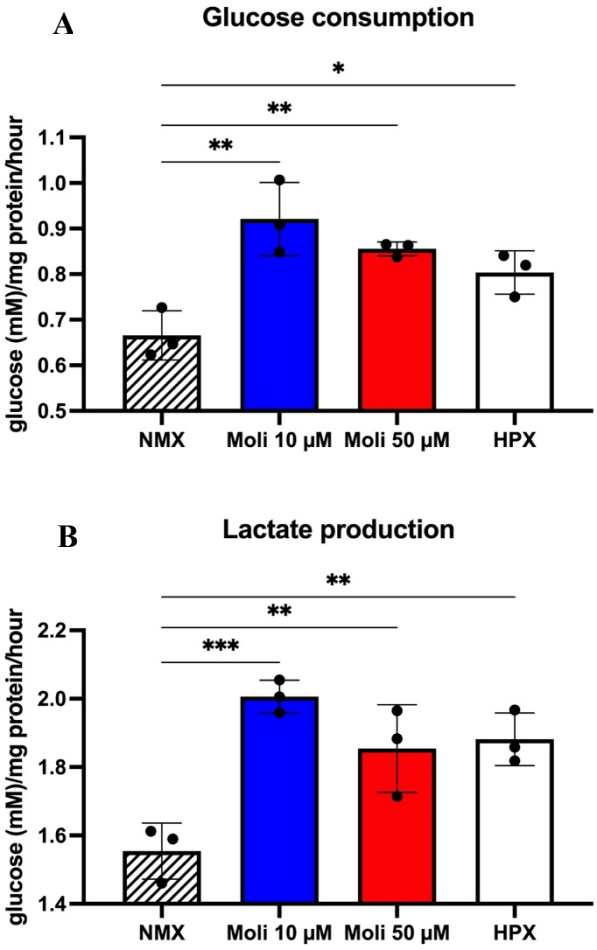


Figure 5.19 The treatment of hiPSC-CM in 2D monolayer with different concentration of molidustat

Glucose consumption (A) and lactate release (B) from untreated and molidustat (moli)-treated cardiomyocytes with concentration of 10 µM and 50 µM incubated in normoxia (NMX) and untreated cells in hypoxia (HPX). *, ** P < 0.05, 0.01 vs. NMX, n=3-6. Moli: molidustat.

I used 50 μM molidustat to further determine whether molidustat could regulate HIF-dependent pathways in hiPSC-CM. In control cardiomyocytes, HIF1α protein was barely detectable. However, following 16 hours exposure to molidustat there was a robust 30-fold stabilization of HIF1α protein (**Figure 5.20A**). Molidustat increased the expression of multiple genes involved in glycolysis, increasing glucose transporter GLUT1 sevenfold, and inducing a more than two-fold increase in the expression of aldolase A, enolase 1, and phosphoglycerate kinase (PGK)1 (**Figure 5.20 B–E**). This resulted in a two-fold increase in glucose metabolism and a 36% increase in lactate release in molidustat-treated human cardiomyocytes (**Figure 5.20 L and M**). Other downstream targets of HIF1α also changed accordingly, with molidustat increasing the expression of the mitophagy gene BNIP3 six-fold and prolyl hydroxylase domain 2 (PHD2) two-fold (**Figure 5.20 D and J**). Molidustat decreased HIF1α mRNA by 33%, FIH, and PGC1α, demonstrating a feedback loop from HIF1α protein stabilization (**Figure 5.20H**). These key findings in the IMR90 hiPSC-CM line were confirmed in the M180 hiPSC-CM line (**Figure 5.21A-J**).

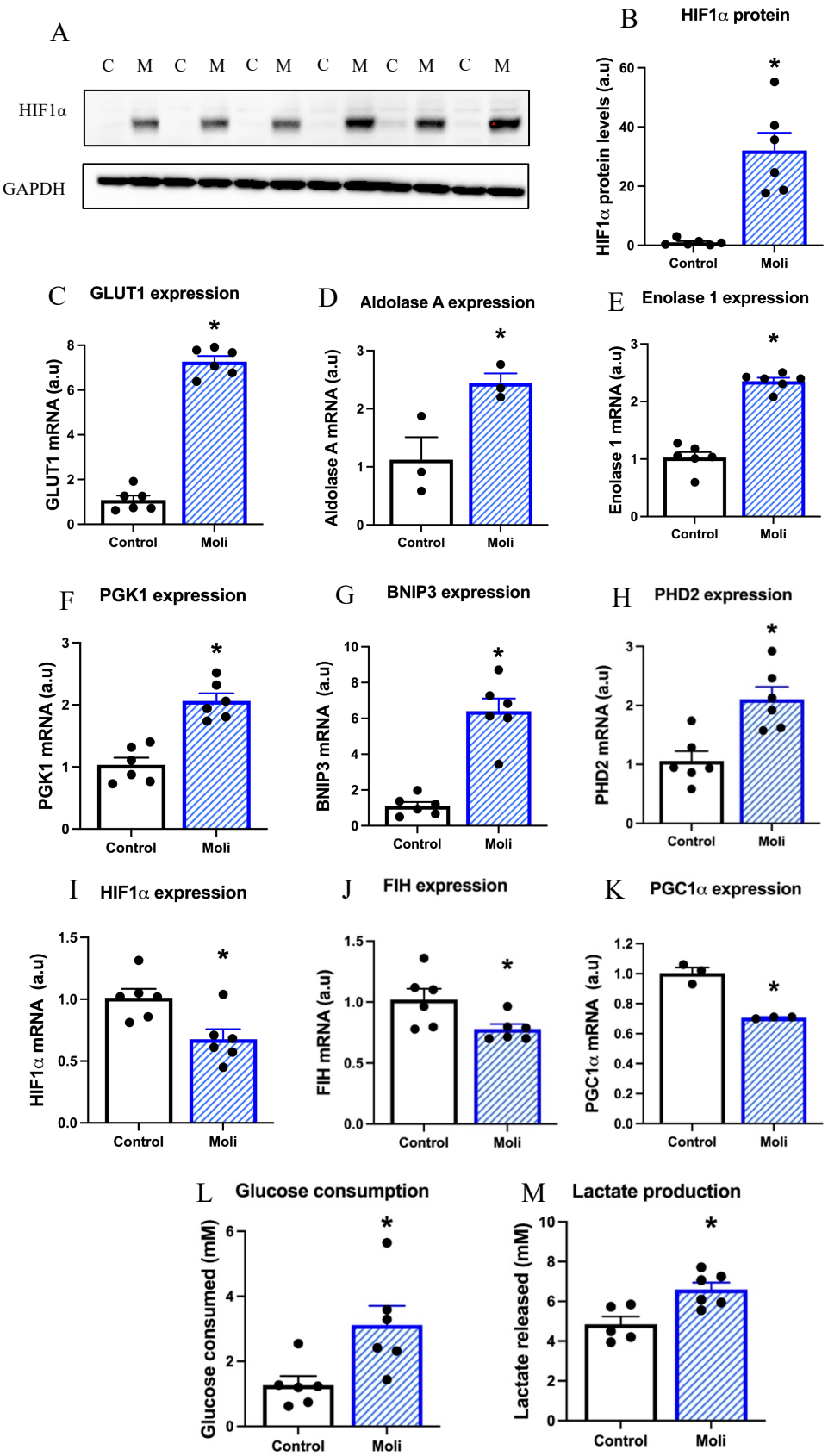


Figure 5.20 Molidustat increases HIF signaling in IMR90 hiPSC-CM

Hypoxia-inducible factor HIF-1α protein levels in control and molidustat-treated (Moli) hiPSC-CM of IMR90 line (A, B). Expression of HIF-1α target genes in control and Moli cardiomyocytes including GLUT1, aldolase A, enolase 1, PGK1, BNIP3, PHD2, FIH, and HIF-1α mRNA (C-K). Glucose consumption by and lactate release from control and Moli cardiomyocytes. *P<0.05 vs. control, n=6, a.u, arbitrary units.

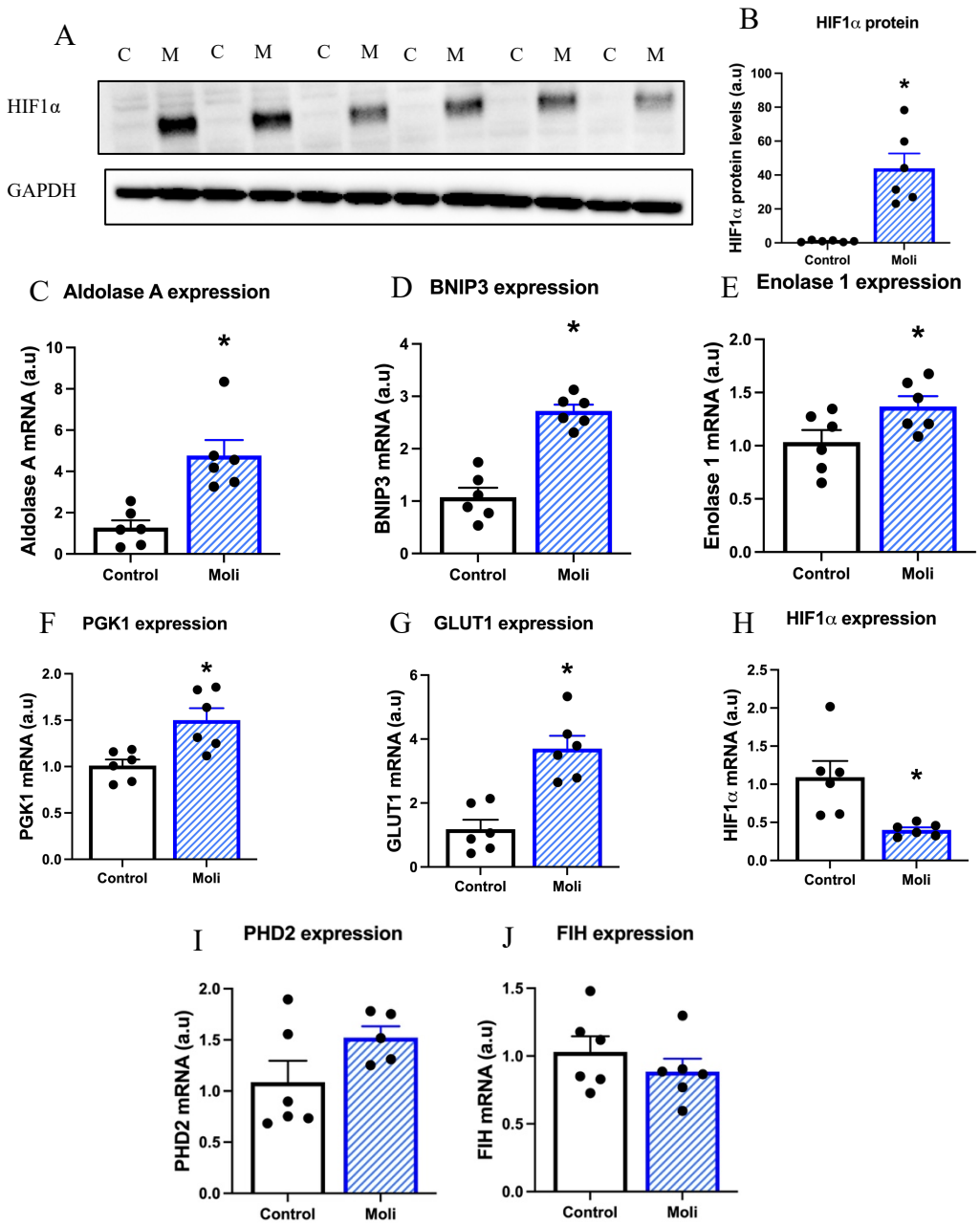


Figure 5.21 Molidustat increases HIF signaling in human cardiomyocytes M180 line

Hypoxia-inducible factor HIF-1α protein levels in control and molidustat-treated (Moli) M180 hiPSC-CM (A, B). Expression of HIF-1α target genes in control and Moli cardiomyocytes including GLUT1, aldolase A, enolase 1, PGK1, BNIP3, PHD2, FIH, and HIF1a mRNA (C-J). *P<0.05 vs. control, n=6, a.u, arbitrary units.

5.5.6 Molidustat overrides the blunted HIF signalling caused by insulin resistance

Exposure of control cardiomyocytes to hypoxia stabilized HIF1α protein and induced transcription of downstream HIF target genes BNIP3, GLUT1, aldolase A, and PHD2 (**Figure 5.22 C-D and F-G**). In contrast, when insulin-resistant human cardiomyocytes were exposed to the same hypoxic challenge, stabilization of HIF1α protein and induction of downstream gene targets were all suppressed, demonstrating a blunted adaptive response to hypoxia in insulin resistance (**Figure 5.22**). Addition of molidustat to insulin-resistant cells just prior to hypoxia improved hypoxic signalling. Molidustat increased HIF1α protein (**Figure 5.22 A-B**) and induced transcription of the HIF target genes (BNIP3, GLUT1, aldolase A, PGK1, and PHD2 (**Figure 5.22 C-G**), overriding the inhibitory effect of insulin resistance on hypoxic adaptation. Thus, molidustat provides a pharmacological approach to restore cardiac HIF signalling and hypoxic adaptation in insulin resistance. Interestingly, PGC1α expression was significantly lower in IR hypoxia compared to normoxia, but molidustat significantly increased PGC1α expression in IR hypoxia compared to untreated IR hypoxia.

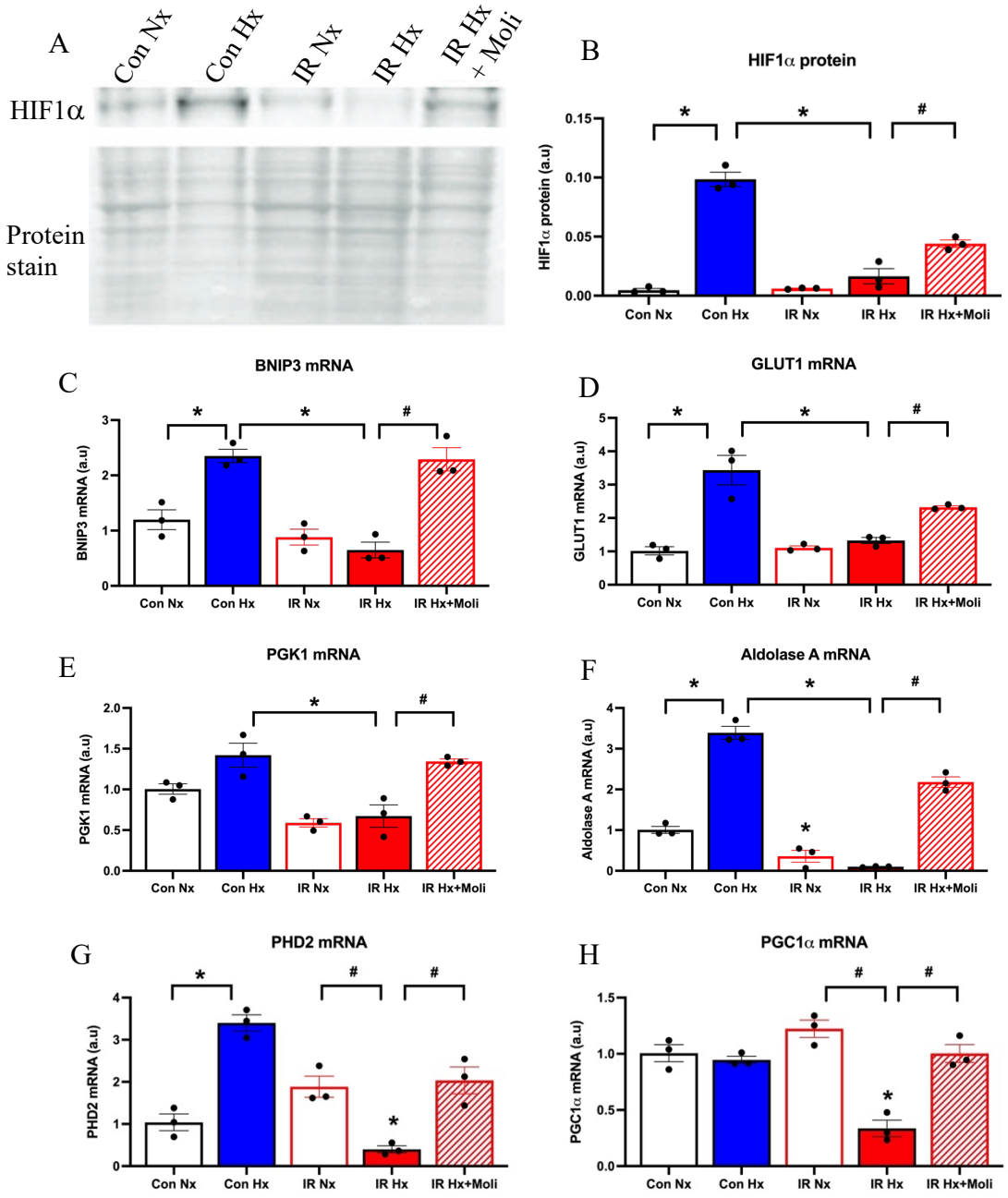


Figure 5.22 Molidustat overrides the impaired HIF signalling caused by insulin resistance in 2D monolayer

Hypoxia-inducible factor HIF1α protein levels in control (Con) and insulin-resistant (IR) human cardiomyocytes, cultured in a state of normoxia (Nx) or hypoxia (Hx) for 16 h. Molidustat (Moli) was added to insulin-resistant cells just prior to entry into hypoxic chamber (A). Expression of HIF1atarget genes under the respective conditions, including bcl2/adenovirus E1B 19kDa–interacting protein 3 (BNIP3), GLUT1, aldolase A, phosphoglycerate kinase 1 (PGK1), prolyl hydroxylase domain (PHD)2, and PGC1 α (C-H). * P <0.05 vs. respective control group; # P<0.05 vs. respective insulin-resistant group, n=3. a.u, arbitrary units.

The effect of molidustat on HIF stabilisation in hiPSC-CMs was further analysed in EHT. Control and IR EHTs were cultured in the presence or absence of 50 μM molidustat and were exposed to hypoxia (2% O2, 5% CO2) for 16h. HIF1α protein expression was significantly lower in IR EHT compared to control which agrees with the result from 2D monolayer, and the data shown in chapter 4. As seen with the cells in 2D, the expression of HIF1α was significantly higher in molidustat-treated IR EHT (**Figure 5.23**), indicating that molidustat successfully protected HIF1α from degradation.

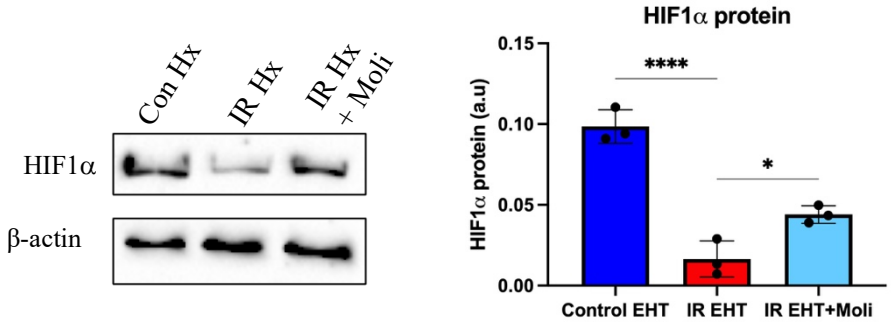


Figure 5.23 Molidustat overrides the impaired HIF signalling caused by insulin resistance in EHT

Hypoxia-inducible factor 1α (HIF1α) protein levels in control (Con) and insulin-resistant (IR) human cardiomyocytes, cultured in a state of normoxia (Nx) or hypoxia (Hx) for 16 h. Molidustat (Moli) was added to insulin-resistant cells just prior to entry into hypoxic chamber.

5.6 Discussion

5.6.1 The effect of isoliquiritigenin and isoprenaline in hiPSC-CMs cultured in 2D and EHT

Human iPSC-CMs have been utilised intensively for drug development since they were first discovered more than a decade ago[365–369]. However, despite the increasing number of groups studying hiPSC-CMs, it is still important to increase understanding of properties such as electrophysiology, contractile function, structure, and metabolism, especially if they are intended for drug testing. I first tested the response of our matured hiPSC-CM to isoliquiritigenin and isoprenaline to determine whether the hiPSC-CM were sufficiently mature to respond as expected to these drugs. A multielectrode array was used to assess the contractility profile of hiPSC-CM in 2D monolayer while Musclemotion was used for EHT (**Figure 5.6**). Although the two methods are very different, they can both detect changes in contractility in response to drug treatment, as previously shown by others[209,210,357]. I found that the cells in the 3D EHT were more sensitive to isoprenaline than the 2D monolayer, as shown by lower effective concentration needed to induce the changes in the heart rate. This is likely due to the increased maturity of the cells in the EHT which may have increased the expression of β-adrenergic receptors since the immature hiPSC-CMs showed an aberrant adrenergic response[232]. The EHTs were seen to respond to drugs which can reduce or increase heart rate.

5.6.2 The effect of metformin on insulin-resistant hiPSC-CM in 2D and EHT

Diabetic cardiomyopathy (DbCM) caused by hyperlipidaemia, hyperglycaemia, and insulin resistance results in contractile dysfunction, reduced mitochondrial Ca^{2+} content and altered mitochondrial bioenergetics[306,370]. Metformin is a commonly used drug to reduce hyperglycaemia, but whether it has a direct effect on cardiomyocyte function is a matter of debate, hence my interest in investigating metformin's effect in hiPSC-CM. Although the

most significant changes were seen at a concentration of 5 mM, this was felt to be above the physiological range used in therapy, so the lower concentration of 0.5 mM was used for further experiments, this dose had induced changes in lactate production and expression of GLUT1 and GLUT4 and had increased levels of Akt phosphorylation in control hiPSC-CM (**Figure 5.9**). Metformin has been shown to be protective in the perfused rat heart by phosphorylation of Akt which inhibited mitochondrial permeability transition pore opening[371]. More study on GLUT4 localisation could be useful to elucidate the direct effect of metformin on enhancing the insulin sensitivity. Literature showed that immature hiPSC-CMs do not exhibit insulin-stimulated glucose uptake and immunoblot analysis and GLUT4-HA were performed to elucidate[140]. Similar experiments could be useful to be performed in elucidating GLUT4 localisation and glucose transport beyond qPCR.

In the previous chapter, I showed that insulin resistance affects the contractile profile in the EHT by increasing the contraction duration which made the IR EHTs beat more slowly. Metformin significantly decreased the contraction duration, peak-to-peak time, and time to peak in insulin-resistant EHT, to values comparable to those in control EHT. This may result from the activation of AMPK that was demonstrated by Western blot, with AMPK activation known to cause increasing influx of Ca^{2+} into mitochondria[372–376]. This result showed that insulin-resistant hiPSC-CM in EHT is a suitable model to study the contractility of human cardiomyocytes and may provide better understanding on how metformin affects the heart.

5.6.3 The effect of Perhexiline on insulin-resistant hiPSC-CM in 2D and EHT

Metabolic modulators have been proposed for the insulin resistant heart by promoting glucose metabolism and decreasing metabolism of free fatty acids[377]. Perhexiline is a metabolic modulator that can inhibit carnitine o-palmitoyl transferase 1 (CPT-1), inhibit fat oxidation and via the Randle cycle promote glucose metabolism[327]. It is currently used as an anti-ischemia agent for prophylactic anti-anginal treatment. Here, I demonstrated the

utilisation of insulin resistant hiPSC-CM in 2D monolayer and EHT to explore the effect of perhexiline on insulin resistant cardiomyocytes.

Perhexiline treatment did not affect glucose consumption in control hiPSC-CM, but I found that 3 μM perhexiline increased glucose consumption and lactate release in the IR hiPSC-CM. This data was also supported by the PGC1α data which showed a small but significant increase after 3 μM perhexiline treatment, although there was a much greater increase in PGC1α expression at higher concentrations of perhexiline. PGC1α protein expression is elevated in the diabetic heart because of high lipid uptake which leads to higher fatty acid oxidation[378]. As perhexiline inhibits CPT-1, this would suggest that lipids are still entering the cardiomyocytes and increasing PGC1α, and we would speculate this could result in a disconnect between a drive to increase mitochondrial fatty acid oxidation and an ability to do this in the presence of a CPT-1 inhibitor. Unfortunately, time limitations due to COVID-19 pandemic interrupted these experiments and meant we could not measure fatty acid oxidation in the perhexiline treated cells, which is the obvious next experiment. Nevertheless, the experiment in hiPSC-CM 2D monolayer validated the pleotropic effect of perhexiline in human heart. Gene expression determination in control and IR EHT after treatment with 3 μM perhexiline showed an increase in expression of GLUT4, PDK4 and IRS2, consistent with a switch from fatty acid to glucose utilisation.

5.6.4 Molidustat can restore HIF signalling in hiPSC-CM in 2D and EHT

It has been shown by us[328] and by others[352] that HIF signalling is blunted in the insulin resistant heart, which could have devastating clinical implications for cardiac function during ischemia. Previous work from our lab has shown that elevated fatty acids in diabetes suppresses myocardial succinate concentrations. Succinate activates HIF by inhibiting the PHD enzymes needed for HIF degradation[256]. Previously I showed that HIF signalling is also suppressed in insulin-resistant hiPSC-CMs cardiomyocytes. In this chapter, I used the

insulin-resistant model to test molidustat, a PHD inhibitor, to improve HIF signalling in the insulin resistance condition.

Molidustat (BAY85-3934) is a PHD inhibitor that currently is in phase III clinical trial to treat anaemia associated with chronic kidney disease and could potentially be repurposed for the diabetic heart. Having confirmed a dose that increased glucose uptake and lactate release, I showed that molidustat treatment stabilised HIF1α indicated by significantly higher levels of HIF1α protein and expression of HIF target genes expression even where oxygen was present. Treatment of insulin resistant hiPSC-CM under hypoxia with molidustat restored expression of genes associated with glycolysis to similar levels to those seen in control cells under hypoxia. These results confirmed data found by others in our group in the diabetic rat heart thereby providing translational support to research showing that molidustat provides a pharmacological approach to restore cardiac HIF signaling and hypoxic adaptation in insulin resistance[328].

5.7 Conclusion

Human iPSC-CMs made insulin resistant by manipulating the cell culture media were shown to be responsive to a range of drugs at various stages of the developmental pipeline. Data acquired from these human cardiomyocytes can validate experiments in animal models for translation to the clinic and can show the direct effect of drugs on beating cardiomyocytes isolated from other systemic effects. These cells can be a valuable predictive tool to speed up the drug discovery process and improve candidate drug success in clinical trials.

6

Modelling the effect of Duchenne muscular dystrophy on human iPSC-CM in 2D and EHT

CHAPTER 6

6. MODELLING THE EFFECT OF DUCHENNE MUSCULAR DYSTROPHY ON HUMAN IPSC-CM IN 2D AND EHT

6.1 Abstract

Duchenne muscular dystrophy (DMD) is an X-linked recessive disorder and progressive muscle-wasting disease. Recent work in patients and animals suggest that dystrophic muscle cells may become insulin resistant and exhibit abnormal glucose metabolism. Here, I aimed to explore changes in substrate metabolism in human induced pluripotent stem cell derived cardiomyocytes (hiPSC-CM) in 2D and 3D engineered heart tissue (EHT) from DMD patients, compared with healthy controls. This model may provide a testbed for pharmacological treatments aimed at restoring insulin sensitivity in the heart of DMD patients. I found that the full-length dystrophin isoform, Dp427m, was expressed in control hiPSC-CM but not in those from DMD patients, confirming that the mutation was retained after differentiation. Structural and metabolic maturation of DMD hiPSC-CMs appeared delayed in comparison to control and, in EHT, DMD hiPSC-CMs showed reduced contraction speed and force. The glycolytic rate of control hiPSC-CMs was significantly increased from 85 to 130 nmol/10^6/hour cells in response to insulin stimulation, whereas there was no significant increase in the glycolytic rate of DMD hiPSC-CMs. The absence of dystrophin resulted in delayed maturation of the cardiomyocytes and an impaired response to insulin, confirming results seen in animal models and patients. Therefore, hiPSC-CMs can be used to model DMD in the heart and provide the opportunity to investigate dystrophin deficiency-mediated mechanisms responsible for cardiac insulin resistance.

6.2 Introduction

Duchenne muscular dystrophy (DMD) is a recessive disorder encoded by the dystrophin gene on chromosome Xp21 (mostly between exons 45-55) causing a non-functional dystrophin protein to be produced[96,379]. Dystrophin provides strength and stability to the muscle, acting as the cellular scaffold[380,381]. Metabolic alterations have been documented in humans, dogs, and mice with DMD, with insulin resistance and abnormal glucose metabolism as a potentially direct consequence of dystrophin deficiency rather than a side effect of treatments. One particular interesting finding is the lower glucose uptake rates in the perfused mouse DMD heart in response to insulin[99] as this suggests myocardial insulin resistance[382]. However, this is a relatively unexplored area, requiring further research to determine what is causing these metabolic changes.

Currently, there is no cure for DMD, but there have been many approaches to investigate how to re-express functional dystrophin protein[383]. There is significant interest in utilising gene editing such as using adeno-associated viruses as a viral vector to provide a healthy copy of the micro-dystrophin gene or to fix the non-functional copy using CRISPR-Cas9 gene editing[384–386]. Another method is exon skipping by using antisense oligonucleotides to remove the exon inhibiting it from being encoded. This method resulted in a slightly shorter but functioning dystrophin[383,387]. However, these approaches are hindered by the size of what can be transferred within the vector, low accuracy, and low efficiency of the methods[388]. Although this method increases the dystrophin expression, this is not always followed by physiological improvements[389].

An alternative potential treatment for DMD is to reduce the effect of the lack of dystrophin by using pharmacological agents. Metformin has been demonstrated to reduce the muscle damage, increasing muscle strength, and increasing the activation of AMPK[390–393]. Metformin has also been shown to be effective in decreasing muscle damage in human DMD

patients. However, whether this is related to the effect of metformin on sensitizing the insulin response in cardiomyocytes is unknown.

Various models have been used to study DMD, the most common being the mdx mouse which lacks full-length dystrophin. The limitation of this rodent model is the minimal clinical symptoms in younger mice and higher life expectancy (25% decrease in lifespan compared to 75% in human DMD)[111]. Canine DMD (cDMD) is able to replicate the clinical courses of human DMD such as poor regeneration of muscle, however young cDMD dogs do not usually suffer complete loss of ambulation[394]. A human derived in vitro system can have potential benefit to study the DMD heart in a dish, and to understand the relationship between abnormal metabolism, structure, and function in the genetic disease.

6.3 Chapter aims

The aim of this project is to utilise hiPSC-CMs in 2D and 3D (EHT) investigating insulin resistance in the human heart of DMD patients. Furthermore, this model will be used to investigate the potential for metformin to improve the metabolic alterations found in the DMD heart.

6.4 Materials and methods

Materials and methods have previously been described in the chapter 2 general methods. The healthy cell line used for the experiment was IMR90 as control and DMD cell line used for the experiments was M202 cell line with deletion in exons 8 – 43 which was kindly provided by Emmanuelle Massourides (CECS/I-STEM, France) under a Material Transfer Agreement (MTA). The hiPSCs were cultured and differentiated into hiPSC-CM using the same methods as previously described. The hiPSC-CMs cultured in the RB+ media (containing 11 mM glucose and little/no fatty acid) were immature hiPSC-CM, those cultured in the media containing 5 mM glucose and 400 μM oleic acid (OA) were mature hiPSC-CM. The generation of engineered heart tissue (EHT) and characterization and

measurement using qPCR, Western blot, radiolabeled flux measurement, Musclemotion are as described in chapter 2 general methods. For the metformin experiment, the control and DMD cells in 2D monolayer were treated with 0.5 mM at 37°C and 5% CO_2 for 24 hours before isolating the cells for Western blotting.

6.5 Results

6.5.1 Investigating the effect of Duchenne muscular dystrophy (DMD) on metabolism in the heart using hiPSC-CMs model in 2D and EHTs

This chapter will describe experiments using hiPSC-CMs from Duchenne muscular dystrophy patients, which are hypothesised to have an insulin resistant phenotype linked to a genetic mutation in dystrophin. This work was performed in collaboration with undergraduate students, Anna McQueen and Madeline Oshodi.

6.5.2 Validation of dystrophin mutation in hiPSC-CM

The M202 DMD cell line was from a patient with a deletion in exons 8 – 43 of the dystrophin gene (**Figure 6.1)** and these cells were compared with the IMR90 cell line as a control. To validate this reported deletion, we used qPCR to look at expression of different dystrophin isoforms and exon junctions. Comparisons were made between control and DMD hiPSC at different stages of maturation: as immature cardiomyocytes cultured in RB+ (containing 11 mM glucose and little/no fatty acid), as mature cardiomyocytes cultured with the addition of oleic acid as described in chapter 3, and in the DMD cells, we also compared hiPSC-CM with the undifferentiated hiPSC.

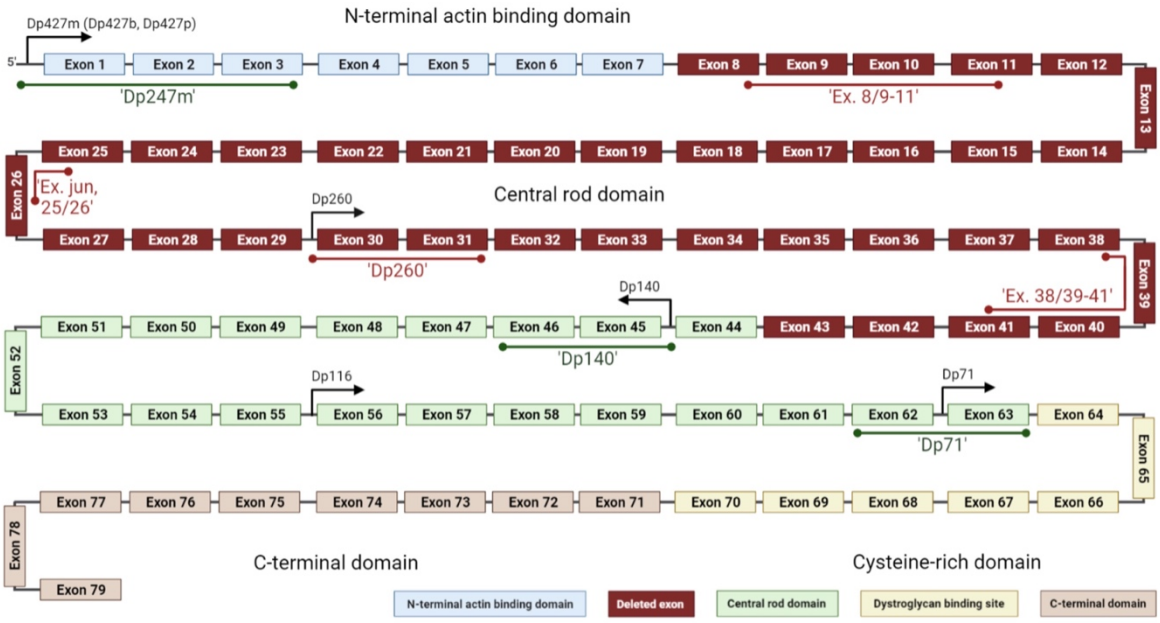


Figure 6.1 Dystrophin gene sequence in hiPSC-CM from DMD patient of M202cell line, deletion on exon 8-43
Dystrophin exon map of hiPSC from DMD patient of M202cell line with deletion in exon 8-43. Non deleted region (blue, green, yellow, and brown) and deleted region (red).

The full-length dystrophin isoform, Dp427m, was expressed in both mature and immature control cells (**Figure 6.2 A**). In contrast it was absent in the immature DMD and iPSC DMD. We used primers for isoforms Dp140 and Dp71 which are outside the deletion of exons 8-43 and should be present in all cell line. We could confirm that Dp140 and Dp71 were expressed in both cell lines (**Figure 6.2 B-C**). High fold change of Dp140 on DMD iPSC was observed due to technical issue. We also used primers for exons 8/9-11, Dp260 isoform, exons 38/39-41, and exon junction 25/26 to indicate the full-length dystrophin. Although there was a high level of variability in some samples, which meant that not all differences were statistically significant, the primers did not detect expression in DMD cells, but full-length dystrophin was confirmed in the control cells (**Figure 6.2 D-G**).

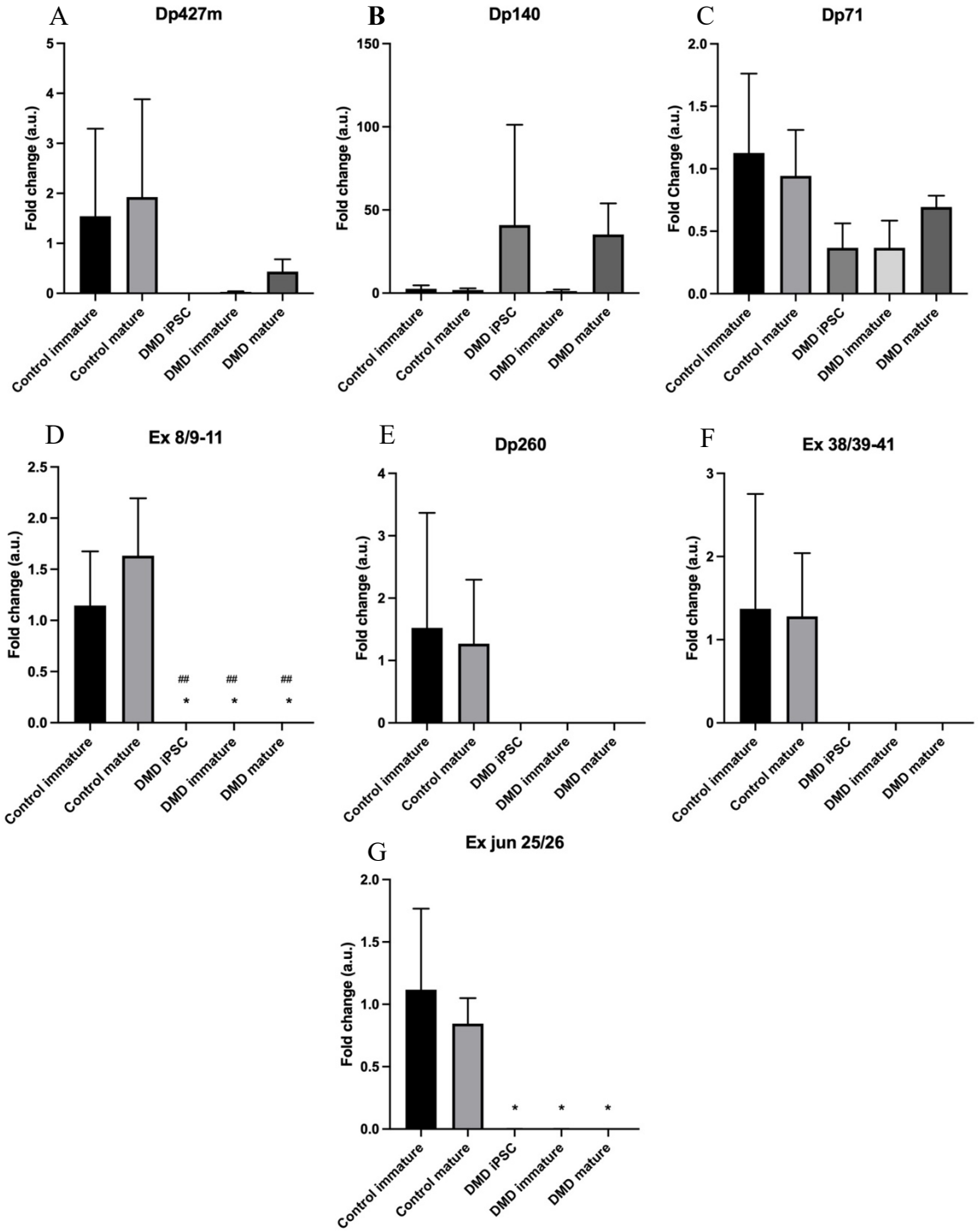


Figure 6.2 The expression of the genes encoded dystrophin protein in control versus DMD cells

Dystrophin protein expression as shown in **Figure 6.1** with the colour coded label. Detection of regions of dystrophin mRNA of DMD cell by qPCR compared to hiPSC-CMs from control cell line (A-G). *, ** $p<0.05$, <0.01 respectively, compared with control imamture hiPSC-CMs, ## $p<0.01$ compared with control mature hiPSC-CM, analysed using one-way ANOVA followed by Tukey's test, n=3.

6.5.3 Characterisation of the structure of hiPSC-CM from DMD patients

The exon deletion in the dystrophin sequence should result in the loss of dystrophin expression, which might affect the structural integrity of the hiPSC-CM. We initially performed qPCR analysis to look at the expression of the cardiomyocyte genes NKX2.5, cardiac muscle cTnT, ventricular myosin light chain 2 (MLC2v), and myosin heavy chain 6 (MYH6). Moreover, connexin-43 (Cx-43) expression, a gap junction protein that is found in mammalian cell such as hiPSCs and hiPSC-CMs and required for reprogramming to hiPSC, was also analysed. NKX2.5 and cTnT were lower in the immature DMD cells than in the immature control cells. Although expression did increase as the DMD cells were matured, NKX2.5 expression remained lower than in mature control cells **(Figure 6.3 A-B)**. Overall, there were no differences in expression of MLC2v, MYH6 and Cx-43 between cardiomyocytes from control or DMD patients (**Figure 6.3 C-E**). Interestingly, expression of MLC2v expression in mature cells was substantially increased compared to immature cells from both cell lines. Expression of connexin-43 (Cx-43) was significantly higher in DMD hiPSC than DMD hiPSC-CM, suggesting it decreased with differentiation.

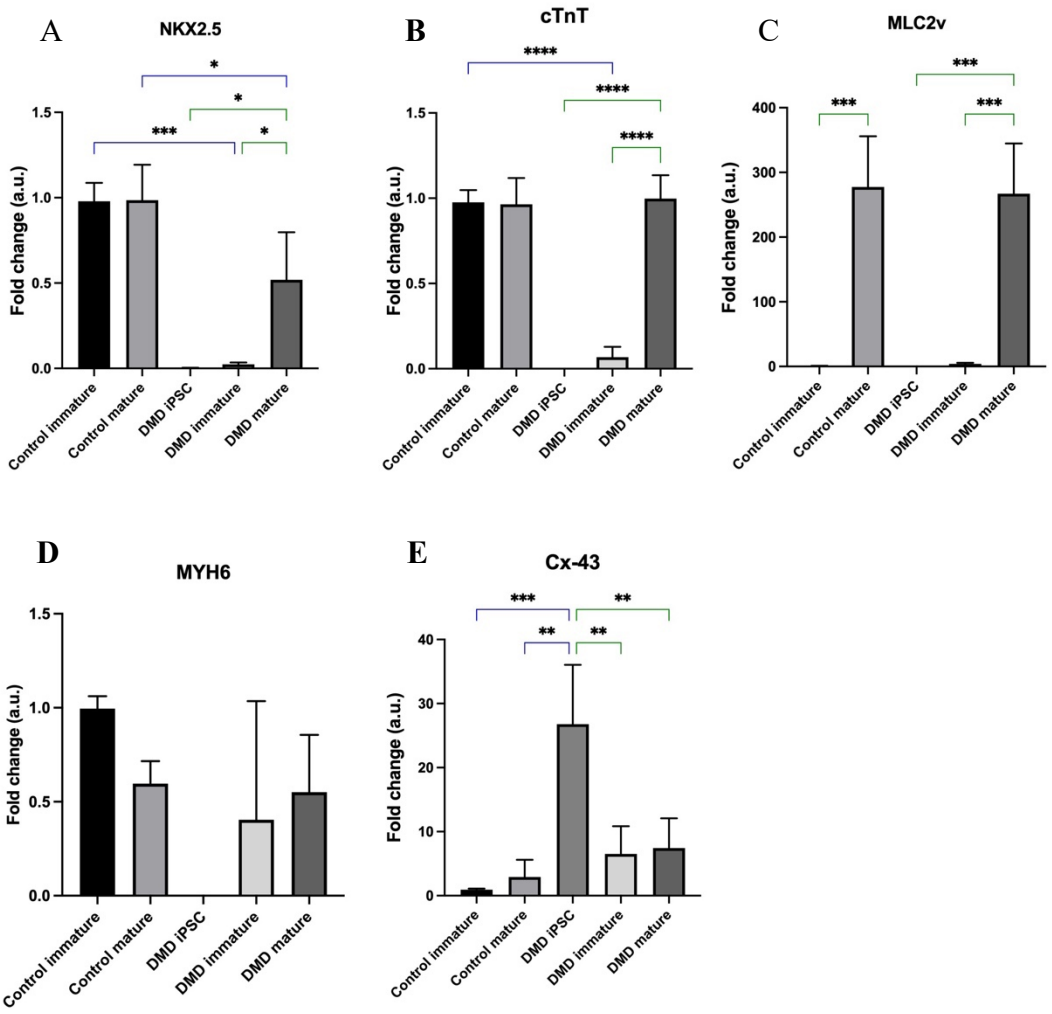
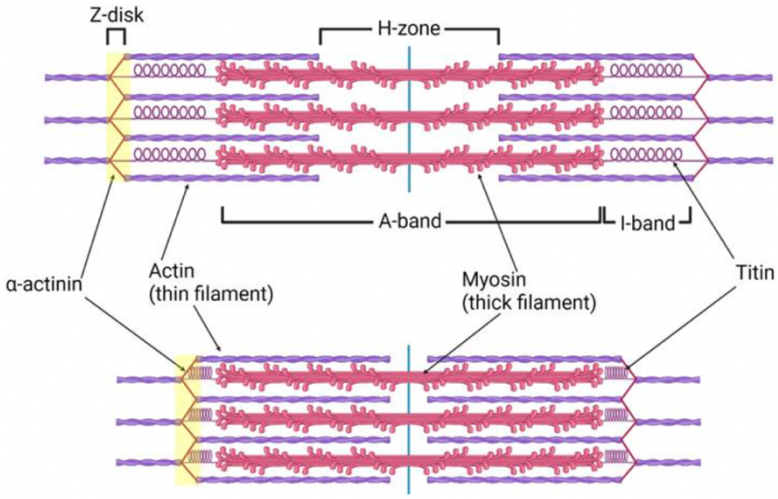


Figure 6.3 Comparison of the expression of structural cardiomyocytes genes in the control and DMD cells

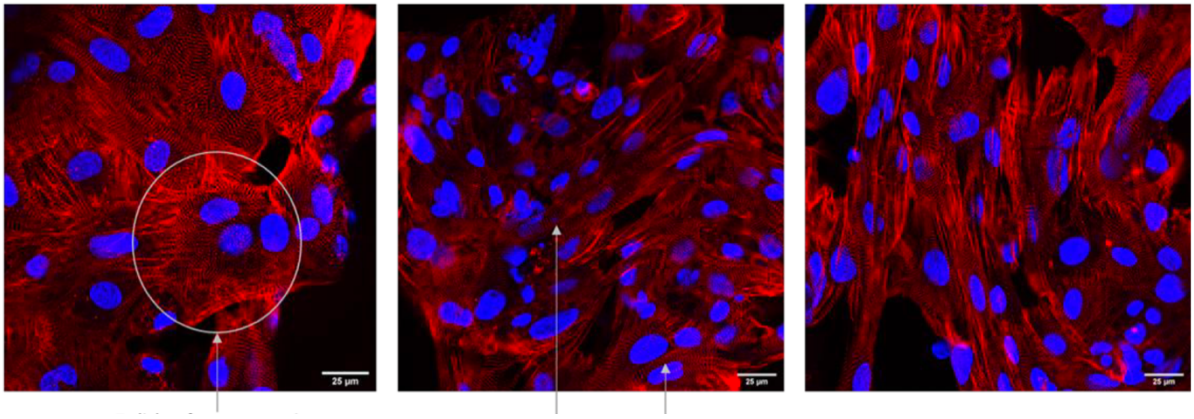
The structural genes of cardiomyocytes including NKX2.5, cTnT, MLC2v, MYH6, and Cx-43 expression were analysed by qPCR. *, ** P<0.05, <0.01 respectively, compared with immature IMR90 iPSC-CMs using one-way ANOVA followed by a Tukey's test, n=3.

We used confocal microscopy to visualise the structure and alignment of the sarcomeres of cardiomyocytes from mature control and DMD cells cultured in the media containing OA (mature cardiomyocytes). As shown in **Figure 6.4,** although relatively aligned sarcomeres were found in hiPSC-CM from both control and DMD cells in 2D monolayer, some of the cells from both cell lines were not well aligned or well-organised, suggesting that these cells were structurally not fully matured in 2D monolayer.

A



B **Mature control cells in 2D monolayer**



C **Mature DMD cells in 2D monolayer**

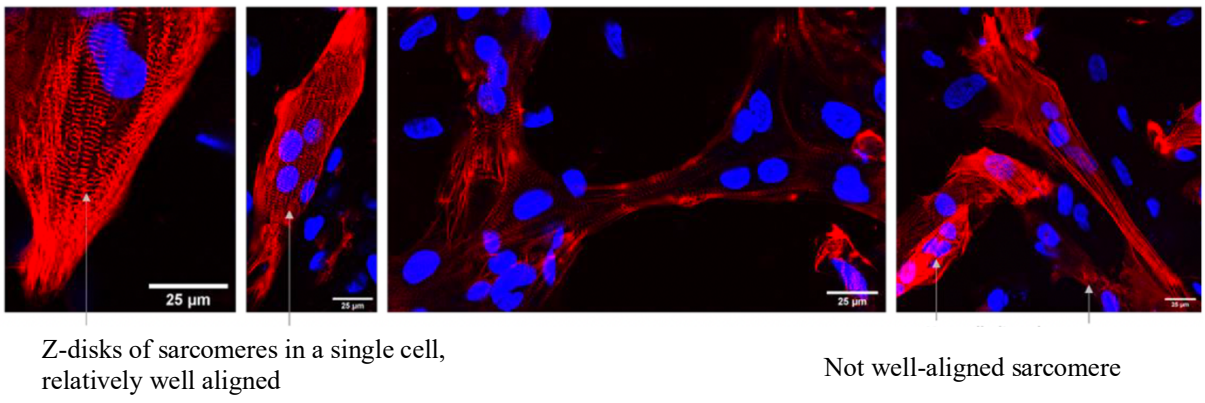


Figure 6.4 Images of hiPSC-CMs stained with anti α-actinin antibody using confocal microscopy
Basic schematic of the sarcomere composed of thick filament (myosin) and thin filaments (actin) (A). Confocal microscopy images of mature hiPSC-CM from control and DMD cell line (B-C). Nuclei (DAPI stain, blue) and α-actinin (Alexa Fluor 594 and anti-α-actinin antibody, red).

6.5.4 Metabolism in hiPSC-CM from DMD patients

One of the aims of the projects was to assess if the insulin resistance found in animal models of DMD could also be observed in hiPSC-CMs. We analysed the metabolic gene expression of GLUT4, PDK1, IRS2, PGC1α, CD36, and PDK4 using qPCR on both immature and mature hiPSC-CMs from control and DMD. For GLUT4 and PDK1, the immature DMD cells had lower expression of these glucose-related genes **(Figure 6.5 A-B)**. However, the control cells decreased expression with increasing maturation, but in contrast, the DMD cells increased their mRNA expression with maturity. Maturing the DMD cells promoted large increases in IRS2 and PGC1α (**Figure 6.5 D**), which was not seen in control cells. In contrast, CD36 and PDK4 showed similar profiles between group (**Figure 6.5 E-F**).

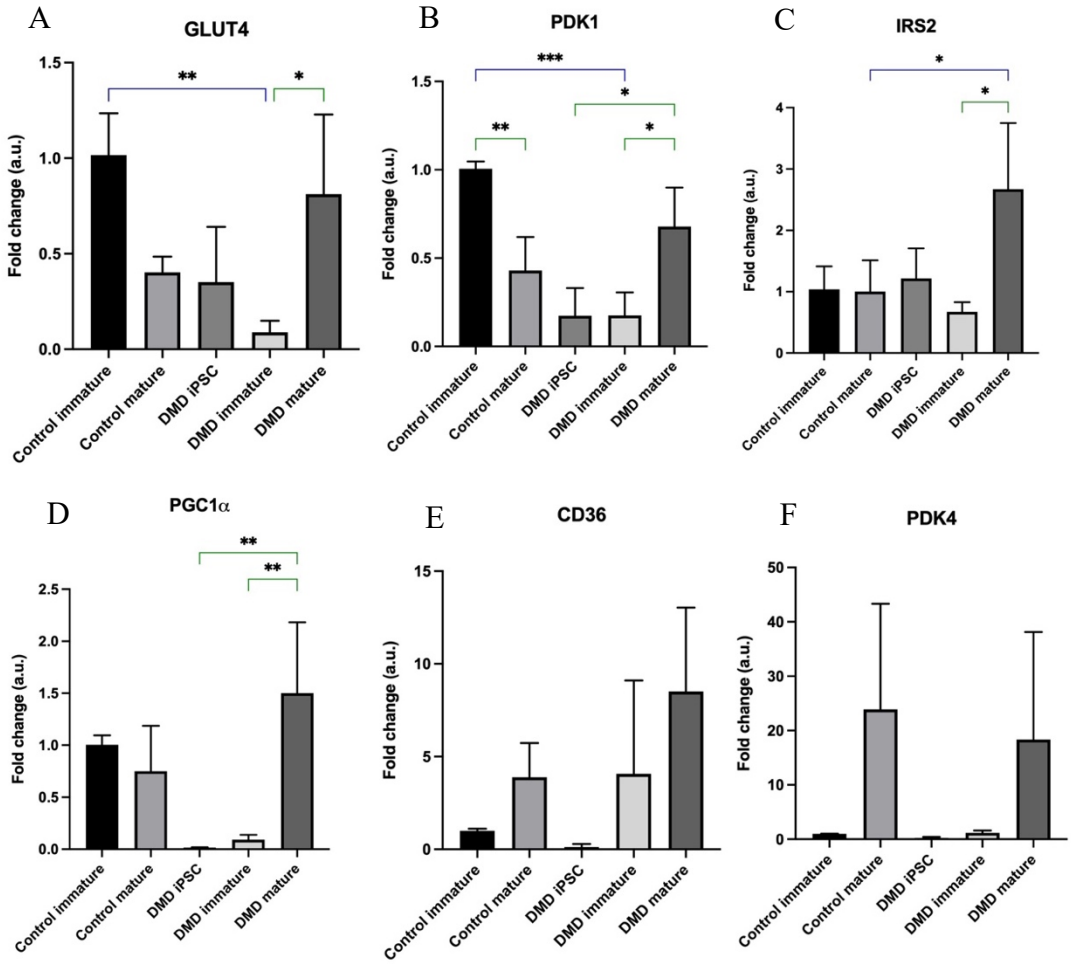


Figure 6.5 Expression of metabolism-related genes in immature and mature cardiomyocytes from control and DMD cells

The metabolic related genes of cardiomyocytes including GLUT4, PDK1, IRS2, PGC1α, CD36, and PDK4 expression were analysed by qPCR. *, **, *** P<0.05, <0.01, <0.005 respectively, compared with immature DMD iPSC-CMs using one-way ANOVA followed by a Tukey's test, n=3.

Glycolytic flux in the matured hiPSC-CM from control and DMD hiPSC-CM was measured in the presence and absence of insulin (**Figure 6.6**). In response to insulin stimulation there was an upregulation of glycolytic flux in control cells. However, in DMD cells insulin had no effect on glycolytic rate, indicating that DMD cardiomyocytes were insulin resistant.

The pAkt/Akt ratio significantly increased in the control hiPSC-CMs in the presence of insulin compared to that in control cells without insulin, indicating that more Akt is phosphorylated in response to insulin (**Figure 6.6 C-D**). In contrast, the pAkt/Akt ratio was not significantly different in DMD hiPSC-CMs in the absence and presence of insulin. Unexpectedly, pAkt/Akt/tubulin was significantly higher in DMD hiPSC-CMs at baseline (without insulin) compared with control cells. This indicates that DMD cells had raised pAkt levels in the absence of insulin, but this did not result in high glycolytic flux.

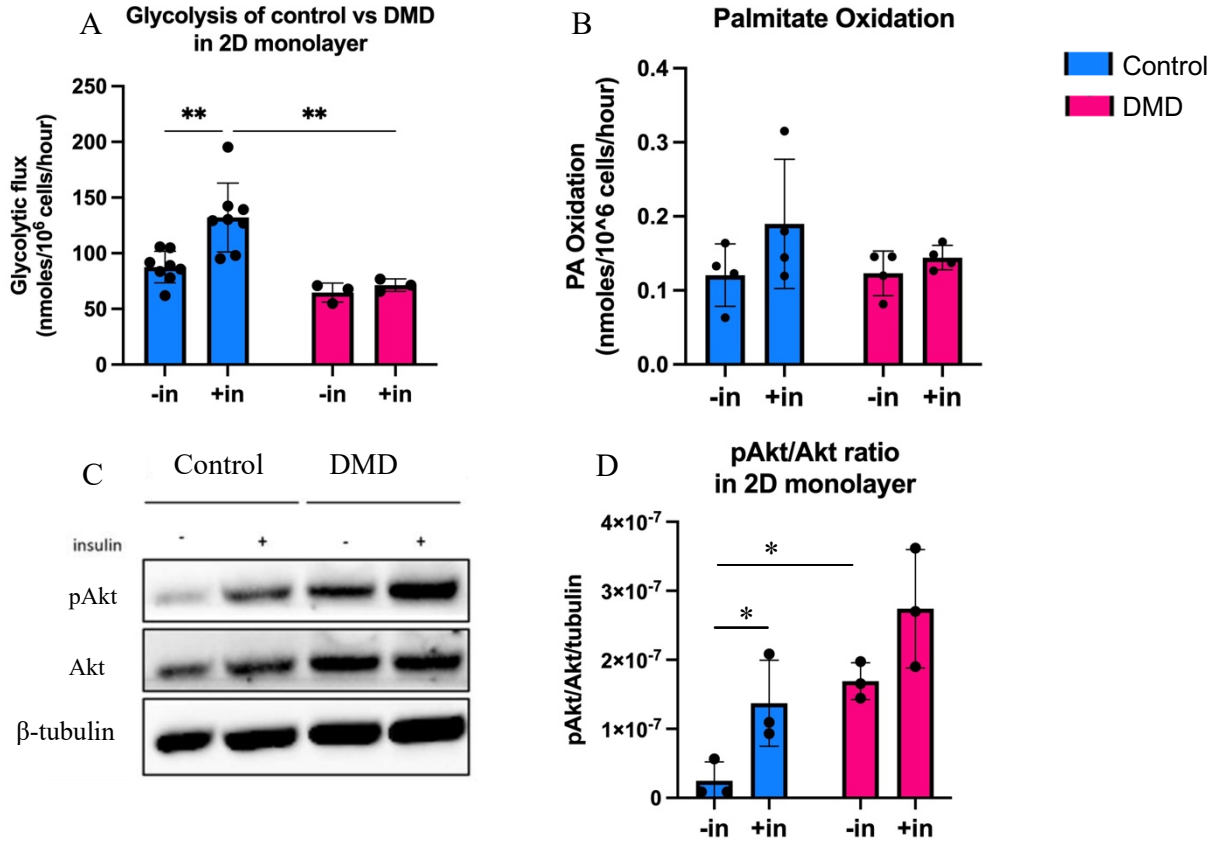


Figure 6.6 Human iPSC-CMs response to insulin stimulation in control and DMD cells

Glucose consumption (nmoles/min/10^5 cells) through glycolysis in the absence and presence of insulin stimulation in mature control and DMD hiPSC-CMs (A), palmitate oxidation (B), Western blot of pAkt, Akt, and β-tubulin (loading control) in control and DMD hiPSC-CMs in absence and presence of insulin (C) and the quantification (D), Plot of pAkt/Akt/β-tubulin in each sample. *, ** P<0.05, <0.01, respectively, analysed using two-way ANOVA followed by a Tukey's test, n=3.

6.5.5 The contractility of hiPSC-CM from control and DMD

The contractility profile of hiPSC-CM from DMD patients was compared to that from the control hiPSC-CMs, measured using Musclemotion, both in 2D monolayer and EHT. When cultured in 2D monolayer, the contractility data was very variable and no significant differences were detected in contraction duration, relaxation time, and time to peak were detected (**Figure 6.7 A, D, F**). Peak amplitude, peak-to-peak time, and contraction amplitude of DMD hiPSC-CM were significantly lower compared with control hiPSC-CM (**Figure 6.7 B-C, E**).

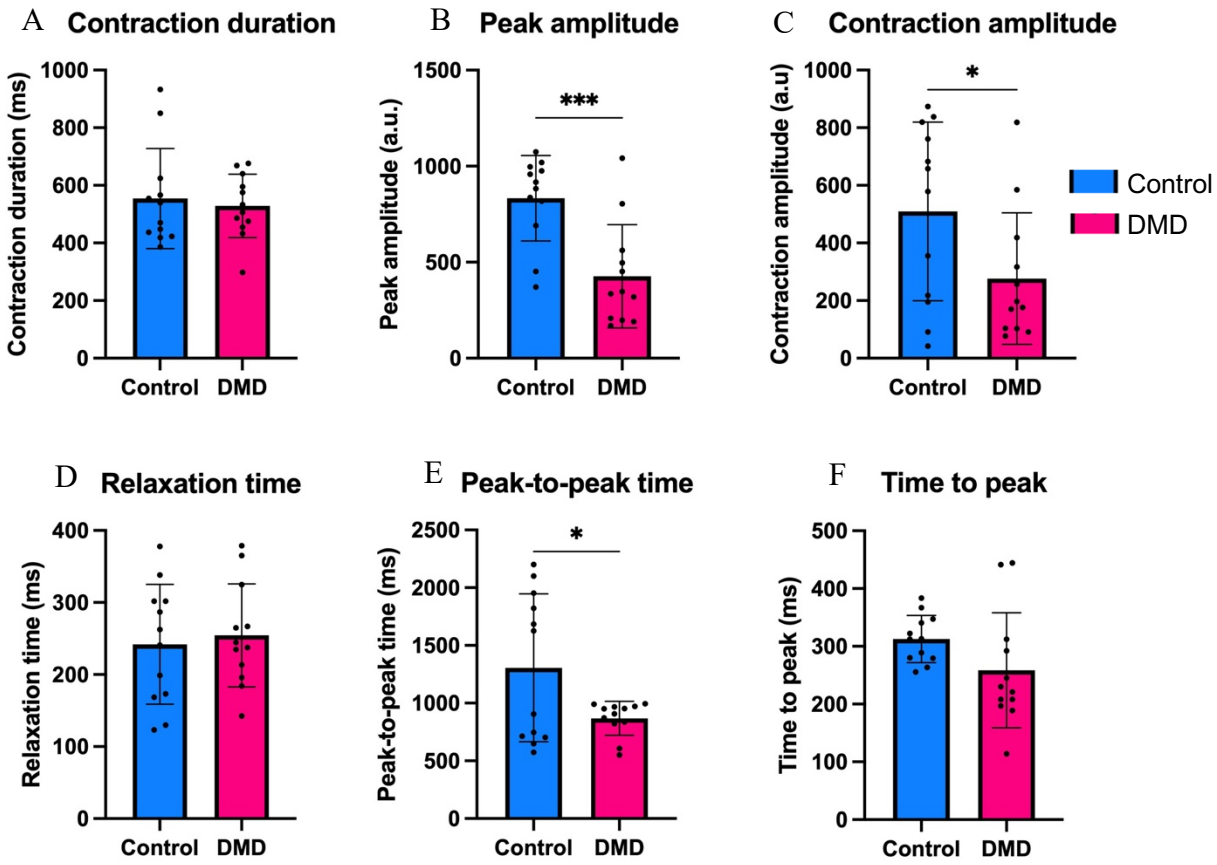


Figure 6.7 Contraction parameters of hiPSC-CMs from DMD patient and control in 2D monolayer determined by Musclemotion

Contraction parameters including contraction duration (A), peak amplitude (B), contraction amplitude (C), relaxation time (D), peak-to-peak time (E), time to peak (F) of hiPSC-CMs in 2D monolayer cultured with maturation media (containing 5 mM glucose and 400 µM OA). *, *** $P<0.05$, <0.001 respectively, compared with control hiPSC-CMs using t-test, n=12.

In EHT there was no difference in the contraction duration (**Figure 6.8 A**) between the two cell lines. In addition, no significant difference was found in relaxation time, peak-to-peak time, and time to peak between control and DMD (**Figure 6.8 D-F**). However, peak amplitude and contraction amplitude showed significantly lower values in EHT from DMD hiPSC-CM compared with EHT from control cells, suggesting that the dystrophic EHT were not beating as strongly as those from the control hiPSC-CM (**Figure 6.8 B-C**).

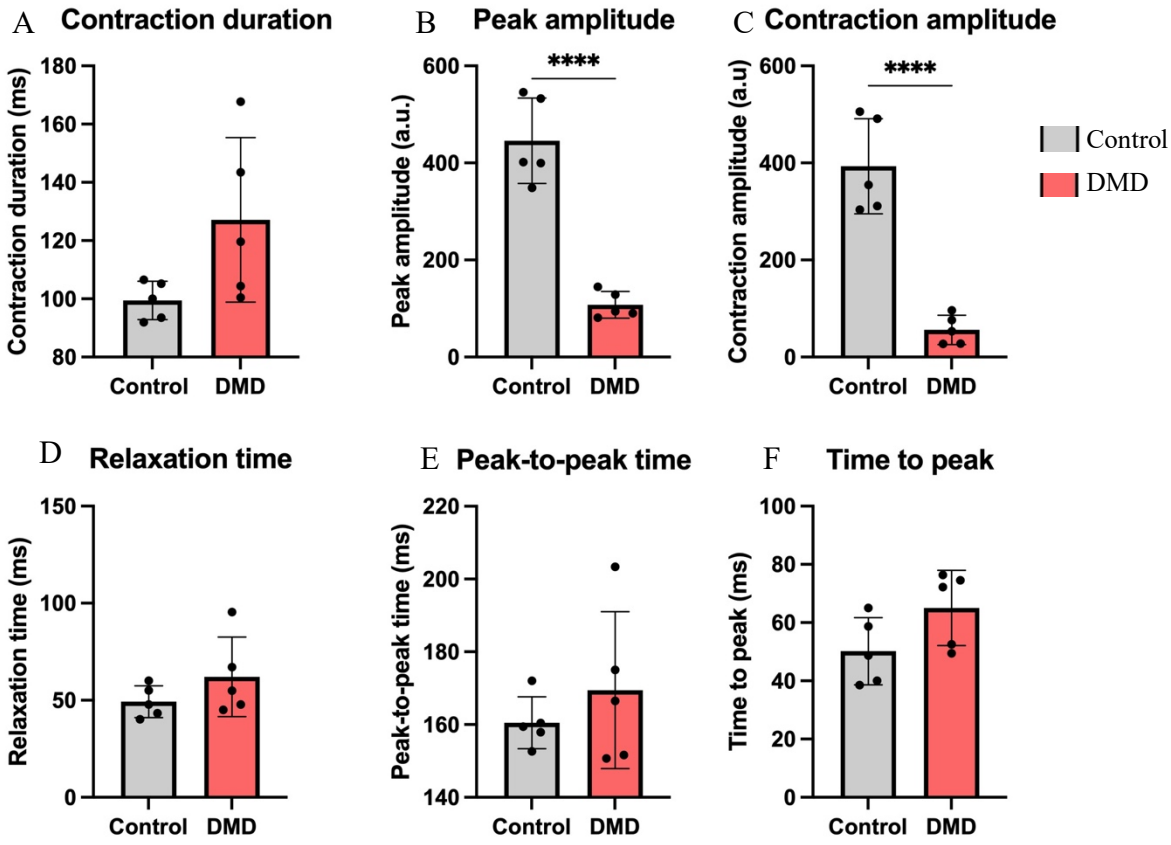


Figure 6.8 Contraction parameters of hiPSC-CMs from DMD and control cell in EHT determined by Musclemotion

Contraction parameters including contraction duration (A), peak amplitude (B), contraction amplitude (C), relaxation time (D), peak-to-peak time (E), and time to peak (F) of hiPSC-CMs of control and DMD cells in EHT cultured with maturation media. Statistical tests used was an unpaired t-test, where **** indicates $p<0.0001$, n=5.

6.5.6 The effect of isoprenaline on DMD EHT

In chapter 5, it was found that isoprenaline induced changes in contractility in control EHT which could be quantified using Musclemotion We investigated the effect of isoprenaline on control and DMD EHT. As before, the control EHTs showed a decrease in contraction duration, relaxation time, contraction amplitude and peak-to-peak time with increasing concentrations of isoprenaline (**Figure 6.9 A-C, E**). However, isoprenaline did not affect time to peak in control EHT **(Figure 6.9 D**). Isoprenaline had a similar effect on the contraction duration and relaxation time of the EHTs from the DMD cell line to that seen in control. Contraction amplitude was significantly lower in DMD EHT than in control EHT at low concentrations of isoprenaline and there was no significant response to isoprenaline as seen in **Figure 6.9.**

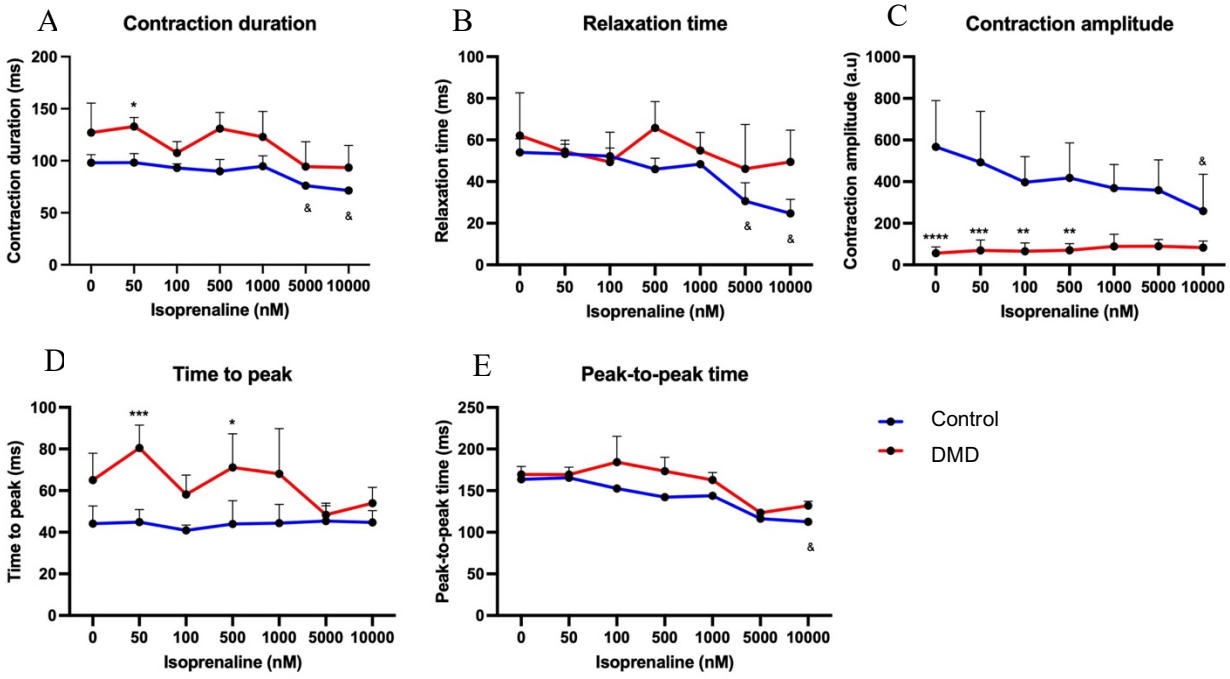


Figure 6.9 The effect of isoprenaline on the control and DMD EHT measured by Musclemotion
The effect of different dose isoprenaline on contraction duration (A), relaxation time (B), contraction amplitude (C), time to peak (D) and peak-to-peak time (E) on control and DMD EHT measured using Musclemotion. Data represents mean value and SEM analysed using two-way repeated measures ANOVA followed by Tukey's test with a *, **, ***, **** $p < 0.05$, 0.01, 0.005, 0.001 compared to control EHT, & $p < 0.05$ compared to 0 nM isoprenaline control EHT, n=5.

6.5.7 The effect of metformin on DMD hiPSC-CM in 2D and EHT

We assessed the effect of metformin addition on the glycolytic and palmitate oxidation rates in hiPSC-CM from control and DMD in 2D monolayer. The rate of the glycolytic flux was significantly lower in DMD hiPSC-CM compared to control hiPSC-CM in 2D monolayer (**Figure 6.10**). However, in this experiment there was no significant increase in the rate of glycolysis and palmitate oxidation in response to metformin in either control or DMD cells.

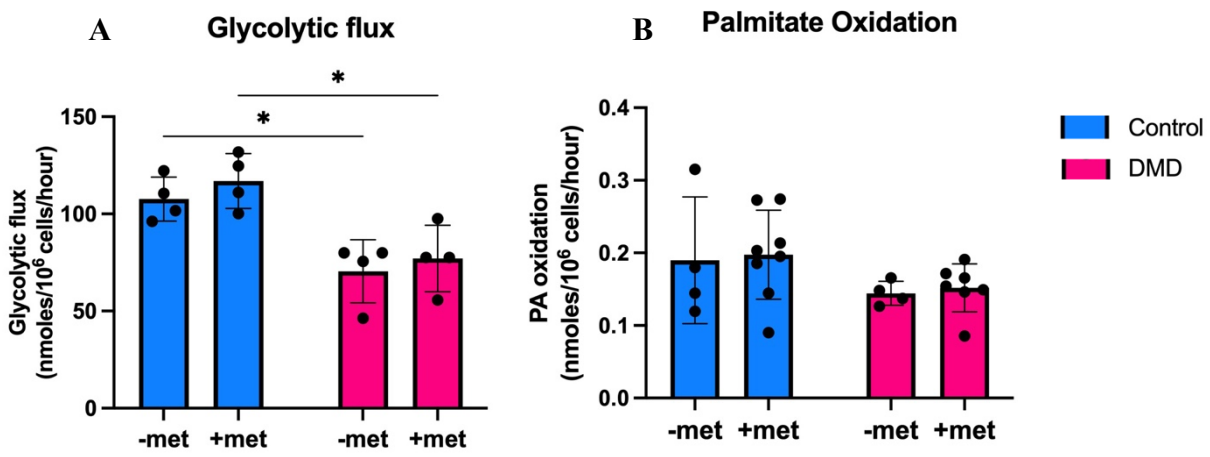


Figure 6.10 The effect of insulin and metformin addition on metabolic flux on the control and DMD hiPSC-CM in 2D monolayer

Glycolytic flux of control and DMD measured using ^{3}H-glucose (A). Palmitate oxidation of control and DMD measured using ^{3}H-palmitate (D), * $p < 0.05$, analysed using two-way ANOVA, n=4-8.

To determine the effect of 0.5 mM metformin on the insulin signalling pathway in both healthy and DMD cells in 2D monolayer, the ratio of phosphorylated Akt (pAkt) to Akt in response to insulin was quantified using Western blotting. As was seen in the measurement of glycolytic flux, there was no significant difference observed in the control and DMD hiPSC-CM after addition of insulin in this experiment. This may be due to variability between samples which limit the interpretation of the results (**Figure 6.11**).

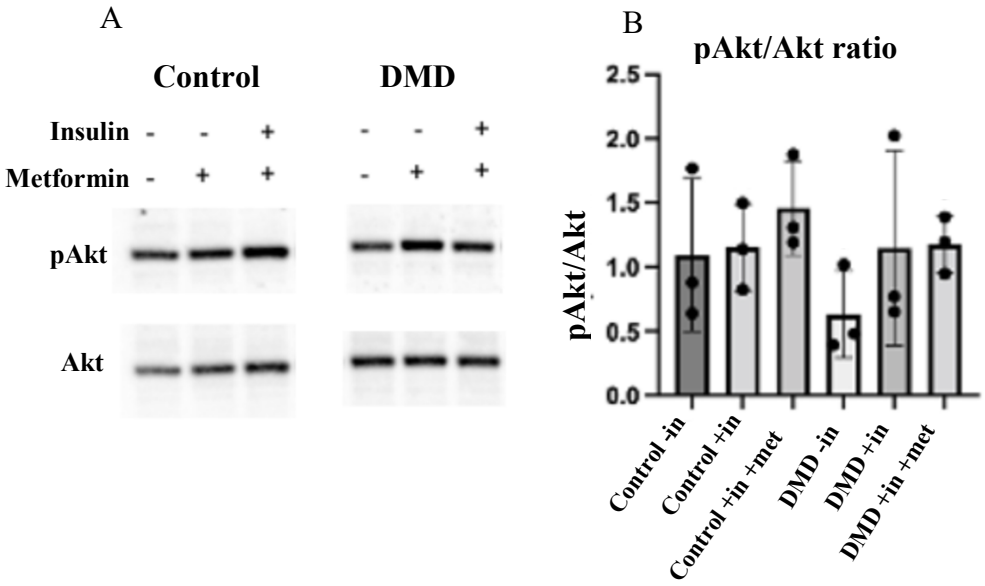


Figure 6.11 The effect of metformin on insulin response in control vs DMD hiPSC-CM 2D monolayer

Western blot image representative of pAkt and Akt protein expression in hiPSC-CMs cultured in 2D monolayer with or without insulin and metformin (A), quantitative analysis of pAkt/Akt ratio (B), analysed using two-way ANOVA, n=3.

To further investigate the cell's response to metformin, a Western blot was performed to determine the pAMPK/AMPK ratio after 0.5 mM metformin treatment for 24 hours of control and DMD hiPSC-CM. There was no significant difference observed between the proportion of AMPK phosphorylation with and without the presence of metformin (**Figure 6.12**). Again, there was a wide variation in the results, particularly in the control cell line. It may be that 2D monolayer might not be sufficient for determining the effect of metformin on the cells due to different levels of cell maturity.

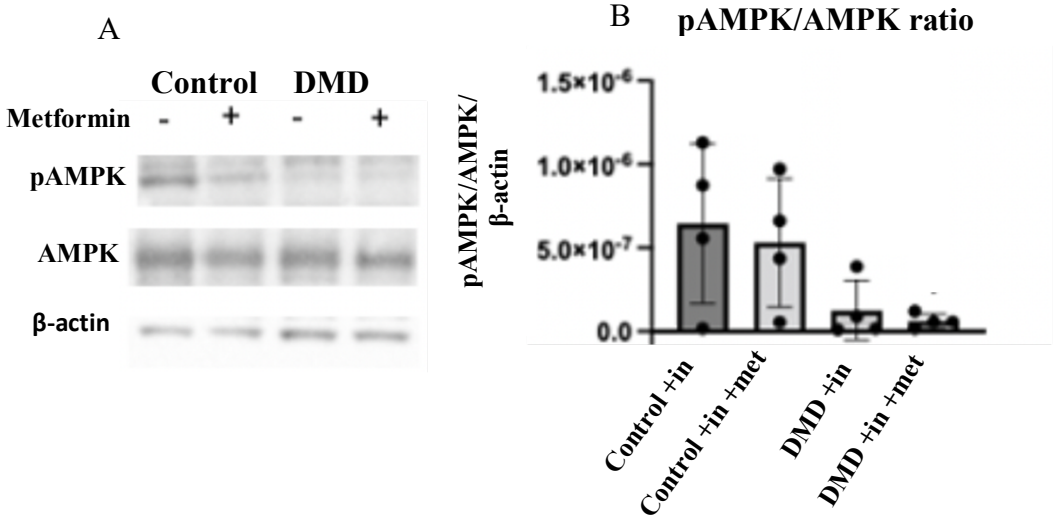


Figure 6.12 The effect of metformin on AMPK phosphorylation in control and DMD hiPSC-CM in 2D monolayer

The effect metformin on the AMPK phosphorylation on the Thr172, α2-AMPK, and β-actin as housekeeping protein (A) and quantification of the protein as ratio of pAMPK/AMPK/β-actin (B) in the control and DMD hiPSC-CM, analysed by two-way ANOVA, n=3.

6.6 Discussion

The current understanding of DMD is that the heart is not only affected by structural changes but may also have underlying metabolic alterations, including dyslipidaemia and insulin resistance, which are independent from other disease factors such as obesity and diabetes[395]. Previous findings have suggested multiple interacting molecular processes including an inflammatory response, oxidative stress, and increased Akt phosphorylation/activation in muscle cells from the mdx mouse in response to mechanical stretch, suggesting that dystrophin deficiency may directly result in activation of Akt signalling in these cells[396]. It has been hypothesised that dystrophin deficiency in DMD patients might be the cause of insulin resistance. Data from the mdx mouse model also suggested that the heart may be insulin resistant[380]. The metabolic alteration in DMD is linked to the abnormal regulation of Ca^{2+}, ROS, and NO that seems to cause many pathological effects of the disease. One explanation is that lack of dystrophin causes the loss of membrane integrity and increase in

membrane permeability which influence Ca^{2+} transport[397]. Therefore, this project aimed to use hiPSC-CMs from dystrophin deficient humans to investigate the link with insulin resistance, and to provide an alternative model to study DMD in the heart.

To study the effect of DMD on hiPSC-CMs, we used hiPSCs M202 cell line from a DMD patient with a deletion in exon 8-43. The deletion of the full-length muscular isoform of dystrophin, Dp427m in the M202 (DMD) hiPSC was confirmed using qPCR. The presence of Dp427m expression in the DMD cell is the result of correct initiation of dystrophin transcription since the primer targeted the 5'-end regions of Dp427m (exon 1-3). mRNA from primers within the deleted region, such as Dp260 isoform, was not detected in the DMD hiPSC-CM, indicating that the full-length dystrophin was not present. Primers for Dp140 and Dp70 were included and indeed expressed in both control and DMD, indicating that the deletion did not pass exon 43. There was high variability in the data due to the high degree of variability in hiPSC-CMs such as batch to batch variation during differentiation. Therefore, additional data on the protein level would explain whether the dystrophin was truly not expressed in DMD hiPSC-CM. We were not able to do this because we could not find the appropriate antibody at the time available (during the covid pandemic).

We used hiPSC-CMs in 2D monolayer and EHT to explore whether the cardiomyocytes derived from the DMD patient were insulin resistant. The DMD cells showed an increase in GLUT4 and PDK1 expression as a result of the metabolic maturation. This matches what was seen by Lopez et al[135] but curiously, this was not seen in the control cells in our experiment. However, the glycolytic flux analysis showed that DMD hiPSC-CMs were not responsive towards insulin, in contrast to the control hiPSC-CMs (**Figure 6.10**). This was supported by the pAkt/Akt ratio whereby there was no significant difference in pAkt/Akt/tubulin in DMD hiPSC-CMs in response to insulin stimulation. This indicates a lack of insulin sensitivity in DMD hiPSC-CMs, and also provides the basis for a potential

mechanism. This observation is aligned with what Zhang et al demonstrated in the mdx mouse model[398]. The hiPSC-CM data suggests that the insulin resistance could be the direct effect of the dystrophin deficiency in the cardiomyocytes model since the cell model is independent from systemic effects.

Dystrophin deficiency results in weakened myofibril tension-generating capacity resulting in less forceful contraction and slower relaxation kinetics[399]. We used Musclemotion to analyse the contraction properties of the cardiomyocytes from control and DMD cells in both 2D monolayer and EHT. When analysing the cell in 2D monolayer, contraction amplitude was significantly lower in DMD compared to control hiPSC-CM, indicating that the contraction was less powerful in DMD cells. Interestingly, peak-to-peak time was much lower in DMD indicating faster contraction although the error bars in the data from 2D monolayer were large because the cells cultured in 2D monolayer do not have uniform beating area and result in high variability when analysed using Musclemotion. In the EHT, peak and contraction amplitude were significantly lower in DMD EHT compared to control matching the decreased cardiac output and contractility seen in patients[400], suggesting that this model could be useful to study factors influencing functional changes in the DMD heart.

Maturity of the cells has an influence when comparing the effect of drugs on control and DMD hiPSC-CM. The different responses seen here between control and DMD cells towards isoprenaline stimulations may have been due to the different maturity level of the control and DMD cells as the latter had been shown to mature slower than control hiPSC-CM.

Metformin did not have any effect on Akt phosphorylation in DMD cells. This result is unexpected as metformin has previously showed to increase the phosphorylation of Akt in insulin resistant hiPSC-CM caused by environmental influence such as hyperlipidemia, hyperglycemia, and hyperinsulinemia in our model of insulin resistant hiPSC-CM in chapter

5. This may suggest that metformin is not beneficial for every type of insulin resistance (environmental compared with genetic origins). Since the mechanism of metformin on increasing insulin sensitivity is still unknown, how insulin resistant cells respond to insulin may vary depending on the mechanism of the insulin resistance. Furthermore, there is already evidence that there is inhibition of complex I in DMD patients and inhibition of complex I is hypothesised to be one of the mechanisms of action of metformin. Therefore, administering metformin to DMD cells could potentially make the DMD phenotype worse by reducing the generation of ATP in the electron transport chain

6.7 Conclusion

Human iPSC-CMs in 2D monolayer and EHT were used to model metabolic changes seen in Duchenne muscular dystrophy. This model has shown that there was delayed differentiation and impaired glycolytic flux and Akt phosphorylation in response to insulin, suggesting insulin resistance in DMD hiPSC-CMs. Moreover, the DMD hiPSC-CM in EHT showed a distinct contractility profile from the control. This model provides the opportunity to study the effect of dystrophin deficiency on insulin signalling specifically without the influence of systemic effects.

7

General discussion

CHAPTER 7

7. GENERAL DISCUSSION

7.1 Thesis findings and discussion

Human induced-pluripotent stem cell derived cardiomyocytes (hiPSC-CM) have a great potential for use in biomedical research, such as for disease modelling, drug discovery, and regeneration. This is due to numerous benefits that hiPSC-CMs can offer, providing human-derived cells that are patient specific and easy to manipulate (e.g., by gene editing using CRISPR-Cas9) and which can be cultured in the dish for a long period of time. However, immediately post differentiation hiPSC-CMs are hindered by their immature phenotype and therefore may not be suitable to study diseases that affect the adult heart. Furthermore, to be useful for drug discovery the cells need to express the transporters and signalling pathways found in the mature tissue. Although hiPSC-CMs are useful to study human diseases, there is growing concern as to whether hiPSC-CMs, particularly in 2D monolayer, have an appropriate electrophysiology profile[401,402] or if the calcium handling is comparable to more adult cardiomyocytes[403,404].

In this thesis, I have studied the potential of hiPSC-CMs for modelling cardiometabolic diseases and for testing drugs to improve the disease phenotype and cardiac function. To achieve this, the project was started by exploring ways to culture more mature hiPSC-CM by optimising the media composition to promote fatty acid oxidation and culturing the cells as engineered heart tissue. To assess the maturation state of hiPSC-CMs, the information gained by using the novel method of synchrotron-based micro-FTIR absorption spectroscopy was explored. The more mature hiPSC-CMs in 2D monolayer and EHT were used to study the effect of diabetic (acquired disease) and Duchenne muscular dystrophy

(in-born disease) in the heart. Finally, the disease models were used to test the known or potential drugs, metformin, perhexiline, and molidustat.

Several approaches to drive hiPSC-CMs to become more mature cardiomyocytes have been performed by many researchers including culturing the cells for a long period of time, manipulation of the media composition, gene editing, small molecules, hormones, microRNA, mechanical and electrical stimulation, culturing cells as 3D organoids, and tissue engineering[263–265,405–409]. Some reported a combination of these approaches, but as yet scientists in the community have not agreed on one single protocol or approach for maturation. Moreover, the system of hiPSC-CMs differentiation and culture varies between labs. Therefore, there is room for improvement and to provide the most effective systems that can be replicated by other labs.

In the study I performed, hiPSC-CMs were cultured in 2D monolayer and 3D as engineered heart tissue (EHT) under physiological maturation media consisting of 5.5 mM glucose and 400 μM oleic acid. EHT was chosen from other 3D cultures because it has been shown to promote maturation and it is useful for a robust measurement of contractility using Musclemotion[209–211]. I found that culturing hiPSC-CM as a 2D monolayer in maturation media led to enhanced metabolic maturation characterised by changes in gene and protein expression, mitochondrial activity, and a metabolic switch towards more fatty acid oxidation. Culturing the cells in EHT led to increased metabolic maturation compared to 2D monolayer. Although, there have been numerous studies aimed at maturing of hiPSC-CMs[144,410,411], we are the first to study PPARα stimulation using oleic acid with and without WY-14643 for maturation in EHT[149]. Although the addition of a PPARα agonist caused a small increase in fatty acid oxidation compared to cells cultured with oleic acid alone, the agonist was somewhat toxic and “the benefits did not outweigh the cost”.

I went on to use hiPSC-CM to study the effect of diabetes and Duchenne muscular dystrophy in the heart. The aim of the study was to provide a human cell-based model to complement animal studies into cardiometabolic diseases. Other studies had reported methods to modulate culture media to create a diabetic model, but these were generally either using hyperglycaemia or hyperlipidaemia in isolation[377,412–414]. In this thesis, I created the media consisting of hyperglycaemia, hyperlipidaemia, and hyperinsulinemia to induce insulin resistance in the hiPSC-CM in 2D monolayer and EHT. The protocol successfully altered the metabolism, changed contraction parameters, and blunted IR/IRS-PI3K-Akt pathway, mirroring changes seen in the human insulin resistant heart and in animal models of insulin resistance. Changes in gene and protein expression were explored using transcriptomics and proteomics, identifying both expected changes and potential new signalling pathways to explore.

The effect of DMD on the heart was explored using patient-derived iPS cells. I found that the DM hiPSC-CM were slower to differentiate than control cells and showed impaired glycolytic flux and Akt phosphorylation in response to insulin. I observed that Akt was already phosphorylated in the DMD hiPSC-CM cultured in basal media which was different from what observed in the control hiPSC-CM, this discrepancy could be due to the maturity level of hiPSC-CM. More detail experiment such as phosphoproteomic could be performed to understand the phosphorylation of Akt and other proteins.

Finally, I tested the applicability of the model for drug testing. I used metformin, a drug that is routinely used to treat insulin resistance, but for which the direct effects on the heart are not fully characterised; perhexiline which inhibits fatty acid oxidation and has been tested in a clinical trial; and molidustat, a drug in clinical trial for anaemia and which had shown promising effects to protect against ischaemia in the insulin resistant rat heart. Although it was not within the scope of this thesis to explore the effects of these drugs in detail, I showed

that metformin improved the response of insulin signalling in the insulin resistance model through AMPK activation but did not influence the insulin signalling in hiPSC-CM from DMD patients. This difference is most likely due to the different origins of insulin resistance in the two models environmental versus genetics. In studies using molidustat I demonstrated that the model was capable of validating effects seen in the rodent heart and therefore provided a bridge to translation to the human condition.

7.2 Conclusion

This thesis project has successfully shown that the hiPSC-CMs were metabolically and phenotypically more mature when cultured in 3D as engineered heart tissue and in media promoting fatty acid oxidation. More mature cardiomyocytes in 2D monolayer and EHT could be used to study the changes induced by the lack of dystrophin in DMD, showing that maturation in hiPSC-CMs from DMD patients was delayed and that the cells were insulin resistant. Culturing the more mature cardiomyocytes in 2D monolayer and EHTs with 'diabetic-like' or insulin resistance media containing 12 mM glucose (hyperglycemia), 300 μM palmitic acid (hyperlipidemia), and 50 nM insulin (hyperinsulinemia) induced insulin resistance. This insulin resistant model was shown to mimic the early diabetic heart, metabolically and in changes to gene and protein expression. Finally, I showed that these human cell models can be used to explore potential treatments for cardiometabolic diseases.

7.3 Study limitations and challenges

As with any other research projects, this thesis project also faced challenges which limited the scope of the study. When the project was started, I faced many challenges in optimising the differentiation of hiPSC to become hiPSC-CMs. There are many different cardiac differentiation protocols that have been extensively studied by different groups and the efficiency of the protocol is known to vary between cell lines. Although I was able to optimise the protocol used in our lab, by changing factors including cell confluency, time in

culture, dissociation method and the inhibitors used, some variability in the differentiation efficiency remained. This is in part due to my inexperience at that stage of my research, but also the cells in a batch culture will be at different points in the cell cycle when exposed to the differentiation process and this inevitably results in different rates of differentiation.

Another challenge is the cell contamination which delayed some of the experiments. Although this did not happen often, when it did occur it delayed all the planned experiments. We sterilised the incubator frequently to prevent the contamination. Delayed of experiments were also caused by spontaneous differentiation of hiPSC in some batches which I outlined in chapter 3. This spontaneous differentiation might be caused by stress in the cells such as adding cold media, pressure from moving the cells during dissociation process, and centrifugation.

Another limitation of this study is that we used one cell line predominantly. It is increasingly understood now that lines can vary in their differentiation efficiency and the characterisation of the cardiomyocytes. In the study of the DMD cells we did not use an isogenic cell line, comparing either hiPSCs derived from DMD patient and an unaffected close relative, or healthy hiPSCs and mutated hiPSCs derived from the same cell line using gene editing through CRISPR-Cas9. This reduces the effect of non-specific differences in the genetic make-up of the control and diseased cells masking or confounding the effect of the mutation of interest. The DMD study was also limited by the large variability in the data we acquired. This may be because the study was performed over two years with two MBiochem students. Their inexperience may have affected the consistency of the differentiations. However, our results have been confirmed by a study conducted using a healthy cell line, healthy control line and its isogenic dystrophin-deficient counterpart, identifying the effect of dystrophin deficiency towards cell phenotype including maturation[399].

General limitations of this thesis were also caused by work disruption because of the COVID-19 pandemic which limited the time for experiments at certain points. If time allowed, I would do more in depth studies such as GLUT4 imaging using HA-GLUT-GFP antibody which required optimisation of the viral transfection but would have generated interesting results. This can be done by transfecting the cells with a fusion protein of HA-GLUT4-GFP. To study the internalization of GLUT4, the cells are incubated with anti-HA antibody for a defined pulse time which then fixed and imaged after secondary antibody incubation. More time would also have allowed a more in-depth investigation of the changes induced by treatment with perhexiline. Finally, it would complement our story to have a measurement of metabolism of the EHTs using radiolabelled substrates in the diabetic and DMD condition exposed to hypoxia.

7.4 Future directions

The field of human induced-pluripotent stem cell derived cardiomyocytes has been advancing for decades and the work on disease modelling and drug discovery has been applied to many cardiac diseases. The project in my thesis has enabled the study of the effect of diabetes and DMD in 3D culture as engineered heart tissue and will be useful to complement work in rodent models in our lab and others. The use of a more sophisticated 3D culture involving, for example, electrical stimulation and co-culture with other cell types would be beneficial. Moreover, the use of a microfluidic system which would allow us to study the flow of the substrate would be beneficial to study complex nutrient circulation in the heart. It has been reported that it is possible to create a multi-organ system which connects the heart and other organs such as liver, skin, and brain. My thesis project on studying the effect of ‘diabetic-like’ media in the EHT would be beneficial to be integrated in such a multiorgan system.

APPENDICES

Appendix A Antibodies

Immunochemistry antibodies

Antibody	Company	Catalogue number	Host species	Dilution
Anti-actinin (sarcomeric)	Sigma Aldrich	A7811	Mouse (mono)	1:1000
HIF1α	Cayman Chemical	10006421	Rabbit (poly)	1:200
GAPDH	Proteintech	10701-1-AP	Rabbit (poly)	1:3000
Alexa Fluor 488	ThermoFisher	A-11008	Donkey anti-rabbit	1:200
Alexa Fluor 488	ThermoFisher	A-21202	Donkey anti-mouse	1:200
Alexa Fluor 568	ThermoFisher	A-11011	Donkey anti-rabbit	1:200
Alexa Fluor 594	ThermoFisher	A-11005	Goat anti-mouse	1:200
Alexa Fluor 594	ThermoFisher	A-11012	Goat anti-rabbit	1:200
Alexa Fluor 647	ThermoFisher	A-21235	Donkey anti-mouse	1:200

Western blot antibodies

Antibody	Company	Catalogue number	Host species	Dilution
Anti-actinin (sarcomeric)	Sigma Aldrich	A7811	Mouse (mono)	1:1000
HIF1α	Cayman Chemical	10006421	Rabbit (poly)	1:200
AMPKα	Cell signaling	2603	Rabbit (mono)	1:1000
pAMPKα (Th172)	Cell signalling	2535	Rabbit (mono)	1:1000
GAPDH	Proteintech	10701-1-AP	Rabbit (poly)	1:40000
pAkt (Ser473)	Abcam	Ab81283	Rabbit (mono)	1:5000
Akt	Abcam	Ab32505	Rabbit (mono)	1:2000
β-tubulin	Abcam	Ab7751	Mouse (mono)	1:2000
β-actin	Abcam	Ab8227	Rabbit (Poly)	1:1000
Anti-rabbit HRP secondary antibody	Abcam	Ab205718	Goat	1:2000
Anti-mouse HRP secondary antibody	Abcam	Ab97023	Goat	1:2000

Appendix B Primer sequences

Category/Chapter	Target	Sequence
Housekeeping	TBP	TGACCCAGCATCACTGTTTCTT (FW) CAAGCCCTGAGCGTAAGGTG (RV)
Housekeeping	UBC	CCTGGTGCTCCGTCTTAGAG (FW) TTTCCCAGCAAAGATCAACC (RV)
HIF1α target gene	VEGF	CAAGCCAAGGCGGTGAGCCA (FW) TCTGCCGGAGTCTCGCCCTC (RV)
HIF1α target gene	PHD2	CAGAAGGCAAAGCCCAGTTTG (FW) CCTCACACCTTTTTCACCTTGTAG (RV)
HIF1α target gene	BNIP3	GAATTTCTGAAAGTTTTCCTTCCA (FW) TTGTCAGACGCCTTCCAATA (RV)
HIF1α target gene	GLUT1	AAGCTGACGGGTCGCCTCATG (FW) CTCTCCCCATAGCGGTGGACC (RV)
HIF1α target gene	Aldolase A	GGGGCTTCAGGTTTCCCTA (FW) GGTAGTAGCAAGTTCCTGCGG (RV)
HIF1α target gene	Enolase 1	GCCCTGGTTAGCAAGAAACT (FW) GAATGGCGTTCGCACCAAAC (RV)
HIF1α target gene	PGK1	GAATGGGAAGCTTTTGCCCG (FW) GCAGTGTCTCCACCACCTATG (RV)
HIF1α target gene	HIFα	CCACAGGACAGTACAGGATG (FW) TCAAGTCGTGCTGAATAATACC (RV)
HIF1α target gene	FIH	GCGCAGTTATAGCTTCCCGAC (FW) GCACCACAGGCTCCTCATTCT (RV)
Heart	MYL7	GGAGTTCAAAGAAGCCTTCAGC (FW) GTCCCATTGAGCTTCTCCCC (RV)
Heart	MYH6	TCCTGCGGCCCAGATTCTTC (FW) TCTTCCTTGTCATCGGGCAC (RV)
Heart	MYH7	AAGGTCAAGGCCTACAAGCG (FW) CCAGGGCTGAGCAGATCAA (RV)
Heart	TNNT2	GACAGAGCGGAAAAGTGGGA (FW) CTCCTTGGCCTTCTCCCTC (RV)
Metabolism	GLUT4	GTTCTTTCATCTTCGCCGCC (FW) CAATCACCTTCTGAGGGGCA (RV)
Metabolism	IRS1	ACTGGACATCACAGCAGAATGA (FW) ACTGAAATGGATGCATCGTACC (RV)
Metabolism	IRS2	GCCACCATCGTGAAAGAGTG (FW) CCATCCGGGAACAAGGGAAA (RV)
Metabolism	PDK4	TGGTCCAAGATGCCTTTGAGT (FW) GTTGCCCGCATTGCATTCTT (RV)
Metabolism	PPARα	GGACAAGGCCTCAGGCTATC (FW) AACGAATCGCGTTGTGTGAC (RV)
Metabolism	PGC1α	TCTCAGTAAGGGGCTGGTTG (FW) ACCAGAGCAGCACACTCGAT (RV)
Metabolism	IKK-β	AACCAGCATCCAGATTGACC (FW) CTCTAGGTCGTCCAGCGTTC (RV)

Metabolism	FOXO1	GCTGCATCCATGGACAACAACA (FW) CGAGGGCGAAATGTACTCCAGTT (RV)
Cytokines	IL-6	TCCAGAACAGATTTGAGAGTAGTG (FW) GCATTTGTGGTTGGGTCAGG (RV)
Cytokines	IL-1β	AGATGATAAGCCCACTCTACAG (FW) ACATTCAGCACAGGACTCTC (RV)
Dystrophin	Dp427m (exons 1-3)	TCGCTGCCTTGATATACACTTTTCA (FW) GGTTCTCAATATGCTGCTTCCA (RV)
Dystrophin	Dp260	AGGAAGCTGCGAAATCTGTCTTAC (FW) GGCAGACTGGATGCTCTGTTCA (RV)
Dystrophin	Dp140	ACCGAAAGAGGTTTTTGCACACC (FW) ACTGGCATCTGTTTTTGAGGATTGC (RV)
Dystrophin	Dp71	CATGAGGGAACAGCTCAAAGGC (FW) CAGTCTTCGGAGTTTCATGGCA (RV)
Dystrophin	Exon junction 25/26	GGCCTGCCCTTGGGGATTCA (FW) TCTGGCATAGACCTGTTGGCACA (RV)
Dystrophin	Exons 8/9-11	TTCTCAACAGATCACGGTCA (FW) CCAATCAGCTTACTTCCCAA (RV)
Dystrophin	Exons 38/39-41	GAATGAAGACAATGAGGGTA (FW) GCTTGCCTACGCACTGCATT (RV)
Dystrophin	NKX2.5	GCGATTATGCAGCGTGCAATGAGT (FW) AACATAAATACGGGTGGGTGCGTG (RV)
Dystrophin	MLC2v	ACATCATCACCCACGGAGAAGAGA (FW) ATTGGAACATGGCCTCTGGATGGA (RV)
Dystrophin	Cx-43	TACCAAACAGCAGCGGAGTT (FW) TGGGCACCACTCTTTTGCTT (RV)
Dystrophin	CD36	GCACCACTGTGTACAGACAG (FW) GTGCAGCTGCTACAGCCAG (RV)

Appendix C

Experiment	**Reagent**	**Company**	**Cat. number**
hiPSC maintenance	mTeSR1	StemCell Technologies	85850
	TeSR-E8	StemCell Technologies	05990
	Matrigel	Corning	354277
	ROCK Inhibitor (Y-27632)	Merck	SCM075
	Dulbecco's Phosphate Buffered Saline	Sigma Aldrich	D8537
Cell dissociation	TrypLE Express	Gibco	12604-013
	ReLeSR	StemCell Technologies	05872
Cell freezing	CryoStor CS10	StemCell Technologies	07959
Cell differentiation	GFR Matrigel	Corning	354230
	RPMI 1640	ThermoFisher	11875085
	RPMI 1640, no glucose	ThermoFisher	11879020
	B27 minus insulin	ThermoFisher	A1895601

	B27 complete	ThermoFisher	17504044
	CHIR99021	Tocris	4423
	Wnt-C59	Tocris	5148
Maturation media	DMEM	Sigma Aldrich	D5546
	Oleic acid:BSA	Sigma Aldrich	O3008-5ML
	Insulin	Merck	I9278-5ML
	Vitamin B12	Merck	V2876
	Vitamin C	Merck	A92902
	Biotin	Merck	B4639
	Horse Serum	Gibco	26050088
IR media	DMEM, no glucose	ThermoFisher	11966025
	DMEM, low glucose	ThermoFisher	11885084
	Insulin solution human	Sigma Aldrich	I9278
	Horse serum	ThermoFisher	26050088
	Palmitic acid	Sigma Aldrich	P0500
	Bovine Serum Albumin (BSA)	Sigma Aldrich	A9418
	Potassium carbonate anhydrous	Sigma Aldrich	590681
	Sodium chloride	Sigma Aldrich	S9888
	Ethanol absolute	Sigma Aldrich	100983
EHT	Aprotinin	Sigma Aldrich	A1153-100mg
	Fibrinogen	Sigma Aldrich	F8630-5g
	Thrombin	Biopur	BP11-10-1104
	Agarose	Invitrogen	15510-021
	10x DMEM	Gibco	52100-021
	Glutamine	Life Technologies	25030-081
	Silicone racks	EHT Technologies	C0001
	Teflon Spacers	EHT Technologies	C0002
Single cell dissociation	HEPES	Thermo Fisher	15630106
	N-Benzyl-p-toluensulfonamide (BTS)	TCI America	B3082
	Dimethyl Sulfoxide (DMSO)	Sigma Aldrich	DD2650
	DNase I, RNase-free	Thermo Fisher	EN0521
	Fetal Bovine Serum (FBS)	Thermo Fisher	16000044
	Papain from Carica papaya	Sigma Aldrich	76220
^{3}H Glycolysis	Glucose, D-[5-3H(N)]-, 1mCi (37MBq)	PerkinElmer	NET531001MC
	Dowex	Sigma Aldrich	428590-500g
	Glass Pasteur Pipettes	Thermo Fisher	FB50251
	Glass wool	Sigma Aldrich	18421-500g
	Sodium Hydroxide	Thermo Fisher	S/4920//60

	Boric acid	Thermo Fisher	B/3800/60
	EcoLite(+) liquid scintillation cocktail	MP	0188247501
	Super polyethylene vial 20mL Quick Closure	Perkin Elmer	6008117
^{3}H Palmitate ^{3}H Oleic	Palmitic Acid, [9,10-3H(N)]-, 1mCi (37MBq)	Perkin Elmer	NET043001MC
	Centrifuge Tube 15ml (Falcon 2097) Rack of 50	DPAG stores	352097-SP
	Chloroform	Thermo Fisher	C/4966/15
	Methanol	Sigma Aldrich	
	Potassium Chloride	Sigma Aldrich	P9541-500g
	Hydrochloric Acid Solution 1M		
	Glass Pasteur Pipettes	Thermo Fisher	FB50251
	Oleic Acid, [9,10-3H(N)]-, 1mCi (37MBq)	Perkin Elmer	NET289001MC
Metabolic flux: enzymatic reaction and Pentra	Glucose assay reagent	Sigma Aldrich	G3293
	L-lactic dehydrogenase from bovine heart	Sigma Aldrich	L3916
	NAD^{+} sodium salt	Sigma Aldrich	N0632
	Lactate reagent	Horiba	A11A01721
	Glucose PAP CP	Horiba	A11A01668
	LDH CP	Horiba	A11A01824
Cell viability	Alamar blue	BioRad	BUF012B
	CCK-8	Sigma Aldrich	96992
	ReadyProbes	ThermoFisher	R37609
	Countess cell counting slide	ThermoFisher	C10312
Cell staining	MitoTracker Red CMXRos	ThermoFisher	M7512
	Oil-Red-O	ThermoFisher	A12989.14
	DAPI	ThermoFisher	D1306
Drug testing	Metformin	MP Biomedicals	0215169105
	Perhexiline maleate	Merck	SML0120
	Molidustat	Advanced ChemBlocks	R16009
	Molidustat	Merck	ADV465750852
	Isoprenaline	Merck	I5627
	Isoliquiritigenin	Merck	I3766
Cryosection	Paraformaldehyde 4% solution	Santa Cruz Biotechnology	Sc-281692
	OCT embedding	Fisher Scientific	12678646

Western blot	Triton X-100	Sigma Aldrich	T8787
	SDS-PAGE gels	ThermoFisher	NP0321BOX
	BCA Protein Assay	ThermoFisher	23225
	Protease inhibitor	Roche	4693116001
	Phosphatase inhibitor (PhosSTOP)	Roche	4906845001
Quantitative PCR	RNeasy Mini Kit	Qiagen	74104
	Trizol reagent	ThermoFisher	15596026
	High-Capacity cDNA Reverse Transcription Kit	ThermoFisher	4368814
	SYBR Green Master Mix	ThermoFisher	4309155
Flow Cytometry	Zombie Violet Fixable Viability Kit	ThermoFisher	423115

Appendix D

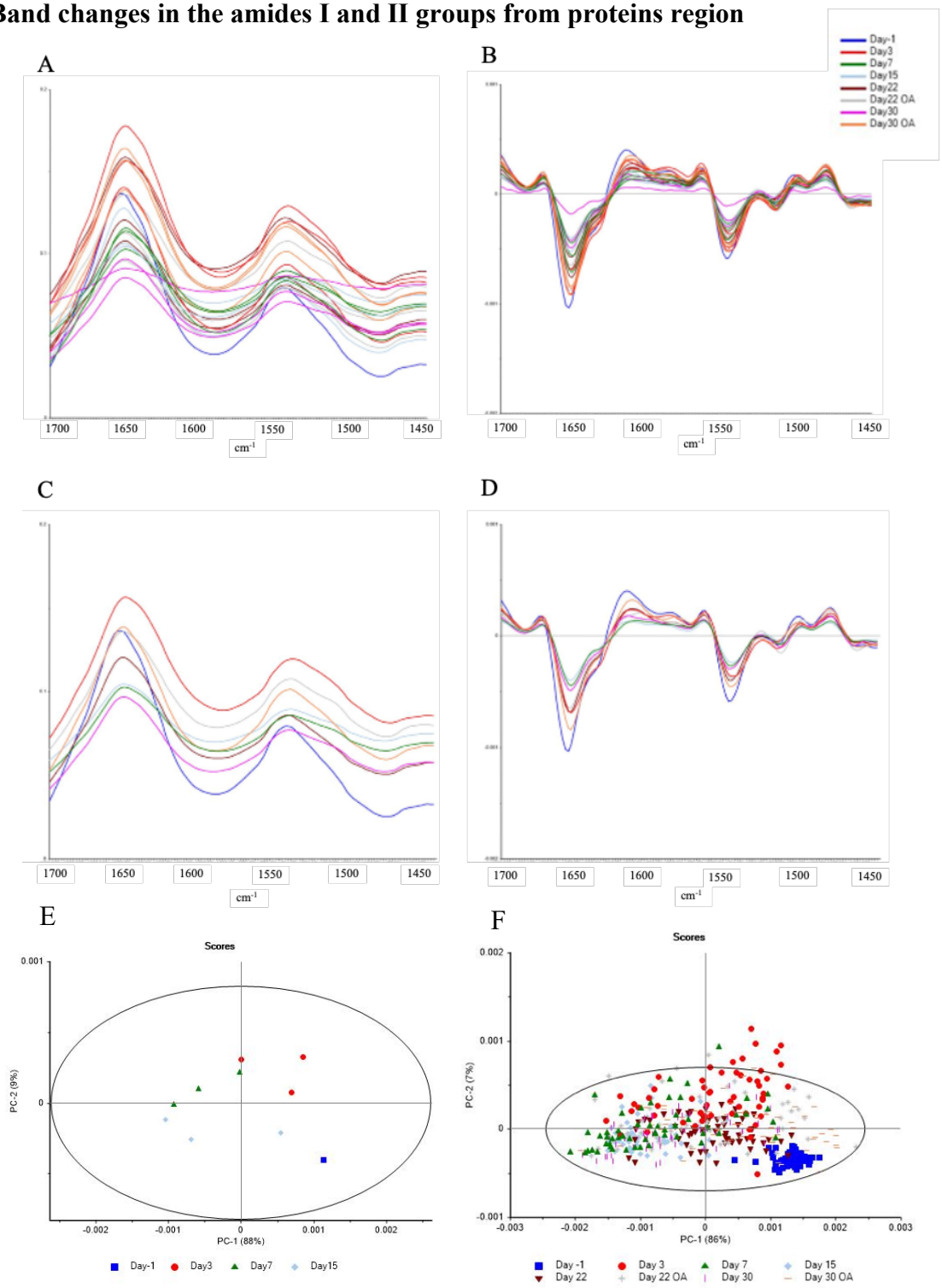
Characterisation of fatty acid enhancement of maturation of cardiomyocytes during differentiation by synchrotron based micro-FTIR absorption spectroscopy

This content of appendix D is the supplementary data for chapter 3 about synchrotron based micro-FTIR absorption spectroscopy for characterising oleate enhancement of maturation of cardiomyocytes.

1. Analysis of spectral data

The software OPUS 8.0 (Bruker Optics, Germany) was used for instrument control, data acquisition and pre-processing. All IR spectra presented in this work were corrected using the automated fitting algorithm for the removal of atmospheric bands. After CO_2 and water vapor subtraction, raw spectra were baseline corrected (Concave Rubber band with 64 points), normalized (vector normalization) and second derivative (Savitzky-Golay algorithm with 13 adjacent smoothing points). Principal Component Analysis (PCA) was performed after pre-processing spectra using Unscrambler X software (Camo, Norway). The mid-IR spectral region (3800 cm^{-1} – 1000 cm^{-1}), excluding the CO_2 region (2400 cm^{-1}– 2100 cm^{-1}) was used for PCA. Additionally, the spectra were cropped to the specific regions of interest to be analysed (3100–2800 cm^{-1} for the lipid region, 1700 cm^{-1}– 1480cm^{-1} for the amides and 1800 cm^{-1} –1000 cm^{-1} for the fingerprint region). Score plots were used to visualize any clustering of the data, and the loading plot was used to determine which spectral regions contributed most to the variance in the data set, accounting for any clustering of spectra seen in scores plots. SR-FTIR spectra were processed as the second derivate to enhance spectral features and minimize the influence of residual, spectrally-slowly varying baseline features. Data presented here includes band changes associated with protein, carbohydrate, phosphates, and nucleic acids, glycogen and other carbohydrates, and fingerprint region.

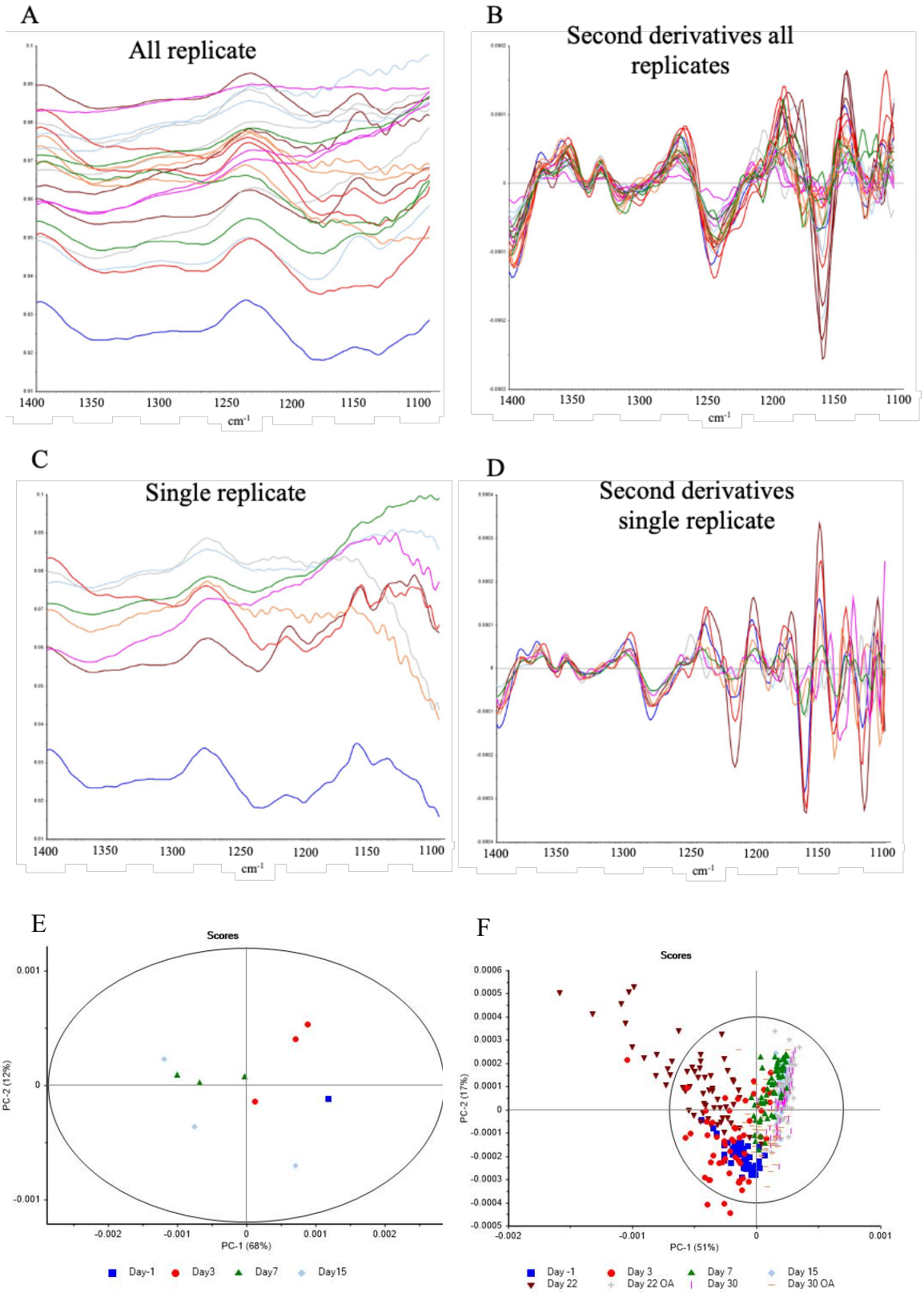
2. Band changes in the amides I and II groups from proteins region



Supplementary figure 1 The average absorbance and second derivative absorbance spectra of hiPSCs in the amide region

The average absorbance and second derivatives absorbance of all replicates (A, B), one replica (C, D), PCA plot from second derivative (E, F) during hiPSCs differentiation into cardiomyocytes and fatty acid stimulation at Day -1, 3, 7, 15, 22, 22 OA, 30, 30 OA in Amides I and II region (1700 cm-1 to 1450 cm-1).

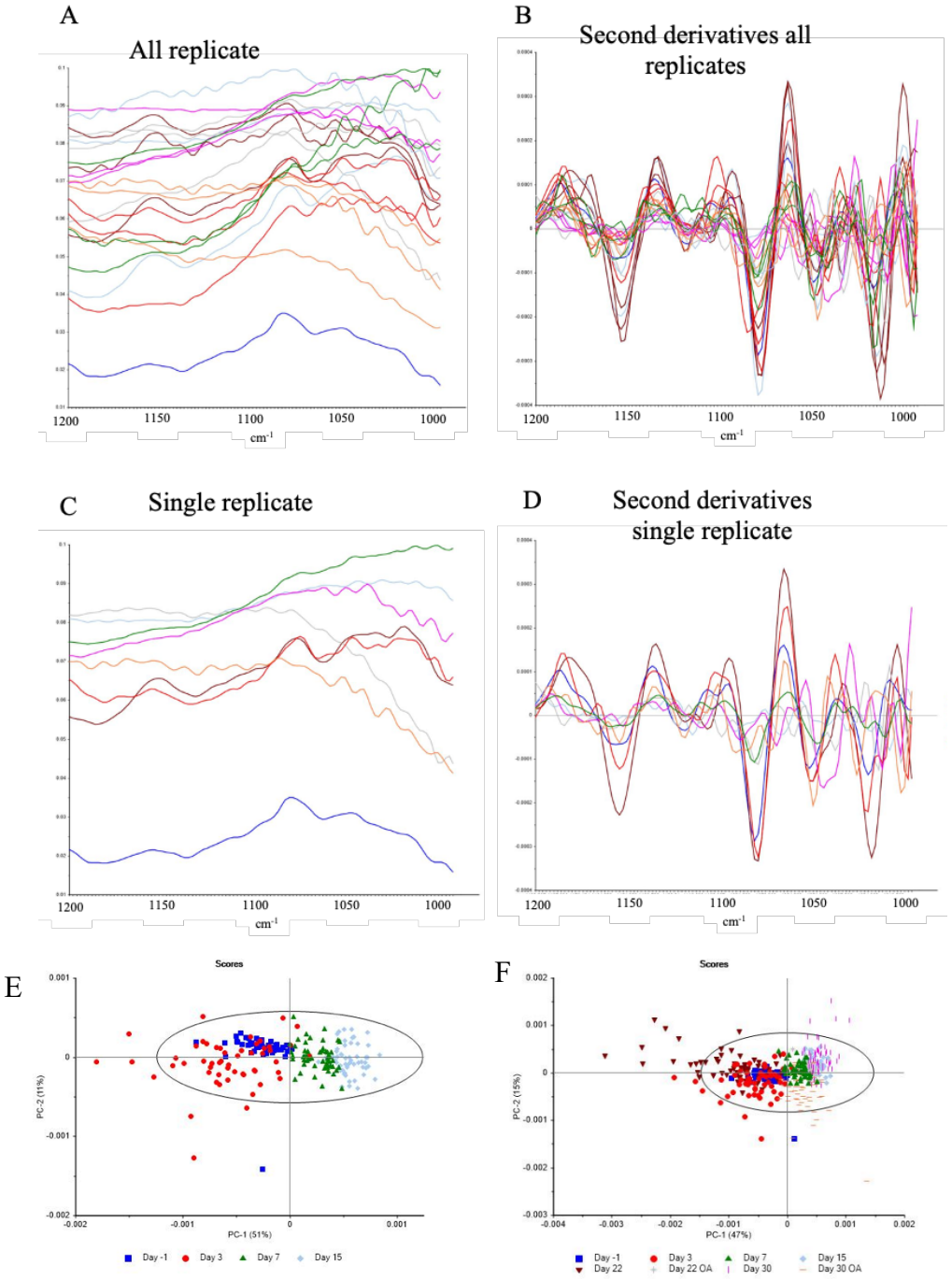
3. Band changes in the carbohydrates, phospholipids, and nucleic acids region



Supplementary figure 2 The average absorbance and second derivative absorbance spectra of hiPSCs in the carbohydrates, phospholipids, and nucleic acids region

The average absorbance and second derivatives absorbance of all replicates (A, B), one replica (C, D), and PCA plot from second derivative (E, F) during hiPSCs differentiation into cardiomyocytes and fatty acid stimulation at Day -1, 3, 7, 15, 22, 22OA, 30, 30OA in carbohydrates, phospholipids, nucleic acids region 1400 cm^{-1} to 1100cm^{-1}.

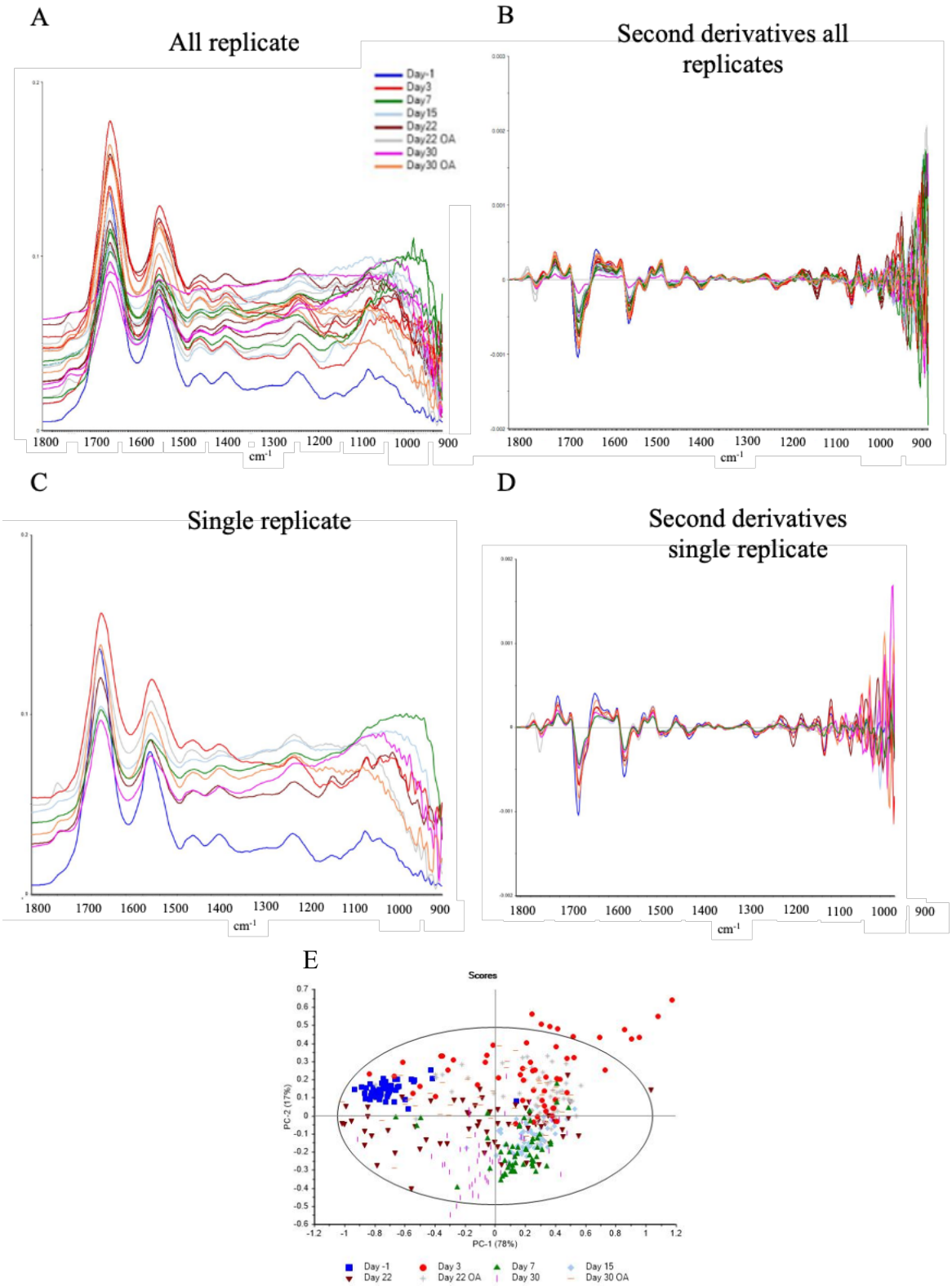
4. Band changes in the glycogen and other carbohydrates region



Supplementary figure 3 The average absorbance and second derivative absorbance spectra of hiPSCs in the glycogen and other carbohydrates region

The average absorbance and second derivatives absorbance of all replicates (A, B), one replica (C, D), and PCA plot of second derivative (E, F) during hiPSCs differentiation into cardiomyocytes and fatty acid stimulation at Day -1, 3, 7, 15, 22, 22OA, 30, 30OA in the glycogen and other carbohydrates (1200–1000 cm^{-1}).

5. Band changes in the fingerprint region



Supplementary figure 4 The average absorbance and second derivative absorbance spectra of hiPSCs in the fingerprint region

The average absorbance and second derivatives absorbance of all replicates (A, B), one replica (C, D) and PCA plots of second derivative (E) during hiPSCs differentiation into cardiomyocytes and fatty acid stimulation at Day -1, 3, 7, 15, 22, 22 OA, 30, 30 OA in fingerprint region 1800 cm^{-1} to 920 cm^{-1}.

BIBLIOGRAPHY

1. International Diabetes Federation. IDF Diabetes Atlas 9th ed. *International Diabetes Federation* (2019). ISBN: 9782930229874
2. Einarson, T. R., Acs, A., Ludwig, C. & Panton, U. H. Prevalence of cardiovascular disease in type 2 diabetes: A systematic literature review of scientific evidence from across the world in 2007-2017. *Cardiovascular Diabetology* **17**, (2018).
3. Malik, V. S., Willett, W. C. & Hu, F. B. Global obesity: Trends, risk factors and policy implications. *Nature Reviews Endocrinology* **9,** 13–27 (2013).
4. Mottillo, S. *et al.* The metabolic syndrome and cardiovascular risk: A systematic review and meta-analysis. *J Am Coll Cardiol* **56**, 1113–1132 (2010).
5. Lopaschuk, G. D. & Ussher, J. R. Evolving concepts of myocardial energy metabolism: more than just fats and carbohydrates. *Circulation Research* **119**, 1173–1176 (2016).
6. Stanley, W. C. & Chandler, M. P. Energy metabolism in the normal and failing heart: Potential for therapeutic interventions. *Heart Failure Reviews* **7** (2002).
7. Stanley, W. C., Recchia, F. A. & Lopaschuk, G. D. Myocardial substrate metabolism in the normal and failing heart. Physiol Rev **85**, 1093-1129 (2005).
8. Heather, L. C. & Clarke, K. Metabolism, hypoxia, and the diabetic heart. *J Mol Cell Cardiol* **50**, 598–605 (2011).
9. Jeppesen, J. *et al.* Contraction-induced skeletal muscle FAT/CD36 trafficking, and FA uptake is AMPK independent. *J Lipid Res* **52**, 699–711 (2011).
10. Luiken, J. J. F. P. *et al.* Insulin Stimulates long-chain fatty acid Uuilization by Rat cardiac myocytes through cellular redistribution of FAT/CD36. *Diabetes* **51**, 3113-3119 (2002).
11. Richter, E. A. & Ruderman, N. B. AMPK and the biochemistry of exercise: Implications for human health and disease. *Biochemical Journal* **418**, 261–275 (2009).
12. Bertrand, L., Horman, S., Beauloye, C. & Vanoverschelde, J. L. Insulin signalling in the heart. *Cardiovascular Research* **79**, 238–248 (2008).
13. Bertrand, L. *et al.* AMPK activation restores the stimulation of glucose uptake in an in vitro model of insulin-resistant cardiomyocytes via the activation of protein kinase B. *Am J Physiol Heart Circ Physiol* **291**, 239–250 (2006).
14. Goodpaster, B. H. & Sparks, L. M. Metabolic Flexibility in Health and Disease. *Cell Metabolism* **25**, 1027–1036 (2017).
15. Neubauer, S. The failing heart - An engine out of fuel. *New England Journal of Medicine* **356**, 1140–1151 (2007).
16. Evans, R. D. & Heather, L. C. Human metabolism: pathways and clinical aspects. *Surgery (United Kingdom)* **37**, 302–309 (2019).
17. Lopaschuk, G. D., Collins-Nakai, R. L. & Itoi, T. Developmental changes in energy substrate use by the heart. *Cardiovascular Research* **26** (1992).
18. Comline, R. S. & Silver, M. Some aspects of foetal and uteroplacental metabolism in cows with indwelling umbilical and uterine vascular catheters. *J. Phyiol* **260** (1976).

19. Semenza, G. L. Hypoxia-inducible factor 1 and cardiovascular disease. *Annu Rev Physiol* **76**, 39–56 (2014).
20. Lopaschuk, G. D., Ussher, J. R., Folmes, C. D. L., Jaswal, J. S. & Stanley, W. C. Myocardial fatty acid metabolism in health and disease. *Physiol Rev* **90**, 207–258 (2010).
21. Hallman, M. Changes in mitochondrial respiratory chain proteins during perinatal development evidence of the importance of environmental oxygen tension. *Biochemica et Biophysica Acta* **46**, 204 (1971).
22. Su, X. *et al.* RNAase III-type enzyme dicer regulates mitochondrial fatty acid oxidative metabolism in cardiac mesenchymal stem cells. *Int J Mol Sci* **20**, (2019).
23. Mühlfeld, C. *et al.* Myocardial ischemia tolerance in the new-born rat involving opioid receptors and mitochondrial K+ channels. *Anatomical Record - Part A Discoveries in Molecular, Cellular, and Evolutionary Biology* **288**, 297–303 (2006).
24. Nakano, H. *et al.* Glucose inhibits cardiac muscle maturation through nucleotide biosynthesis. *Elife* **6**, (2017).
25. Piquereau, J. & Ventura-Clapier, R. Maturation of cardiac energy metabolism during perinatal development. *Frontiers in Physiology* **9** (2018).
26. Walejko, J. M., Koelmel, J. P., Garrett, T. J., Edison, A. S. & Keller-Wood, M. Multiomics approach reveals metabolic changes in the heart at birth. *Am J Physiol Endocrinol Metab* **315**, 1212–1223 (2018).
27. Razeghi, P. *et al.* Metabolic gene expression in fetal and failing human heart. *Circulation* **104**, 2923-31 (2001).
28. Rubler, S. *et al.* New type of cardiomyopathy associated with diabetic glomerulosclerosis. *Am J Cardiol* **30**, 595–602 (1972).
29. Bailey, C.J. & Day, C. Treatment of type 2 diabetes: future approaches. *British Medical Bulletin* **126,** 123-137 (2018).
30. Jia, G., Hill, M. A. & Sowers, J. R. Diabetic cardiomyopathy: An update of mechanisms contributing to this clinical entity. *Circulation Research* **122**, 624–638 (2018).
31. Thanaj, M. *et al.* Genetic and environmental determinants of diastolic heart function. *Nature Cardiovascular Research* **1**, 361–371 (2022).
32. Peterson, L. R. *et al.* Type 2 diabetes, obesity, and sex difference affect the fate of glucose in the human heart. *Am J Physiol Heart Circ Physiol* **308**, 1510–1516 (2015).
33. Kerr, M., Dodd, M. S. & Heather, L. C. The 'Goldilocks zone' of fatty acid metabolism; to ensure that the relationship with cardiac function is just right. *Clin Sci* **131**, 2079–2094 (2017).
34. Zhang, X. *et al.* High glucose-induced cardiomyocyte death may be linked to unbalanced branched-chain amino acids and energy metabolism. *Molecules* **23**, (2018).
35. Taniguchi, C. M., Emanuelli, B. & Kahn, C. R. Critical nodes in signalling pathways: Insights into insulin action. *Nature Reviews Molecular Cell Biology* **7**, 85–96 (2006).
36. Palomer, X., Salvadó, L., Barroso, E. & Vázquez-Carrera, M. An overview of the crosstalk between inflammatory processes and metabolic dysregulation during diabetic cardiomyopathy. *Int J Cardiol* **168**, 3160–3172 (2013).

37. Hölscher, M. E., Bode, C. & Bugger, H. Diabetic cardiomyopathy: Does the type of diabetes matter? *International Journal of Molecular Sciences* **17** (2016).
38. Dobrin, J. S., Lebeche, D. & Place, G. L. L. Diabetic cardiomyopathy: Signalling defects and therapeutic approaches. *Expert Rev. Cardiovasc.Ther.* **8**, 373–391 (2010).
39. Poornima, I. G., Parikh, P. & Shannon, R. P. Diabetic cardiomyopathy: The search for a unifying hypothesis. *Circ Res* **98**, 596–605 (2006).
40. Battault, S. *et al.* Myocardial glucotoxicity: Mechanisms and potential therapeutic targets. *Archives of Cardiovascular Diseases* **113,** 736–748 (2020).
41. Singh, R., Barden, A., Mori, T. & Beilin, L. Advanced glycation end-products: A review. *Diabetologia* **44**, 129–146 (2001).
42. Kuzan, A. Toxicity of advanced glycation end products (Review). *Biomed Rep* **14**, (2021).
43. Cave, A., Grieve, D., Johar, S., Zhang, M. & Shah, A. M. NADPH oxidase-derived reactive oxygen species in cardiac pathophysiology. *Philosophical Transactions of the Royal Society B: Biological Sciences* **360**, 2327–2334 (2005).
44. Du, X., Matsumura, T., Edelstein, D., Rossetti, L. & Brownlee, M. Inhibition of GAPDH activity. *Journal of Clinical Investigation* **112**, 1049–1057 (2003).
45. Chatham, J. C., Young, M. E. & Zhang, J. Reprint of: Role of O-linked N-acetylglucosamine (O-GlcNAc) modification of proteins in diabetic cardiovascular complications. *Current Opinion in Pharmacology* **54**, 209–220 (2020).
46. Greenman, A. C. *et al.* Increased myofilament calcium sensitivity is associated with decreased cardiac troponin I phosphorylation in the diabetic rat heart. *Exp Physiol* **106**, 2235–2247 (2021).
47. Hu, Y. *et al.* Increased enzymatic O-GlcNAcylation of mitochondrial proteins impairs mitochondrial function in cardiac myocytes exposed to high glucose. *Journal of Biological Chemistry* **284**, 547–555 (2009).
48. Banerjee, P. S., Ma, J. & Hart, G. W. Diabetes-associated dysregulation of O-GlcNAcylation in rat cardiac mitochondria. *Proc Natl Acad Sci U S A* **112**, 6050–6055 (2015).
49. Deng, J., Liao, Y., Liu, J., Liu, W. & Yan, D. Research Progress on Epigenetics of Diabetic Cardiomyopathy in Type 2 Diabetes. *Frontiers in Cell and Developmental Biology* **9** (2021).
50. Van Steenbergen, A. *et al.* Sodium-myoinositol cotransporter-1, SMIT1, mediates the production of reactive oxygen species induced by hyperglycemia in the heart. *Sci Rep* **7**, (2017).
51. Cooper, M. E. Importance of advanced glycation end products in diabetes-associated cardiovascular and renal disease. *Am J Hypertens* **17**, S31–S38 (2004).
52. Clark, R. J. *et al.* Diabetes and the Accompanying Hyperglycemia Impairs Cardiomyocyte Calcium Cycling through Increased Nuclear O-GlcNAcylation. *Journal of Biological Chemistry* **278**, 44230–44237 (2003).
53. Galvez, A. S. *et al.* Aldose reductase induced by hyperosmotic stress mediates cardiomyocyte apoptosis. Differential effects of sorbitol and mannitol. *Journal of Biological Chemistry* **278**, 38484–38494 (2003).

54. Guo, M., Wu, M. H., Korompai, F. & Yuan, S. Y. Upregulation of PKC genes and isozymes in cardiovascular tissues during early stages of experimental diabetes. *Physiol Genomics* **12**, 139-46. (2003).
55. M.a., J. & Hart, G. W. Protein O-GlcNAcylation in diabetes and diabetic complications. *Expert Review of Proteomics* **10**, 365–380 (2013).
56. Palomer, X., Pizarro-Delgado, J., Barroso, E. & Vázquez-Carrera, M. Palmitic and Oleic Acid: The Yin and Yang of Fatty Acids in Type 2 Diabetes Mellitus. *Trends in Endocrinology and Metabolism* **29**, 178–190 (2018).
57. Perdomo, L. *et al.* Protective role of oleic acid against cardiovascular insulin resistance and in the early and late cellular atherosclerotic process. *Cardiovasc Diabetol* **14**, 1–12 (2015).
58. He, Y., Zhou, L., Fan, Z., Liu, S. & Fang, W. Palmitic acid, but not high-glucose, induced myocardial apoptosis is alleviated by N-acetylcysteine due to attenuated mitochondrial-derived ROS accumulation-induced endoplasmic reticulum stress. *Cell Death Dis* **9**, (2018).
59. Wende, A. R. & Abel, E. D. Lipotoxicity in the heart. *Biochimica et Biophysica Acta - Molecular and Cell Biology of Lipids* **1801**, 311–319 (2010).
60. Bekhite, M. *et al.* The role of ceramide accumulation in human induced pluripotent stem cell-derived cardiomyocytes on mitochondrial oxidative stress and mitophagy. *Free Radic Biol Med* **167**, 66–80 (2021).
61. Ricchi, M. *et al.* Differential effect of oleic and palmitic acid on lipid accumulation and apoptosis in cultured hepatocytes. *Journal of Gastroenterology and Hepatology (Australia)* **24**, 830–840 (2009).
62. Baylin, A., Kabagambe, E. K., Siles, X. & Campos, H. *Adipose tissue biomarkers of fatty acid intake 1-3*. *Am J Clin Nutr* **76** (2002).
63. Dyntar, D. *et al.* Glucose and Palmitic Acid Induce Degeneration of Myofibrils and Modulate Apoptosis in Rat Adult Cardiomyocytes. *Diabetes* **50**, 2105–2113 (2001).
64. Kaneto, H., Katakami, N., Matsuhisa, M. & Matsuoka, T. A. Role of reactive oxygen species in the progression of type 2 diabetes and atherosclerosis. *Mediators of Inflammation* **2010** (2010).
65. Hansen, S. S., Aasum, E. & Hafstad, A. D. The role of NADPH oxidases in diabetic cardiomyopathy. *Biochimica et Biophysica Acta - Molecular Basis of Disease* **1864**, 1908–1913 (2018).
66. Yan, L. Redox imbalance stress in diabetes mellitus: Role of the polyol pathway. *Animal Model Exp Med* **1**, 7–13 (2018).
67. Lorenzo, O., Ramírez, E., Picatoste, B., Egido, J. & Tuñón, J. Alteration of energy substrates and ROS production in diabetic cardiomyopathy. *Mediators of Inflammation* **2013** (2013).
68. Ly, L. D. *et al.* Oxidative stress and calcium dysregulation by palmitate in type 2 diabetes. *Exp Mol Med* **49**, e291–e291 (2017).
69. Murphy, M. P. How mitochondria produce reactive oxygen species. *Biochemical Journal* **417**, 1–13 (2009).

70. Peoples, J. N., Saraf, A., Ghazal, N., Pham, T. T. & Kwong, J. Q. Mitochondrial dysfunction, and oxidative stress in heart disease. *Experimental and Molecular Medicine* **51** (2019).
71. Bugger, H. & Abel, E. D. Mitochondria in the diabetic heart. *Cardiovasc Res* **88**, 229–240 (2010).
72. Heinen, A. *et al.* Reverse electron flow-induced ROS production is attenuated by activation of mitochrondrial Ca^{2+}- sensitive K^{+} channels. *Am J Physiol Heart Circ Physiol* **293**, 1400–1407 (2007).
73. Karwi, Q. G., Sun, Q. & Lopaschuk, G. D. The contribution of cardiac fatty acid oxidation to diabetic cardiomyopathy severity. *Cells* **10** (2021).
74. Bai, J., Liu, C., Zhu, P. & Li, Y. Novel Insights into Molecular Mechanism of Mitochondria in Diabetic Cardiomyopathy. *Frontiers in Physiology* **11** (2021).
75. Boudina, S. *et al.* Mitochondrial energetics in the heart in obesity-related diabetes: Direct evidence for increased uncoupled respiration and activation of uncoupling proteins. *Diabetes* **56**, 2457–2466 (2007).
76. Dludla, P. v. *et al.* Uncoupling proteins as a therapeutic target to protect the diabetic heart. *Pharmacological Research* **137**, 11–24 (2018).
77. Giacco, F. & Brownlee, M. Oxidative stress and diabetic complications. *Circulation Research* **107**, 1058–1070 (2010).
78. Casis, O., Gallego, M., Iriarte, M. & Sánchez-Chapula, J. A. Effects of diabetic cardiomyopathy on regional electrophysiologic characteristics of rat ventricle. *Diabetologia* **43**, 101–109 (2000).
79. Bohne, L. J. *et al.* Electrical and structural remodeling contribute to atrial fibrillation in type 2 diabetic db/db mice. *Heart Rhythm* **18**, 118–129 (2021).
80. Bilginoglu, A., Kandilci, H. B. & Turan, B. Intracellular levels of Na+ and TTX-sensitive Na+ channel current in diabetic rat ventricular cardiomyocytes. *Cardiovasc Toxicol* **13**, 138–147 (2013).
81. Contreras, L., Drago, I., Zampese, E. & Pozzan, T. Mitochondria: The calcium connection. *Biochimica et Biophysica Acta - Bioenergetics* **1797**, 607–618 (2010).
82. Finkel, T. *et al.* The ins and outs of mitochondrial calcium. *Circulation Research* **116**, 1810–1819 (2015).
83. Meo, M. *et al.* Reduction in kv current enhances the temporal dispersion of theaction potential in diabetic myocytes: Insights from a novelrepolarization algorithm. *J Am Heart Assoc* **5**, 1–18 (2016).
84. Hadova, K. *et al.* Isolated downregulation of HCN2 in ventricles of rats with streptozotocin-induced diabetic cardiomyopathy. *BMC Cardiovasc Disord* **21**, 1–11 (2021).
85. Ladage, D. *et al.* Inhibition of PKCα/β with ruboxistaurin antagonizes heart failure in pigs after myocardial infarction injury. *Circ Res* **109**, 1396–1400 (2011).
86. Mcgreevy, J. W., Hakim, C. H., Mcintosh, M. A. & Duan, D. Animal models of Duchenne muscular dystrophy: from basic mechanisms to gene therapy. *Disease models & mechanisms*, **8**, 195–213 (2015).
87. Zatti, S. *et al.* Complete restoration of multiple dystrophin isoforms in genetically corrected Duchenne muscular dystrophy patient–derived cardiomyocytes. *Mol Ther Methods Clin Dev* **1**, 1 (2014).

88. Mercuri, E., Bönnemann, C. G. & Muntoni, F. Muscular dystrophies. *The Lancet* **394** (2019).
89. Birnkrant, D. J. *et al.* Diagnosis and management of Duchenne muscular dystrophy, part 2: respiratory, cardiac, bone health, and orthopaedic management. *The Lancet Neurology* **17**, 347–361 (2018).
90. Passamano, L. *et al*. Improvement of survival in Duchenne Muscular Dystrophy: retrospective analysis of 835 patients. *Acta Myol*. **31**, 121-125 (2012).
91. Spitali, P. *et al.* Tracking disease progression non-invasively in Duchenne and Becker muscular dystrophies. *J Cachexia Sarcopenia Muscle* **9**, 715–726 (2018).
92. Mavrogeni, S. Cardiac involvement in Duchenne and Becker muscular dystrophy. *World J Cardiol* **7**, 410 (2015).
93. Broomfield, J., Hill, M., Guglieri, M., Crowther, M. & Abrams, K. Life expectancy in Duchenne muscular dystrophy. *Neurology* **97**, E2304–E2314 (2021).
94. Rahimov, F. & Kunkel, L. M. Cellular and molecular mechanisms underlying muscular dystrophy. *Journal of Cell Biology* **201**, 499–510 (2013).
95. Mokri, B. & Engel, A. G. Duchenne dystrophy: Electron microscopic findings pointing to a basic or early abnormality in the plasma membrane of the muscle fiber. *Neurology* **25**, 1111-20 (1975).
96. Duan, D., Goemans, N., Takeda, S., Mercuri, E. & Aartsma-Rus, A. Duchenne muscular dystrophy. *Nature Reviews Disease Primers* **7** (2021).
97. McNally, E. M. New approaches in the therapy of cardiomyopathy in muscular dystrophy. *Annual Review of Medicine* **58**, 75–88 (2007).
98. Saito, M. *et al.* Cardiac dysfunction with Becker muscular dystrophy. *Am Heart J*. 132 (3): 642-7 (1996).
99. Zhang, W., Sang, A. E., ten Hove, M., Neubauer, S. & Clarke, K. Data on uncoupling protein-3 levels, hypoxia, low flow ischemia, and insulin stimulation in dystrophin-deficient mdx mouse hearts. *Data Brief* **20**, 277–280 (2018).
100. Even, P. C., Decrouyt, A. & Chinett, A. Defective regulation of energy metabolism in mdx-mouse skeletal muscles. *Biochem. J* **304,** (1994).
101. Stapleton, D. I. *et al.* Dysfunctional muscle and liver glycogen metabolism in mdx dystrophic mice. *PLoS One* **9**, (2014).
102. Mantuano, P. *et al.* Effect of a long-term treatment with metformin in dystrophic mdx mice: A reconsideration of its potential clinical interest in Duchenne muscular dystrophy. *Biochem Pharmacol* **154**, 89–103 (2018).
103. Schneider, S. M. *et al.* Glucose Metabolism as a Pre-clinical Biomarker for the Golden Retriever Model of Duchenne Muscular Dystrophy. *Mol Imaging Biol* **20**, 780–788 (2018).
104. Bostock, E. L. *et al.* Impaired glucose tolerance in adults with duchenne and becker muscular dystrophy. *Nutrients* **10** (2018).
105. Amaral, A. R. *et al.* Abnormal carbohydrate metabolism in a canine model for muscular dystrophy. *J Nutr Sci* **6** (2017).
106. Rodríguez-Cruz, M. *et al.* Evidence of insulin resistance and other metabolic alterations in boys with duchenne or becker muscular dystrophy. *Int J Endocrinol* **2015**, (2015).

107. Amor, F. *et al.* Cholesterol metabolism is a therapeutic target in Duchene Muscular Dystrophy. *Journal of Cachexia Sarcopenia Muscle* vol **12**, 677-693 (2021).
108. Srivastava, N. K., Yadav, R., Mukherjee, S., Pal, L. & Sinha, N. Abnormal lipid metabolism in skeletal muscle tissue of patients with muscular dystrophy: In vitro, high-resolution NMR spectroscopy-based observation in early phase of the disease. *Magn Reson Imaging* **38**, 163–173 (2017).
109. Eid Mutlak, Y. *et al.* A signaling hub of insulin receptor, dystrophin glycoprotein complex and plakoglobin regulates muscle size. *Nat Commun* **11**, (2020).
110. Carlson, W. D. Animal models of heart failure: a scientific statement from the American Heart Association **111**, 131-50 (2012).
111. Janssen, P. M. L., Hiranandani, N., Mays, T. A. & Rafael-Fortney, J. A. Utrophin deficiency worsens cardiac contractile dysfunction present in dystrophin-deficient mdx mice. *Am J Physiol Heart Circ Physiol* **289**, 2373–2378 (2005).
112. Betts, C. A. *et al.* Prevention of exercised induced cardiomyopathy following Pip-PMO treatment in dystrophic mdx mice. *Sci Rep* **5**, (2015).
113. Stuckey, D. J. *et al.* In vivo MRI characterization of progressive cardiac dysfunction in the mdx mouse model of muscular dystrophy. *PLoS One* **7**, (2012).
114. Leiter, E. H. & Schile, A. Genetic and Pharmacologic Models for Type 1 Diabetes. *Curr Protoc Mouse Biol* **3**, 9–19 (2013).
115. Wang, B., Chandrasekera, P. C. & Pippin, J. J. Leptin-and Leptin Receptor-Deficient Rodent Models: Relevance for Human Type 2 Diabetes. *Curr Diabetes Rev* **10**, 131-45 (2014).
116. Perbellini, F. *et al.* Chronic high-fat feeding affects the mesenchymal cell population expanded from adipose tissue but not cardiac atria. *Stem Cells Transl Med* **4**, 1403–1414 (2015).
117. Mansor, L. S. *et al.* Cardiac metabolism in a new rat model of type 2 diabetes using high-fat diet with low dose streptozotocin. *Cardiovasc Diabetol* **12**, (2013).
118. Wong, L. yen *et al.* Comparison of human and rodent cell models to study myocardial lipid-induced insulin resistance. *Prostaglandins Leukot Essent Fatty Acids* **167**, (2021).
119. Onódi, Z. *et al.* Systematic transcriptomic and phenotypic characterization of human and murine cardiac myocyte cell lines and primary cardiomyocytes reveals serious limitations and low resemblances to adult cardiac phenotype. *J Mol Cell Cardiol* **165**, 19–30 (2022).
120. Kuznetsov, A. v., Javadov, S., Sickinger, S., Frotschnig, S. & Grimm, M. H9c2 and HL-1 cells demonstrate distinct features of energy metabolism, mitochondrial function and sensitivity to hypoxia-reoxygenation. *Biochim Biophys Acta Mol Cell Res* **1853**, 276–284 (2015).
121. Wang, Y. *et al.* Genome editing of isogenic human induced pluripotent stem cells recapitulates long QT phenotype for drug testing. J Am Coll Cardiol **64**, 451-9 (2014).
122. Sapp, V. *et al.* Genome-wide CRISPR/Cas9 screening in human iPS derived cardiomyocytes uncovers novel mediators of doxorubicin cardiotoxicity. *Sci Rep* **11** (2021).

123. Gähwiler, E. K. N. *et al.* Human iPSCs and genome editing technologies for precision cardiovascular tissue engineering. *Frontiers in Cell and Developmental Biology* **9** (2021).
124. Takahashi, K. & Yamanaka, S. Induced pluripotent stem cells in medicine and biology. *Development (Cambridge)* **140**, 2457–2461 (2013).
125. Takahashi, K. & Yamanaka, S. Induction of pluripotent stem cells from mouse embryonic and adult fibroblast cultures by defined factors. *Cell* **126**, 663–676 (2006).
126. Okita, K. & Yamanaka, S. Induced pluripotent stem cells: opportunities and challenges. *Philos Trans R Soc Lon B Biol Sci* **366**, 2198-2207 (2011).
127. Yoshida, Y., Takahashi, K., Okita, K., Ichisaka, T. & Yamanaka, S. Hypoxia Enhances the Generation of induced pluripotent stem cells. *Cell Stem Cell* **5**, 237–241 (2009).
128. Ye, L., Swingen, C. & Zhang, J. Induced pluripotent stem cells and their potential for basic and clinical sciences. *Curr Cardio Rev* **9**, 63–72 (2013).
129. Kondo, T. *et al.* Modeling Alzheimer's disease with iPSCs reveals stress phenotypes associated with intracellular Aß and Differential Drug Responsiveness. *Stem Cell* **12**, 487–496 (2013).
130. Crombie, D. E. *et al.* Friedreich's ataxia induced pluripotent stem cell-derived cardiomyocytes display electrophysiological abnormalities and calcium handling deficiency. *Aging (Albany NY)* **9**, 1440-1452 (2017).
131. McCauley, K. B. *et al.* Efficient derivation of functional human airway epithelium from pluripotent stem cells via temporal regulation of Wnt Signaling. *Cell Stem Cell* **20**, 844-857.e6 (2017).
132. Takahashi, K. *et al.* Induction of pluripotent stem cells from adult human fibroblasts by defined Factors. *Cell* **131**, 861–872 (2007).
133. Harrison, S. P. *et al.* Liver organoids: recent developments, limitations and potential. *Frontiers in Medicine* **8** (2021).
134. Andrysiak, K., Stępniewski, J. & Dulak, J. Human-induced pluripotent stem cell-derived cardiomyocytes, 3D cardiac structures, and heart-on-a-chip as tools for drug research. *Pflugers Archiv European Journal of Physiology* (2021).
135. Berg, C. W. van den *et al.* Transcriptome of human foetal heart compared with cardiomyocytes from pluripotent stem cells. *Development* **142,** 3231–3238 (2015).
136. Zhou, Y. *et al.* Comparative gene expression analyses reveal distinct molecular signatures between differentially reprogrammed cardiomyocytes. *Cell Rep* **20**, 3014–3024 (2017).
137. Al-Qusairi, L. *et al.* T-tubule disorganization and defective excitation-contraction coupling in muscle fibers lacking myotubularin lipid phosphatase. *PNAS Biological Sciences* **106,** 18763-18768 (2009).
138. Denning, C. *et al.* Cardiomyocytes from human pluripotent stem cells: From laboratory curiosity to industrial biomedical platform. *Biochim Biophys Acta Mol Cell Res* **1863**, 1728–1748 (2016).

139. Karakikes, I., Ameen, M., Termglinchan, V. & Wu, J. C. Human induced pluripotent stem cell-derived cardiomyocytes: Insights into molecular, cellular, and functional phenotypes. *Circulation Research* **117**, 80–88 (2015).
140. Bowman, P. R. T., Smith, G. L. & Gould, G. W. GLUT4 expression and glucose transport in human induced pluripotent stem cell-derived cardiomyocytes. *PLoS One* **14**, e0217885 (2019).
141. van Vliet, P., Wu, S. M., Zaffran, S. & Pucéat, M. Early cardiac development: A view from stem cells to embryos. *Cardiovascular Research* **96**, 352–362 (2012).
142. Ueno, S. *et al.* Biphasic role for Wnt/β-catenin signaling in cardiac specification in zebrafish and embryonic stem cells. *PNAS Biological Sciences* **104**, 9685-9690 (2007).
143. Feyen, D. A. M. *et al.* Metabolic maturation media Improve physiological function of human iPSC-derived cardiomyocytes. *Cell Rep* **32**, (2020).
144. Mannhardt, I. *et al.* Human engineered heart tissue: Analysis of contractile force. *Stem Cell Reports* **7**, 29–42 (2016).
145. Ng, R. *et al.* Contractile work directly modulates mitochondrial protein levels in human engineered heart tissues. *American Journal of Physiology-Heart and Circulatory Physiology* 1516–1524 (2020).
146. Mills, R. J., Voges, H. K., Porrello, E. R. & Hudson, J. E. Disease modeling and functional screening using engineered heart tissue. *Curr Opin Physiol* **1**, 80–88 (2018).
147. Breckwoldt, K. *et al.* Differentiation of cardiomyocytes and generation of human engineered heart tissue. *Nat Protoc* **12**, 1177–1197 (2017).
148. Leonard, A. *et al.* Afterload promotes maturation of human induced pluripotent stem cell derived cardiomyocytes in engineered heart tissues. *J Mol Cell Cardiol* **118**, 147–158 (2018).
149. Lopez, C. A. *et al.* Physiological and pharmacological stimulation for in vitro maturation of substrate metabolism in human induced pluripotent stem cell-derived cardiomyocytes. *Sci Rep* **11** (2021).
150. Eschenhagen, T. *et al.* Three-dimensional reconstitution of embryonic cardiomyocytes in a collagen matrix: a new heart muscle model system. *The FASEB Journal* **11**, 683–694 (1997).
151. Katare, R. G., Ando, M., Kakinuma, Y. & Sato, T. Engineered heart tissue: A novel tool to study the ischemic changes of the heart in vitro. *PLoS One* **5** (2010).
152. Lemme, M. *et al.* Atrial-like Engineered Heart Tissue: An In Vitro Model of the Human Atrium. *Stem Cell Reports* **11**, 1378–1390 (2018).
153. Lee, E. J., Kim, D. E., Azeloglu, E. U. & Costa, K. D. Engineered cardiac organoid chambers: Toward a functional biological model ventricle. *Tissue Eng Part A* **14**, 215–225 (2008).
154. Filippo Buono, M. *et al.* Human cardiac organoids for modeling genetic cardiomyopathy. *Cells* **9** (2020).
155. Richards, D. J. *et al.* Human cardiac organoids for the modelling of myocardial infarction and drug cardiotoxicity. *Nat Biomed Eng* **4**, 446–462 (2020).

156. Mills, R. J. *et al.* Functional screening in human cardiac organoids reveals a metabolic mechanism for cardiomyocyte cell cycle arrest. *Proc Natl Acad Sci U S A* **114**, E8372–E8381 (2017).
157. Zhao, Y. *et al.* A Platform for generation of chamber-specific cardiac tissues and disease modeling. *Cell* **176**, 913-927.e18 (2019).
158. Ronaldson-Bouchard, K. *et al.* Advanced maturation of human cardiac tissue grown from pluripotent stem cells. *Nature* **556**, 239–243 (2018).
159. Giacomelli, E. *et al.* Human-iPSC-Derived cardiac stromal cells enhance maturation in 3D cardiac microtissues and reveal non-cardiomyocyte contributions to heart disease. *Cell Stem Cell* **26**, 862-879.e11 (2020).
160. Hofbauer, P. *et al.* Cardioids reveal self-organizing principles of human cardiogenesis. *Cell* **184**, 3299-3317.e22 (2021).
161. Sacchetto, C., Vitiello, L., de Windt, L. J., Rampazzo, A. & Calore, M. Modeling cardiovascular diseases with hipsc-derived cardiomyocytes in 2D and 3D cultures. *Int J Mol Sci* **21** (2020).
162. Mazzola, M. & Di Pasquale, E. Toward cardiac regeneration: Combination of pluripotent stem cell-based therapies and bioengineering strategies. *Front Bioeng Biotechnol* **8**, (2020).
163. Clevers, H. Modeling development and disease with organoids. *Cell* **165**, 1586–1597 (2016).
164. Lewis-Israeli, Y. R. *et al.* Self-assembling human heart organoids for the modeling of cardiac development and congenital heart disease. *Nat Commun* **12**, (2021).
165. Zhao, D., Lei, W. & Hu, S. Cardiac organoid — a promising perspective of preclinical model. *Stem Cell Research and Therapy* **12** (2021).
166. Zhang, Y. *et al.* 3D Modeling of Esophageal Development using human PSC-derived basal progenitors reveals a critical role for Notch signaling. *Cell Stem Cell* **23**, 516-529.e5 (2018).
167. Voges, H. K. *et al.* Development of a human cardiac organoid injury model reveals innate regenerative potential. *Development (Cambridge)* **144**, 1118–1127 (2017).
168. Trisno, S. L. *et al.* Esophageal Organoids from human pluripotent stem cells delineate Sox2 functions during Esophageal Specification. *Cell Stem Cell* **23**, 501-515.e7 (2018).
169. Wu, F. *et al.* Generation of hepatobiliary organoids from human induced pluripotent stem cells. *J Hepatol* **70**, 1145–1158 (2019).
170. Koehler, K. R. *et al.* Generation of inner ear organoids containing functional hair cells from human pluripotent stem cells. *Nat Biotechnol* **35**, 583–589 (2017).
171. Lee, J. *et al.* Hair-bearing human skin generated entirely from pluripotent stem cells. *Nature* **582**, 399–404 (2020).
172. Hohwieler, M. *et al.* Human pluripotent stem cell-derived acinar/ductal organoids generate human pancreas upon orthotopic transplantation and allow disease modelling. *Gut* **66**, 473–486 (2017).
173. Koike, H. *et al.* Modelling human hepato-biliary-pancreatic organogenesis from the foregut–midgut boundary. *Nature* **574**, 112–116 (2019).

174. Abulaiti, M. *et al.* Establishment of a heart-on-a-chip microdevice based on human iPS cells for the evaluation of human heart tissue function. *Sci Rep* **10** (2020).
175. Lewis-Israeli, Y. R., Wasserman, A. H. & Aguirre, A. Heart organoids and engineered heart tissues: Novel tools for modeling human cardiac biology and disease. *Biomolecules* **11** (2021).
176. Nath, S. & Devi, G. R. Three-dimensional culture systems in cancer research: Focus on tumor spheroid model. *Pharmacology and Therapeutics* **163**, 94–108 (2016).
177. Yan, Y. *et al.* Cell population balance of cardiovascular spheroids derived from human induced pluripotent stem cells. *Sci Rep* **9**, 1–12 (2019).
178. Eschenhagen, T. *et al*. Three-dimensional cardiomyocytes muscle model reconstitution in a collagen system of embryonic matrix: a new heart muscle model. *FASEB J* **11**, 683–694.
179. Hansen, A. *et al.* Development of a drug screening platform based on engineered heart tissue. *Circ Res* **107**, 35–44 (2010).
180. Mills, R. J. & Hudson, J. E. Bioengineering adult human heart tissue: How close are we? *APL Bioeng* **3**, 010901 (2019).
181. Zimmermann, W. H., Melnychenko, I. & Eschenhagen, T. Engineered heart tissue for regeneration of diseased hearts. *Biomaterials* **25**, 1639–1647 (2004).
182. Tiburcy, M. *et al.* Defined engineered human myocardium with advanced maturation for applications in heart failure modeling and repair. *Circulation* **135**, 1832–1847 (2017).
183. Mills, R. J. *et al.* Drug screening in human PSC-cardiac organoids identifies pro-proliferative compounds acting via the mevalonate pathway. *Cell Stem Cell* **24**, 895-907.e6 (2019).
184. Bailey, A. L. *et al.* SARS-CoV-2 Infects human engineered heart tissues and models COVID-19 myocarditis. *JACC Basic Transl Sci* **6**, 331–345 (2021).
185. Yu, J. *et al.* Induced pluripotent stem cell lines derived from human somatic cells. *Science* **318** (2007).
186. van Wilgenburg, B., Browne, C., Vowles, J. & Cowley, S. A. Efficient, long-term production of monocyte-derived macrophages from human pluripotent stem cells under partly defined and fully defined conditions. *PLoS One* **8** (2013).
187. Massouridès, E. *et al.* Dp412e: A novel human embryonic dystrophin isoform induced by BMP4 in early differentiated cells. *Skelet Muscle* **5** (2015).
188. Claassen, D. A., Desler, M. M. & Rizzino, A. ROCK inhibition enhances the recovery and growth of cryopreserved human embryonic stem cells and human induced pluripotent stem cells. *Mol Reprod Dev* **76**, 722–732 (2009).
189. Spoerl, S., Peter, R. & Krackhardt, A. M. Biobanking and Cryopreservation of Stem Cells. **951**, 67–76 (2016).
190. Beers, J. *et al.* Passaging and colony expansion of human pluripotent stem cells by enzyme-free dissociation in chemically defined culture conditions. *Nat Protoc* **7**, 2029–2040 (2012).
191. Lin, B. *et al.* Culture in glucose-depleted medium supplemented with fatty acid and 3,3',5-Triiodo-L-thyronine facilitates purification and maturation of human

pluripotent stem cell-derived cardiomyocytes. *Front Endocrinol (Lausanne)* **8** (2017).

192. Sharma, A. *et al.* Derivation of highly purified cardiomyocytes from human induced pluripotent stem cells using small molecule-modulated differentiation and subsequent glucose starvation. *Journal of Visualized Experiments* **2015** (2015).
193. Wang, T. *et al.* A Network Pharmacology study of the multi-targeting profile of an antiarrhythmic Chinese medicine Xin Su Ning. *Front Pharmacol* **10**, 1138 (2019).
194. Fleige, S. & Pfaffl, M. W. RNA integrity and the effect on the real-time qRT-PCR performance. *Molecular Aspects of Medicine* **27**, 126–139 (2006).
195. Livak, K. J. & Schmittgen, T. D. Analysis of relative gene expression data using real-time quantitative PCR and the 2-ΔΔCT method. *Methods* **25**, 402–408 (2001).
196. Lopaschuk, G. D. Advantages and limitations of experimental techniques used to measure cardiac energy metabolism. *Journal of Nuclear Cardiology* **4** (1997).
197. Neely, J. R., Denton, R. M., England, P. J. & Randle, P. J. The Effects of Increased Heart Work on the Tricarboxylate Cycle and its Interactions with Glycolysis in the Perfused Rat Heart. *Biochem. J* **128** (1972).
198. Russell, R. W. & Young, J. W. A Review of metabolism of labeled glucoses for Use in measuring glucoserRecycling. *J Dairy Sci* **73**, 1005–1016 (1990).
199. Onay-Besikci, A. Radioactive measurements as an indicator of metabolic fluxes in myocytes. *The Open Chemical and Biomedical Methods Journal* **3** (2010).
200. Liedtke, A. J., Renstrom, B. & Nellis, S. H. Correlation Between [5-3H]-Glucose and [U-14C]-Deoxyglucose as markers of glycolysis in reperfused myocardium. *Circ Res*. **71** (1992)**.**
201. Barr, R. L. & Lopaschuk, G. D. Methodology for measuring in vitro/ex vivo cardiac energy metabolism. Joural of Pharmacological and Toxicological Methods **43**, 141-152 (2000).
202. Heather, L. C. *et al.* Differential translocation of the fatty acid transporter, FAT/CD36, and the glucose transporter, GLUT4, coordinates changes in cardiac substrate metabolism during ischemia and reperfusion. *Circ Heart Fail* **6**, 1058–1066 (2013).
203. Hammerstedt, R.H. The Use of Dowex-l-Borate to Separate ^{3}HOH from 2-^{3}H-Glucose.Analytical Biochemistry **56**, 292-293 (1973).
204. Teslaa, T. & Teitell, M. A. Techniques to monitor glycolysis. *Methods in Enzymology* **542**, 91–114 (2014).
205. Malandraki-Miller, S. *et al.* Metabolic flux analyses to assess the differentiation of adult cardiac progenitors after fatty acid supplementation. *Stem Cell Res* **38**, 101458 (2019).
206. Itoi, T. & Lopaschuk, G. D. The Contribution of glycolysis, glucose oxidation, lactate oxidation, and fatty acid oxidation to ATP production in isolated biventricular Working hearts from 2-week-old rabbits. *Paediatric Research* **34** (1993).
207. Lopaschuk, G. D. & Tsang, H. Metabolism of palmitate in isolated working hearts from spontaneously diabetic 'BB' Wistar rats. *Circ Res* **61**, 853–858 (1987).

208. Belke, D. D., Larsen, T. S., Lopaschuk, G. D. & Severson, D. L. Glucose and fatty acid metabolism in the isolated working mouse heart. *Am J Physiol Regul Integr Comp Physiol* **277**, 1210–1217 (1999).
209. Sala, L. *et al.* Musclemotion: A versatile open software tool to quantify cardiomyocyte and cardiac muscle contraction in vitro and in vivo. *Circ Res* **122,** e5-e16 (2018)
210. Mummery, C. L. *et al.* New methods in cardiovascular biology MUSCLEMOTION A versatile open software tool to quantify cardiomyocyte and cardiac muscle contraction in vitro and in vivo. *Circ Res* **122**, e5-e16 (2017).
211. van Meer, B. J. *et al.* Quantification of Muscle Contraction In Vitro and In Vivo Using MUSCLEMOTION Software: From Stem Cell-Derived Cardiomyocytes to Zebrafish and Human Hearts. *Curr Protoc Hum Genet* **99**, 1–21 (2018).
212. Hyun, S. W. *et al.* The effects of gentamicin and penicillin/streptomycin on the electrophysiology of human induced pluripotent stem cell-derived cardiomyocytes in manual patch clamp and multi-electrode array system. *J Pharmacol Toxicol Methods* **91**, 1–6 (2018).
213. Mummery, C. *et al.* Differentiation of human embryonic stem cells to cardiomyocytes: Role of coculture with visceral endoderm-like cells. *Circulation* **107**, 2733–2740 (2003).
214. Kattman, S. J. *et al.* Resource Stage-Specific Optimization of Activin / Nodal and BMP Signaling Promotes Cardiac Differentiation of Mouse and Human Pluripotent Stem Cell Lines. *Stem Cell* **8**, 228–240 (2010).
215. Kehat, I. *et al.* Human embryonic stem cells can differentiate into myocytes with structural and functional properties of cardiomyocytes. **108**, 363–364 (2001).
216. Spijker, R. *et al.* Differentiation of Human Embryonic Stem Cells to Cardiomyocytes Role of Coculture with Visceral Endoderm-Like Cells. *Circulation* **107,** 2733–2740 (2003)
217. Jha, R., Xu, R. H. & Xu, C. Efficient differentiation of cardiomyocytes from human pluripotent stem cells with growth factors. Methods Mol Biol **1299**, 115–131 (2015).
218. Minami, I. *et al.* A Small Molecule that Promotes Cardiac Differentiation of Human Pluripotent Stem Cells under Defined, Cytokine- and Xeno-free Conditions. *Cell Rep* **2**, 1448–1460 (2012).
219. Lin, Y. *et al.* Efficient differentiation of cardiomyocytes and generation of calcium-sensor reporter lines from nonhuman primate iPSCs. *Sci Rep* **8**, 1–16 (2018).
220. Lian, X. *et al.* Directed cardiomyocyte differentiation from human pluripotent stem cells by modulating Wnt/β-catenin signaling under fully defined conditions. *Nat Protoc* **8**, 162–175 (2013).
221. Laflamme, M. A. *et al.* Cardiomyocytes derived from human embryonic stem cells in pro-survival factors enhance function of infarcted rat hearts. **25**, 1015–1024 (2007).
222. Paige, S. L. *et al.* Endogenous wnt/β-Catenin signaling is required for cardiac differentiation in human embryonic stem cells. *PLoS One* **5** (2010).
223. Lian, X., Zhang, J., Zhu, K., Kamp, T. J. & Palecek, S. P. Insulin inhibits cardiac mesoderm, not mesendoderm, formation during cardiac differentiation of human

pluripotent stem cells and modulation of canonical wnt signaling can rescue this inhibition. *Stem Cells* **31**, 447–457 (2013).
224. Burridge, P. W., Holmström, A. & Wu, J. C. Chemically Defined Culture and Cardiomyocyte Differentiation of Human Pluripotent Stem Cells. *Curr Protoc Hum Genet* **87**, 21.3.1-21.3.15 (2015).
225. Lee, J. H., Protze, S. I., Laksman, Z., Backx, P. H. & Keller, G. M. Human Pluripotent Stem Cell-Derived Atrial and Ventricular Cardiomyocytes Develop from Distinct Mesoderm Populations. *Cell Stem Cell* **21**, 179-194.e4 (2017).
226. Kleinsorge, M. & Cyganek, L. Subtype-Directed Differentiation of Human iPSCs into Atrial and Ventricular Cardiomyocytes. *STAR Protoc* **1** (2020).
227. Berg, C. W. Van Den *et al.* Transcriptome of human foetal heart compared with cardiomyocytes from pluripotent stem cells. *Development* **14**, 23231–3238 (2015)
228. Fijnvandraat, A. C. *et al.* Cardiomyocytes derived from embryonic stem cells resemble cardiomyocytes of the embryonic heart tube. Cardiovasc Res **58**, 399–409 (2003).
229. Zhu, R. *et al.* Physical developmental cues for the maturation of human pluripotent stem cell-derived cardiomyocytes. *Stem Cell Res Ther* **5**, 1–11 (2014).
230. Robertson, C., Tran, D. D. & George, S. C. Concise review: Maturation phases of human pluripotent stem cell-derived cardiomyocytes. *Stem Cells* **31**, 829–837 (2013).
231. Bruyneel, A. A. N., Sehgal, A., Malandraki-Miller, S. & Carr, C. Stem Cell Therapy for the Heart: Blind Alley or Magic Bullet?. *Journal of Cardiovascular Translational Research* **9**, 405– (2016).
232. Földes, G. *et al.* Aberrant α-adrenergic hypertrophic response in Cardiomyocytes from human induced pluripotent cells. *Stem Cell Reports* **3**, 905–914 (2014).
233. Lopaschuk, G. D., Collins-Nakai, R. L. & Itoi, T. Developmental changes in energy substrate use by the heart. *Cardiovasc Res* **26**, 1172–1180 (1992).
234. Varum, S. *et al.* Energy Metabolism in Human Pluripotent Stem Cells and Their Differentiated Counterparts. *PLoS One* **6** (2011).
235. Ramachandra, C. J. A. *et al.* Fatty acid metabolism driven mitochondrial bioenergetics promotes advanced developmental phenotypes in human induced pluripotent stem cell derived cardiomyocytes. *Int J Cardiol* **272**, 288–297 (2018).
236. Yang, X. *et al.* Fatty Acids Enhance the Maturation of Cardiomyocytes Derived from Human Pluripotent Stem Cells. *Stem Cell Reports* **13**, 657–668 (2019).
237. Hu, D. *et al.* Metabolic maturation of human pluripotent stem cellderived cardiomyocytes by inhibition of HIF1α and LDHA. *Circ Res* **123**, 1066–1079 (2018).
238. Ronaldson-Bouchard, K. *et al.* Advanced maturation of human cardiac tissue grown from pluripotent stem cells. *Nature* **556**, 239–243 (2018).
239. Ulmer, B. M. *et al.* Contractile Work Contributes to Maturation of Energy Metabolism in hiPSC-Derived Cardiomyocytes. *Stem Cell Reports* **10**, 834–847 (2018).
240. Song, H., Zandstra, P. W. & Radisic, M. Engineered heart tissue model of diabetic myocardium. *Tissue Eng Part A* **17**, 1869–1878 (2011).

241. Mihoubi, W., Sahli, E., Gargouri, A. & Amiel, C. FTIR spectroscopy of whole cells for the monitoring of yeast apoptosis mediated by p53 over-expression and its suppression by Nigella sativa extracts. *PLoS One* **12**, (2017).
242. Sabbatini, S., Conti, C., Orilisi, G. & Giorgini, E. Infrared spectroscopy as a new tool for studying single living cells: Is there a niche? *Biomed Spectrosc Imaging* **6**, 85–99 (2017).
243. Mourant, J. R. *et al*. FTIR Spectroscopy Demonstrates Biochemical Differences in Mammalian Cell Cultures at Different Growth Stages. *Biophysical Journal* **85** (2003)
244. Fadlelmoula, A., Pinho, D., Carvalho, V. H., Catarino, S. O. & Minas, G. Fourier Transform Infrared (FTIR) Spectroscopy to Analyse Human Blood over the Last 20 Years: A Review towards Lab-on-a-Chip Devices. *Micromachines* **13** (2022).
245. Drozdz, A. *et al.* FTIR microspectroscopy revealed biochemical changes in liver and kidneys as a result of exposure to low dose of iron oxide nanoparticles. *Spectrochim Acta A Mol Biomol Spectrosc* **236**, (2020).
246. Mata-Miranda, M. M. *et al.* Morphological, molecular and FTIR spectroscopic analysis during the differentiation of kidney cells from pluripotent stem cells. *Biol Res* **50** (2017).
247. Wang, Y. *et al.* Single-Cell Infrared Microspectroscopy Quantifies Dynamic Heterogeneity of Mesenchymal Stem Cells during Adipogenic Differentiation. *Anal Chem* **93**, 671–676 (2021).
248. Vazquez-Zapien, G. J. *et al.* FTIR Spectroscopic and Molecular Analysis during Differentiation of Pluripotent Stem Cells to Pancreatic Cells. *Stem Cells Int* **2016** (2016).
249. Ami, D. *et al.* Embryonic stem cell differentiation studied by FT-IR spectroscopy. *Biochim Biophys Acta Mol Cell Res* **1783**, 98–106 (2008).
250. Chen, L. *et al.* Synchrotron infrared measurements of protein phosphorylation in living single PC12 cells during neuronal differentiation. *Anal Chem* **84**, 4118–4125 (2012).
251. Tobin, M. J. *et al.* FTIR spectroscopy of single live cells in aqueous media by synchrotron IR microscopy using microfabricated sample holders. *Vib Spectrosc* **53**, 34–38 (2010).
252. Chen, G. *et al.* Chemically defined conditions for human iPSC derivation and culture. *Nat Methods* **8**, 424–429 (2011).
253. Lian, X. *et al.* Robust cardiomyocyte differentiation from human pluripotent stem cells via temporal modulation of canonical Wnt signaling. *Proc Natl Acad Sci U S A* **109** (2012).
254. Burridge, P. W. *et al.* Chemically defned generation of human cardiomyocytes. *Nat Methods* **11**, 855–860 (2014).
255. Goldberg, I. J., Trent, C. M. & Schulze, P. C. Lipid metabolism and toxicity in the heart. *Cell Metab* **15**, 805–812 (2012).
256. Dodd, M. S. *et al.* Fatty acids prevent hypoxia-inducible factor-1α signaling through decreased succinate in diabetes. *JACC Basic Transl Sci* **3**, 485–498 (2018).

257. Rieppo, L. *et al.* Application of second derivative spectroscopy for increasing molecular specificity of fourier transform infrared spectroscopic imaging of articular cartilage. *Osteoarthritis Cartilage* **20**, 451–459 (2012).
258. Kattman, S. J. *et al.* Resource Stage-Specific Optimization of Activin / Nodal and BMP Signaling Promotes Cardiac Differentiation of Mouse and Human Pluripotent Stem Cell Lines. *Stem Cell* **8**, 228–240 (2010).
259. Yang, L. *et al.* Human cardiovascular progenitor cells develop from a KDR+ embryonic-stem-cell-derived population. *Nature* **453**, 3–8 (2008).
260. Tam, P. P. L. & Behringer, R. R. Mouse gastrulation: the formation of a mammalian body plan. Mech Dev **68**, 3–25 (1997).
261. Chen, B. *et al.* Small molecule-mediated disruption of Wnt-dependent signaling in tissue regeneration and cancer. *Nat Chem Biol* **5**, 100–107 (2009).
262. Garbern, J. C. *et al.* Inhibition of mTOR Signaling Enhances Maturation of Cardiomyocytes Derived from Human-Induced Pluripotent Stem Cells via p53-Induced Quiescence. *Circulation* 285–300 (2020).
263. Guo, Y. & Pu, W. T. Cardiomyocyte maturation: new phase in development. *Circulation Research* 1086–1106 (2020).
264. Karbassi, E. *et al.* Cardiomyocyte maturation: advances in knowledge and implications for regenerative medicine. *Nature Reviews Cardiology* **17**, 341–359 (2020).
265. Besser, R. R. *et al.* Engineered microenvironments for maturation of stem cell derived cardiac myocytes. *Theranostics* **8**, 124–140 (2018).
266. Alvarez-Dominguez, J. R. & Melton, D. A. Cell maturation: Hallmarks, triggers, and manipulation. *Cell* (2022).
267. Coll, T. *et al.* Palmitate-mediated downregulation of peroxisome proliferator-activated receptor-γ coactivator 1α in skeletal muscle cells involves MEK1/2 and nuclear factor-κB activation. *Diabetes* **55**, 2779–2787 (2006).
268. Horikoshi, Y. *et al.* Fatty Acid-Treated Induced Pluripotent Stem Cell-Derived Human Cardiomyocytes Exhibit Adult Cardiomyocyte-Like Energy Metabolism Phenotypes. *Cells* **8** (2019).
269. Finck, B. N. The PPAR regulatory system in cardiac physiology and disease. *Cardiovascular Research* **73**, 269–277 (2007).
270. Buroker, N. E., Ning, X. H. & Portman, M. Cardiac PPARα protein expression is constant as alternate nuclear receptors and PGC-1 coordinately increase during the postnatal metabolic Transition. *PPAR Res* (2008).
271. Wickramasinghe N. M. *et al.* PPARdelta activation induces metabolic and contractile maturation of human pluripotent stem cell-derived cardiomyocytes. *Cell Stem Cell* **29** (2022).
272. Pappachan, J. M., Varughese, G. I., Sriraman, R. & Arunagirinathan, G. Diabetic cardiomyopathy: Pathophysiology, diagnostic evaluation and management. *World J Diabetes* **4**, 177 (2013).
273. Vasanji, Z. *et al.* Alterations in cardiac contractile performance and sarcoplasmic reticulum function in sucrose-fed rats is associated with insulin resistance. *Am J Physiol Cell Physiol* **291**, 772–780 (2006).

274. Song, Y., Du, Y., Prabhu, S. D. & Epstein, P. N. Diabetic cardiomyopathy in OVE26 mice shows mitochondrial ROS production and divergence between in vivo and in vitro contractility. *Review of Diabetic Studies* **4**, 159–168 (2007).
275. Dong, F. *et al.* Impaired cardiac contractile function in ventricular myocytes from leptin-deficient ob/ob obese mice. *Journal of Endocrinology* **188**, 25–36 (2006).
276. Singh, R. M. *et al.* Hyperglycemia-induced cardiac contractile dysfunction in the diabetic heart. *Heart Failure Reviews* **23**, 37–54 (2018).
277. Cadeddu, C. *et al.* Early impairment of contractility reserve in patients with insulin resistance in comparison with healthy subjects. *Cardiovascular Diabetology* **12** (2013).
278. Ward, M.-L. Mechanisms underlying the impaired contractility of diabetic cardiomyopathy. *World J Cardiol* **6**, 577 (2014).
279. Umbarawan, Y. *et al.* Reduced fatty acid uptake aggravates cardiac contractile dysfunction in streptozotocin-induced diabetic cardiomyopathy. *Sci Rep* **10**, (2020).
280. Bruyneel, A. A., McKeithan, W. L., Feyen, D. A. & Mercola, M. Will iPSC-cardiomyocytes revolutionize the discovery of drugs for heart disease? *Curr Opin Pharmacol* **42**, 55–61 (2018).
281. Granéli, C., Hicks, R., Brolén, G., Synnergren, J. & Sartipy, P. Diabetic Cardiomyopathy Modelling Using Induced Pluripotent Stem Cell Derived Cardiomyocytes: Recent Advances and Emerging Models. *Stem Cell Rev Rep* **15**, 13–22 (2019).
282. Drawnel, F. M. *et al.* Disease modeling and phenotypic drug screening for diabetic cardiomyopathy using human induced pluripotent stem cells. *Cell Rep* **9**, 810–820 (2014).
283. Burkart, A. M. *et al.* Insulin Resistance in Human iPS Cells Reduces Mitochondrial Size and Function. *Sci Rep* **6**, 1–12 (2016).
284. Iovino, S., Burkart, A. M., Warren, L., Patti, M. E. & Kahn, C. R. Myotubes derived from human-induced pluripotent stem cells mirror in vivo insulin resistance. *Proc Natl Acad Sci U S A* **113**, 1889–1894 (2016).
285. Geraets, I. M. E. *et al.* Human embryonic stem cell-derived cardiomyocytes as an in vitro model to study cardiac insulin resistance. *Biochim Biophys Acta Mol Basis Dis* **1864**, 1960–1967 (2018).
286. Lewis-israeli, Y., Wasserman, A., Ball, K. & Li, B. Self-assembling human heart organoids for the modeling of cardiac development and congenital heart disease. *Nat Comm* 12, 5142 (2021).
287. Marfella, R. *et al.* Expression of Angiogenic Factors During Acute Coronary Syndromes in Human Type 2 Diabetes. *Diabetes* **53** (2004).
288. Chou, E. *et al.* Decreased Cardiac Expression of Vascular Endothelial Growth Factor and Its Receptors in Insulin-Resistant and Diabetic States A Possible Explanation for Impaired Collateral Formation in Cardiac Tissue. *Circulation* (2002).
289. Marfella, R. *et al.* Myocardial infarction in diabetic rats: Role of hyperglycaemia on infarct size and early expression of hypoxia-inducible factor 1. *Diabetologia* **45**, 1172–1181 (2002).

290. Ahmadi, N. *et al.* Concomitant insulin resistance and impaired vascular function is associated with increased coronary artery calcification. *Int J Cardiol* **144**, 163–165 (2010).
291. Abe, H., Semba, H. & Takeda, N. The roles of hypoxia signaling in the pathogenesis of cardiovascular diseases. *Journal of Atherosclerosis and Thrombosis* **24**, 884–894 (2017).
292. Szylberg, L. *et al*. Inflammation and hypoxia in atherosclerosis, coronary artery disease, and heart failure. *Folia Medica Copernicana* **3** (2015). ISSN 2300-5432
293. Aronson, D. & Rayfield, E. J. Cardiovascular Diabetology How hyperglycemia promotes atherosclerosis: molecular mechanisms. *Cardiovascular Diabetoology* **1** (2002).
294. Liu, Y. *et al.* Palmitate-induced vacuolar-type H+-ATPase inhibition feeds forward into insulin resistance and contractile dysfunction. in *Diabetes* **66**, 1521–1534 (American Diabetes Association Inc., 2017).
295. Sobczak, A. I. S., Blindauer, C. A. & Stewart, A. J. Changes in plasma free fatty acids associated with type-2 diabetes. *Nutrients* **11** (2019).
296. Basu, A. *et al.* Systemic and regional free fatty acid metabolism in type 2 diabetes. Am J Physiol Endocrinol Metab **280** (2001).
297. Ly, L. D. *et al.* Oxidative stress and calcium dysregulation by palmitate in type 2 diabetes. *Exp Mol Med* **49**, e291–e291 (2017).
298. Shanik, M. H. *et al.* Insulin resistance and hyperinsulinemia: is hyperinsulinemia the cart or the horse? *Diabetes care* **31** (2008).
299. Duncan, J. G., Fong, J. L., Medeiros, D. M., Finck, B. N. & Kelly, D. P. Insulin-resistant heart exhibits a mitochondrial biogenic response driven by the peroxisome proliferator-activated receptor-α/PGC-1α gene regulatory pathway. *Circulation* **115**, 909–917 (2007).
300. Kwon, B., Lee, H. K. & Querfurth, H. W. Oleate prevents palmitate-induced mitochondrial dysfunction, insulin resistance and inflammatory signaling in neuronal cells. *Biochim Biophys Acta Mol Cell Res* **1843**, 1402–1413 (2014).
301. Doehner, W. *et al.* Impaired insulin sensitivity as an independent risk factor for mortality in patients with stable chronic heart failure. *J Am Coll Cardiol* **46**, 1019–1026 (2005).
302. Ingelsson, E., Sundström, J., Ärnlöv, J., Zethelius, B. & Lind, L. Insulin Resistance and Risk of Congestive Heart Failure. JAMA **294** (2005).
303. Aasum, E., Hafstad, A. D., Severson, D. L. & Larsen, T. S. Age-Dependent Changes in Metabolism, Contractile Function, and Ischemic Sensitivity in Hearts From db/db Mice. *Diabetes* **52** (2003).
304. Rijzewijk, L. J. *et al.* Myocardial Steatosis Is an Independent Predictor of Diastolic Dysfunction in Type 2 Diabetes Mellitus. *J Am Coll Cardiol* **52**, 1793–1799 (2008).
305. Bell, D. S. H. Diabetic Cardiomyopathy, a unique entity or a complication of coronary artery disease. *Diabetes Care* **18** (1995).
306. Salvatore, T. *et al.* The Diabetic Cardiomyopathy: The Contributing Pathophysiological Mechanisms. *Frontiers in Medicine* **8** (2021).

307. Bauters, C. *et al.* Influence of diabetes mellitus on heart failure risk and outcome. Cardiovascular Diabetology **2** (2003).
308. Sousa Fialho, M. da L., Abd Jamil, A. H., Stannard, G. A. & Heather, L. C. Hypoxia-inducible factor 1 signalling, metabolism, and its therapeutic potential in cardiovascular disease. *Biochimica et Biophysica Acta - Molecular Basis of Disease* **1865**, 831–843 (2019).
309. Kerr, M. *et al.* Rescue of myocardial energetic dysfunction in diabetes through the correction of mitochondrial hyperacetylation by honokiol. *JCI Insight* **5** (2020).
310. Zhang, R., Hou, T., Cheng, H. & Wang, X. NDUFAB1 protects against obesity and insulin resistance by enhancing mitochondrial metabolism. *FASEB Journal* **33**, 13310–13322 (2019).
311. Hirschey, M. D. *et al.* SIRT3 deficiency and mitochondrial protein hyperacetylation accelerate the development of the metabolic syndrome. *Mol Cell* **44**, 177–190 (2011).
312. Verma, S., Chandra, H. & Banerjee, M. Cyclooxygenase 1 (COX1) expression in Type 2 diabetes mellitus: A preliminary study from north India. *Egyptian Journal of Medical Human Genetics* **17**, 41–45 (2016).
313. Cosentino, F. *et al.* High glucose causes upregulation of cyclooxygenase-2 and alters prostanoid profile in human endothelial cells: Role of protein kinase C and reactive oxygen species. *Circulation* **107**, 1017–1023 (2003).
314. Manivannan, S. *et al.* Single-cell transcriptomic profiling unveils dysregulation of cardiac progenitor cells and cardiomyocytes in a mouse model of maternal hyperglycemia. *Commun Biol* **5**, 820 (2022).
315. Preston, C. C. *et al.* Maternal High Fat Diet and Diabetes Disrupts Transcriptomic Pathways That Regulate Cardiac Metabolism and Cell Fate in Newborn Rat Hearts. *Front Endocrinol (Lausanne)* **11** (2020).
316. Sárközy, M. *et al.* Transcriptomic alterations in the heart of non-obese type 2 diabetic Goto-Kakizaki rats. *Cardiovasc Diabetol* **15** (2016).
317. Glyn-Jones, S. *et al.* Transcriptomic analysis of the cardiac left ventricle in a rodent model of diabetic cardiomyopathy: Molecular snapshot of a severe myocardial disease. *Physiol Genomics* **28**, 284–293 (2007).
318. Thimmappa, P. Y. *et al.* Quantitative phosphoproteomics reveals diverse stimuli activate distinct signaling pathways during neutrophil activation. *Cell Tissue Res* **389**, 241–257 (2022).
319. Sacco, F. *et al.* Phosphoproteomics Reveals the GSK3-PDX1 Axis as a Key Pathogenic Signaling Node in Diabetic Islets. *Cell Metab* **29**, 1422-1432.e3 (2019).
320. Nunez Lopez, Y. O. *et al.* Proteomics and Phosphoproteomics of Circulating Extracellular Vesicles Provide New Insights into Diabetes Pathobiology. *Int J Mol Sci* **23**, (2022).
321. Han, Y. *et al.* Effect of metformin on all-cause and cardiovascular mortality in patients with coronary artery diseases: A systematic review and an updated meta-analysis. *Cardiovasc Diabetol* **18** (2019).
322. Morgan, S., Grootendorst, P., Lexchin, J., Cunningham, C. & Greyson, D. The cost of drug development: A systematic review. *Health Policy* **100**, 4–17 (2011).

323. Warner, J. J. *et al.* Improving Cardiovascular Drug and Device Development and Evidence through Patient-Centered Research and Clinical Trials: A Call to Action from the Value in Healthcare Initiative's Partnering with Regulators Learning Collaborative. *Circ Cardiovasc Qual Outcomes* 485–500 (2020).
324. Paul, S. M. *et al.* How to improve RD productivity: The pharmaceutical industry's grand challenge. *Nature Reviews Drug Discovery* **9**, 203–214 (2010).
325. Bailey, J. & Balls, M. Recent efforts to elucidate the scientific validity of animal-based drug tests by the pharmaceutical industry, pro-testing lobby groups, and animal welfare organisations. *BMC Med Ethics* **20**, 1–7 (2019).
326. Zhang, A. *et al.* Effects of molidustat, a hypoxia-inducible factor prolyl hydroxylase inhibitor, on sodium dynamics in hypertensive subtotally nephrectomized rats. *J Pharmacol Sci* **146**, 98–104 (2021).
327. Chong, C., Liu, S., Sallustio, B., Chirkov, Y. & Horowitz, J. Effects of Perhexiline on Insulin and Nitric Oxide Signalling in Diabetics. *Heart Lung Circ* **25**, S86 (2016).
328. Sousa Fialho, M. da L. *et al.* Activation of HIF1α Rescues the Hypoxic Response and Reverses Metabolic Dysfunction in the Diabetic Heart. *Diabetes* **70**, 2518–2531 (2021).
329. Najafi, A., Sequeira, V., Kuster, D. W. D. & van der Velden, J. β-adrenergic receptor signalling and its functional consequences in the diseased heart. *European Journal of Clinical Investigation* **46**, 362–374 (2016).
330. Hoff, R. & Koh, C.-K. Isoproterenol Induced Insulin Resistance Leading to Diabetic Ketoacidosis in Type 1 Diabetes Mellitus. *Case Rep Endocrinol* **2018**, 1–3 (2018).
331. Soltysinska, E., Speerschneider, T., Winther, S. v. & Thomsen, M. B. Sinoatrial node dysfunction induces cardiac arrhythmias in diabetic mice. *Cardiovasc Diabetol* **13** (2014).
332. Noguchi, C. *et al.* Inhibitory effects of isoliquiritigenin and licorice extract on voltage-dependent K+ currents in H9c2 cells. *J Pharmacol Sci* **108**, 439–445 (2008).
333. American Diabetes Association. Pharmacologic approaches to glycemic treatment: Standards of medical care in diabetes. *Diabetes Care* **43**, S98–S110 (2020).
334. Alph, R. *et al.* Efficacy of metformin in patients with non-insulin-dependent diabetes mellitus. *J Med* **333** (1995).
335. King, P., Peacock, I. & Donnelly, R. The UK Prospective Diabetes Study (UKPDS): clinical and therapeutic implications for type 2 diabetes. *J Clin Pharmacol* **48** (1999).
336. Shang, F. *et al.* Cardiovascular protective effect of metformin and telmisartan: Reduction of PARP1 activity via the AMPK-PARP1 cascade. *PLoS One* **11** (2016).
337. Hawley, S. A., Gadalla, A. E., Olsen, G. S. & Grahame, D. The Antidiabetic Drug Metformin Activates the AMP-Activated Protein Kinase Cascade via an Adenine Nucleotide-Independent Mechanism. *Diabetes* **51** (2002).
338. Shaw, R. J. *et al.* The Kinase LKB1 Mediates Glucose Homeostasis in Liver and Therapeutic Effects of Metformin. *Science* **310** (2005).
339. Hou, W. L. *et al.* Inhibition of mitochondrial complex I improves glucose metabolism independently of AMPK activation. *J Cell Mol Med* **22**, 1316–1328 (2018).

340. Emelyanova, L. *et al.* Biphasic effect of metformin on human cardiac energetics. *Translational Research* **229**, 5–23 (2021).
341. Abozguia, K. *et al.* Metabolic modulator perhexiline corrects energy deficiency and improves exercise capacity in symptomatic hypertrophic cardiomyopathy. *Circulation* **122**, 1562–1569 (2010).
342. Kennedy, J. A., Unger, S. A. & Horowitz, J. D. Inhibition of Camitine Palmitoyltransferase-1 in Rat Heart and Liver by Perhexiline and Amiodarone. Biochemical Pharmacology **52** (1996).
343. Hue, L. & Taegtmeyer, H. The Randle cycle revisited: a new head for an old hat. *Am J Physiol Endocrinol Metab* **297**, 578–591 (2009).
344. Pilcher, J. Comparative trial of perhexiline maleate and oxprenolol in patients with angina pectoris. *Postgrad Med J* **54**, 663–667 (1978).
345. Gehmlich, K. *et al.* Changes in the cardiac metabolome caused by perhexiline treatment in a mouse model of hypertrophic cardiomyopathy. *Mol Biosyst* **11**, 564–573 (2015).
346. Wang, G. L. & Semenza, G. L. Purification and characterization of hypoxia-inducible factor. *Journal of Biological Chemistry* **270**, 1230–1237 (1995).
347. Iyer, N. v *et al.* Cellular and developmental control of O_2 homeostasis by hypoxia-inducible factor 1α. *Gene and Development* **12**, 149-162 (1998).
348. Jatho, A. *et al.* Precisely Tuned Inhibition of HIF Prolyl Hydroxylases Is Key for Cardioprotection after Ischemia. *Circulation Research* **128**, 1208–1210 (2021).
349. Schofield, C. J. & Ratcliffe, P. J. Oxygen sensing by HIF hydroxylases. *Nature Reviews Molecular Cell Biology* **5**, 343–354 (2004).
350. Sano, M. *et al.* p53-induced inhibition of Hif-1 causes cardiac dysfunction during pressure overload. *Nature* **446**, 444–448 (2007).
351. Kido, M. *et al.* Hypoxia-inducible factor 1-alpha reduces infarction and attenuates progression of cardiac dysfunction after myocardial infarction in the mouse. *J Am Coll Cardiol* **46**, 2116–2124 (2005).
352. Cerychova, R. & Pavlinkova, G. HIF1 Metabolism, and Diabetes in the Embryonic and Adult Heart. *Front Endocrinol (Lausanne)* **9**, 460 (2018).
353. Ambrose, L. J. A. *et al.* Investigating mitochondrial metabolism in contracting HL-1 cardiomyocytes following hypoxia and pharmacological HIF activation identifies HIF-dependent and independent mechanisms of regulation. *J Cardiovasc Pharmacol Ther* **19**, 574–585 (2014).
354. Böttcher, M. *et al.* First-in-man–proof of concept study with molidustat: a novel selective oral HIF-prolyl hydroxylase inhibitor for the treatment of renal anaemia. *Br J Clin Pharmacol* **84**, 1557–1565 (2018).
355. Macdougall, I. C., Akizawa, T., Berns, J. S., Bernhardt, T. & Krueger, T. Effects of molidustat in the treatment of anemia in CKD. *Clinical Journal of the American Society of Nephrology* **14**, 28–39 (2019).
356. Beck, H. *et al.* Discovery of Molidustat (BAY 85-3934): A Small-Molecule Oral HIF-Prolyl Hydroxylase (HIF-PH) Inhibitor for the Treatment of Renal Anemia. *ChemMedChem* **13**, 988–1003 (2018).

357. Asakura, K. *et al.* Improvement of acquisition and analysis methods in multi-electrode array experiments with iPS cell-derived cardiomyocytes. *J Pharmacol Toxicol Methods* **75**, 17–26 (2015).
358. Qiao, L. *et al.* Glucose Counteracts Isoprenaline Effects on Ion Channel Functions in Human-Induced Pluripotent Stem Cell-Derived Cardiomyocytes. *J Cardiovasc Dev Dis* **9**, (2022).
359. Brito-Martins, M., Harding, S. E. & Ali, N. N. β 1- and β 2-adrenoceptor responses in cardiomyocytes derived from human embryonic stem cells: Comparison with failing and non-failing adult human heart. *Br J Pharmacol* **153**, 751–759 (2008).
360. Lamoia, T. E. & Shulman, G. I. Cellular and Molecular Mechanisms of Metformin Action. *Endocrine Reviews* **42**, 77–96 (2021).
361. Zake, D. M. *et al.* Physiologically based metformin pharmacokinetics model of mice and scale-up to humans for the estimation of concentrations in various tissues. *PLoS One* **16** (2021).
362. Kajbaf, F., de Broe, M. E. & Lalau, J. D. Therapeutic Concentrations of Metformin: A Systematic Review. *Clinical Pharmacokinetics* **55**, 439–459 (2016).
363. Fontaine, E. Metformin-Induced Mitochondrial Complex I Inhibition: Facts, Uncertainties, and Consequences. *Front Endocrinol (Lausanne)* **9**, (2018).
364. Ota, S. *et al.* Metformin suppresses glucose-6-phosphatase expression by a complex I inhibition and AMPK activation-independent mechanism. *Biochem Biophys Res Commun* **388**, 311–316 (2009).
365. Saleem, U. *et al.* Blinded, multi-centre evaluation of drug-induced changes in contractility using human induced pluripotent stem cell-derived cardiomyocytes. *Toxicol Sci* **176**, 103-123 (2020)
366. Takeda, M. *et al.* Development of in vitro drug-induced cardiotoxicity assay by using three-dimensional cardiac tissues derived from human induced pluripotent stem cells. *Tissue Eng Part C Methods* **24**, 56–67 (2018).
367. Curtis, C. G., Bilyard, K. & Stephenson, H. Ex Vivo Metrics™, a preclinical tool in new drug development. *J Transl Med* **6**, 1–5 (2008).
368. Fermini, B., Coyne, S. T. & Coyne, K. P. Clinical Trials in a Dish: A Perspective on the Coming Revolution in Drug Development. *SLAS Discovery* **23**, 765–776 (2018).
369. Singh, V. K., Kalsan, M., Kumar, N., Saini, A. & Chandra, R. Induced pluripotent stem cells: Applications in regenerative medicine, disease modeling, and drug discovery. *Front Cell Dev Biol* **3**, 1–18 (2015).
370. Turan, B. & Dhalla, N. S. Diabetic Cardiomyopathy: Biochemical and Molecular Mechanisms. Diabetic Cardiomyopathy. *Advances in Biochemistry in Health and Disease* **9** (2014).
371. Bhamra, G. S. *et al.* Metformin protects the ischemic heart by the Akt-mediated inhibition of mitochondrial permeability transition pore opening. *Basic Res Cardiol* **103**, 274–284 (2008).
372. Trefts, E. & Shaw, R. J. AMPK: restoring metabolic homeostasis over space and time. *Molecular Cell* **81**, 3677–3690 (2021).

373. Wu, S. *et al.* Hyperglycemia-Driven Inhibition of AMP-Activated Protein Kinase 2 Induces Diabetic Cardiomyopathy by Promoting Mitochondria-Associated Endoplasmic Reticulum Membranes In Vivo. *Circulation* **139**, 1913–1936 (2019).
374. Bairwa, S. C., Parajuli, N. & Dyck, J. R. B. The role of AMPK in cardiomyocyte health and survival. *Biochimica et Biophysica Acta - Molecular Basis of Disease* **1862**, 2199–2210 (2016).
375. Wu, S. & Zou, M. H. AMPK, mitochondrial function, and cardiovascular disease. *International Journal of Molecular Sciences* **21**, 1–34 (2020).
376. Packer, M. Autophagy-dependent and -independent modulation of oxidative and organellar stress in the diabetic heart by glucose-lowering drugs. *Cardiovascular Diabetology* **19** (2020).
377. Witteles, R. M. & Fowler, M. B. Insulin-Resistant Cardiomyopathy. Clinical Evidence, Mechanisms, and Treatment Options. *Journal of the American College of Cardiology* **51**, 93–102 (2008).
378. Wu, H. *et al.* PGC-1α, glucose metabolism and type 2 diabetes mellitus. *Journal of Endocrinology* **229**, R99–R115 (2016).
379. Hoffman, E. P. The discovery of dystrophin, the protein product of the Duchenne muscular dystrophy gene. *FEBS Journal* **287**, 3879–3887 (2020).
380. Kamdar, F. & Garry, D. J. Dystrophin-Deficient Cardiomyopathy. *Journal of The American College of Cardiology* **67** (2016).
381. Timpani, C. A., Hayes, A. & Rybalka, E. Revisiting the dystrophin-ATP connection: How half a century of research still implicates mitochondrial dysfunction in Duchenne Muscular Dystrophy aetiology. *Med Hypotheses* **85**, 1021–1033 (2015).
382. Ormazabal, V. *et al.* Association between insulin resistance and the development of cardiovascular disease. *Cardiovascular Diabetology* **17** (2018).
383. Yao, S. *et al.* Current Pharmacological Strategies for Duchenne Muscular Dystrophy. *Frontiers in Cell and Developmental Biology* **9** (2021).
384. Soblechero-Martín, P. *et al.* Duchenne muscular dystrophy cell culture models created by CRISPR/Cas9 gene editing and their application in drug screening. *Sci Rep* **11** (2021).
385. Potter, R. A. *et al.* Dose-Escalation Study of Systemically Delivered rAAVrh74.MHCK7 micro-dystrophin in the mdx Mouse Model of Duchenne Muscular Dystrophy. *Hum Gene Ther* **32**, 375–389 (2021).
386. Omairi, S. *et al.* Regulation of the dystrophin-associated glycoprotein complex composition by the metabolic properties of muscle fibres. *Sci Rep* **9** (2019).
387. Dominski, Z. & Kole, R. Restoration of correct splicing in thalassemic pre-mRNA by antisense oligonucleotides. *Proc. Natl.' Acad. Sci. USA* **90** (1993).
388. Manini, A., Abati, E., Nuredini, A., Corti, S. & Comi, G. pietro. Adeno-Associated Virus (AAV)-Mediated Gene Therapy for Duchenne Muscular Dystrophy: The Issue of Transgene Persistence. *Frontiers in Neurology* **12** (2022).
389. Arechavala-Gomeza, V. *et al.* Exon skipping and dystrophin restoration in patients with Duchenne muscular dystrophy after systemic phosphorodiamidate morpholino oligomer treatment: an open-label, phase 2, dose-escalation study. *Lancet* **378**, 595–605 (2011).

390. Meng, S. *et al.* Metformin activates AMP-activated protein kinase by promoting formation of the αβγheterotrimeric complex. *Journal of Biological Chemistry* **290**, 3393–3802 (2015).
391. Kim, J., Yang, G., Kim, Y., Kim, J. & Ha, J. AMPK activators: Mechanisms of action and physiological activities. *Experimental and Molecular Medicine* **48** (2016).
392. Kang, M. J. *et al.* Metformin induces muscle atrophy by transcriptional regulation of myostatin via HDAC6 and FoxO3a. *J Cachexia Sarcopenia Muscle* **13**, 605–620 (2022).
393. Hernández-Álvarez, D. *et al.* Long-Term Moderate Exercise Combined with Metformin Treatment Induces an Hormetic Response That Prevents Strength and Muscle Mass Loss in Old Female Wistar Rats. *Oxid Med Cell Longev* **2019** (2019).
394. McGreevy, J. W., Hakim, C. H., McIntosh, M. A. & Duan, D. Animal models of Duchenne muscular dystrophy: From basic mechanisms to gene therapy. *DMM Disease Models and Mechanisms* **8**, 195–213 (2015).
395. Schultz, T. I., Raucci, F. J. & Salloum, F. N. Cardiovascular Disease in Duchenne Muscular Dystrophy. *JACC Basic Transl Sci* (2022).
396. Shin, J., Tajrishi, M. M., Ogura, Y. & Kumar, A. Wasting mechanisms in muscular dystrophy. *International Journal of Biochemistry and Cell Biology* **45**, 2266–2279 (2013).
397. Allen, D.G., Whitehead, N. P. & Froehner, S. C. Absence of dystrophin disrupts skeletal muscle oxide in the development roles of Ca^{2+}, reactive oxygen species, and nitric oxide in the development of muscular dystrophy. *Physiol Rev* **96,** 253-305 (2016).
398. Zhang, W. *et al.* Abnormal cardiac morphology, function and energy metabolism in the dystrophic mdx mouse: An MRI and MRS study. *J Mol Cell Cardiol* **45**, 754–760 (2008).
399. Pioner, J. M. *et al.* Absence of full-length dystrophin impairs normal maturation and contraction of cardiomyocytes derived from human-induced pluripotent stem cells. *Cardiovasc Res* **116**, 368–382 (2020).
400. Kaspar, R. W., Allen, H. D. & Montanaro, F. Current understanding and management of dilated cardiomyopathy in Duchenne and Becker muscular dystrophy. *J Am Acad Nurse Pract* **21**, 241–249 (2009).
401. Han, L. *et al.* Study familial hypertrophic cardiomyopathy using patient-specific induced pluripotent stem cells. *Cardiovasc Res* **104**, 258–269 (2014).
402. Christ, T., Koivumäki, J. T. & Eschenhagen, T. Prolonged action potentials in HCM-derived iPSC-biology or artefact? *Cardiovascular Research* **106**, 6 (2015).
403. Hwang, H. S. *et al.* Comparable calcium handling of human iPSC-derived cardiomyocytes generated by multiple laboratories. *J Mol Cell Cardiol* **85**, 79–88 (2015).
404. Kane, C. & Terracciano, C. M. Induced pluripotent stem cell-derived cardiac myocytes to understand and test calcium handling: Pie in the sky? *Journal of Molecular and Cellular Cardiology* **89**, 376–378 (2015).

405. Zhang, M., Qian, L., Liu, C., Huang, G. N. & Tao, G. Editorial: Cardiomyocyte Maturation: Novel Insights for Regenerative Medicine. *Frontiers in Cell and Developmental Biology* **9** (2021).
406. Piquereau, J. & Ventura-Clapier, R. Maturation of cardiac energy metabolism during perinatal development. *Front Physiol* **9**, 1–10 (2018).
407. Machiraju, P. & Greenway, S. C. Current methods for the maturation of induced pluripotent stem cellderived cardiomyocytes. *World Journal of Stem Cells* **11**, 33–43 (2019).
408. Ronaldson-Bouchard, K. *et al.* Advanced maturation of human cardiac tissue grown from pluripotent stem cells. *Nature* **556**, 239–243 (2018).
409. Lundy, S. D., Zhu, W. Z., Regnier, M. & Laflamme, M. A. Structural and functional maturation of cardiomyocytes derived from human pluripotent stem cells. *Stem Cells Dev* **22**, 1991–2002 (2013).
410. Hansen, D. K., Inselman, A. L. & Yang, X. Effects of Culture Conditions on Maturation of Stem Cell-Derived Cardiomyocytes. *Stem Cells in Toxicology and Medicine* 71–84 (2016)
411. Schaaf, S. *et al.* Human engineered heart tissue as a versatile tool in basic research and preclinical toxicology. *PLoS One* **6** (2011).
412. Jia, G., Whaley-Connell, A. & Sowers, J. R. Diabetic cardiomyopathy: a hyperglycaemia- and insulin-resistance-induced heart disease. *Diabetologia* **61**, 21–28 (2018).
413. Mazumder, P. K. *et al.* Impaired Cardiac Efficiency and Increased Fatty Acid Oxidation in Insulin-Resistant ob/ob Mouse Hearts. *Diabetes* **53** (2004).
414. van Oort, M. M. *et al.* Insulin-induced translocation of CD36 to the plasma membrane is reversible and shows similarity to that of GLUT4. *Biochim Biophys Acta Mol Cell Biol Lipids* **1781**, 61–71 (2008).